Pathomechanisms underlying ischemic stroke

•••

Pathomechanismen des ischämischen Schlaganfalles

Doctoral thesis for a doctoral degree at the Graduate School of Life Sciences,
Julius-Maximilians-Universität Würzburg,

Section Biomedicine

Submitted by

Vanessa Aline Domenica Göb née Klaus

from Nuremberg

Würzburg, 2022

Submitted on:

Members of the Thesis Committee:

Chairperson: Prof. Dr. Georg Gasteiger

Primary Supervisor: Prof. Dr. David Stegner

Supervisor (Second): Prof. Dr. Katrin G. Heinze

Supervisor (Third): Prof. Dr. Guido Stoll

Date of Public Defense: ____________________

Date of receipt of Certificates: ____________________

Table of contents

Summary

Every year, stroke affects over 100 million people worldwide and the number of cases continues to grow. Ischemic stroke is the most prevalent form of stroke and rapid restoration of blood flow is the primary therapeutic aim. However, recanalization might fail or reperfusion itself induces detrimental processes leading to infarct progression. Previous studies identified platelets and immune cells as drivers of this so-called ischemia/reperfusion (I/R) injury, establishing the concept of ischemic stroke as thrombo-inflammatory disease. Reduced cerebral blood flow despite recanalization promoted the hypothesis that thrombus formation within the cerebral microcirculation induces further tissue damage. The results presented in this thesis refute this: using complementary methodologies, it was shown that infarct growth precedes the occurrence of thrombi excluding them as I/R injury-underlying cause. Blood brain barrier disruption is one of the hallmarks of ischemic stroke pathology and was confirmed as early event during reperfusion injury in the second part of this study. Abolished platelet α-granule release protects mice from vascular leakage in the early reperfusion phase resulting in smaller infarcts. Using *in vitro* assays, platelet α-granule-derived PDGF-AB was identified as one factor contributing to blood-brain barrier disruption.

In vivo visualization of platelet activation would provide important insights in the spatio-temporal context of platelet activation in stroke pathology. As platelet signaling results in elevated intracellular Ca^{2+} levels, this is an ideal readout. To overcome the limitations of chemical calcium indicators, a mouse line expressing an endogenous calcium reporter specifically in platelets and megakaryocytes was generated. Presence of the reporter did not interfere with platelet function, consequently these mice were characterized in *in vivo* and *ex vivo* models.

Upon ischemic stroke, neutrophils are among the first cells that are recruited to the brain. Since for neutrophils both, beneficial and detrimental effects are described, their role was investigated within this thesis. Neither neutrophil depletion nor absence of NADPH-dependent ROS production (*Ncf*$^{-/-}$ mice) affected stroke outcome. In contrast, abolished NET-formation in *Pad4*$^{-/-}$ mice resulted in reduced infarct sizes, revealing detrimental effects of NETosis in the context of ischemic stroke, which might become a potential therapeutic target.

Cerebral venous (sinus) thrombosis, CV(S)T is a rare type of stroke with mainly idiopathic onset. Whereas for arterial thrombosis a critical contribution of platelets is known and widely accepted, for venous thrombosis this is less clear but considered more and more. In the last part of this thesis, it was shown that fab-fragments of the anti-CLEC-2 antibody INU1 trigger pathological platelet activation *in vivo*, resulting in foudroyant CVT accompanied by heavy neurological symptoms. Using this novel animal model for CVT, cooperative signaling of the two platelet receptors CLEC-2 and GPIIb/IIIa was revealed as major trigger of CVT and potential target for treatment.

Zusammenfassung

Jährlich sind weltweit über 100 Millionen Menschen von einem Schlaganfall betroffen, wobei die Zahl der Fälle weiter zunimmt. Der ischämische Schlaganfall ist die häufigste Form des Schlaganfalls, und die sofortige Wiederherstellung des Blutflusses ist das oberste Therapieziel. Allerdings kommt es vor, dass die Rekanalisierung des betroffenen Gefäßes fehlschlägt oder die Reperfusion selbst zu schädlichen Prozessen führt, die das Fortschreiten des Infarkts begünstigen. In vorangegangen Studien wurden Thrombozyten und Immunzellen als treibende Kräfte dieser so genannten Ischämie/Reperfusion (I/R)-Schädigung identifiziert und der ischämische Schlaganfall als thrombo-inflammatorische Erkrankung definiert. Eine verminderte zerebrale Durchblutung trotz Rekanalisation führte zu der Hypothese, dass die Bildung von Thromben in der zerebralen Mikrozirkulation zu weiteren Gewebeschäden führt. Die hier vorgestellten Ergebnisse widerlegen dies: Mit Hilfe komplementärer Methoden konnte gezeigt werden, dass das Infarktwachstum dem Auftreten von Thromben vorausgeht, was diese als Ursache für die I/R-Verletzung ausschließt.

Die Störung der Blut-Hirn-Schranke ist eines der charakteristischen Kennzeichen der Pathologie des ischämischen Schlaganfalls und wurde im zweiten Teil dieser Studie als frühes Ereignis während des Reperfusionsschadens bestätigt. Mit Hilfe transgener Mäuse konnte gezeigt werden, dass die Ausschüttung von α-Granula aus Thrombozyten in der frühen Reperfusionsphase an Störungen der Blut-Hirn-Schranke beteiligt ist und somit zum Infarktwachstum beiträgt. In *in-vitro*-Versuchen konnte gezeigt werden, dass PDGF-AB, ein Bestandteil der α-Granula, an Prozessen, die für die Beeinträchtigung der Blut-Hirn-Schranke verantwortlich sind, beteiligt ist.

Die Sichtbarmachung von aktivierten Thrombozyten *in vivo*, würde wichtige Erkenntnisse über den räumlichen und zeitlichen Kontext der Aktivierung von Thrombozyten im Verlauf des Schlaganfalls liefern. Da alle aktivierenden Signalwege zum Anstieg des intrazellulären Kalziumspiegels führen, ist Kalzium ein idealer Indikator der Thrombozytenaktivierung. Um die Grenzen chemischer Kalziumindikatoren zu überwinden, wurde eine transgene Mauslinie erzeugt, welche einen endogenen Kalziumreporter speziell in Thrombozyten und Megakaryozyten exprimiert. Die Anwesenheit des Reporters hatte keine Auswirkung auf die Funktionalität der Thrombozyten und die Mäuse wurden *in vivo* sowie *ex vivo* in verschiedenen Experimenten charakterisiert.

In der Folge eines ischämischen Schlaganfalles gehören Neutrophile zu den am frühesten ins Gehirn einwandernden Zellen. Dabei werden Neutrophilen sowohl günstige als auch schädliche Wirkungen auf den Verlauf des ischämischen Schlaganfalls zugeschrieben. Aus diesem Grund wurde ihre Rolle in dieser Arbeit näher untersucht. Weder die Abwesenheit von Neutrophilen noch das Fehlen der NADPH-abhängigen Produktion von reaktiven Sauerstoffspezies (*Ncf1*$^{-/-}$ Mäuse) beeinflussen den Ausgang eines Schlaganfalls. Im

Gegensatz dazu, führte die Verhinderung der NET-Bildung (NET = *neutrophil extracellular traps*) in *Pad4*$^{-/-}$ Mäusen zu verringerten Infarktgrößen, was auf eine schädliche Wirkung der NETose im Zusammenhang des Schlaganfalls hinweist und somit ein therapeutisches Angriffsziel darstellen könnte.

Sinusvenenthrombosen sind eine seltene Form des Schlaganfalls, die meist ohne bekannte Ursache auftreten. Während für die arterielle Thrombose ein kritischer Beitrag der Thrombozyten bekannt und weithin akzeptiert ist, ist dies für venöse Thrombosen weniger klar, wird aber immer mehr in Betracht gezogen. Im letzten Teil dieser Arbeit wurde gezeigt, dass Fab-Fragmente des anti-CLEC-2-Antikörpers INU1 *in vivo* eine pathologische Aktivierung von Thrombozyten auslösen, die zu einer fulminanten Sinusvenenthrombose mit schweren neurologischen Symptomen führt. Mit Hilfe dieses neuartigen Tiermodells wurde die zusammenwirkende Signalübertragung der beiden Thrombozytenrezeptoren CLEC-2 und GPIIb/IIIa als Hauptauslöser der Sinusvenenthrombose und damit potenzielles Ziel für eine Behandlung identifiziert.

1 Introduction

In 2017, the global prevalence of stroke was 104.2 million people [1] and 6.2 million deaths every year can be attributed to cerebrovascular disease. Affecting so many people, stroke is among the leading causes of death and a major cause for adult disability worldwide with increasing tendency. By 2047, an increase in stroke incidence of 28% in the EU population is estimated [2]. With populations becoming older and medical support getting better, more people are likely to survive a stroke. Therefore, also the demand for long-term care and rehabilitation will increase. Already now, direct and indirect costs of stroke are estimated at 45 € billion per year [2]. Stroke can be caused either by a clot obstructing the blood supply to the brain (ischemic stroke) or by a blood vessel rupture preventing blood flow to the brain. About 87% of strokes are ischemic, 10% are due to intracerebral hemorrhage (ICH) and 3% are due to subarachnoidal hemorrhage (SAH) [1]. Being long known only for their role in hemostasis, platelets are increasingly recognized also for emerging roles besides thrombosis and hemostasis in various diseases. In the context of stroke, numerous experimental studies have established a contribution of platelets and immune cells to ischemia/reperfusion injury of the brain. Due to the high prevalence of stroke and the so far limited therapeutic options, understanding of the underlying pathomechanisms is critical for the development of new therapeutic strategies. Improving therapy would increase survival, increase the quality of life of stroke survivors and reduce the need for long-term care.

1.1 The brain

The brain is a complex organ that controls thought, emotion, touch, motor skills, breathing, memory, hunger, temperature and almost every other process that regulates our body. Of note, it consists of about 60% fat, while the rest is a combination of water, protein, carbohydrates, and salts. Together with the spinal cord, the brain makes up the central nervous system (CNS). It consists of cerebrum, brainstem and cerebellum. The cerebrum is the largest part and is composed of two cerebral hemispheres. The cerebral cortex, the outer region of the hemispheres is the grey matter, which consists of cortical layers of neurons. The subcortical, deeper regions contain myelinated axons and are called the white matter. The cerebellum is a small part of the brain that coordinates voluntary muscle movements, maintenance of posture and balance, and the brainstem connects the cerebrum with the spinal cord. The CNS is covered by three membranes, called meninges: the outer, though dura mater, the arachnoid mater and the inner, delicate pia mater. The space between the latter (subarachnoid space) contains the cerebrospinal fluid (CSF).

The brain is a highly metabolic organ but lacks effective mechanisms of glucose and oxygen storage. Although the brain comprises only about 2% of the total body weight, it utilizes 25%

of total oxygen consumption. Therefore, a constant supply of oxygen via large amounts of blood is mandatory [3]. The intracranial vasculature is special. Arteries and veins are surrounded by CSF after they penetrate the dura mater and arachnoid membranes. The intracranial veins drain in the dural venous sinuses which do not exist outside the skull [3]. The brain is supplied with blood from two arterial systems: the internal carotid arteries which come from the common carotid artery in the neck, and the vertebral arteries (Figure 1-1). The internal carotid arteries branch into the anterior and middle cerebral arteries. The right and left vertebral arteries come together and form the basilar artery, which unites the blood supply from the internal carotids in an arterial ring at the base of the brain, the circle of Willis [4]. Here, the posterior cerebral arteries originate and two bridging arteries, the posterior and anterior communicating arteries, are formed. Hence, the circle of Willis represents an interconnection between the anterior and posterior cerebral circulation. (Figure 1-1A, Zoom-in). The circle of Willis is part of the collateral circulation of the brain, which is a network of cerebral vessels and serves to stabilize and secure the blood supply. Especially in conditions like ischemic stroke, collaterals are important since they can maintain residual blood flow to brain regions distal to an arterial occlusion (Figure 1-7). The circle of Willis is the main network which enables the brain vasculature to compensate for a larger artery occlusion [5]. If this is not possible, compensation can be achieved by the leptomeningeal anastomoses. These are cortical pial arteries that connect the major branches of the anterior cerebral artery (ACA), the middle cerebral artery (MCA) and the posterior cerebral artery (PCA). In the leptomeningeal anastomoses, retrograde perfusion is possible, allowing at least partial perfusion in the ischemic penumbra, protecting the brain tissue in this area from sudden irreversible cellular death [6]. Studies show that the degree and quality of the collateral circulation influence the final infarct size and functional deficit in stroke patients [5, 7].

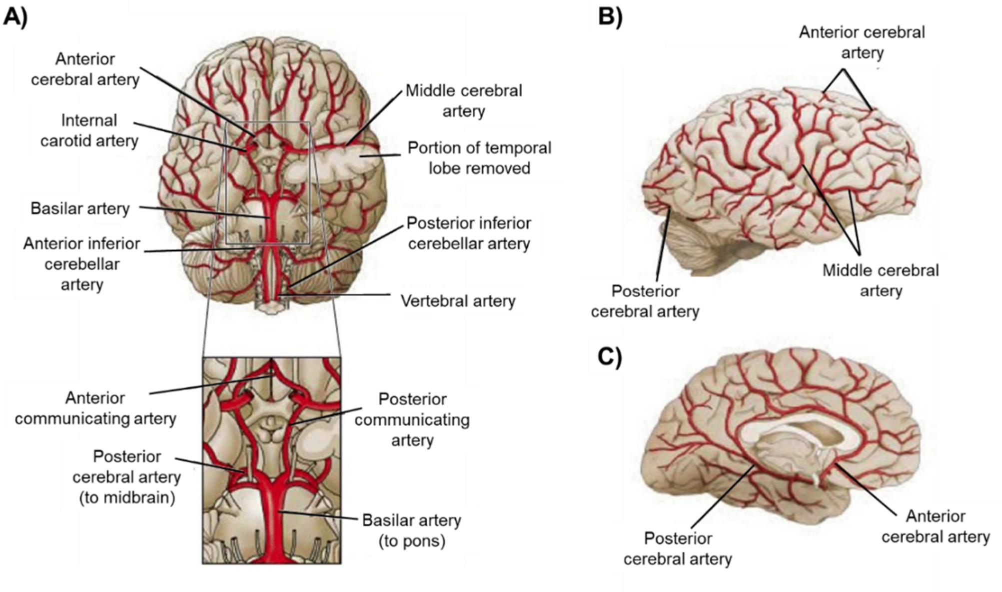

Figure 1-1: The major arteries of the brain. (A) Ventral view. The enlargement shows the circle of Willis. Lateral **(B)** and midsagittal **(C)** views showing anterior, middle and posterior arteries. Modified from Purves D, 2001 [4].

The cerebral venous system can be divided into a deep and a superficial system. The sagittal sinuses and cortical veins belong to the superficial system. They drain the superficial surfaces of both hemispheres and lie on the surface of the cerebral cortex [8] (Figure 1-2). The deep system contains the lateral sinus, the straight sinus, the sigmoid sinus and deeper cortical veins and drains the deep white and grey matter [8, 9]. In general, venous blood is collected in the nearest sinus, or in case of blood from the deepest structures, into deep veins. Ultimately, both systems mostly drain in the jugular veins [8]. Figure 1-2 gives an overview of the main parts of the cerebral venous system.

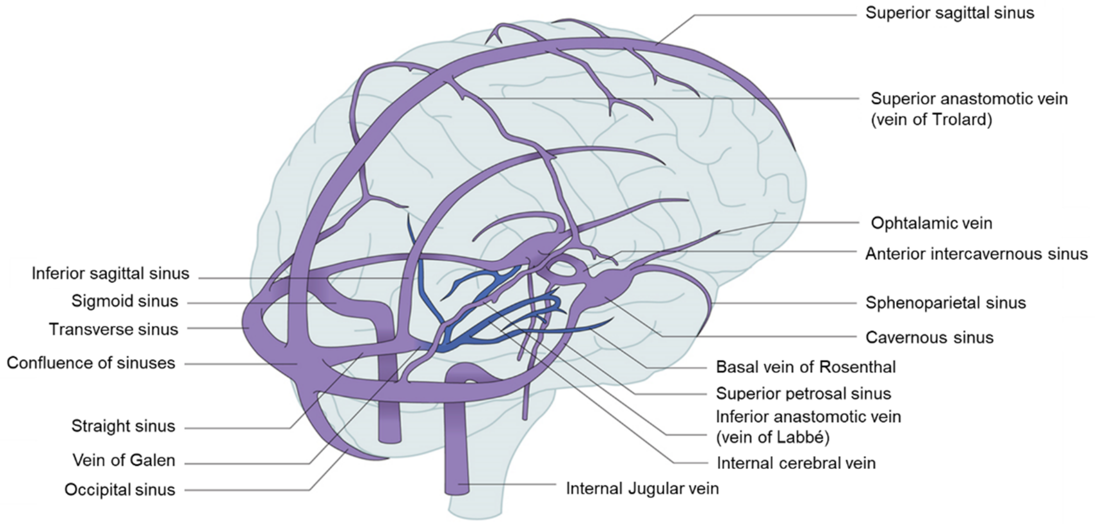

Figure 1-2: Anatomy of the cerebral venous system. Main components of the cerebral venous system. Blue vessels represent the deep venous system**.** Taken from Silvis *et al.*, 2017 [10].

The mouse brain differs in some regards from the human brain. It is smaller and has a lisencephalic surface (no folding), whereas the human brain has a folded cortex (gyrencephalic surface). This translates into a markedly reduced cell number in the murine brain (approx. 33 million cells) compared to the human brain (approx. 86 billion cells) [11]. Another difference is the ratio of grey and white matter, which is 40:60 in humans and 90:10 in mice. Regarding the vasculature, however, rodents have a very similar vascularization pattern in the cortex, even down to the capillary bed [12, 13].

1.2 Platelets

Platelets are small anucleated cell fragments with a discoid shape. They are released into the circulation as so-called proplatelets by megakaryocytes (MKs) in the bone marrow. Due to the occurring shear forces in the blood, proplatelets are further fragmented into platelets [14]. In parallel, aged platelets are constantly removed from the circulation mainly by macrophages in the reticuloendothelial system of liver and spleen, maintaining platelet counts of 150,000-450,000/µl in humans and approximately 1,000,000/µl in mice. With a diameter of 3-4 µm (approx. 2 µm in mice), platelets represent the smallest cells in the blood where they circulate for about 7–10 days in humans and approximately 5 days in mice. Platelets are essential to safeguard vascular integrity and ensure hemostasis, meaning the prevention and stopping of bleeding in case of vascular injury. Although most of them never undergo activation or firm adhesion, platelets can respond immediately to damages in the endothelial layer by forming a plug preventing blood loss. Here, the exposure of components of the extracellular matrix (ECM), such as collagens and laminins, triggers initial platelet adhesion and activation. Besides platelets, ensuring proper hemostasis requires a functional coagulation cascade. The activation of the coagulation system results in the formation of thrombin, which induces the conversion of fibrinogen to fibrin. In turn, thrombin also acts as a powerful platelet activator. The coagulation cascade can either be initiated by locally exposed tissue factor (TF) (extrinsic pathway) or by the activation of coagulation factor (F)XII (intrinsic pathway or contact-activation). Activated platelets release soluble mediators leading to the recruitment and activation of other circulating platelets, finally resulting in thrombus formation. Under pathological conditions however, this may lead to irreversible vessel occlusion and consequently to ischemic tissue damage. If this occurs in coronary arteries or in the brain, it may result in myocardial infarction or stroke, respectively.

To ensure functional hemostasis and simultaneously avoid uncontrolled vessel occlusion, platelets possess a complex signaling network with both, activating and inhibiting pathways.

1.2.1 Platelet activation and thrombus formation

Platelet activation and thrombus formation at sites of vascular injury involve multiple signaling processes which can be divided into three major steps: tethering, activation and firm adhesion (Figure 1-3).

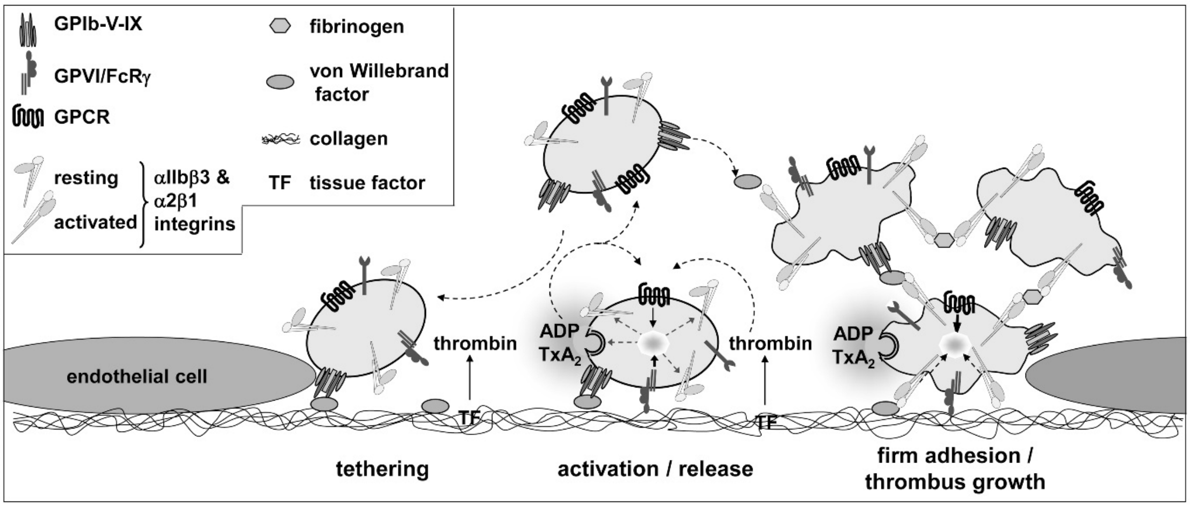

Figure 1-3: Model for platelet adhesion to the subendothelial matrix at sites of vascular injury and subsequent thrombus formation. Interaction of GPIb with vWF mediates the initial contact of platelets to the ECM (tethering). Deceleration enables GPVI-collagen interactions resulting in platelet activation, the shift of low affinity integrins to a high affinity state and the release of soluble mediators like ADP, ATP and TxA_2. In parallel, locally exposed TF induces thrombin formation which activates additional platelets allowing the thrombus to grow. Firm adhesion and stable thrombus formation are secured by αIIbβ3-bound fibrinogen or vWF. GP, glycoprotein; vWF, von Willebrand factor; ADP, adenosine diphosphate; TxA_2, thromboxane A_2; TF, tissue factor. Taken from Stegner *et al.,* 2011 [15].

Due to different vessel diameters in the vascular system, different rheological conditions are present in the circulation. In arterioles or stenoses arteries, high shear rates require platelet deceleration to enable platelet receptors to come into contact with their ligands. Initial platelet tethering to the ECM is mediated by Glycoprotein (GP) Ib - vWF (von Willebrand factor) interactions. Since this binding is only transient and reversible, it is not sufficient for firm adhesion but facilitates platelet “rolling” along the side of injury and enables closer contact to the ECM [16]. However, evidence is given that GPIb itself can transduce weak αIIbβ3-integrin activation [17]. In the second step in thrombus formation platelets bind to exposed collagen via the major collagen receptor GPVI. This triggers the activation of platelet integrins and the subsequent release of secondary mediators such as thromboxane (Tx) A_2 and adenosine diphosphate (ADP). Together with locally produced thrombin, these mediators enhance platelet activation by binding to G protein-coupled receptors (GPCR) (Gq, G12/13, Gi) [18]. Finally, firm adhesion is mediated by activation of β1 integrins binding to collagen (α2β1), fibronectin (α5β1) and laminin (α6β1) and active β3 integrins binding to vitronectin (αvβ3) as well as to fibronectin and vWF via the major platelet integrin αIIbβ3 (GPIIb/IIIa) [19]. Thrombus growth is achieved by the recruitment and activation of further platelets, bridging them via fibrinogen and vWF binding to integrin αIIbβ3 [20]. During platelet activation, degranulation is a major step to achieve full activation and formation of stable thrombi. Platelets contain three major types of granules: α-granules, dense granules and lysosomes. With 50-80 granules per platelet, α-granules are the most abundant type [21]. They contain more than 300 different proteins such as vWF, fibrinogen and thrombospondin as well as growth and coagulation factors. α-granule content is known to be involved in many processes such as platelet adhesion, hemostasis, wound healing, host defense and tumor growth [21]. Dense granules (5-6 granules/mouse platelet) contain high concentrations of Ca^{2+}, Mg^{2+}, ADP, ATP and serotonin [22]. Together with locally produced TxA_2, ADP and ATP they are the most important secondary mediators for autocrine and paracrine platelet activation. Lysosomes contain proteolytic enzymes like proteases, glycosidases and cationic proteins with bactericidal activity proteins [23].

1.2.2 Platelet signaling

In general, platelet signaling can be classified according to two major pathways. Depending on downstream signal transduction, receptors are grouped in (hem)ITAM-bearing receptors (see 1.2.2.1) and GPCRs. This enables a complex network of interacting signaling pathways, finally resulting in the activation of phospholipase C (PLC) isoforms (Figure 1-4). After activation, PLC converts phosphatidylinositol-2-phosphate (PIP_2) to inositol-1,4,5-triphosphate (IP_3) and diacylglycerol (DAG) [15]. IP_3 and DAG trigger Ca^{2+} mobilization from intracellular stores by different mechanisms (see 1.2.2.2). Rise in cytosolic Ca^{2+} concentration is essential for platelet activation processes such as granule release, integrin activation and procoagulant activity as well as rearrangement of the cytoskeleton [15, 24].

GPCRs are stimulated via soluble platelet agonists like ADP, thrombin or thromboxane A_2 (TxA_2). Depending on the coupled G protein, different signaling pathways are initiated being involved in integrin activation, aggregation and degranulation as well as platelet shape change [18].

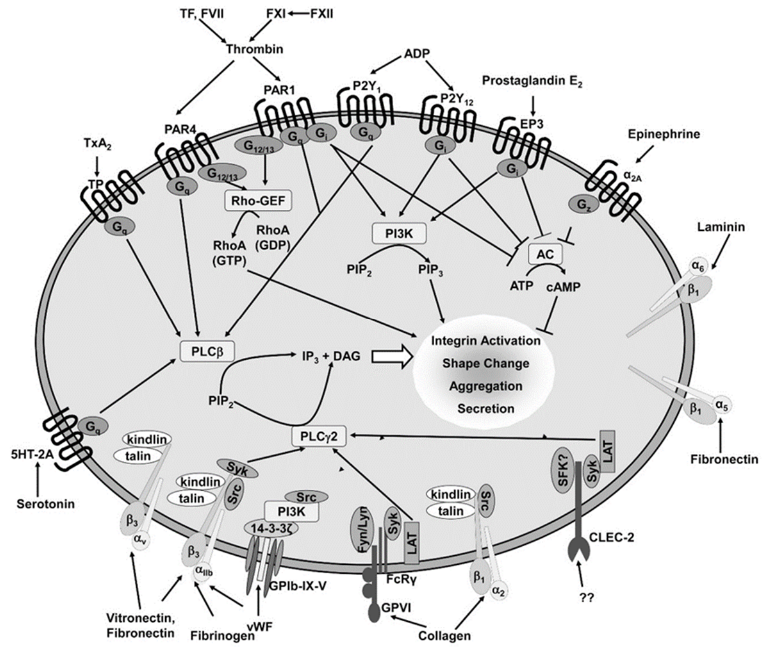

Figure 1-4: Platelet receptors and important signaling molecules leading to platelet activation. Platelet activation is transduced via different types of receptors. G protein-coupled receptors are activated by soluble agonists triggering pathways involving the respective G protein, finally leading to activation of phospholipase (PL) Cβ or phosphatidylinositol-4,5-biphosphate 3-kinase (PI3K). (Hem)ITAM-coupled receptors such as GPVI and CLEC-2 result in the activation of phospholipase (PL) Cγ2. PIP_2, phosphatidylinositol-4,5-bisphosphate; PAR, protease-activated receptor; TxA_2, thromboxane A_2; TP, TxA_2 receptor; RhoGEF, Rho-specific guanine nucleotide exchange factor; PI3K, phosphoinositide-3-kinase; PIP_3, phosphatidylinositol-3,4,5-trisphosphate; AC, adenylcyclase. Taken from Stegner *et al.*, 2011 [15].

1.2.2.1 (hem)ITAM receptor signaling

The immunoreceptor tyrosine-based activation motif (ITAM) is a highly conserved signaling motif which is used by a variety of receptors expressed on hematopoietic cells like B and T lymphocytes, macrophages and platelets [25]. Murine platelets express two receptors that signal via an ITAM: the GPVI/FcRγ-complex and the C-type lectin receptor 2 (CLEC-2). On human platelets a third ITAM receptor, the FcγRIIA is expressed [26]. GPVI is the major collagen receptor [15] and CLEC-2 has been discovered to bind the snake venom rhodocytin and the, so far, only known endogenous ligand podoplanin [27].

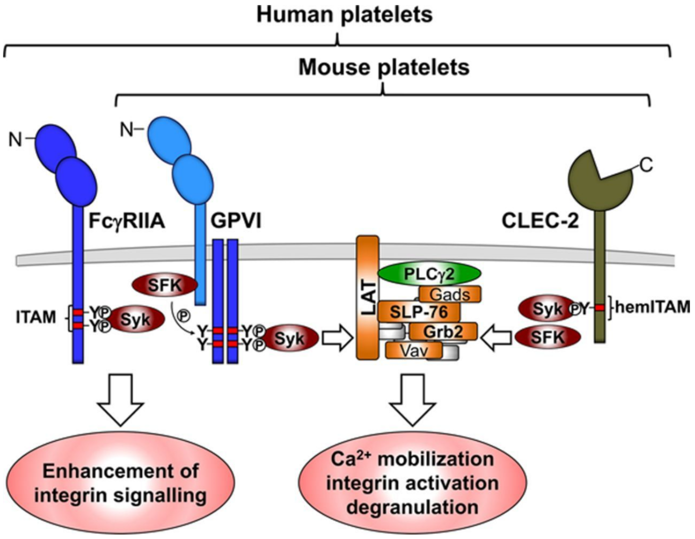

Figure 1-5: (hem)ITAM receptors in platelets. Glycoprotein VI (GPVI) is constitutively associated with the Fc receptor γ (FcRγ) chain, which bears an ITAM. Receptor clustering by ligands initiates phosphorylation of the FcRγ chain in the ITAM motif by the Src family kinases (SFK), which induce the recruitment and subsequent activation of spleen tyrosine kinase (Syk). The recruitment of Syk to the ITAM initiates a signaling cascade that involves a large number of kinases, adaptor, and effector molecules, critically including linker for activation of T cells (LAT), SH2 domain–containing leukocyte protein of 76 kDa (SLP-76), growth factor receptor–bound protein 2 (Grb-2), Grb2-related adapter protein 2 (Gads), Vav proteins, and phospholipase C γ2 (PLCγ2), which form the GPVI signalosome. The Fc receptor FcγRIIA, which is expressed on human but not on mouse platelets, also signals through an ITAM and contributes to integrin outside-in signaling through Syk. C-type lectin-like receptor 2 (CLEC-2) contains half an ITAM (a YxxL sequence with an upstream stretch of acid amino acids) in its cytoplasmic tail and so is termed a (hem)ITAM receptor. In contrast to the classical ITAM signaling, the (hem)ITAM seems to be phosphorylated by Syk, which then, in combination with SFK activation, results in a tyrosine phosphorylation cascade similar to that downstream of GPVI. Taken form Stegner *et al.*, 2014 [28].

The ITAM consists of paired YxxL/I (x denotes an unspecific aa) motifs that are separated by a defined interval (YxxL/I-(x)$_{6\text{-}8}$-YxxL/I). The hemITAM consists of only one such sequence [25]. Ligand binding to GPVI recruits Src family tyrosine kinases Fyn and Lyn to the ITAM motif of the associated FcRγ, initiating a phosphorylation cascade including Syk, the adaptors linker of activated T cells (LAT) and Src homology 2 domain-containing leukocyte protein of 76 kDa (SLP-76). This results in the activation of effector proteins, namely phospholipase (PL) Cγ2, Phosphatidylinositol-4,5-biphosphate 3-kinase (PI3K) and small G proteins, finally inducing calcium (Ca^{2+}) mobilization, degranulation, integrin activation and aggregation (Figure 1-5) [29-31]. Downstream signaling of CLEC-2 is similar to that of GPVI including Syk phosphorylation, LAT and PLCγ2 [28, 32]. Since CLEC-2 only contains one YxxL/I motif, it exists as homodimer on the cell surface to enable Syk binding to two phosphorylated hemITAMs [33].

1.2.2.2 Platelet calcium signaling

Ca^{2+} is an essential second messenger in nearly all cells [24]. In platelets, increase in cytosolic Ca^{2+} is the final central step during platelet activation mediating integrin activation, degranulation, aggregation and shape change. Independent of the ligand/agonist, all platelet activation pathways lead to the activation of PLC isoforms and the production of IP_3 and DAG (Figure 1-4), which both contribute to Ca^{2+} mobilization. IP_3 induces the release of Ca^{2+} from intracellular stores whereas DAG mediates Ca^{2+} influx from the extracellular compartment [24]. IP_3 activates IP_3-sensitive Ca^{2+} channels located in the sarcoplasmic reticulum in platelets and thereby directly induces Ca^{2+}-release and increase in intracellular Ca^{2+} $[Ca^{2+}]_i$. The resulting decrease of Ca^{2+} in the store is, in turn, recognized by STIM1 and induces opening of store-operated calcium channels like Orai1 (Figure 1-6). This process is named store-operated calcium entry (SOCE) and is the major route of Ca^{2+} influx in platelets [15, 24]. DAG mediates another route of Ca^{2+} entry, the so called non-SOCE, as it directly activates Ca^{2+} channels in the plasma membrane like the transient receptor potential channel 6 (TRPC6). The third way of Ca^{2+} entry is the receptor-operated calcium entry (ROCE) which is facilitated by ATP and the purinoreceptor $P2X_1$ in the plasma membrane and serves to amplify platelet activation (Figure 1-6) [24].

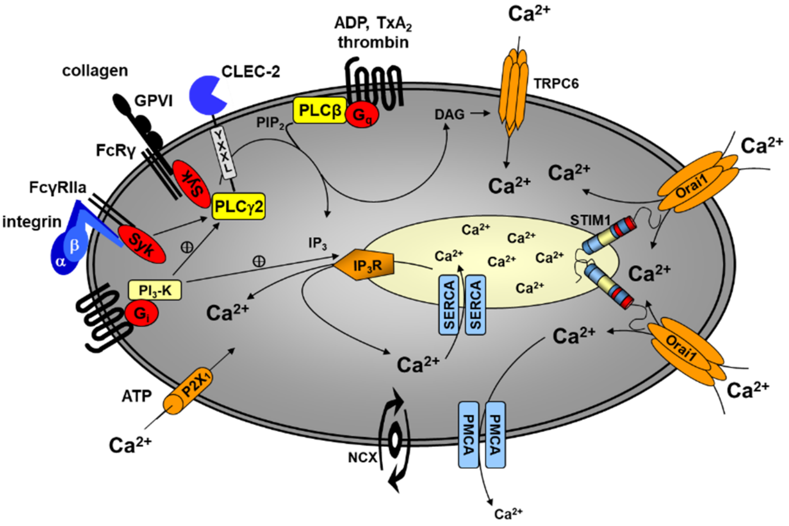

Figure 1-6: Platelet calcium signaling. Upon receptor activation different phospholipase (PL) C isoforms hydrolyze phosphatidilinositol-4,5-bisphosphate (PIP_2) to inositol-1,4,5-trisphosphate (IP_3) and diacyl-glycerol (DAG). IP_3 releases Ca^{2+} from the intracellular stores and in turn STIM1 opens Orai1 channels in the plasma membrane, a process called store-operated calcium entry (SOCE), whereas DAG mediates non-SOCE through canonical transient receptor potential channel 6 (TRPC6). Additionally, a direct receptor-operated calcium (ROC) channel, P2X1, and a Na^+/ Ca^{2+} exchanger (NCX) contribute to the elevation in $[Ca^{2+}]_i$. The counteracting mechanisms involve sarcoplasmic/endoplasmic reticulum Ca^{2+} ATPases (SERCAs) and plasma membrane Ca^{2+} ATPases (PMCAs), which pump Ca^{2+} back into the stores or through the plasma membrane out of the cell, respectively. IP3R, IP3-receptor; ATP, adenosine triphosphate; ADP, adenosine diphosphate; GPVI, glycoprotein VI; FcRγ, Fc receptor γ chain; FcγRIIa, Fc γ receptor IIa; CLEC-2, C-type lectin-like receptor 2; PI3-K, phosphatidylinositol 3-kinase; Syk, spleen tyrosine kinase. Taken from Varga-Szabo *et al.,* 2009 [24].

Since platelets are very sensitive to already small increases in $[Ca^{2+}]_i$, the maintenance of stable cytosolic Ca^{2+} concentration is indispensable to prevent unwanted platelet activation and thrombus formation. To counterbalance a constant leak from the intracellular Ca^{2+} stores, two mechanisms exist in platelets. Sarcoplasmic/endoplasmic Ca^{2+} ATPases (SERCAs) pump Ca^{2+} back to the intracellular stores and plasma membrane Ca^{2+} ATPases (PMCAs) facilitate the transport out of the cell (Figure 1-6) [24].

1.3 Ischemic Stroke

Ischemic stroke is the most frequent type of stroke (87% of the cases) and can either be caused by a thrombotic event in the cerebral vasculature or by an embolus that breaks off from a distant site of thrombus formation. This embolus is flushed into the brain vasculature, gets stuck there and consequently blocks a brain-supplying vessel. These thrombi can for example be formed at atherosclerotic plaques or they originate from the heart, where they are often caused by atrial fibrillation [34]. In approximately 70% of infarcts, the middle cerebral artery (MCA) and its branches are affected by an occlusion [35]. The pathophysiology of ischemic stroke is both, simple and complex. The initiating event is simple: the obstruction of an intracranial or neck blood vessel that impairs or blocks blood supply, and with this oxygen and nutrient supply, to a certain area of the brain, leading to its infarction. The complexity comes from the many different cellular consequences, resulting from the reduced cerebral blood flow (CBF) [36]. In the early hours of an acute ischemic stroke, the affected brain tissue can be divided in three regions: The ischemic core is the part of the brain with only little or no residual blood supply. The ischemic penumbra surrounds the ischemic core and suffers from only moderate CBF reduction (Figure 1-7). In the region of oligemia the decrease in CBF is not sufficient to result in brain infarction [37]. In contrast to the irreversibly damaged ischemic core, the penumbra is potentially salvageable. Therefore, saving all or most parts of the ischemic penumbra is the goal of acute stroke therapy. Over time, the ischemic core expands to the penumbral tissue with more and more parts of the brain getting irreversibly damaged, emphasizing the concept of “time is brain”. In a typical large-vessel anterior circulation ischemic stroke, 1.9 million neurons, 14 billion synapses and 12 km of myelinated fibers are destroyed every minute without treatment [38]. The sooner arterial recanalization is achieved, the smaller will be the volume of definitely infarcted brain tissue. In 1995 a landmark study was published, which established the use of (recombinant) tissue Plasminogen Activator (rtPA) in stroke therapy [39]. tPA induces the generation of plasmin from plasminogen, which cleaves the fibrin meshwork of the clot. This leads to thrombolysis and therefore allows recanalization of the occluded vessel [40]. However, one severe side effect of tPA is the risk of intracerebral hemorrhage. The therapeutic window of tPA administration is 3 – 4.5 h after stroke onset. When given later, the risk of hemorrhagic complications increases immensely and overcomes a potential benefit [40].

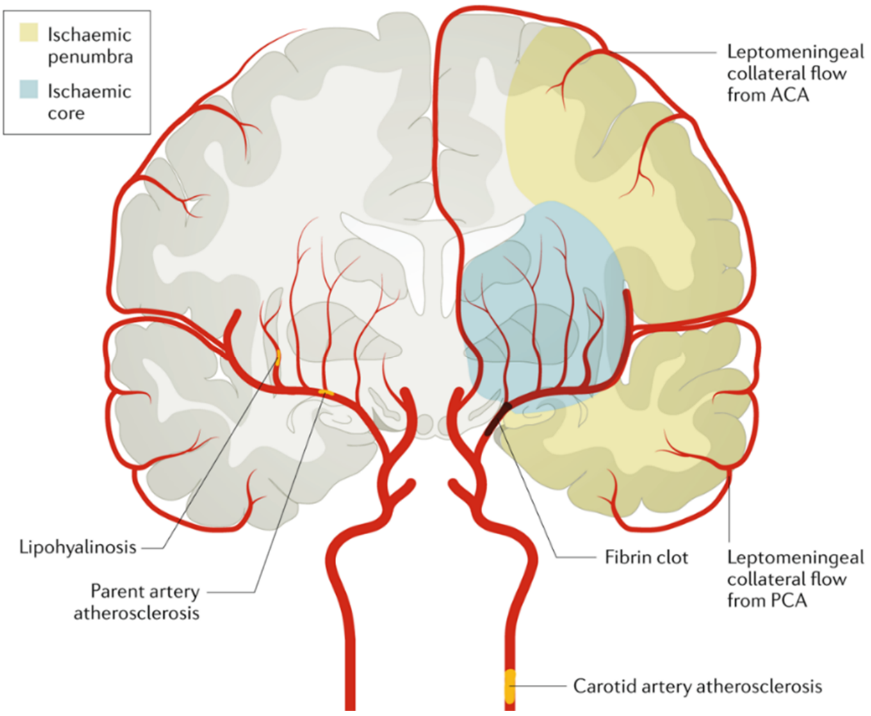

Figure 1-7: The ischemic penumbra. Occlusion of a major cerebral artery such as the middle cerebral artery results in changes and inhomogeneous reduction in cerebral blood flow (CBF). In the infarct core, the greatest reduction in CBF occurs, resulting in rapid cell death. Retrograde blood flow from leptomeningeal anastomoses might be sufficient to sustain metabolic viability but not electrical activity in the ischemic penumbra, the tissue surrounding the infarct core. Rapid reperfusion in the penumbral tissue can reverse the damage but the extent of irreversible injury (infarct core) expands with time. Modified from Campbell *et al.,* 2019 [41].

Starting in the early 2000s, direct clot retrieval from the occluded vessel was tested for the first time in clinical trials, assessing a potential use in the treatment of acute ischemic stroke [42]. Widespread acceptance of the efficacy of mechanical thrombectomy (MT) was achieved in 2015 when a series of clinical trials was published demonstrating beneficial effects with MT for up to 6 h after stroke onset. Recently, for patients with a small ischemic core and a large penumbra, the therapeutic time window of MT could even further be expanded to 24 h [43]. By using thrombectomy, reperfusion is achieved in a markedly higher proportion of patients (70-80%) compared to rtPA alone (20% of cases) [5]. MT is most powerful in larger arterial occlusions, for smaller occlusions, rtPA is still the most suitable therapy, although going along with lower success rates [5], emphasizing the need for novel therapeutic targets.

1.3.1 Reperfusion therapy and reperfusion injury

Despite the success of markedly increased reperfusion rates by the invention of mechanical thrombectomy, 30-68% of stroke patients have still an unfavorable clinical outcome [44]. Recanalization of the occluded vessel is essential, but not sufficient to guarantee survival of the penumbra [45]. The phenomenon of ongoing lesion development despite recanalization is referred to as reperfusion injury. Infarct growth after recanalization can result from a failure in reperfusion therapy or detrimental processes induced by the reperfusion itself. Very likely a combination of both. Unsuccessful reperfusion therapy might be caused by several reasons. (1) recanalization fails, (2) no reperfusion due to “no-reflow” or re-occlusion and (3) vascular complications like hemorrhagic transformation (Figure 1-8). Reperfusion of ischemic tissue itself can have deleterious consequences such as disruption of the blood brain barrier (BBB) inducing neuronal damage (see section 1.3.3 for details). Multiple reasons for infarct expansion are discussed but the exact mechanisms remain to be identified.

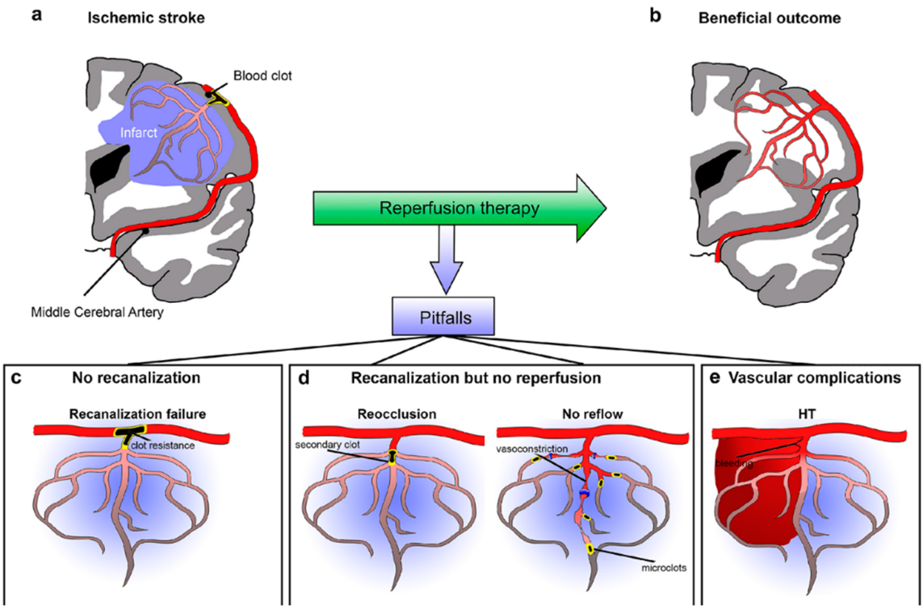

Figure 1-8: Vascular challenges for reperfusion therapy. (A) Schematic diagram of a coronal section of the brain. The middle cerebral artery (MCA) is occluded with a blood clot. The blue areas correspond to the infarct that could be saved with reperfusion therapy **(B)**. The different possible pitfalls of reperfusion are shown as no recanalization **(C)**, recanalization but no reperfusion and arterial re-occlusion and no-reflow **(D)**, and vascular complications: hemorrhagic transformation **(E)**. Taken from El Amki and Wegener, 2017 [5].

Complete recanalization fails in 22-41% of patients that are treated with rtPA. This already excludes patients that cannot be treated with pharmacological or mechanical thrombectomy. But even after successful recanalization, not all patients benefit. This is mainly because recanalization at the time point of therapy must not be seen equivalent to completely restored reperfusion [46]. Maintenance of recanalization might fail and absent reperfusion can be caused by vascular re-occlusion at the site of the initial thrombus (Figure 1-8) [47].

Thrombolytic therapy creates a procoagulant environment since the generated plasmin activates platelets and generates thrombin. This led to the concept that a newly formed thrombus at the site of the primary thrombus causes further tissue infarction (Figure 1-8) [48]. Another reason for the absent or reduced reperfusion could be the failure of the microcirculation more distal of the initial occlusion (“no-reflow”). Collapse of the microcirculation can have various reasons and so far, involvement of astrocytes, pericytes, endothelial cells, leukocytes and small molecules like nitric oxide or acetylcholine has been shown [5]. In the setting of “no reflow” platelet activation and the formation or embolization of microthrombi is seen as a plausible cause for the collapse and blockade of the cerebral microvasculature. However, this is controversially discussed: The failure of blocking complete platelet aggregation via anti-GPIIb/IIIa treatment in stroke therapy in mice [49] and men [50, 51] argues against thrombus formation as primary cause for absent reperfusion despite successful recanalization. So far, this question is not clearly answered and is therefore a main part of this thesis. Another complication of recanalization therapy is the hemorrhagic transformation (HT), which means bleeding in the infarcted area of a primarily ischemic stroke (Figure 1-8). HT rates vary between 10-40% and thrombolytic therapy was found to increase the risk of HT [5].

A variety of experimental stroke models has been developed to cover different aspects of the complex nature of human stroke [52]. To investigate brain ischemia with subsequent reperfusion (=ischemia/reperfusion (I/R)), the model of transient middle cerebral artery occlusion (tMCAO) was developed. This model closely reflects the pathophysiology of reperfusion injury and is therefore widely used, mainly in rodents [53]. In this model, a filament is inserted in the internal carotid artery and advanced further to occlude the middle cerebral artery. The filament is left in place usually for 1 h. After the occlusion, the filament can be removed, mimicking the situation of clot retrieval in the clinics, and allowing reperfusion of the MCA territory.

Numerous experimental studies have established a contribution of platelets and immune cells to ischemic stroke and reperfusion injury [46, 54, 55] leading to the concept of stroke as thrombo-inflammatory disease.

1.3.2 The blood brain barrier and the neurovascular unit

The brain vasculature is unique in its structure as it forms the blood brain barrier (BBB). The BBB is a highly specialized structural and biochemical barrier regulating the entry of molecules in the brain and preserving ionic homeostasis within the brain microenvironment.

The special architecture of the BBB leads to a very high electrical resistance (1500-2000 Ω/cm^2) compared to other tissues (3-33 Ω/cm^2) and a low paracellular permeability [56, 57]. In addition to the physical barrier, the endothelial cells (ECs) of the BBB have a polarized expression of transporters, metabolite-degrading enzymes, receptors and ion channels on their luminal and abluminal membrane. This allows a directed and restricted transport of nutrients such as glucose from the blood to the brain and the efflux of metabolite waste from the brain to the blood [58]. The endothelial cells of the brain microvasculature are extremely thin (~39% thinner than muscle ECs) with a distance of less than 0.25 µm from the luminal to the parenchymal side [59]. They are not fenestrated, have a low pinocytotic activity and are connected via tight junctions [60] (Figure 1-9). Compared to other endothelial cells, cerebral ECs have an increased mitochondrial content due to the high energy demand to facilitate transport of solutes from the blood to the brain and *vice versa* [61]. The BBB properties are mainly determined by junctional complexes between the endothelial cells. These complexes consist of tight junctions (TJ) and adherens junctions (AJ). Figure 1-9 gives an overview of the junctional complex between two brain endothelial cells.

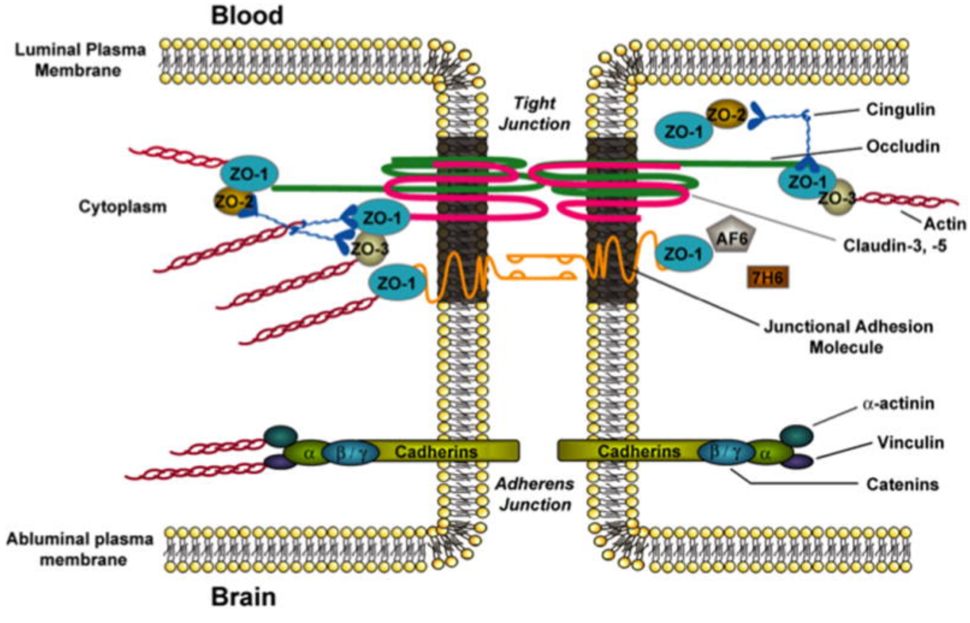

Figure 1-9: Molecular organization of tight junction protein complexes at the mammalian blood brain barrier. Tight junctions at the blood brain barrier (BBB) are formed by transmembrane proteins like Occludin, Claudins and junctional adhesion molecules that are linked to the cytoskeleton by accessory proteins zonula occludens (ZO) -1, -2 and -3. Cadherins, that are linked to the cytoskeleton via catenins, form adherens junctions that further stabilize the BBB. Following onset of ischemic stroke, tight junction protein complexes are disrupted, which leads to breakdown of the BBB. BBB disruption is further exacerbated by degradation of integrins, which are also expressed at the plasma membrane of brain microvascular endothelial cells. ZO-1, zonula occludens-1. Taken from Ronaldson and Davis, 2014 [62].

Tight junctions of the BBB involve specific transmembrane proteins, such as Occludin, Claudins, Tricellulin, and junctional adhesion molecules (JAMs) that are linked to the cytoskeleton via interaction with accessory proteins [59, 61] (Figure 1-9). Claudins are the main barrier-forming proteins. They are small (20-24 kDa) proteins that “seal” the tight junction [63]. In BBB formation, Claudin-1, -3, -5 and -12 are known to be involved, whereby Claudin-5 is the predominant form and limits paracellular diffusion of small molecules [56, 63]. Occludin (60-65 kDa) is critical for BBB integrity. It forms dimers and higher order oligomers between the cells and thereby controls paracellular permeability [61]. JAMs belong to the immunoglobulin superfamily. They are expressed at the intracellular junctions of epithelial and endothelial cells and have patterns of homo- and heterophilic adhesions [56]. JAM isoforms are particularly important for the regulation of immune cell trafficking across the brain endothelium [61]. Loss of JAM protein expression or incorrect localization leads to the loss of BBB integrity at the microvascular endothelium [61]. Association of the transmembrane tight junction proteins with cytoplasmic accessory proteins is critical for proper physiological functioning of the BBB. Here, three membrane-associated guanylate kinase-like (MAGUK) proteins are involved in the correct clustering of the TJ complex to the cell membrane: zonula occludens (ZO) -1, -2 and -3 link the TJ proteins to the actin cytoskeleton [56, 64]. ZO-1 is critical for tight junction stability and function, since dissociation of ZO-1 from the TJ complex induces increased permeability [61].

Besides the TJ, also the formation of adherens junctions is mandatory for an intact BBB. These are formed by cadherins and associated proteins that are linked to actin filaments (Figure 1-9). Cadherin-mediated signaling is essential for the integrity of the endothelial layer [65]. In barrier-forming endothelium, cadherin-10 is expressed at high levels. In contrast, non-barrier forming endothelium primarily expresses VE-cadherin [66]. For proper function, cadherins need to be associated with linkers to the actin cytoskeleton, the catenins [67]. At the BBB, expression of at least four catenins is known, catenin β, α, X and p120 [67].

The unique properties of the BBB allow the tight regulation of movement of cells, ions and molecules from the blood and the CNS. This is critical for proper neuronal function and the protection of the CNS from any injury or damage. Loss of barrier function is associated with certain diseases such as stroke, multiple sclerosis, trauma and neurodegenerative disorders. BBB dysfunction may lead to neuronal dysfunction and degeneration due to ion dysregulation, altered signaling and the entry of immune cells [59].

The brain endothelial cells interact with other cells in the brain, forming the so-called neurovascular unit (NVU, Figure 1-10). The NVU is responsible for the regulation of the cerebral blood flow, the maintenance of a highly selective BBB and cerebral homeostasis. It is composed of neurons, perivascular astrocytes, microglia, pericytes, endothelial cells and the basement membrane [68]. Local blood supply to certain brain areas is matched to neuronal demand via changes in the vascular intraluminal diameter by a mechanism termed neurovascular coupling. In this process the NVU plays a key role since it provides the basis for linking the neurons to cerebral vessels [69]. Communication within the NVU is thought to be mediated by glutamate, which is released from activated neurons. Pericytes and astrocytes get activated via glutamate, which induces the release of vasoactive mediators. The balance of vasodilatory and vasoconstrictive mediators controls the tone of the vasculature thereby regulating local CBF [68]. The BBB is fundamental in maintaining an optimal environment for brain function and the associated cells of the NVU are critically involved in its regulation.

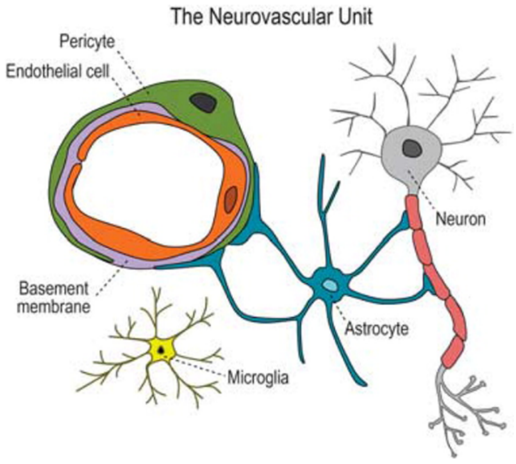

Figure 1-10: Diagram of the neurovascular unit (NVU). Endothelial cells surrounded by a basement membrane and pericytes are connected to neurons via astrocytes and interneurons in the brain parenchyma. Resident microglia sense the microenvironment to respond to potential insults. Taken from Sweeney *et al.*, 2015 [70].

1.3.3 The blood brain barrier during stroke

BBB breakdown is one of the hallmarks of the pathology of ischemic stroke and one of the main initiating factors of brain damage. Cerebral ischemia induces profound changes in the BBB which leads to a remarkable increase in paracellular permeability. In stroke patients, BBB disruption can be visualized by MRI imaging, and it was shown that the progression of stroke correlates with BBB breakdown [71-73]. The use of albumin binding tracer molecules such as Evans Blue or Gadofluorine, showed accumulation of these tracers in the ipsilateral hemisphere after experimental stroke [74, 75]. BBB breakdown occurs in several phases. 30-60 min after I/R injury, a subtle impairment of the BBB can be noted, which allows the extravasation of small macromolecules (≤3 kDa) into the brain parenchyma [76]. After more than 3 h, a second phase of leakage can be observed with larger macromolecules (≥40 kDa) being able to cross the brain endothelium [76]. At later stages (48 - 58 h after I/R), another increase in BBB permeability can be observed [72]. Considerable pathological stress is necessary for solutes with a large molecular mass (~60 kDa) to cross the BBB. These dramatic changes in BBB permeability are mediated by the redistribution of tight junction proteins, resulting in the formation of intracellular clefts between brain endothelial cells [77]. Early after cerebral ischemic injury (1 h), stress fiber formation in the ECs creates tension which leads to the disassembly of the tight junction complex and the extracellular matrix, leading to the initial loss of BBB integrity [72, 76]. At this time point, overall TJ protein expression is still unaltered. Later, cerebral ischemia induces the upregulation of matrix metalloproteinases, enabling degradation and/or further redistribution of the TJ proteins, further contributing to BBB breakdown [61, 72, 76].

Ischemia/reperfusion injury provokes a pro-inflammatory environment in the brain. Pro-inflammatory signals are generated contributing to BBB disruption [61, 78] and promoting immune cell invasion and transmigration of activated neutrophils, monocytes or lymphocytes into the brain parenchyma [79]. Changes in the BBB also affect the NVU, since swelling of the astrocyte endfeet protrusions and reduced pericyte coverage is observed after ischemic injury [80, 81].

1.3.4 Platelets and ischemic stroke

It has long been recognized that overshooting platelet activity contributes to the initiation of ischemic stroke. Meanwhile, increasing evidence is given that platelets are also major contributors to I/R injury and reperfusion failure. Here, the platelet’s role most probably goes beyond thrombosis and is of rather immune-modulatory nature [5, 46, 54]. The exact mechanisms, signaling pathways, time course and nature of cellular interaction remain in large parts elusive. So far, several receptors and platelet components have been shown to contribute to I/R injury of the brain [54]. Figure 1-11 represents a summary of major findings from experimental stroke studies where the lack or inhibition of platelet receptors and its effect on infarct development was investigated.

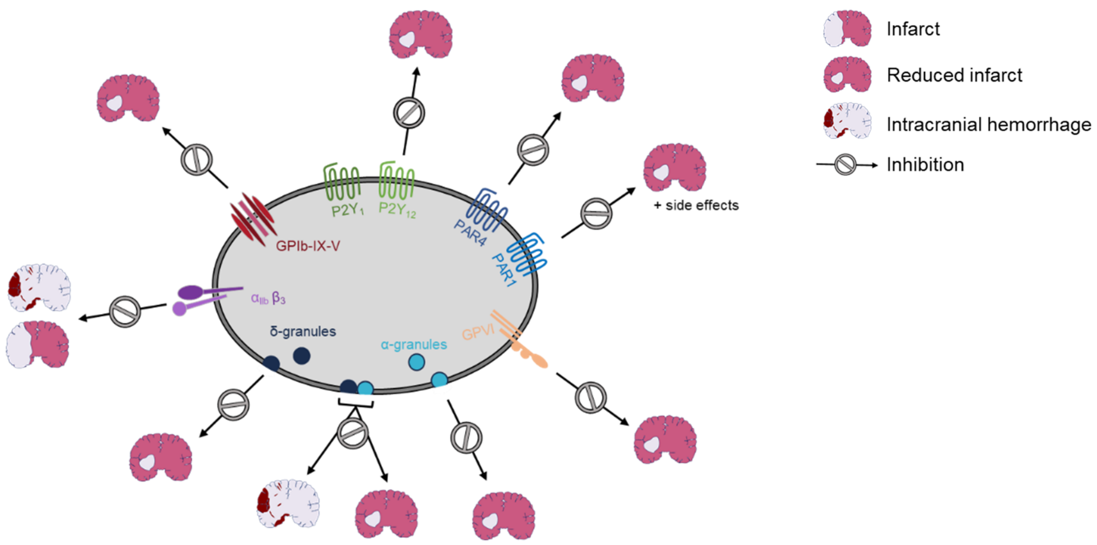

Figure 1-11: Inhibition of platelet activation or degranulation, but not GPIIb/IIIa blockade results in reduced infarct sizes in experimental stroke. Blockade or genetic deficiency of GPIbα, GPVI, P2Y1, P2Y12, PAR1 or PAR4 reduces infarct sizes following cerebral ischemia/reperfusion injury. Likewise, lack of either dense (δ) or α-granule secretion improves the outcome following experimental stroke. In contrast, combined loss of dense and α-granule secretion or GPIIb/IIIa blockade is accompanied by intracranial hemorrhage. Taken from Stegner, Klaus, Nieswandt, 2019 [54].

Blocking initial platelet adhesion and activation but not platelet aggregation was seen to improve the outcome after experimental stroke [49]. Blockade of the vWF binding site of GPIbα reduces infarct sizes, better reperfusion and neurological outcome after tMCAO, independent if the treatment is applied prophylactically or therapeutically [49, 82]. In line with this, mice with a genetic deficiency in GPIbα as well as vWF-deficient mice were protected from experimental stroke [83, 84]. Targeting downstream signaling of GPIbα was also protective after tMCAO, as demonstrated by improved outcome upon the deficiency or inhibition of phospholipase D1 and D2 [85, 86]. These results underline the contribution of the GPIbα-vWF axis to the pathomechanism of ischemic stroke. Similar results were obtained with disrupting platelet activation by targeting the main platelet collagen receptor GPVI. GPVI-deficiency profoundly protected mice in the tMCAO model without induction of intracerebral bleedings [49]. Deficiency or inhibition of the essential downstream molecule spleen tyrosine kinase (Syk) was beneficial and led to decreased infarct sizes [54, 87], indicating a critical involvement of downstream GPVI-ITAM signaling. The protection from stroke (and also arterial occlusion [88]) without increasing the risk of major bleeding makes GPVI an interesting target. Promising therapeutics targeting GPVI are currently investigated in clinical trials [89] (NCT 01645306 and NCT 03803007). Given the essential role of GPIIb/IIIa (integrin αIIbβ3) in platelet aggregation and thrombus formation (see also section 1.2), it is not surprising that it is involved in thrombotic diseases. Consequently, this glycoprotein is used as powerful anti-platelet therapy target. There are three currently approved GPIIb/IIIa inhibitors: The recombinant anti-GPIIb/IIIa fab fragment abciximab, the small peptide eptifibatide and the small non-peptide compound tirofiban [90]. Although these inhibitors are a powerful tool in the treatment of ischemic heart disease, in the setting of ischemic stroke, GPIIb/IIIa-blockers are contraindicated. In experimental stroke models, blocking GPIIb/IIIa markedly increased mortality and the risk of intracerebral hemorrhage. At the same time, surviving animals failed to show improvements in terms of infarct size or neurological behavior [49]. In clinical trials, use of GPIIb/IIIa inhibitors in the setting of ischemic stroke, significantly increased the rate of fatal intracerebral hemorrhage [50, 51, 54]. These results point to a diverse role of platelets in ischemic stroke that goes beyond platelet aggregation and thrombus formation but critically involves platelet activation. One central step of platelet activation is the release of platelet granule content. The released molecules from primarily α- and dense granules act as second wave mediators and amplify platelet activation but might also act on the surrounding. In the context of ischemic stroke, this might affect vascular integrity and modulate endothelial and immune cells. In experimental stroke models it was shown that mice lacking dense granule secretion (*Unc13d*$^{-/-}$*)* display smaller infarcts and a better neurological outcome. The absence of hemorrhage demonstrates that dense granule content is involved in the pathogenesis of ischemic stroke, but is not required to preserve vascular integrity [91]. ADP/ATP are central components of platelet dense granules and – upon platelet secretion – they promote secondary platelet activation. Inhibition of the ADP receptor P2Y$_{12}$ by ticagrelor reduced infarct sizes and led to better neurological outcome after tMCAO in mice [92]. This suggests that the amplification of platelet activation by dense granule content is promoting I/R injury in the brain. Platelet α-granules contain over 300 proteins, among these several pro- and anti-angiogenic factors. A model to study the impact of α-granule content in different processes is the *Nbeal2*$^{-/-}$ mouse. Nbeal2-deficiency leads to lack of α-granules in platelets and causes macrothrombocytopenia (approx. 40% reduction in platelet count) [93]. When applied to the tMCAO model, infarct sizes were significantly reduced, and neurological outcome was improved when compared to the respective wildtype controls. No signs of intracranial hemorrhage were observed, indicating that platelet α-granule content is an important mediator of cerebral I/R injury [93]. Of note, *Nbeal2*$^{-/-}$ mice used in this study are constitutive knockouts, so the observed effects might not entirely be platelet-specific. NBEAL2 expression is not restricted to platelets, and it could be shown that Nbeal2-deficiency alters immune responses [94] which could contribute to the observed effects. Interestingly, upon defective α- and dense granule secretion (*Unc13d*$^{-/-}$*/Nbeal2*$^{-/-}$ double KO mice), vascular integrity could not be maintained in the setting of experimental stroke, and the mice showed increased rates of intracranial hemorrhage and mortality after tMCAO [95]. Of note, platelets of *Unc13d*$^{-/-}$ mice also show a reduction in α-granule secretion (~60%), which can be attributed to the absence of secondary mediators (resulting from the ablated dense granule secretion). However, this seemed sufficient to maintain vascular integrity during stroke. This fits with the observation that a platelet count of 5% is sufficient to maintain vascular integrity, indicating that certain defects might be overcome. Only severely thrombocytopenic mice with platelet counts below 2.5% suffered from intracranial hemorrhages following tMCAO [96]. The plethora of proteins that is released upon platelet activation from the α-granules and the fact, that many of them can also be released by other cells, makes it difficult to identify single key players that contribute to I/R injury in the brain. However, there is evidence that platelet α-granule content is involved in a variety of processes, such as inflammation, wound repair and angiogenesis. Therefore, platelet granule secretion might be a contributing factor to the loss of BBB integrity during ischemic stroke and is investigated in this thesis.

1.3.5 The role of neutrophils in ischemic stroke

Ischemia induces an inflammatory environment in the brain, which causes the activation of resident cell populations like endothelial cells, microglia/macrophages and astrocytes. This in turn leads to the production and secretion of inflammatory proteins that recruit and activate leukocytes, thereby further amplifying the inflammatory response [97, 98]. In the cerebral microcirculation this contributes to enhanced production of reactive oxygen species, BBB disruption, recruitment of inflammatory cells and platelets. There is growing evidence that this inflammatory response, mainly driven by platelets and immune cells (thrombo-inflammation), is the major driver of infarct progression during I/R injury of the brain [46, 97]. Within minutes to a few hours after ischemic injury, an early accumulation of adherent leukocytes can be observed and the numbers progressively rise up to 48 h after reperfusion [97]. 4 h following reperfusion the recruited leukocyte population mainly consists of neutrophils. However, this shifts towards the non-PMN (polymorphonuclear) leukocytes at later time points (24 h reperfusion). These are likely mononuclear cells like monocytes and T-lymphocytes [97]. In this thesis, the focus was set on early processes leading to tissue damage in the course of reperfusion injury. Since neutrophils are the first cells to invade the infarcted territory, contribution of neutrophils to the pathogenesis of I/R injury in the brain was investigated into more detail. Neutrophils are detectable in the microvessels within the first hour following stroke [99] and reach a peak after 1 - 3 days [79]. Circulating neutrophils are captured by selectins on the brain endothelial cells. Further contact with adhesion molecules allows firm adhesion and migration through the endothelial wall (Figure 1-12) [100]. Although high neutrophil numbers in the blood are associated with larger infarct volumes in stroke patients [101], the pathogenic role of neutrophils in ischemic stroke is not clear.

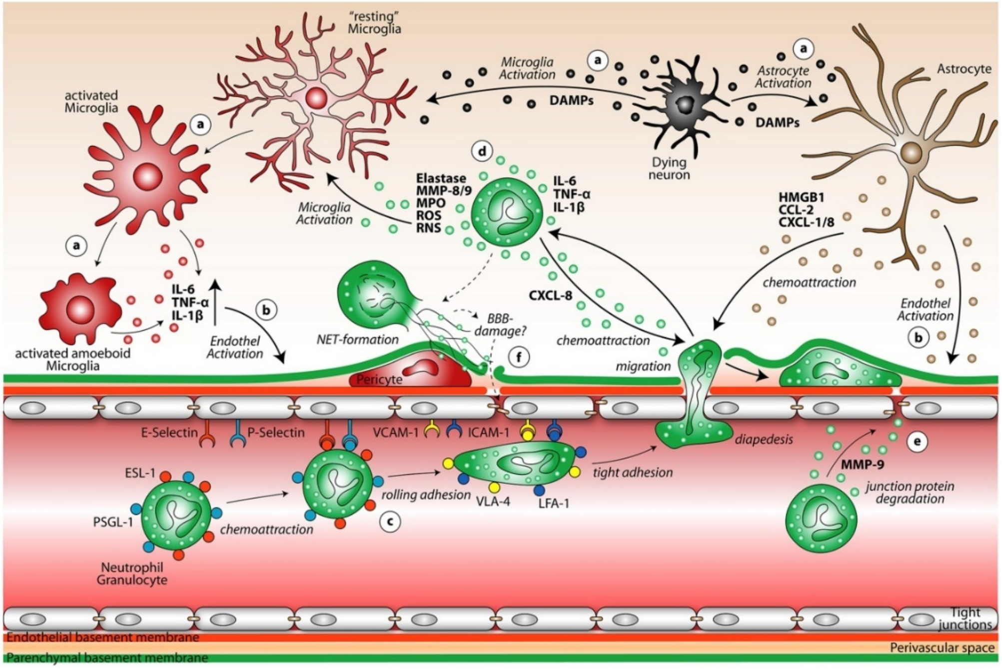

Figure 1-12: Stroke induced recruitment and action of polymorphonuclear neutrophils. (A) Oxygen and nutrient deprived neurons release DAMPs which activate particularly glial toll-like-receptors leading to the activation of local micro-and astroglia. **(B)** Glial chemokines trigger endothelial activation, which in turn present selectins and adhesion molecules on the luminal vessel wall. **(C)** Circulating PMNs are captured by selectins and are subsequently tethered to the endothelial wall. Further contact with adhesion molecules leads to firm adhesion and rolling of PMNs following the chemokine gradients. Finally, PMNs migrate through the endothelial wall and arrive at the site of inflammation within the parenchyma or perivascular space. **(D)** At the site of infarction, PMNs release a plethora of anti-microbial enzymes, chemokines and reactive oxygen/nitrogen species resulting in further inflammation and chemoattraction/activation of adjacent immune cells. **(E, F)** The release of proteases like MMP-9 contributes to further damage of the blood-brain barrier, as well as PMNs undergoing NETosis close to the endothelial wall and perivascular macrophages. CCL-2, CC-chemokine ligand-2; CXCL-8, Chemokine (C-X-C motif) ligand-8; DAMPS, Damage-associated molecular patterns; ESL-1, E-selectin-ligand-1; HMGB-1, High-Mobility-Group-Protein B1; ICAM-1, Intercellular Adhesion Molecule-1; IL-1β, Interleukin-1β; IL-6, Interleukin-6; LFA-1, Lymphocyte function-associated antigen-1; MMP-8/9, Matrix metallopeptidase-8/9; MPO, Myeloperoxidase; PSGL-1, P-Selectin glycoprotein ligand-1; RNS, Reactive nitrogen species; TNF-α, Tumor necrosis factor-α; VCAM-1, Vascular cell adhesion protein-1; VLA-4, Very Late Antigen-4. Taken from Strecker *et al.*, 2017 [100].

Contradictory results on the effect of neutrophil depletion in experimental stroke models have been reported [102]. Of note, neutrophils are involved in obstructing blood flow after recanalization in terms of the no-reflow phenomenon [103, 104]. In the vessel lumen or in perivascular spaces, neutrophils can damage the BBB by the release of proteolytic enzymes, reactive oxygen/nitrogen species and chemokines, thereby amplifying inflammation [100, 105]. It is still under debate whether neutrophils even reach the ischemic brain parenchyma. Experimental and clinical studies show neutrophil accumulation in the perivascular spaces, whereas only few could be found in the parenchyma [106, 107]. Following permanent ischemia models, more neutrophils were found in the brain parenchyma [102, 108].

Neutrophils are recruited to the brain in a specific time-window and have a short lifetime in tissues [102]. Thus, especially regarding a potential dual role of neutrophils in stroke, the temporal context might be essential considering beneficial or detrimental effects of targeting neutrophil function in stroke therapy.

Ischemia induces a cascade of metabolic events, many of them involving the generation of reactive oxygen species (ROS) mediating damage in the penumbral tissue [109]. ROS are highly reactive chemicals formed from O_2. Among the several species, superoxide (O_2^-) is one of the most important ROS in the CNS. Under healthy conditions, antioxidant mechanisms remove ROS and prevent excessive accumulation [109]. In ischemic stroke, the oxidative stress is too high, and ROS accumulate and damage the neurovascular unit by harming endothelial cells, pericytes, smooth muscle cells and astrocytes contributing to BBB breakdown. Recruitment of neutrophils leads to massive liberation of ROS in the brain tissue (Figure 1-12). The enzyme being mainly responsible for superoxide production is the NADPH oxidase, also called respiratory burst oxidase. It consists of two transmembrane proteins (p22phox and gp91phox) and four cytosolic proteins (p47phox, p67phox, p40phox and a GTPase Rac1 or Rac2). Upon activation, the subunits assemble at the membrane. NADPH activation is dependent on the phosphorylation of the p47phox subunit and is induced by a large number of agents [110]. p47phox or NCF1 (neutrophil cytosolic factor 1) is a 45 kDa protein being present in the cytosol of neutrophils [110]. In resting cells, NCF1 is not phosphorylated but upon stimulation, stepwise phosphorylation occurs, which is essential for NADPH oxidase activation [110]. Genetic deletion of a NADPH subunit prevented early BBB dysfunction and protected from brain swelling after stroke, indicating an important role of the NADPH oxidase [111]. The brain is highly vulnerable to ROS since neurons have low amounts of antioxidant enzymes but at the same time a high O_2 consumption, high levels of iron and a high concentration of peroxidizable lipids which all act as pro-oxidants under pathological conditions [109]. In the early phase of BBB disruption, ROS contribute to direct damage of the endothelial cells. In the late disruption of the BBB, ROS are also involved, contributing to the activation of matrix metalloproteinases, which degrade components of the basal lamina and lead to destabilization of the BBB [109].

Besides their ability to release ROS and proteinases, neutrophils are known to form neutrophil extracellular traps (NETs) consisting of DNA, histones and enzymes (Figure 1-13). These structures were first identified as defense mechanisms against infection, since they trap for example bacteria, limiting their spread [112].

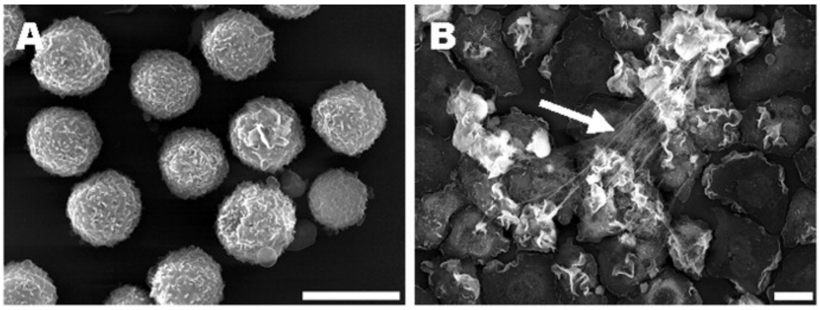

Figure 1-13: Electron microscopical analysis of resting and activated neutrophils. (A) Resting neutrophils are round and devoid of fibers. **(B)** Upon stimulation with 25 nM PMA (phorbol 12-myristate 13-acetate), the cells flatten, make many membrane protrusions, and form fibers (NETs, white arrow). Scale bar: 10 µm. Modified from Brinkmann *et al.*, 2004 [112].

Release of NETs (NETosis) is triggered by a variety of stimuli, including microorganisms, activated platelets, pro-inflammatory cytokines (like IL-8), TNFα or ROS. In resting neutrophils, most of the DNA is transcriptionally inactive. It is condensed into heterochromatin in the nucleus, where it is wrapped around histones and forms nucleosomes. A critical step for NET formation is chromatin decondensation, that is mediated by peptidyl arginase deaminase 4 (PAD4). PAD4 catalyzes the conversion of histone arginine to citrulline. The resulting loss of one positive charge per arginine weakens the DNA-histone binding and thereby unwraps the nucleosomes [113]. Inhibition of PAD4 activity was sufficient to disrupt human and mouse NET formation. Neutrophils from PAD4-deficient mice were unable to form NETs after stimulation with bacteria or chemokines [114, 115]. PAD4 is a 74 kDa protein that belongs to a family of five PAD enzymes (PAD1-4 and 6) mainly differing in their tissue localization [116]. The most important regulator of PAD activity is calcium. Its binding promotes the bioactive conformation and leads to an increased activity (for PAD4 this is 10,000-fold) [114, 117].

The inflammatory environment upon brain ischemia triggers NET formation and the release of extracellular chromatin of recruited neutrophils in the ischemic brain (Figure 1-12). The presence of NETs was detected in the brain of mice that underwent permanent as well as transient brain ischemia [108]. However, the role of NETosis in I/R injury of the brain is not clear yet. Thrombi that were retrieved from ischemic stroke patients contained NETs [118] and in the serum of stroke patients with early cerebral stroke, elevated levels of nucleosomes could be detected [119]. Although nucleosomes are used as a nonspecific cell death marker, they might contribute to stroke pathology when released by neutrophils. In line with this, elevated levels of nucleosomes and circulating DNA were found in the plasma of mice that underwent experimental stroke [120]. Furthermore, treatment of mice with recombinant DNase I improved the outcome following tMCAO, indicating that extracellular chromatin might be an important mediator of ischemic stroke in mice [120]. To further investigate if and how NET formation contributes to I/R injury of the brain, PAD4-deficient mice were studied in experimental stroke in this thesis.

1.4 Cerebral venous sinus thrombosis

In contrast to arterial stroke, thrombosis in cerebral veins (cerebral vein thrombosis, CVT) most often affects children and young adults. Females are at higher risk, which is mainly due to sex-specific risk factors like oral contraception, pregnancy and puerperium [10, 121]. In recent studies, the incidence of CVT is given with approximately 13-15.7 per million [10, 122, 123]. Of note, due to the challenging diagnosis, this number varies a lot in different reports. Symptoms are highly variable with severe headache as the most common symptom, reported by 60-90% of patients. 30-40% of patients suffer from acute symptomatic seizures, a markedly higher percentage compared to its incidence in acute arterial stroke patients (2-9%) [10]. The diagnosis of CVT in patients is based on neuroimaging. Here, MRI, to image the thrombosed vessel, is combined with magnetic resonance venography to detect the non-visualization of the same vessel [124]. Figure 1-14 gives an overview of the frequency of thrombosis in the major cerebral veins and sinuses. Of note, venous obstruction and thrombosis of a major sinus occur simultaneously in most patients [121].

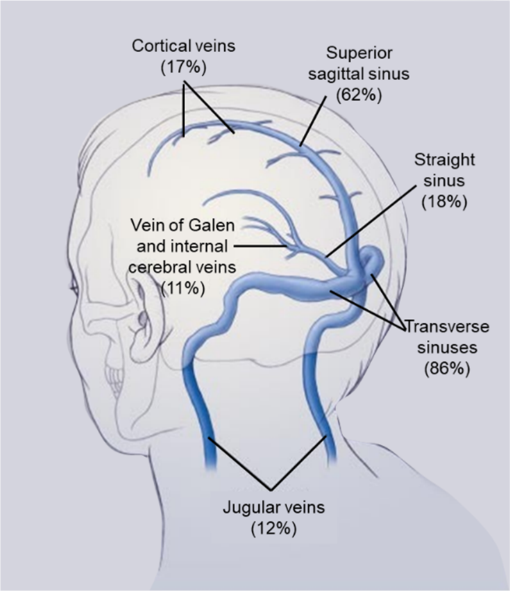

Figure 1-14: Frequency of thrombosis of the major cerebral veins and sinuses. The frequencies of thrombosis in the various sinuses are given as percentages and are based on data from the International Study on Cerebral Vein and Dural Sinus Thrombosis. In most patients, thrombosis occurs in more than one sinus. Modified from Stam *et al.*, 2005 [121].

Validated laboratory tests or pretest clinical probability scores to diagnose CVT are missing. Proposed biomarkers, like D-dimer levels failed to be reliable [125]. The current treatment guideline for CVT in the acute phase is anticoagulation with either unfractionated heparin or low molecular weight heparin (LMWH). In case of acute symptomatic seizures, antiepileptic drugs are administered [10, 125]. In contrast to arterial stroke, endovascular treatment is not yet recommended upon CVT due to the lack of reliable studies [125]. Nowadays, low death rates (0-2%) are reported for acute CVT and the long-term risk of death is approximately 8-10% [10]. However, about 6-10% of the surviving patients live with severe and permanent disability. Although 80% of patients recover without physical disability, many of them suffer from chronic symptoms and about one third cannot return to their prior work life [10]. In the past months, CVT has shifted into the focus of public attention, due to increased rates of CVT in patients being infected with the SARS-CoV-2 virus or after vaccination with the ChAdOx1 nCov-19 vaccine – the risk of CVT following infection still being many folds higher [126]. Since many cases of CVT are idiopathic and only few experimental studies exist, the underlying pathomechanisms are largely unknown [127] but potentially involve platelet activation and an imbalance of prothrombotic and thrombolytic processes.

1.5 Aim of the study

Despite important advances in the field of stroke research, a lot is still unknown and the underlying pathomechanisms are so far only party understood. Accounting for almost 90% of strokes, ischemic stroke is the most prevalent type and affects millions of people every year. Upon acute ischemic stroke, re-opening of the occluded vessel is the first goal and so far, the main therapeutic option. However, even if recanalization is successful, cerebral perfusion is not always fully restored and reperfusion itself causes tissue damage resulting in further infarct growth (= reperfusion injury). Previous work identified platelets and immune cells as essential contributors to reperfusion injury, which is why ischemic stroke is considered as thrombo-inflammatory disease. Since treatment options are limited, unraveling the underlying mechanisms is key for the identification of new therapeutic targets. Therefore, gaining new insights in the role of platelets and immune cells, in particular neutrophils, in stroke pathology is the main aim of this thesis.

The persisting low rates of cerebral perfusion even after recanalization indicates that the cerebral microvasculature is severely impaired following the ischemic event. Since platelet aggregation is critically involved in the initial development of stroke, the hypothesis arose in the field that during reperfusion, cerebral thrombi are formed that obstruct the microcirculation. The resulting tissue ischemia would then promote further infarct growth. Studies showing that blocking platelet aggregation fails in stroke therapy argue against this hypothesis, however this was never clearly investigated. Aim of the first part of this thesis was to examine whether thrombus formation precedes infarct growth and thus could be the cause.

In the second part of the thesis, the role of platelets on BBB integrity was investigated. Tissue ischemia promotes a platelet-activating environment, and one key process of platelet activation is the release of α- and dense granules. By combining an *in vitro* model of the BBB with intravital microscopy and use of respective knockout mouse strains, the effects of platelet granule content on brain endothelial cells and vascular integrity are investigated.

Neutrophils are among the first cells that are recruited to the brain after an ischemic insult. In the context of ischemic stroke, the role of neutrophils is controversially discussed. Aim of the third part of the thesis was to investigate the contribution of neutrophil-derived ROS production and NET formation to infarct progression during reperfusion injury.

Platelet activation is involved in many (patho-)physiological processes. Visualization of platelet activation especially in the living mouse in respective disease models would be extremely beneficial for revealing underlying mechanisms. The increase in intracellular Ca^{2+} levels is the common endpoint of all platelet-activating signaling pathways and thus an ideal marker for early platelet activation. However, current tools to visualize calcium in platelets are not suited for the *in vivo* situation. This is why in the fourth part of this thesis, a genetically modified mouse line was generated and tested on its suitability to visualize platelet activation by means of intracellular Ca^{2+} increase without disturbing platelet function.

CLEC-2 is one of the two (hem)ITAM coupled receptors on the platelet surface and has multiple roles in thrombo-inflammation and thrombosis. In previous work, our group developed and characterized an antibody against CLEC-2, named INU1 [32, 128]. Injection of fab-fragments of this antibody into mice resulted in generalized neurological deficits, thrombocytopenia, and death. However, to that time, the underlying mechanism could not be identified. Aim of the last part of this thesis was to reveal the reason for platelet consumption and the drastic neurological symptoms upon INU1-fab injection.

2 Materials and Methods

2.1 Materials

2.1.1 Devices

Device	**Company**
Aggregometer	APACT Laborgeräte und Analysensysteme (Hamburg, Germany)
Amersham^{TM} Imager 680	GE Healthcare (Freiburg, Germany)
Axiovert 200M microscope	Zeiss (Jena, Germany)
Cryotom CM1950	Leica (Wetzlar, Germany)
Eppendorf Centrifuge 5415C	Eppendorf AG (Hamburg, Germany)
Eppendorf Centrifuge 5415D	Eppendorf AG (Hamburg, Germany)
Eppendorf Centrifuge 5427R	Eppendorf AG (Hamburg, Germany)
FACSCalibur	BD Biosciences (Heidelberg, Germany)
FACSCanto	BD Biosciences (Heidelberg, Germany)
FACSCelesta	BD Biosciences (Heidelberg, Germany)
Gene Touch Thermal Cycler	Biozym Scientific GmbH (Oldenburg, Germany)
Hera Cell 240 incubator	ThermoFisher Scientific (Dreiech, Germany)
Heraeus Multifuge 3S-R	ThermoFisher Scientific (Dreiech, Germany)
Heraeus Multifuge x3	ThermoFisher Scientific (Dreiech, Germany)
Leica DMI 400B	Leica (Wetzlar, Germany)
Leica DMI 6000B	Leica (Wetzlar, Germany)
MulitImage II FC Light Cabinet	Alpha Innotech Corporation (Kasendorf, Germany)
PeriCam PSI HR	Perimed Instruments GmbH (Rommerskirchen, Germany)
Perkin Elmer FL-6500	Perkin Elmer (Waltham, USA)
Phenom Pro	ThermoFisher Scientific (Dreiech, Germany)
Sysmex KX 21N	Sysmex GmbH (Norderstedt, Germany)
TCS SP5 CLSM	Leica (Wetzlar, Germany)
TCS SP8 CLSM	Leica (Wetzlar, Germany)
TCS SP8 2-Photon Microscope	Leica (Wetzlar, Germany)
Thermomixer comfort	Eppendorf AG (Hamburg, Germany)

2.1.2 Reagents, Kits and Chemicals

Reagent	Company
2,3,5-triphenyltetrazolium chloride (TTC)	Sigma-Aldrich (Schnelldorf, Germany)
Acetic acid	Roth (Karlsruhe, Germany)
Adenosine diphosphate (ADP)	Sigma-Aldrich (Schnelldorf, Germany)
Agarose	Roth (Karlsruhe, Germany)
Ammonium chloride (NH_4Cl)	Merck (Darmstadt, Germany)
Ammonium persulfate (APS)	Roth (Karlsruhe, Germany)
Apyrase (grade III)	Sigma-Aldrich (Schnelldorf, Germany)
Benzyl alcohol	Sigma-Aldrich (Schnelldorf, Germany)
Benzyl benzoate	Sigma-Aldrich (Schnelldorf, Germany)
Biozym Taq polymerase buffer	Biozym (Hessisch-Oldendorf, Germany)
Biozym Taq polymerase	Biozym (Hessisch-Oldendorf, Germany)
BlueStar Plus Prestained protein marker	Nippon Genetics Europe (Düren, Germany)
Bovine serum albumin (BSA)	Sigma-Aldrich (Schnelldorf, Germany)
Bovine serum albumin (BSA), endotoxin-free	AppliChem (Darmstadt, Germany)
Bromophenol blue (3', 3'', 5', 5''-tetrabromophenolsulfonphthalein)	Sigma-Aldrich (Schnelldorf, Germany)
Calcium chloride ($CaCl_2$)	Roth (Karlsruhe, Germany)
Cacodylate	AppliChem (Darmstadt, Germany)
Clopidogrel (Plavix®)	Sanofi-Aventis (Paris, France)
Collagen IV	Sigma-Aldrich (Schnelldorf, Germany)
Collagenase CLS2	Worthington (Columbus, USA)
Collagenase-dispase	Roche (Granzach-Whylen, Germany)
Collagen related peptide (CRP)	kindly provided by Paul Bray (Baylor Collage, USA) and crosslinked in house
Deoxynucleotide triphosphates (dNTP) mix	Life Technologies (Darmstadt, Germany)
Dexamethasone	Pharma Partner (Hamburg, Germany)
Dimethyl sulfoxide (DMSO)	Sigma Aldrich (Steinheim, Germany)
DirectPCR-tail lysis buffer	VWR Int. GmbH (Vienna, Austria)
DNA loading dye	Life Technologies (Darmstadt, Germany)
DNase	Sigma-Aldrich (Schnelldorf, Germany)
Dream Taq polymerase buffer	Life Technologies (Darmstadt, Germany)
Dream Taq Green DNA Polymerase	Life Technologies (Darmstadt, Germany)
Dulbecco's Modified Eagle's Medium (DMEM)	Gibco (Karlsruhe, Germany)

Dulbecco’s modified PBS (endotoxin free)	Sigma-Aldrich (Schnelldorf, Germany)
Eosin G solution	Roth (Karlsruhe, Germany)
Eptifibatide acetate	Sigma-Aldrich (Schnelldorf, Germany)
Ethanol	Roth (Karlsruhe, Germany)
Ethylene glycol tetraacetic acid (EGTA)	Roth (Karlsruhe, Germany)
Ethylenediaminetetraacetic (EDTA)	AppliChem (Darmstadt, Germany)
Ethylenediaminetetraacetic acid disodium (Na_2EDTA)	Sigma-Aldrich (Schnelldorf, Germany)
Eukitt	VWR (Darmstadt, Germany)
Fentanyl	Janssen-Cilag GmbH (Neuss, Germany)
Fetal calf serum (FCS)	Perbio (Bonn, Germany)
Fibrinogen	Sigma-Aldrich (Schnelldorf, Germany)
Flumazenil	AlleMan Pharma (Pfullingen, Germany)
Fluoroshield^{TM} with DAPI	Sigma-Aldrich (Schnelldorf, Germany)
Fura-2-acetoxymethyl ester (AM)	ThermoFisher Scientific (Waltham, USA)
GeneRuler Mix DNA ladder	Life Technologies (Darmstadt, Germany)
Glucose	Roth (Karlsruhe, Germany)
Glutaraldehyde	EMS (Hatfield, USA)
Glycerol	Roth (Karlsruhe, Germany)
Glycine	AppliChem (Darmstadt, Germany)
Glyoxal solution stock	Sigma-Aldrich (Schnelldorf, Germany)
H_2O (nuclease free)	Roth (Karlsruhe, Germany)
Hank's balanced salt solution (HBSS)	GE Healthcare (Chicago, USA)
Hematoxylin solution Gill No. 3	Sigma-Aldrich (Schnelldorf, Germany)
Heparin for endothelial cells	Signal-Aldrich (Schnelldorf, Germany)
Hexamethyldisilazan (HDMS), $CH_{16}NSi_2$	Merck (Darmstadt, Germany)
High molecular weight heparin	Ratiopharm (Ulm, Germany)
Horm Collagen type I	Takeda (Linz, Austria)
Hydrochloric acid (HCl)	Roth (Karlsruhe, Germany)
IGEPAL CA-630	Sigma-Aldrich (Schnelldorf, Germany)
Immersol 518F immersion oil	ThermoFisher Scientific (Waltham, USA)
Iron-III-chloride hexahydrate ($FeCl_3$ x 6 H_20)	Roth (Karlsruhe, Germany)
Isofluran CP®	cp-pharma (Burgdorf, Germany)
Isopropanol	Roth (Karlsruhe, Germany)
Lysine	Sigma-Aldrich (Schnelldorf, Germany)
Medetomidine (Dormitor)	Pfizer (Karlsruhe, Germany)

Membright 640	Idylle (Paris, France)
Methanol	Roth (Karlsruhe, Germany)
Magnesium chloride ($MgCl_2$)	Roth (Karlsruhe, Germany)
Midazolam (Dormicum)	Roche (Grenzach-Wyhlen, Germany)
Midori Green^{TM} Advanced DNA stain	Nippon Genetics Europe (Düren, Germany)
Milk, powerded, blotting grade, fat free	Roth (Karlsruhe, Germany)
Mineral oil	Roth (Karlsruhe, Germany)
N-2-Hydroxyethylpiperazine-N'-2-ethanesulfonic acid (HEPES)	Roth (Karlsruhe, Germany)
Naloxone	AlleMan Pharma (Pfullingen, Germany)
Paraformaldehyde (PFA)	Roth (Karlsruhe, Germany)
PDGF-AB ELISA Kit	R&D Systems (Minneapolis, USA)
Percoll	Sigma-Aldrich (Schnelldorf, Germany)
Phenol/chloroform/isoamyl alcohol	AppliChem (Darmstadt, Germany)
Phosphatase Inhibitor	Roche (Granzach-Whylen, Germany)
PierceTM BCA Protein Assay Kit	ThermoFisher Scientific (Waltham, USA)
Plasma-derived serum (PDS)	First Link UK Ltd. (Birmingham, UK)
Pluronic F-127	ThermoFisher Scientific (Waltham, USA)
Poly-L-lysine	Sigma-Aldrich (Schnelldorf, Germany)
Potassium chloride (KCl)	Roth (Karlsruhe, Germany)
Potassium hydrogen carbonate ($KHCO_3$)	Roth (Karlsruhe, Germany)
Prostacyclin (PGI_2)	Sigma-Aldrich (Schnelldorf, Germany)
Protease Inhibitor Cocktail	Sigma-Aldrich (Schnelldorf, Germany)
Protase Inhibitor Cocktail	Roche (Grenzach-Whylen, Germany)
Proteinase K	NEB GmbH (Frankfurt am Main, Germany)
Rhodocytin	kindly provided by J. Eble (University of Münster, Germany)
Rotiphorese® Gel 30 acrylamide	Roth (Karlsruhe, Germany)
Sodium azide (NaN_3)	Sigma-Aldrich (Schnelldorf, Germany)
Sodium chloride (NaCl)	AppliChem (Darmstadt, Germany)
Sodium chloride for injection (0.9%)	Braun (Melsungen, Germany)
Sodium dodecyl sulphate (SDS)	Roth (Karlsruhe, Germany)
Sodium hydrogencarbonate ($NaHCO_3$)	Roth (Karlsruhe, Germany)
Sodium hydrogen phosphate (NaH_2PO_4)	AppliChem (Darmstadt, Germany)
(di-)Sodium hydrogen phosphate (Na_2HPO_4)	Roth (Karlsruhe, Germany)
Sodium hydroxide (NaOH)	AppliChem (Darmstadt, Germany)

Sodium (meta) periodate (NaIO)	Sigma-Aldrich (Schnelldorf, Germany)
Sodium orthovanadate (Na_3VO_4)	Sigma-Aldrich (Schnelldorf, Germany)
Sucrose	Sigma-Aldrich (Schnelldorf, Germany)
Tetramethylethylendiamine (TEMED)	Roth (Karlsruhe, Germany)
Thrombin	Roche Diagnostics (Mannheim, Germany)
Tissue-Tec (O.C.T^{TM} compound)	Sakura (Alphen aan den Rijn, Netherlands)
TRIS/HCl	Roth (Karlsruhe, Germany)
Trypsin-EDTA (0,05%)	Gibco (Karlsruhe, Germany)
Tween-20®	Roth (Karlsruhe, Germany)
U46619	Alexis Biochemicals (San Diego, USA)
Western Lightning Plus-ECL, enhanced chemiluminescence substrate	PerkinElmer (Waltham, USA)
Xylol	Roth (Karlsruhe, Germany)
β-mercaptoethanol	Roth (Karlsruhe, Germany)

All other non-listed chemicals were obtained either from AppliChem (Darmstadt, Germany), Sigma (Schnelldorf, Germany) or Roth (Karsruhe, Germany). Primers were obtained from Biomers (Ulm, Germany).

2.1.3 Other materials

Material	**Company**
22G venous catheter BD Insyte®	Mercateo (München, Germany)
3M^{TM} VetBond^{TM} Tissue Adhesive	ThermoFisher Scientific (Dreieich, Germany)
Braun alcohol pads (Isopropyl alcohol 70%)	VWR (Darmstadt, Germany)
Braun Sterican Canula (18G, 20G, 26G, 30G)	Hartenstein (Würzburg, Germany)
Capillaries for blood taking	Hartenstein (Würzburg, Germany)
Chamber slides (8-Well, 18-Well)	Ibidi (Gräfelfing, Germany)
Corning® Transwell® polycarbonate membrane cell culture inserts (0.4 µm)	Sigma-Aldrich (Schnelldorf, Germany)
Cyanoacrylate glue	Weicon (Münster, Germany)
Dental Cement AquaCem Set	Gerl Dental (Rodenkirchen, Germany)
Glass cover slide Ø 6 mm and 12 mm	VWR (Darmstadt, Germany)
Glass cover slides 24x60	Roth (Karlsruhe, Germany)
MCAO suture (6-0; L910 PK10)	Doccol Corporation (Sharon, USA)
Nitrocellulose membrane	GE Healthcare Life Science (Buckinghamshire, UK)

Polyvinylidene difluoride (PVDF) membrane amersham hybond 0.45 µm	VWR (Darmstadt, Germany)
Superfrost plus object slides	ThermoFisher Scientific (Dreieich, Germany)
Surgical sutures (Ethicon; 5-0, 7-0, 4-0)	Johnson & Johnson Medical GmbH (Norderstedt, Germany)
Syringe filters (ROTILABO ®, PVDF, 0.22 µm)	Roth (Karlsruhe, Germany)
Syringes (1 ml)	Dispomed (Gelnhausen, Germany)
T75 cell culture flask	Sarstedt (Nümbrecht, Germany)
Tissue-Tek® Cryomold®	Hartenstein (Würzburg, Germany)
Well plates (12-Well, 24-Well)	Sarstedt (Nümbrecht, Germany)

2.1.4 Recombinant proteins

Protein	**Company**
bFGF	Peprotech (Rocky Hill, NJ, USA)
CXCL 5	Peprotech (Rocky Hill, NJ, USA)
PDGF-AB	BioLegend (Dan Diego, USA)
PDGF-BB	BioLegend (San Diego, USA)
PF4	ChromaTec GmbH (Greifswald, Germany)
VEGFA121	BioLegend (San Diego, USA)
VEGFA165	BioLegend (San Diego, USA)

2.1.5 Cell lines

Cell line	**Source**
b.END3 (mouse brain endothelioma)	LGC Standards GmbH (Wesel, Germany)
b.END5 (mouse brain endothelioma)	Sigma-Aldrich (Steinheim, Germany)

2.1.6 Buffers and Media

All buffers were prepared in deionized water generated with a MilliQ Water Purification System (Millipore, Schwalbach, Germany). pH was adjusted with HCl or NaOH, if not stated otherwise.

ACK buffer

NH_4Cl	155 mM
$KHCO_3$	10 mM
Na_2EDTA	110 µM

Coating buffer, pH 9.0

$NaHCO_3$	50 mM

Culture Medium for b.END3 and b.END5 cells

Dulbecco's Modified Eagle Medium (DMEM)	
FCS	10%

Culture Medium for MBMECs

DMEM	80%
PDS	20%
L-Glutamine	1%
Penicillin/Streptomycin	1%
Heparin	0.1%
bFGF	0.005%

Freezing medium for b.END3 and b.END5 cells

DMEM	40%
FCS	50%
DMSO	10%

Glyoxal fixation buffer, pH 5.0

Ethanol	20%
Glyoxal solution stock	3%
Acetic acid	0.75%

HEPES buffer for SEM

HEPES	-
Glucose	5 mM
BSA	0.35%

Laemmli buffer for SDS-PAGE

TRIS	40 nM
Glycine	0.95 M
SDS	0.5%

Lysis buffer for tyrosine phosphorylation (2%)

NaCl	300 mM
TRIS	20 mM
EGTA	2 mM
EDTA	2 mM
IGEPAL CA-630	2%
Protease Inhibitor Cocktail	2%
Na_3VO_4	0.01%

Measuring Medium for MBMECs

RPMI Medium	97%
Penicillin/Streptomycin	1%
B27 Supplement	2%

Phosphate buffered saline (PBS), pH 7.14

NaCl	137 mM (0.9%)
KCl	2.7 mM
KH_2PO_4	1.5 mM
$Na_2HPO_4 \times 2H_2O$	8 mM

PLP fixation buffer

Lysine	13.5 µg/ml
NaH_2PO_4	28 mM
Na_2HPO_4	9.5 mM
PFA	3%
NaIO	2.5 mg/ml

Protein lysis buffer

TRIS HCl	15 mM
NaCl	155 mM
EDTA (pH 8.0)	1 mM
NaN_3	0.005%
IGEPAL-CA-630	1%
Protease Inhibitor Cocktail	1%

RIPA buffer for brain lysates

TRIS, pH 7.4	25 mM
NaCl	150 mM
NP-40	1%
SDS	0.1%
Protease inhibitors sigma cOmplete	4%

SDS sample buffer (4x)

TRIS buffer, pH 6.8	200 mM
SDS	8%
Bromophenol blue (3′,3″,5′,5″-tetrabromophenolsulfonphthalein)	0.04%
β-mercaptoethanol (for reducing conditions)	20%

SDS-PAGE sample buffer for brain lysates (2x)

TRIS buffer, pH 6.8	60 mM
SDS	5%
Glycerol	10%
β-mercaptoethanol	5%

Separating gel buffer (Western Blot), pH 8.8

TRIS/HCl	1.5 M

Stacking gel buffer (Western Blot), pH 6.8

TRIS/HCl	0.5 M

TAE (50x)

TRIS base	0.2 M
Acetic acid	5.7%
EDTA (0.5 M, pH 8.0)	10%

TE buffer

TRIS base	10 mM
EDTA	1 mM

Transfer Buffer for Western Blot

TRIS Ultra	50 mM
Glycine	40 mM
Methanol	20%

Tris-buffered saline (TBS), pH 7.3

TRIS/HCl	20 mM
NaCl	137 mM

Tyrode's buffer, pH 7.3 (with Ca^{2+})

NaCl	137 mM
KCl	2.7 mM
$NaHCO_3$	12 mM
NaH_2PO_4	0.43 mM
Glucose	0.1%
HEPES	5 mM
BSA	0.35%
$MgCl_2$	1 mM
($CaCl_2$	2 mM)

Washing buffer for Western Blot (TBS-T)

Tween 20	0.1% in TBS

2.1.7 Antibodies

2.1.7.1 Purchased primary and secondary antibodies

Antibody (anti-)	Host	Cat.No.	Company
β-Actin	Mouse	A5441	Merck (Taufkirchen, Germany)
Albumin	Rabbit	Ab207327	Abcam (Cambridge, UK)
CD146-PE	Rat	134704	BioLegend (San Diego, USA)
CD31	Rat	102402	BioLegend (San Diego, USA)
CD31	Rat	MCA2388	Bio-Rad (Feldkirchen, Germany)
Claudin-1	Rabbit	37-4900	ThermoFisher Scientific (Dreiech, Germany)
Claudin-3	Rabbit	37-1700	ThermoFisher Scientific (Dreieich, Germany)
Claudin-5	Rabbit	34-1600	ThermoFisher Scientific (Dreieich, Germany)
GAPDH	Rabbit	G5262	Sigma-Aldrich (Schnelldorf, Germany)
H3Cit	Rabbit	ab5103	Abcam (Cambridge, UK)
Ly6G (clone 1A8)	Rat	127602	BioLegend (San Diego, USA)
Mouse IgG-HRP	Rabbit	P0260	Agilent; DAKO (Hamburg, Germany)
Occludin	Rabbit	40-4700	ThermoFisher Scientific (Dreieich, Germany)
Pad4	Rabbit	ab214810	Abcam (Cambridge, UK)
Rabbit IgG-Alexa488	Goat	A32731	Life Technologies (Darmstadt, Germany)
Rabbit IgG-Alexa546	Goat	A11010	Life Technologies (Darmstadt, Germany)
Rabbit IgG-Alexa594	Goat	A11012	Life Technologies (Darmstadt, Germany)
Rabbit IgG-Alexa647	Donkey	A-31573	Life Technologies (Darmstadt, Germany)
Rabbit IgG-Atto647N	Goat	40839	Sigma-Aldrich (Schnelldorf, Germany)
Rabbit IgG-HRP	Goat	7074	Cell Signaling (Denver, USA)
Rat IgG-Alexa488	Goat	A11006	Life Technologies (Darmstadt, Germany)
Rat IgG-DyLight488	Donkey	ab102232	Abcam (Cambridge, UK)
Rat IgG-HRP	Donkey	712035153	Dianova (Hamburg, Germany)
vWF	Mouse	A008229-2	Agilent; DAKO (Hamburg, Germany)
ZO-1	Rabbit	61-7300	ThermoFisher Scientific (Dreieich, Germany)

2.1.7.2 In-house generated antibodies

The monoclonal antibodies listed below (all rat IgG antibodies) were generated in our laboratory. Depending on the need, the antibodies were labeled to fluorescein isothiocyanate (FITC), phycoerythrin (PE) or Alexa fluorophores using respective antibody labeling kits (Life Technologies, Darmstadt, Germany) according to the manufacturer's protocols.

Antibody	**Clone**	**Isotype**	**Antigen**	**Described in**
BAR1	25B11	unknown	α5 integrin	[129]
CD105	MJ7/18	IgG2a	CD105	[130]
DOM1	89H11	IgG1	GPV	[131]
EDL-1	57B10	IgG2a	β3 integrin	[131]
HB.197™	2.4G2	IgG2b	FcγR	[132]
INU1	11E9	IgG1	CLEC-2	[128]
JAQ1	98A3	IgG2a	GPVI	[133]
JON/A	4H5	IgG2b	αIIbβ3	[134]
JER1	10B6	IgG1	CD84	[135]
JON6	14A3	IgG2b	αIIbβ3	[131]
LEN1	12C6	IgG1	α2 integrin	[136]
Ly6G/Ly6C	RB6-8C5	IgG2b	Ly6G	[137]
p0p/B	57E12	IgG2b	GPIbα	[88]
p0p1	3G6	IgG1	GPIbβ	[131]
p0p4	15E2	IgG2b	GPIb	[131]
p0p6	56F8	IgG1	GPIX	[131]
ULF3	96H10	IgG2b	CD9	unpublished
WUG1.9	5C8	IgG1	P-Selectin	unpublished

2.1.8 Animals

C57BL/6J mice were purchased from Charles River (Sulzfeld, Germany) or JANVIER LABS (Le Genest-Saint-Isle, France) and bred in the animal facility of the Rudolf Virchow Center Würzburg. The genetically modified mice and knockout mice used for this work are listed below.

Mouse strain	**Publication/Stock number**
Clec1b$^{Y7A/Y7A}$	[138]
Nbeal2$^{-/-}$	[93]
Ncf1$^{-/-}$	Jax-Nr.: 027331
Pad4$^{-/-}$	Jax-Nr.: 026708
Polr2a$^{Tn(pb\text{-}CAG\text{-}GCaMP5g,\text{-}tdTomato)Tvrd}$	Jax-Nr.: 024477
Syk$^{fl/fl,\ Pf4\text{-}cre+/-}$	[87]
Unc13d$^{-/-}$	[91]

All mice are on the genetic background of C57BL/6J and were kept either in the animal facility of the Rudolf-Virchow-Center or the animal facility of the Center of Molecular Medicine (ZEMM), University of Würzburg. Mice were kept in a temperature- and humidity-controlled environment and food and water were accessible *ad libitum*. All animal studies were approved by local authorities (Bezirksregierung Unterfranken, Würzburg, Germany).

2.2 Methods

2.2.1 Mouse genotyping

2.2.1.1 Isolation of genomic DNA

500 µl of DNA lysis buffer containing 0.1 mg/ml Proteinase K was added to a small part of mouse ear and incubated overnight (o/n) at 56°C under shaking conditions (950 rpm). After the addition of 500 µl phenol/chloroform, samples were mixed and then centrifuged at 10,000 rpm for 10 min at 4°C. The supernatant was transferred into a new tube containing 500 µl isopropanol. Samples were shaken and then centrifuged at 14,000 rpm for 10 min at 4°C. Subsequently, the remaining pellet was washed with 500 µl 70% ethanol and the samples were centrifuged once more at 14,000 rpm for 10 min at 4°C. Finally, the pellet was left to dry for 30 min at 37°C and afterwards resuspended in 70 µl TE buffer (upon shaking at 550 rpm for 30 min at 37°C). Centrifugation steps were done in an Eppendorf 5417R centrifuge.

Or

A small part of the mouse ear was lysed in tail lysis buffer for 2 h at 56°C followed by 30 min at 85°C. Afterwards, the suspension could directly be used for polymerase chain reaction (PCR).

2.2.1.2 Genotyping of transgenic mice using polymerase chain reaction (PCR)

For genotyping, genomic DNA isolated from mouse ear biopsies (2.2.1.1) was used for PCR with respective primers and programs for the used mouse lines indicated below.

Detection of the PC-G5-tdT transgene

Primer:

PC-G5-tdT_fwd: 5’ TAG ACA CAT GCC ACC AAA CC 3’
PC-G5-tdT_WT rev: 5’ TCT CTC CAG CAC CAT AAC TCC 3’
PC-G5-tdT_Kin rev: 5’ GAT CGA TAA AAC ACA TGC GTC A 3’

Pipetting scheme		PCR program		
1 µl	genomic DNA	94°C	2:00 min	
2.5 µl	Dream Taq buffer (10x)	94°C	0:20 min	10 cycles
0.5 µl	$MgCl_2$ (25 mM)	65°C	0:15 min	
0.5 µl	dNTP's (10 mM)		(0.5°C/cycle decrease)	
1 µl	fwd primer (1:10)	68°C	0:10 min	
1 µl	WT rev primer (1:10)			
1 µl	Kin rev primer (1:10)	94°C	0:15 min	28 cycles
0.25 µl	DreamTaq Green DNA Polymerase	60°C	0:15 min	
		72°C	0:10 min	
to 25 µl	H_2O	72°C	2:00 min	

Expected product size:
WT 395 bp
Kin 272 bp

Detection of the Syk floxed allele

Primer:

Syk flox fwd: 5'- GGT GCC TAC AGG TCT ACA GC-3'
Syk flox rev: 5'- AAC CTG GTA ATT TCA TAA CAG C-3'

Pipetting scheme		PCR program		
1 µl	genomic DNA	95°C	3:00 min	
2.5 µl	Dream Taq buffer (10x)	95°C	0:30 min	35 cycles
0.5 µl	$MgCl_2$ (25 mM)	60°C	0:45 min	
0.5 µl	dNTP's (10 mM)	72°C	1:00 min	
1 µl	fwd primer (1:10)	72°C	5:00 min	
1 µl	rev primer (1:10)	15°C	∞	
0.25 µl	DreamTaq Green DNA Polymerase			
to 25 µl	H_2O			

Expected product size:
WT: 198 bp
Flox: 285 bp

Detection of the PF4-Cre transgene

Primer:

PF4-Cre_fwd: 5' CCC ATA CAG CAC ACC TTT TG 3'
PF4-Cre_rev: 5' TGC ACA GTC AGC AGG TT 3'

Pipetting scheme		PCR program		
1 µl	genomic DNA	96°C	5:00 min	
2.5 µl	Dream Taq buffer (10x)	94°C	0:30 min	35 cycles
0.5 µl	$MgCl_2$ (25 mM)	48.5°C	0:30 min	
0.5 µl	dNTP's (10 mM)	72°C	0:45 min	
1 µl	fwd primer (1:10)	72°C	3:00 min	
1 µl	rev primer (1:10)	22°C	∞	
0.25 µl	DreamTaq Green DNA Polymerase			
to 25 µl	H_2O			

Expected product size:
WT: no PCR product
PF4-Cre: 450 bp

Detection of the *Unc13d*$^{-/-}$ allele

Primer WT PCR

Unc13d-TUF: 5’ GGG ACG CCG TGT CTT TCT AC 3’
Unc13d-TUR: 5’ ACA CTC TCC CAA CAT CTC CTC TTA C 3’

Primer KO PCR

Unc13d-SU: 5’ CTC TCC CCA GAG CCT CCG TG 3’
Und13d-LacZrev: 5’ GTC TGT CCT AGC TTC CTC ACT G 3’

Pipetting scheme		PCR program		
1 µl	genomic DNA	96°C	3:00 min	
2.5 µl	Dream Taq buffer (10x)	95°C	0:30 min	35 cycles
2.5 µl	$MgCl_2$ (25 mM)	68°C	0:30 min	
0.5 µl	dNTP's (10 mM)	72°C	1:00 min	
0.1 µl	fwd primer	72°C	10:00 min	
0.1 µl	rev primer	12°C	∞	
0.25 µl	DreamTaq Green DNA Polymerase			
to 25 µl	H_2O			

Run WT and KO PCR separately

Expected product size:
WT: 73 bp
KO: 392 bp

Detection of the *Nbeal2*$^{-/-}$ allele

Primer:

Nbeal2_fwd: 5’ GTC CTG CTT GAC CTA CCG TC 3’
Nbeal2 WT_rev: 5’ CAG GGA GGA TAA CGA GAT AGT CTT 3’
Nbeal2 IRES-RP: 5’ CCT AGG AAT GCT CGT CAA GA 3’

Pipetting scheme		PCR program		
1 µl	genomic DNA	96°C	3:00 min	
2.5 µl	Dream Taq buffer (10x)	94°C	0:30 min	35 cycles
0.5 µl	$MgCl_2$ (25 mM)	51.4°C	0:30 min	
0.5 µl	dNTP's (10 mM)	72°C	1:00 min	
0.3 µl	fwd primer	72°C	10:00 min	
0.1 µl	rev primer	12°C	∞	
0.1 µl	IRES-RP			
0.25 µl	DreamTaq Green DNA Polymerase			
to 25 µl	H_2O			

Expected product size:
WT: 223 bp
KO: 401 bp

Detection of the *Pad4*$^{-/-}$ allele

Primer WT PCR

Pad4 WT_fwd: 5’ ACG TTT GTA AGG GGC ATC CT 3’
Pad4_common: 5’ TCA AAG TAC CTG ATG TGT TGA CTG 3’

Primer KO PCR

Pad4 KO_fwd: 5’ TCA TGA CCC CCA ACA CTC A 3’
Pad4_common: 5’ TCA AAG TAC CTG ATG TGT TGA CTG 3’

Pipetting scheme		PCR program		
1 µl	genomic DNA	94°C	2:00 min	
2.5 µl	Dream Taq buffer (10x)	94°C	0:20 min	10 cycles
0.5 µl	$MgCl_2$ (25 mM)	65°C	0:15 min	
0.5 µl	dNTP's (10 mM)		(0.5°C/cycle decrease)	
1 µl	fwd primer (1:10)	68°C	0:10 min	
1 µl	common primer (1:10)			
0.25 µl	DreamTaq Green DNA	94°C	0:15 min	28 cycles
	Polymerase	60°C	0:15 min	
to 25 µl	H_2O	72°C	0:10 min	
		72°C	2:00 min	

Run WT and KO PCR separately

Expected product size:
WT: 300 bp
KO: 165 bp

Detection of the *Clec1b*$^{Y7A/Y7A}$ allele

Primer:

Clec2hl_F2: 5’ GAA TGC AAT ACT GGG GTG CT 3’
Clec2hl_R2: 5’ CGC TTC CCT CCA GAA CAT TA 3’

Pipetting scheme		PCR program		
1 µl	genomic DNA	95°C	3:00 min	
2.5 µl	Dream Taq buffer (10x)	95°C	0:30 min	35 cycles
0.5 µl	$MgCl_2$ (25 mM)	60°C	0:45 min	
0.5 µl	dNTP's (10 mM)	72°C	1:00 min	
1 µl	fwd primer (1:10)	72°C	5:00 min	
1 µl	rev primer (1:10)	15°C	∞	
0.25 µl	DreamTaq Green DNA			
	Polymerase			
to 25 µl	H_2O			

Expected product size:
WT 152 bp
Kin 234 bp

Detection of the *Ncf1*$^{-/-}$ allele

Primer:

Ncf1_fwd: 5’ TGG ACG TTG TGG AGA AGA GC 3’
Ncf1 KO_rev: 5’ ACA CCC GCT ATT GCC TCA G 3’
Ncf1 WT_rev: 5’ CTC GTG CTT TAC GGT ATC GC 3’

Pipetting scheme		PCR program		
1 µl	genomic DNA	94°C	2:00 min	
5 µl	Biozym Taq buffer (5x)	94°C	0:20 min	10 cycles
0.75 µl	$MgCl_2$ (25 mM)	65°C	0:15 min	
0.5 µl	dNTP's (10 mM)		(0.5°C/cycle decrease)	
1 µl	Ncf1_fwd primer (1:10)	68°C	0:10 min	
1 µl	Ncf1 KO_rev primer (1:10)			
1 µl	Ncf1 WT_rev primer (1:10)	94°C	0:15 min	28 cycles
0.25 µl	Biozym Taq Polymerase	60°C	0:15 min	
		72°C	0:10 min	
to 25 µl	H_2O	72°C	2:00 min	

Expected product size:
WT: 500 bp
KO: 200 bp

2.2.1.3 Agarose gel electrophoresis

After the PCR, the DNA samples were separated according to their differences in electrophoretic motility. For the gel electrophoresis, 1-2% agarose gels were used (depending on expected size of the PCR product) and the respective amount of agarose was dissolved in 1x TAE buffer and boiled in a microwave oven. After cooling down the agarose to approximately 60°C, 5 µl of Midori Green per 100 ml were added and the fluid was poured into a tray containing a comb. The gel congeals at room temperature and was transferred in the electrophoresis chamber already being filled up with 1x TAE buffer. Subsequently, 2 µl of 6x loading dye were added to 25 µl DNA product and all samples were loaded into the slots of the gel. In the first slot a GeneRuler Mix DNA ladder was loaded to determine the size of the received DNA bands after electrophoresis. Electrophoresis was performed at 120-160 V and DNA bands were visualized by UV light.

2.2.2 Generation of murine plasma

700 µl blood were drawn from the retroorbital plexus of anesthetized mice and collected in Eppendorf tubes already containing 300 µl heparin (20 U/ml in TBS). Samples were centrifuged at 2,800 rpm for 5 min and supernatant was collected and centrifuged again at 2,800 rpm for 5 min. To remove residual cells, supernatant was centrifuged at 14,000 rpm for 5 min and plasma was collected and either used directly or stored at -20°C until further use.

2.2.3 Biochemistry

2.2.3.1 Preparation of total protein lysates

2.2.3.1.1 Peripheral white blood cell lysate

700 µl blood were drawn from the retroorbital plexus of anesthetized mice and collected in Eppendorf tubes already containing 300 µl heparin (20 U/ml in TBS). Sample was divided in 2 Eppendorf tubes (500 µl each) and 1 ml of ACK buffer was added per tube and incubated for 5 min on ice. Afterwards, the sample was centrifuged at 1,500 rpm for 5 min. The pellet was resuspended in 1 ml ACK buffer and again incubated for 5 min on ice and subsequently centrifuged. This time the pellet was resuspended in 25 µl lysis buffer in total (pool cells from both tubes) and cells were lysed for 30 min on ice. To remove the cell debris, the sample was centrifuged at 14,000 rpm for 10 min at 4°C. The supernatant was mixed with 10 µl of 4 x sample buffer and boiled for 5 min at 95°C. Samples were stored at -20°C before further use.

2.2.3.1.2 Brain tissue lysate

Mice were subjected to the tMCAO model and infarct volumes were quantified from three 2 mm thick coronal sections (see section 2.2.8.1). For the generation of total protein lysate from brain tissue, the rear segment was used, and the two hemispheres were separated. Further, cortices and basal ganglia of each hemisphere were separated, and the tissue was homogenized in RIPA buffer and sonified for 10 s. To remove the cell debris, samples were centrifuged at 15,000 *g* for 30 min at 4°C (or longer if no clear pellet was visible after 30 min). Before Western Blot analysis, protein content was determined using bicinchonic acid (BCA) protein assay. For Western Blot analysis, the lysates were mixed with 2x SDS-PAGE loading buffer and boiled for 10 min at 95°C.

2.2.3.2 Western Blot

For protein separation, sodium dodecyl sulfate polyacrylamide gel electrophoresis (SDS-PAGE) was used. Therefore, polyacrylamide gels were prepared with a 10 or 12% separating gel and a 4% stacking gel. 20 µl of the white blood cell samples prepared as described above were loaded into the slots of the stacking gel. The gel was run at 15 mA. As soon as the bands reached the separating gel, the current was raised to 25 mA. After separation, the proteins were transferred onto a polyvinylidene difluoride (PVDF) membrane via semidry immunoblotting at 50 mA per membrane for 1.5 h. Next, the membranes were blocked with 5% non-fat dry milk in TBS-T o/n at 4°C and afterwards incubated with the primary antibody o/n at 4°C. Before incubation with the respective HRP-coupled secondary antibody for 1 h at RT, membranes were washed three times with washing buffer for 10 min at RT. After another three washing steps protein bands were detected by ECL. Images were acquired at an Amersham^{TM} Imager 680.

For brain lysates, 20 µg of total protein was loaded on the gel and after electrophoresis transferred to a nitrocellulose membrane. Membranes were blocked with 5% non-fat dry milk in PBS containing 0.05% Tween-20 for 30 min at RT and afterwards incubated with the primary antibody o/n at 4°C. Before incubation with the respective HRP-coupled secondary antibody for 1 h at RT, membranes were washed three times with washing buffer for 10 min at RT. After another three washing steps protein bands were detected by ECL. Images were acquired at a ChemiDoc Touch imaging system (Bio-Rad, Hercules, CA, USA).

2.2.4 Cell culture

2.2.4.1 Cultivation of murine brain endothelial cell lines b.END3 and b.END5

The brain endothelial cell lines b.END3 and b.END5 were cultivated in T75 flasks for adherent cells in DMEM GlutaMAX supplemented with 10% FCS at 37°C and 5% CO_2. Upon confluency, cells were detached using trypsin, splitted and transferred to a new cell culture flask.

2.2.4.2 Isolation and cultivation of primary murine brain microvascular cells (MBMEC)

Experiment was performed by Lena Zimmermann, Department of Neurology, University Hospital Würzburg.

Mice were sacrificed (10 per isolation) by cervical dislocation and brains were isolated and brain stem, cerebellum and thalami were removed using forceps. Meninges were detached by carefully rolling the brains on a sterile blotting paper. Brains were collected in DMEM and tissue was minced by pipetting the solution repeatedly first with a 25 ml and then with a 10 ml pipette until the solution becomes milky. Afterwards the tissue was digested by incubation in a mixture of 0.6 ml collagenase CLS2 (10 mg/ml in DMEM) and 0.2 ml DNAse (1 mg/ml in

PBS) in DMEM for 1 h at 37°C in an orbital shaker at 180 rpm. Before centrifugation at 1000 *g* for 10 min at 4°C, 10 ml DMEM were added. The pellet was resuspended in 25 ml 20% BSA/DMEM using a 25 ml pipette (approx. 25 times) and sample was centrifuged at 1000 *g* for 20 min at 4°C. The upper myelin layer was removed with a broken glass Pasteur pipette (larger diameter) and then the remaining supernatant was discarded. The pellet was resuspended in 10 ml DMEM containing 1 mg/ml collagenase/dispase and DNAse. The sample was digested again by incubation for 1 h at 37°C in an orbital shaker at 180 rpm. Meanwhile the percoll solution (19 ml PBS, 1 ml 10x PBS, 1 ml FCS and 10 ml percoll) was centrifuged at 3000 *g* for 1 h at 4°C (no brake) to set up the density gradient. After digestion, 10 ml DMEM were added to the cell solution, the sample was centrifuged at 1000 *g* for 10 min at 4°C and the pellet was resuspended in 2 ml DMEM. The cell suspension was carefully layered on the prepared percoll gradient and centrifuged at 700 *g* for 10 min at 4°C (no acceleration, no brake). Afterwards the endothelial cells were visible as cloud at the interface. Approx. 12 ml of the interphase were transferred in a new Falcon tube, mixed with DMEM and centrifuged at 1000 *g* for 10 min at 4°C. The cells were resuspended in culture medium and seeded in collagen IV (0.4 mg/ml) and fibronectin (0.1 mg/ml) coated wells (o/n at 4°C). Endothelial cells were maintained in a cell culture incubator at 37°C and 5% CO_2. Medium was changed every two to three days and cells were splitted at 90% confluency. Protocol taken from Ruck *et al.*, 2014 [139].

2.2.4.3 Measurement of trans endothelial resistance (TEER) of MBMECs

Experiment was performed by Lena Zimmermann, Department of Neurology, University Hospital Würzburg.

MBMECs were isolated as described above (2.2.4.2) and cultivated in collagen IV/fibronectin coated Transwell Pore Polyester Membrane inserts with 0.4 µm pore size ($2x10^4$ cells per insert) at 37°C and 5% CO_2. Cells were treated with 1 µM hydrocortisone for 48 h before performing experiments. When cells reached approx. 80% confluency, medium was changed to measuring medium and the electrical resistance across the MBMEC monolayer (TEER) was measured using a resistance meter (CellZcope, San Francisco, USA). Cells were treated with the platelet supernatant, recombinant proteins, or buffers when TEER values were at the maximum (approx. 24 h after changing to measuring medium).

2.2.5 *In vitro* analysis of platelet morphology and function

2.2.5.1 Platelet preparation and washing

Mice were anesthetized with isoflurane and bled from the retro-orbital plexus. Blood was collected in Eppendorf tubes containing 300 µl heparin in TBS (20 U/ml, pH 7.3). Subsequently, the blood was centrifuged at 800 rpm (*300 g* in an Eppendorf Centrifuge 5415C) for 6 min. Supernatant and buffy coat were transferred into a new tube and the centrifugation step was repeated in order to get platelet rich plasma (PRP). For the preparation of washed platelets, PRP was centrifuged, at 2,800 rpm (*800 g*) for 5 min. The resulting pellet was washed twice with 1 ml Tyrode's - Ca^{2+} containing apyrase (0.02 U/ml) and PGI_2 (50 mM). After these washing steps, the pellet was resuspended in the same buffer and the platelet count of the suspension was determined using a Sysmex KX-21N Hematology Analyzer. The platelets were spun down once more at 2,800 rpm for 5 min and finally resuspended in the appropriate amount of buffer (either Tyrode's with or without Ca^{2+} containing 0.02 U/ml apyrase depending on the subsequent experiment) in order to achieve the desired platelet count. Platelets were set to rest for 30 min at 37°C before further analysis.

2.2.5.2 Generation of platelet releasate

Washed platelets were prepared from the indicated genotypes as described above (2.2.5.1). After the last washing step, platelets were resuspended in Tyrode's + Ca^{2+} (500,000/µl) and stimulated with 10 µg/ml CRP for 15 min at 37°C. To separate the platelet releasate from the platelet debris, platelets were centrifuged at 2,800 rpm for 5 min at RT and the supernatant was removed and centrifuged at 14,000 rpm for 5 min at 4°C. Platelet releasate was filtered through a syringe filter with a pore size of 0.22 µm before aliquots were prepared and stored at -80°C until further use. For cooked platelet releasate, the aliquots were thawed and boiled at 95°C for 10 min before use in cell culture experiments.

2.2.5.3 Aggregometry

Washed platelets were prepared as described in 2.2.5.1. For aggregation studies, 50 µl washed platelets (500,000/µl) were mixed with 110 µl Tyrode's + Ca^{2+} containing 100 µl human fibrinogen. Measurements with thrombin as agonist were conducted without fibrinogen. Aggregation was measured by recording light transmission using an Apact 4-channel aggregometer (APACT, Laborgeräte und Analysensysteme, Hamburg) for 10 min after activation with the indicated agonists, proteins or antibodies (added 100x concentrated). Before the measurements, calibration was performed setting fibrinogen containing Tyrode's buffer as 100% aggregation and diluted platelet solution as 0% aggregation.

2.2.5.4 Platelet spreading on fibrinogen

Coverslips (24x60 mm) were coated with 100 µl human fibrinogen (100 µg/ml) o/n at 4°C in a humid chamber. The next day, the slides were blocked with sterile 1% BSA/PBS for at least 1 h at RT. Meanwhile, 700 µl of blood were collected in 300 µl heparin (20 U/ml, pH 7.3) and washed platelets were prepared as described in 2.2.5.1. After the second washing step, the platelet concentration was adjusted to 300,000/µl in Tyrode's - Ca^{2+} containing 0.02 U/ml apyrase and the platelets were set to rest for 30 min at 37°C. After blocking, the coverslips were washed once with 300 µl of PBS and rinsed twice with Tyrode's buffer containing Ca^{2+}. Depending on the spreading time, platelet suspension was diluted differently in Tyrode's + Ca^{2+} (5 min 1:1, 15 min 2:3, 30 min 3:7). Per timepoint, 100 µl platelet suspension was activated with 0.01 U/ml thrombin and immediately pipetted on the fibrinogen coated coverslip. Spreading was stopped at the respective time points by the addition of 300 µl of 4% PFA/PBS and fixed for 5 min. Sample analysis was performed by differential interference contrast (DIC) microscopy using an inverted microscope Zeiss HBO 100 (Axiovert 200M, Zeiss). Images were taken of at least 7 different microscopic fields and phase abundance of the different spreading stages was determined (1, resting; 2, formation of filopodia; 3, formation of filopodia and lamellipodia; 4, fully spread).

For the observation of calcium signals during spreading, 8-Well Ibidi glass bottom chamber slides were coated with 100 µg/ml fibrinogen o/n at 4°C. The next day, slides were blocked with 1% BSA/PBS for 1 h at RT. Washed platelets were prepared from PC-G5-tdT.PF4Cre$^{+/-}$ as described in 2.2.5.1 and after the final washing step resuspended at a concentration of 300,000/µl in Tyrodes's – Ca^{2+} supplemented with 2 µl apyrase and set to rest for 30 min at 37°C. Platelets were stained with Membright 640 (0.3 µl per 120 µl platelet suspension) for 5 min at 37°C. Before adding platelets, wells were washed three times with sterile 1x PBS followed by one washing step with Tyrode's + Ca^{2+}. Per Well, 60 µl platelet suspension was mixed with 120 µl Tyrode's + Ca^{2+} and directly before imaging, platelets were stimulated with 0.1 U/ml thrombin. Imaging was performed using a SP8 confocal microscope (Leica) and a HC PL APO CS2 100x/1.40 OIL objective. Platelet spreading process was followed for 40 min whereby every 8 seconds one image was recorded. Afterwards, images were deconvolved using the Express Deconvolution mode of Huygens software.

2.2.5.5 Measurement of intracellular Ca^{2+} levels in platelets

Washed platelets were prepared as described in 2.2.5.1 and resuspended at a concentration of 200,000/µl in Tyrode's + Ca^{2+}. 100 µl of platelet suspension were labeled with Fura-2-AM (5 µM) for 20 min at 37°C in the presence of 0.2 µg/ml pluronic acid (F-127). Residual Fura-2 was removed by centrifugation of the sample at 2,800 rpm for 2 min and resuspension of the pellet in 500 µl HBSS supplemented with 1 mM $MgCl_2$ and 1 mM $CaCl_2$. Fluorescent emission was measured at 509 nm with a Perkin Elmer FL-6500 (PerkinElmer, Waltham, USA) under stirring conditions for 50 s with an alternating excitation between 340 and 380 nm to determine the baseline fluorescence. After adding the respective agonists, the emission was measured for another 250 s. For calibration, 1% Triton-X were added followed by addition of 0.5 M EGTA to determine total and zero emission values respectively, allowing calculation of the absolute values. Data were analyzed using the Spectrum FL software (Perkin Elmer) and Microsoft Excel.

2.2.5.6 Tyrosine phosphorylation assay

Platelets were washed as described in 2.2.5.1 but with the use of BSA-free Tyrode's-Ca^{2+} instead of BSA containing buffer for the second washing step. Platelets were resuspended to a final concentration of 500,000/µl and incubated with 2.4 µg/ml rhodocytin, 10 µg/ml INU1-IgG, INU1-$F(ab)_2$ or INU1-fab *in vitro* for 15 min or were left untreated. Afterwards, platelets were lysed in using lysis buffer for tyrosine phosphorylation. Lysates were centrifuged at 14,000 rpm for 10 min at 4°C and to remove cell debris. The phosphorylation pattern of tyrosine residues was analyzed by Western Blot analysis using the anti-pan-phosphotyrosine antibody 4G10 (1:1000).

2.2.5.7 Platelet adhesion under flow

To study platelet adhesion and thrombus formation on collagen, rectangular cover slips (24x60 mm) were coated with 80 µl of collagen (200 µg/ml fibrillar type I collagen) o/n at 37°C. The next day, slides were blocked with 300 µl of 1% BSA/PBS for at least 1 h at RT. 700 µl of blood were collected in 300 µl heparin (20 U/ml in TBS) and 2 parts of blood were diluted with one part Tyrode's + Ca^{2+} and platelets were labelled with 0.3 mg/ml anti-GPIX-Alexa647 for 5 min at 37°C before perfusion. The cover slips were placed in a custom-made transparent flow chamber with a slit depth of 50 µm and blood was filled in a 1 ml syringe and perfused over the collagen coated slide using a pulse-free pump and a shear rate of $1000s^{-1}$ for 4 min (run). To remove residual non-bound cells, Tyrode's + Ca^{2+} was perfused over the slide for another 4 min (washing). The run was monitored using a Leica DMI6000B inverted microscope (63x/1.3 glycerol HCX PL APO objective). After 4 min of washing at least 8 images from different visual fields and fluorescence images from the Alexa647 signal were taken and analyzed with ImageJ software (NIH). Results were depicted as mean percentage of total area covered by platelets and thrombus volume as arbitrary units of mean integrated fluorescence intensity.

For platelet immobilization on vWF, cover slips (24x60 mm) were coated with a polyclonal rabbit anti-human vWF antibody (1:500 diluted in coating buffer) o/n at 4°C in a humid chamber. The next day, slides were blocked with 300 µl of 1% BSA/PBS for 1 h at RT. After blocking, cover slips were incubated with 200 µl murine plasma for 2 h at 37°C to allow binding of plasma vWF to the immobilized antibody. Perfusion of blood was performed as described above, but at a shear rate of 1700 s^{-1}. To activate platelets after washing, 0.1 U/ml thrombin in Tyrode's + Ca^{2+} was perfused over the platelet monolayer.

2.2.5.8 Scanning electron microscopy (SEM)

Washed platelets were prepared as described in 2.2.5.1. After the last washing step, the pellet was resuspended and washed once in modified Tyrodes-N-2-hydroxyethlpiperazine-N-2-ethanesulfonicacid (HEPES, 5 mM glucose, 0.35% BSA, pH 7.4) buffer supplemented with prostaglandin I_2 (0.1 µg/mL) and apyrase (0.02 U/mL). Prior to analysis, platelets were suspended in the same buffer (0.02 U/mL apyrase) and allowed to rest for at least 30 min at 37°C.

Washed platelets (250,000/µL f.c.) were incubated with 10 µg/mL INU1-fab, INU1-$F(ab)_2$ or INU1-IgG, respectively, *in vitro* for 15 min or left untreated. Samples were fixed in solution with 2x Karnovsky buffer for 5 min at 37°C prior to fixation on poly-L Lysin coated coverslides for 1 h at RT followed by o/n fixation at 4°C with 1x Karnovsky buffer (2.5% glutaraldehyde in 100 mM cacodylate buffer). On the next day, samples were fixed with 4% PFA/0.4% glutaraldehyde for 20 min at 4°C and washed twice with distilled H_2O for 5 min, 4°C. After washing with 100 mM cacodylate buffer for 5 min, 4°C, samples were dehydrated using an increasing EtOH series (4x 5 min EtOH 75%, 5 min EtOH 80%, 5 min EtOH 95%, all at 4°C and 2x 20 min EtOH 100% at RT). Next, samples were incubated with increasing HMDS concentrations (Hexamethyldisilazane; 5 min 25% HMDS diluted in 100% EtOH, 5 min 50% HMDS, 5 min 75% HMDS and twice 5 min 100% HMDS, all at RT). Afterwards, samples were dried by evaporating HMDS, mounted, sputter coated with Au/Pd and examined under a scanning electron microscope (Phenom Pro, Thermofisher Scientific).

2.2.6 Flow cytometry

2.2.6.1 Determination of platelet count, size and major glycoproteins

To determine platelet count, size and surface protein expression, 50 µl blood from anesthetized mice was taken in Eppendorf tubes containing 300 µl heparin (20 U/ml, pH 7.3). The blood was filled up to 1 ml with Tyrode's - Ca^{2+} and distributed (50 µl each) in FACS tubes already containing saturating amounts of respective fluorophore-conjugated antibodies. The antibodies were incubated with the blood for 15 min at RT in the dark. Afterwards the reaction was stopped by the addition of 500 µl of PBS and samples were measured using a FACSCelesta (BD, Heidelberg, Germany) equipped with the BD FACSDiva^{TM} Software.

2.2.6.2 Analysis of platelet activation response

For the analysis of platelet integrin αIIbβ3-activation and P-selectin exposure by flow cytometry, 50 µl of blood were taken as described above and filled up to 1 ml with Tyrode's - Ca^{2+}. To remove the heparin, the blood was washed twice with 1 ml Tyrode's - Ca^{2+} (centrifugation between the washing steps at 2,800 rpm for 5 min). After the second washing step, the blood pellet was resuspended in 750 µl Tyrode's + Ca^{2+} and the washed blood was distributed (50 µl each) in the FACS tubes already containing saturating amounts of the respective fluorophore-conjugated antibodies and the respective 10x concentrated agonist. For the measurement of activated αIIbβ3 and P-Selectin exposure, a 1:1 mixture of the PE-labeled JON/A antibody (4H5-PE) and the FITC-labeled anti-P-Selectin antibody (5C8-FITC) was used (10 µl of each antibody solution). Washed blood was incubated with the antibodies for 7 min at 37°C, followed by 7 min at RT in the dark. The reaction was stopped by the addition of 500 µl of PBS and samples were measured using a BD FACSCelesta and the BD FACSDiva^{TM} Software.

For the analysis of platelet activation in response to INU1-IgG, INU1-F(ab)$_2$ or INU-fab, washed platelets were prepared (2.2.5.1) and resuspended in Tyrode's + Ca^{2+} to achieve a concentration of 500,000/µl. 50 µl platelet suspension was incubated with 50 µl 1:1 mixture of 4H5-PE and 5C8-FITC and 10 µg/ml of the respective INU1 antibody derivative. Samples were incubated for 7 min at 37°C, followed by 7 min at RT in the dark. After stopping the reaction by addition of 500 µl PBS, samples were measured using a BD FACSCalibur and the CellQuest Pro Software.

2.2.6.3 Determination of peripheral platelet counts after INU1-fab induced CVT

At the indicated time points, 50 µl blood were withdrawn in 300 µl heparin from the retroorbital plexus and blood was diluted with 700 µl PBS. 50 µl diluted blood was incubated with JON6-PE and p0p4-FITC (10 µl each) for 15 min at RT. The reaction was stopped by the addition of 500 µl PBS and the number of double positive platelets was measured using a BD FACSCalibur and the CellQuest Pro Software.

2.2.6.4 Quantification of circulating neutrophils

On day 3 after neutrophil depletion (see 2.2.8.8), 700 µl blood was withdrawn in 300 µl heparin from the retroorbital plexus of anesthetized mice. Per 300 µl blood, 1700 µl ACK buffer were added and incubated for 10 min at RT to lyse red blood cells. After centrifugation at 300 *g* for 5 min at 4°C, cells were resuspended in 300 µl 1% FCS/PBS. 50 µl of the cell suspension were stained with anti-Gr1-FITC (1:1500) for 30 min on ice in the dark. After staining, cells were centrifuged at 400 *g* for 5 min at 4°C, washed with 1% FCS/PBS and centrifuged again. Afterwards cells were fixed with 1% PFA/PBS for 30 min on ice in the dark and subsequently centrifuged at 400 *g* for 5 min at 4°C. The pellet was resuspended in 300 µl 1% FCS/PBS and samples were analyzed by flow cytometry using a BD FACSCanto and the FACSDiva^{TM} Software.

2.2.6.5 Flow cytometric analysis of b.END cells

Endothelial cells were detached by incubation with trypsin for 1 min at 37°C, taken in suspension with 10 ml medium and centrifuged at 400 *g* for 5 min at 4°C. The supernatant was discarded, and the cell pellet was resuspended in FACS buffer to achieve a concentration of $2*10^7$/ml. Unspecific binding sites were blocked with 10 µg/ml Fc-block (2.4G2) for 15 min on ice. For the staining of surface markers, cell suspension (50 µl) was incubated with the respective, fluorescently labeled antibodies for 30 min on ice in the dark. Afterwards, cells were washed by adding 200 µl FACS buffer and centrifugation at 400 *g* for 5 min at 4°C. The pellet was resuspended in 200 µl FACS buffer and immediately analyzed by flow cytometry using a BD FACSCanto. For intracellular markers, cells were fixed and permeabilized before staining with the respective fluorescently labeled antibodies for 30 min on ice in the dark. For fixation, cells were incubated with 1% PFA/PBS for 30 min at RT, washed twice with FACS buffer followed by centrifugation at 400 *g* for 5 min at 4°C and permeabilized with 0.1% NP-40/PBS for 20 min at 4°C in the dark. After staining, samples were directly analyzed by flow cytometry.

2.2.7 Immunofluorescence and histology

2.2.7.1 Staining of endothelial cells

For the staining of tight junction proteins in b.END3 and b.END5 cells, these were cultivated on 12 mm glass cover slides in 12-Well cell culture plates. When grown to confluency, cells were washed twice with 1x PBS and subsequently fixed with 1% PLP for 1 h at RT. After another three washing steps (10 min each) with 5% FCS/PBS, unspecific binding sites were blocked by the addition of 5% BSA/PBS for 1 h at RT. Before permeabilization with 0.1% NP-40/PBS for 30 min at RT, cells were washed once with 1x PBS. Afterwards, cells were washed once with 5% FCS/PBS, blocked with 5% BSA/PBS for 1 h at RT and incubated with the respective primary antibodies o/n at 4°C in 5% FCS/PBS. Rabbit anti-Claudin-1 (3 µg/ml), rabbit anti-Claudin-3 (1:300), rabbit anti-Claudin-5 (1:100), rabbit anti-Occludin (1:100) and rabbit anti-ZO-1 (5 µg/ml). The next day, cells were washed three times for 10 min with 5% FCS/PBS and incubated with the secondary antibody, anti-rabbit-Alexa488 (1:300) in 5% FCS/PBS. After two washing steps with 1x PBS, cover slips were taken out of the well plate and mounted on object slides using Fluoroshield containing DAPI to stain nuclei. For the staining of endothelial markers CD31 and CD105 on b.END3 and b.END5 cells, cells were grown on 12 mm glass cover slides in 12-Well cell culture plates. When grown to confluency, cells were washed twice with 1x PBS and incubated with fluorescently labeled anti-CD31-A488 (5 µg/ml) and anti-CD105-A647 (5 µg/ml) in 5% FCS/PBS for 1 h at RT in the dark. Afterwards, cells were washed three times for 10 min with 5% FCS/PBS and fixed by the addition of 1% PLP for 1 h at RT followed by another three washing steps (10 min each) with 5% FCS/PBS. Glass cover slides were removed from the well plate and mounted on object slides using Fluoroshied containing DAPI to stain nuclei. Images were acquired using a SP5 confocal microscope (Leica) equipped with a HCX PL APO CS 40.0x1.25 OIL UV objective.

Staining of tight junction proteins in primary MBMECs was performed after TEER measurements in untreated samples (2.2.4.3). Cells were fixed with glyoxal for 20 min at RT, washed with PBS and blocked with 0.5% BSA/0.1% Triton-X in PBS for 30 min at RT. For staining, cells were incubated with rabbit anti-Claudin-1 (3 µg/ml), rabbit anti-Claudin-3 (1:300), rabbit anti-Claudin-5 (1:100), rabbit anti-Occludin (1:100) or rabbit anti-ZO-1 (5 µg/ml) and rat anti-CD31 (1:100) in 1% BSA/PBS o/n at 4°C. The next day, cells were washed three times with PBS and incubated with the secondary antibodies, goat anti-rabbit-A594 (1:400) and donkey anti-rat-DyLight488 (1:400) in 1% BSA/PBS for 1 h at RT. Cells were washed three times with PBS, nets were cut out of the inserts and mounted on object slides using Prolong Gold with DAPI. Images were acquired using a SP8 confocal microscope (Leica) equipped with a HC PL APO CS2 40x/1.30 OIL objective.

2.2.7.2 Quantification of gaps between MBMECs

MBMECs were seeded in an Ibidi 18-Well-Chamber slide und grown to confluence. Then, cells were treated with platelet releasate from the indicated genotypes, with control buffer (10 µg/ml CRP in Tyrodes's + Ca^{2+}) or left untreated for 18 h. Afterwards cells were washed with PBS and fixed with glyoxal for 20 min at RT. Samples rinsed with PBS and blocked with 0.5% BSA/0.1% Triton-X in PBS for 1 h at RT. Staining of CD31 was performed by incubation of the fixed cells with rat anti-mouse CD31 (1:100) in 1% BSA/PBS for 1 h at RT followed by incubation with the secondary antibody donkey anti-rat-DyLight488 (1:400 in 1% BSA/PBS) for 1 h at RT. In between cells were washed three times with PBS. After staining, cells were again washed three times with PBS and mounted with Prolong Gold containing DAPI. Samples were imaged using a SP8 confocal microscope (Leica) equipped with a HC PL APO CS2 40x/1.30 OIL objective using Immersol 518F immersion oil since this is required by the Ibidi 18-Well Chamber slides. 36 tiles were acquired from each sample in the middle area of the well to avoid artefacts from the well borders. For the quantification of holes between individual cells, an analysis pipeline was developed by Dr. Katherina Hemmen from the Core Unit Fluorescence Imaging (Rudolf-Virchow-Center for Integrative and Translational Bioimaging, University of Würzburg). First, the collected data was exported from the lif-files as 8-bit grey scale tiff-images using Fiji. Next, data was processed using the scikit image package for python. Entropy of the images was calculated, generating ‘entropy images’. Due to the lack of CD31 staining in the gaps between cells, entropy was lower in these holes. By setting a respective threshold, holes were identified using watershed-segmentation and the area covered by holes was calculated. The applied script is given in the appendix.

2.2.7.3 Cryosections

Collection of mouse organs for histology: Mice were euthanized by an overdose of isoflurane. The lungs were exposed by opening the rib cage. For a better preservation of the lung structure, the lungs were filled with 0.8 ml optimum cutting temperature (O.C.T$^{\mathrm{TM}}$) compound mixed with 10% sucrose in PBS in a 1:1 ratio. The mixture was introduced into the collapsed lungs by cannulation of the trachea with a 22G venous catheter (BD Insyte®). Afterwards, the trachea was tied up, lungs were harvested *en bloc*, rinsed in 1x PBS and the heart was removed. Furthermore, kidney, spleen, brain and the left lobe of the liver were removed. Before snap freezing in isopentane pre-cooled on dry ice, organs were carefully dabbed dry on a paper towel and embedded in O.C.T$^{\mathrm{TM}}$ in Tissue-Tek® Cryomolds.

For brain cryosections of mice after tMCAO, brains were processed as described in 2.2.8.1 and the middle segment was snap frozen after TTC staining as described above. Blocks were stored at -80°C until 7 µm cross-sections were cut with a Leica CM1950 cryostat (Leica) and mounted on Superfrost Plus slides (Thermo Scientific).

For cryosection of the femur, bones were removed and fixed in 4% PFA/PBS containing 5 mM sucrose for 24 h at 4°C. Before embedding in O.C.T$^{\mathrm{TM}}$, bones undergo a serial incubation in solutions with increasing sucrose concentration for 24 h at 4°C each (10%, 20% and 2 x 30%).

2.2.7.3.1 Staining of cryosections of lung and brain with hematoxylin and eosin (H&E)

For hematoxylin and eosin (H&E) staining, cryosections of lung and brain were thawed at RT for 10 min and immediately fixed with 4% paraformaldehyde (PFA, pH 7.2) for 10 min. After fixation, the sections were washed three times with PBS followed by a short wash in deionized water. Slides were stained for 30 s (lung) or 60 s (brain) in hematoxylin (Hematoxylin Solution, Gill No.3, Sigma Aldrich) and bluing was performed under running tab water for 10 min. Afterwards, sections were stained for 3 min (lung) or 90 s (brain) with acidified 0.05% Eosin G solution (Carl Roth) and rinsed with deionized water. To dehydrate the sections, they were incubated for 2 min each in ethanol solutions with increasing concentrations (70% EtOH, 80% EtOH, 90% EtOH, 96% EtOH and 100% EtOH). Dehydrated sections were dried under the fume hood and mounted with Eukitt®. Before imaging, they were kept at RT o/n.

2.2.7.3.2 Immunofluorescence staining of cryosections from different organs

For immunofluorescence staining of spleen, kidney, liver, lung and brain sections, slides were thawed, fixed with glyoxal fixation buffer and washed three times (5 min) with wash buffer for fluorescence staining. Unspecific binding sites were blocked by incubation of the sections with 5% BSA and 10 µg/ml Fc-Block (2.4G2) in 1x PBS for 30 min at RT. Fluorescently labeled antibodies were incubated sequentially (60 min each) at a concentration of 5 µg/ml diluted in staining buffer. After each antibody incubation step, sections were washed three times with staining buffer. Anti-GPIX-Alexa546 was used to stain platelets and endothelial cells were stained using anti-CD31-Alexa647 (clone 390, BioLegend). After the final washing step, sections were mounted with Fluoroshield^{TM} containing DAPI to stain nuclei. Slides were kept at 4°C o/n before imaging.

For staining of NETs in lung sections, sections were fixed with 4% PFA for 10 min at RT and washed three times for 5 min with 1x PBS. Unspecific binding sites were blocked with 3% goat serum, 5% BSA, 10 µg/ml Fc-Block (2.4G2) in wash buffer (0.1% Tween-20 in 1x PBS pH 7.4) for 30 min at RT in a humid chamber. For NET staining, slides were incubated with rabbit anti-mouse H3Cit (2 µg/ml in wash buffer containing 3% goat serum and 5% BSA=dilution buffer) for 1 h at RT in a humid chamber. After washing the slides three times with wash buffer for 5 min each, they were incubated with the fluorescently labeled secondary antibody (goat anti-rabbit-Alexa546, 1:300 in dilution buffer) for 45 min at RT in a humid chamber. Again, slides were washed three times for 5 min with wash buffer and subsequently, neutrophils were stained for 1 h at RT in a humid chamber using rat anti-mouse Ly6G-Alexa647 (1A8, BioLegend) at 5 µg/ml in dilution buffer. Afterwards slides were washed three times for 5 min in wash buffer and mounted using Fluoroshield containing DAPI to stain nuclei. Slides were stored at 4°C until imaging.

Imaging was performed using a Leica Thunder Imager DMi8, equipped with a LEICA DFC9000GT fluorescence and an Andor Zyla 4.2 bright field camera. 10x or 20x objectives were used and the Leica Application Suite (LAS) X software (version 3.7). Images were deconvolved directly after imaging using the LAS X Thunder software. For quantification in section 3.5, the number of cerebral thrombi was counted in separate horizontal sections per animal and used for statistical analysis. Representative images of the different organs were processed and visualized using ImageJ software.

For the staining of NETs in brain sections after tMCAO in *Pad4*$^{-/-}$ mice and respective WT controls, the same protocol and buffers were used but with the following variations: rabbit anti-mouse H3Cit was used at a concentration of 1 µg/ml and incubated o/n at 4°C in a humid chamber and as secondary antibody, donkey anti-rabbit-Alexa647 (1:300 in dilution buffer) was used. For the staining of neutrophils anti-Ly6G-Alexa488 (clone RB6-8C5) was used. Sections were imaged using a SP8 confocal microscope (Leica) equipped with a HC PL APO CS2 40x/1.30 OIL objective.

2.2.7.3.3 Quantification of vascular leakage in brain cryosections

Quantification of vascular leakage and thrombus number was performed using the same brain sections. Therefore, sections were cut as described above and dried for 30 min at RT, fixed with ice-cold (-20°C) acetone for 10 min and dried again for 30 min at RT. Afterwards, slides were washed three times with 1x PBS and unspecific binding sites were blocked using 10% BSA in PBS for 30 min at RT. Staining of albumin and endothelial cells was performed simultaneously by incubation of the slides with rabbit anti-albumin (1:200 in 1% BSA/PBS) and rat anti-CD31 (Bio-Rad; 1:1000 in 1% BSA/PBS) o/n at 4°C. The next day, slides were washed three times with 1x PBS and incubated for 45 min at RT with the secondary antibodies: goat anti-rabbit-Atto647N (1:200 in 1% BSA/PBS) and goat anti-rat-Alexa488 (1:300 in 1% BSA/PBS). After another three washing steps with 1x PBS, platelets were stained with anti-GPIX-Alexa594 (5 µg/ml in 1% BSA/PBS) for 1 h at RT. Slides were washed three times with 1x PBS and mounted with Fluoroshield containing DAPI to stain nuclei. Slides were stored at 4°C in the dark until imaging.

Z-Scans (z-size 4 µm) of the whole brain section were recorded as tile scans using a Leica SP8 confocal microscope (HC PL FLUOTAR 10x/0.30 DRY objective, resonant scanner 8000 Hz, line average 3, 1248x1248 pixel, digital zoom 2). After imaging, tile scans were stitched using the Leica Application Suite (LAS) software. From the stitched tile scans, maximum projections from the albumin channel were generated in Fiji. The degree of leakage was analyzed based on the albumin signal and scored in a 5-point scoring system (from 0, no leakage to 4, heavy leakage) indicated below.

Leakage Score

0: no leakage
1: small leakage spots
2: minor leakages
3: major leakages
4: heavy leakage

2.2.7.3.4 Quantification of occluded vessels and thrombi in brain cryosections

For the quantification of occluded vessels, cryosections of the brain were stained with hematoxylin & eosin (see 2.2.7.3.1) or with fluorescently labeled antibodies (here the same sections were used as for the quantification of albumin leakage; see 2.2.7.3.3). From the stitched tile scans, maximum projections from the platelet channel were generated in Fiji and deconvolved using Huygens software (Deconvolution algorithm CMLE, maximum iterations: 40, signal to noise ratio: 20, quality threshold: 0.05, iteration mode: optimized, brick layout: auto) and exported as .tiff files. To quantify thrombus number, a binary image was generated from the tiff-files by setting a respective threshold to separate the platelet signal from the background. Binary images were analyzed using the Analyze Particle Tool in Fiji counting every particle larger than 5 μm^2 as thrombus.

2.2.8 *In vivo* experiments

2.2.8.1 Transient middle cerebral artery occlusion and quantification of infarct volumes

Mice (10- to 14- weeks old) were anesthetized with 2% isoflurane/oxygen and placed on the back on a feedback-controlled heating pad to maintain a body temperature of 37°C. The incision site at the neck was disinfected using 70% ethanol before cutting the skin and gently exposing the carotid artery. Afterwards, a silicon rubber-coated 6.0 nylon monofilament was inserted into the right common carotid artery and advanced via the internal carotid artery to occlude the origin of the middle cerebral artery (MCA). The surgical procedure was kept below 10 min for each mouse and mice were left in a heated cage during the time of MCA occlusion. After 60 min, mice were re-anesthetized, and the filament was removed allowing reperfusion. The skin was closed by suturing the neck incision and mice were placed in fresh cages with crushed food soaked in water. After the indicated reperfusion times, infarct sizes and/or neurological impairment (see 2.2.8.2) were assessed. For the quantification of infarct sizes, brains were removed and cut into three coronal, consecutive 2 mm thick slices. Viable tissue was stained with 2% 2,3,5-triphenyltetrazolium chloride (TTC) approx. 15 min until good staining could be observed. Stained brain slices were scanned, and edema-corrected infarct volumes were calculated by planimetry using following equation $V_{indirect}$ (mm^3) = $V_{infarct}$ x (1 - (VI – VC)/VC). VI: Volume ischemic hemisphere, VC: Volume control hemisphere. Measurements were performed using Fiji.

2.2.8.2 Bederson Score and Grip Test

The degree of neurological deficits due to brain infarction induced by the tMCAO model was assessed with two neurobehavioral tests. The Bederson Score (0-5) evaluates the movement pattern of mice. 0: no deficit, 1: flexion of the contralateral forepaw, 2: as 1 but additionally reduced lateral position reflex, 3: occasional unidirectional running in circles (circling), 4: as 3 plus occasional spinning around the longitudinal axis of the body (spinning), 5: no spontaneous movement. The Grip Test (5-0) is used to evaluate the motor functions and coordination of the mice. For this purpose, the animals are lifted on a rope at a height of 20 cm and their abilities are classified according to the following criteria. 0: mouse falls off, 1: mouse hangs on the rope with one or two forepaws, 2: mouse hangs on the rope with one or both forepaws and shows efforts to climb the rope, 3: mouse hangs on the rope with one or two forepaws and one or both hind paws, 4: mouse hangs on the rope with both front and hind paws and wraps tail around the rope, 5: mouse hangs on the rope with both front and hind paws, wraps tail around the rope and escapes to the outer rack.

2.2.8.3 $FeCl_3$ induced model of arterial thrombosis

Mice (15 – 18 g body weight) were anesthetized and the mesentery was exteriorized through a midline abdominal incision and arterioles with a diameter of 35 – 60 µm were visualized using a Leica TC SP8 inverted confocal microscope. Platelets and endothelial cells were stained by intravenous injection of anti-GPIX-A546 (10 µg/mouse) and anti-CD105-A647 (15 µg/mouse) 15 min before imaging. Endothelial injury was induced by topical application of a 3 mm^2 filter paper soaked with 20% $FeCl_3$. Adhesion and aggregation of fluorescently labeled platelets to the side of injury was monitored and z-stacks (z-size 2 µm) were recorded every 8 s.

2.2.8.4 Open Cranial Window (OCW) surgery

To allow access to the brain vasculature for intravital microscopy, an open cranial window (OCW) was applied in the skull of the mice. Therefore, mice were anesthetized by intraperitoneal injection of medetomidine (0.5 µg/g), midazolam (5 µg/g) and fentanyl (0.05 µg/g) and 5 µg/mouse dexamethasone were injected subcutaneously in the neck fold. At the site of surgery, hair was removed, and the skin was disinfected with 70% isopropyl alcohol. By removing the skin, the skull was exposed. To remove the bone on top of the MCA territory or the superior sagittal sinus (SSS), a circle with a diameter of approx. 5 mm was cut in the corresponding region on the bone using a high-speed microdrill. To avoid overheating, the skull was repeatedly cooled with saline. The cut skull region was removed using forceps without damaging the dura. Subsequently, the exposed brain region was covered with a small drop of saline and a sterile, round coverslip (diameter of 6 mm) which was fixed with cyanoacrylate glue. The exposed skull was covered with dental cement. When surgery was completed, anesthesia was antagonized by intraperitoneal injection of atipam (2.5 µg/g), flumazenil (0.05 µg/g) and naloxone (1.2 µg/g) and mice were placed in fresh cages with crushed food soaked in water. Mice were left to recover and monitored daily for two weeks. In case of CVT, mice were directly used for intravital imaging, without antagonization of the anesthesia and recovery phase.

2.2.8.5 Jugular vein catheter

To place a catheter in the jugular vein, mice were anesthetized using medetomidine (0.5 µg/g), midazolam (5 µg/g) and fentanyl (0.05 µg/g). To remove hair from the neck region, mice were first shaved, and residual hair was removed by application of hair removal cream for 5 min. Afterwards, the skin was disinfected with 70% isopropyl alcohol and a small incision was made in the region of the jugular vein. By removing the surrounding tissue, the jugular vein was carefully exposed and ligated in the upper (towards the head) part. A second suture was placed around the distal part but not ligated yet. With the help of a bent needle (taken from a surgical suture), a small hole was inserted in the vein so that a diagonally sharpened tube could be inserted in the vein. Carefully check that no residual air is in the tubing. The tube was fixed with the second suture and well tied. When the tube is in place, the skin is closed using VetBond tissue adhesive glue.

2.2.8.6 Intravital microscopy of the brain vasculature

Before imaging, an open cranial window (OCW) was induced into the skull (2.2.8.4). In case of CVT, allowing intravenous injection during microscopy required placement of a catheter in the jugular vein (2.2.8.5). Brain vasculature was visualized by injection of BSA-A546 (8 µg/g body weight) and anti-CD105-A546 (clone MJ7/19, purified in-house, 0.4 µg/g body weight). Platelets were visualized by injection of anti-GPIX-A488 derivative (0.6 µg/g). Then, a custom designed metal plate was fixed to the open cranial window and the mouse was mounted on a custom-built stereotactic frame to reduce head movement during imaging. Mice were placed under an upright Leica SP8 confocal microscope or a Leica TCS SP8 2-Photon Microscope and imaging was performed using a 10x (in case of SSS) or 25x objective (in case of MCA territory), respectively. To investigate formation of thrombosis in the SSS, after 5 min of imaging, mice were treated with INU1-fab (0.5 ug/g), INU1-IgG (0.75 µg/g) or vehicle without stopping image acquisition. Image stacks were processed, visualized, and analyzed using Fiji.

2.2.8.7 Measurement of cerebral perfusion by Laser Speckle Contrast Imaging (LASCA)

10- to 14-week-old C57BL/6J mice were anesthetized using 2% isoflurane/oxygen inhalation narcotics and placed on a feedback-controlled heating pad to ensure a constant body temperature of 37°C. Mice were subjected to the tMCAO model (see section 2.2.8.1) and the scull was exposed by removing the scalp. Cerebral perfusion was measured using a PeriCam PSI HR perfusion imager (Perimed) either while the MCA was occluded or after filament removal. Cerebral perfusion of naïve mice was measured as baseline control.

2.2.8.8 Depletion of neutrophils

Neutrophil depletion was performed by intraperitoneal injection of 500 µg anti-Ly6G antibody (clone RB6-8C5) 3 days prior to the experiment.

2.2.8.9 INU1-fab induced cerebral venous thrombosis and treatments

INU1-fab (0.5 µg/g bodyweight) was administered intravenously under short (< 5 min) isoflurane anesthesia. INU1-F(ab)$_2$ (0.5 µg/g), INU1-IgG (0.75 µg/g), platelet depletion antibodies (R300, 2 µg/g), JON/A-F(ab)$_2$ and p0p/B-fab (2 µg(g) were also administered intravenously under isoflurane anesthesia. Unfractionated heparin (2 U/g) was injected i.p. in case of pre-treatment and i.v. in case of therapeutic treatment. CLEC-2-deficiency on platelets was induced by injection of INU1-IgG (100 µg/mouse) 7 and 5 days before the experiment. After injection of INU1-fab, mice were constantly monitored and neurological symptoms were classified according to a six-point scoring system 0: death, 1: severe seizures or circling behavior, 2: post-seizure lethargy, 3: mouse lying ‘exhausted’ on the belly, 4: backward bending of the head and backside, 5: reduced motor control of the hind limbs, 6: seemingly unaffected behavior.

2.2.8.10 Light sheet fluorescence microscopy (LSFM) of cleared tissue

Sample preparation: Platelets and the vasculature were stained by injecting Alexa Fluor 750-labeled anti-GPIX derivative (0.6 µg/g), anti-CD31 Alexa Fluor 647 (0.4 µg/g) and anti-CD105 Alexa Fluor 647 (0.4 µg/g), respectively, 10 min before administering INU1-derivatives. 20 min after injection of INU1-derivatives, mice were transcardially perfused with ice-cold PBS to wash out the blood and subsequently with ice-cold 4% PFA to fix the tissues. Brains were harvested and stored in 4% PFA for 30 minutes. Samples were then washed in PBS, followed by dehydration in a graded methanol series (50%, 70%, 95%, 100% for 30 minutes each) at RT and stored at 4°C o/n. The methanol was replaced stepwise by a clearing solution. After incubation in the clearing solution for at least 2 h at RT, tissue specimens became optically transparent and were used for LSFM imaging on the following day.

LSFM setup and data acquisition: The LSFM setup is tailor-made for organ imaging and custom-built. Major parts have been described before [140]. Laser lines were provided by a custom-made laser box. In brief visible lasers (Obis 488 nm LS 60 mW, Obis 532 nm LS 50 mW, Obis 561 nm LS 50 mW, Obis 640 nm Lx 100 mW, Coherent, Utrecht, The Netherlands) were combined with suitable dichroic beam splitter (593/LP BrightLine, 542/LP BrightLine, 500/LP BrightLine, AHF, Tübingen, Germany) to pass a Acousto-Optic Tunable Filter (AA.AOTF.nC-T 642, AA Opto Electronic, Orsay, France) and to be coupled into a single mode fiber (kineFLEX-P-3-S-730-0.7-FCP-P2, Qioptiq, Groebenzell, Germany). Infrared laser (LuxX CW 730nm 40mW, Omicron Laserage, Rodgau, Germany) was directed to single mode fiber (kineFLEX-P-3-S-730-0.7-FCP-P2, Qioptiq, Groebenzell, Germany). For excitation both infrared and visible beam paths were collimated with 10x objectives (UPlanFL N 10x/0.30 for VIS, PlanN 10x/0,25 for 730 nm, Olympus, Hamburg, Germany) respectively and merged via dichroic beam splitter (DCLP 660, AHF Analysentechnik, Tuebingen, Germany) and adjusted to fit beam size and divergence with a beam expander (BE03M-A, Thorlabs, Newton, NJ, USA) in de-magnifying arrangement. The beam was elongated by a dual-axis galvanometer scanner (6210H, Cambridge Technologies, Bedford, MA, USA) to create a virtual light sheet in combination with a theta lens (VISIR, Leica, Mannheim, Germany), which is projected onto the sample via a tube lens (model 452960, Zeiss, Goettingen, Germany) and the illumination objective (EC Epiplan-Neofluar 2.5/0.06 M27, Zeiss, Goettingen, Germany). Alternating two-sided illumination was realized for larger objects. Fluorescence from the sample was collected perpendicularly to the light sheet by a 5x objective (HC PL Fluotar 5x/0.15, Leica, Mannheim, Germany) and an infinity-corrected tube lens (model Valentine RTC, Leica, Mannheim, Germany) and projected onto a scientific complementary metal oxide semiconductor (sCMOS) camera (Neo 5.5, Andor, Belfast, United Kingdom). The fluorescence was spectrally filtered by suitable emission filters (BrightLine HC 525/50 (Autofluorescence), HQ697/58 (Alexa Fluor 647), BrightLine HC 785/62 (Alexa Fluor 750), AHF Analysentechnik, Tuebingen, Germany) driven by a motorized filter wheel (HA110A with ES10 controller, Prior Scientific GmbH, Jena, Germany) placed between detection objective and tube lens. Samples were mounted on a holder moved by a motorized (8MS00-25-28, Standa, Vilnius, Lithuania) 3-axis stage (M-423-MIC, Newport, Darmstadt, Germany) and placed in custom made chamber filled with clearing solution to match the refractive index. For stack acquisition, the sample was traveled through the light sheet. Hardware components for image acquisition (laser, camera, stage, filter wheel) were controlled by commercial software (IQ 2.9, Andor, Belfast, United Kingdom).

Image Acquisition of a cleared brain samples was performed as a tile scan sequentially with 220 ms exposure time to get a stack of typically 2048x2048x1200 voxels with voxel size of 1.3 µm x 1.3 µm x 5 µm. Images were saved as .tiff files and analyzed as described below.

Deconvolution. Platelet (Alexa Fluor 750) and endothelium (Alexa Fluor 647) channels were deconvolved using the batch option in Huygens Professional 20.04 (SVI, Netherlands). For the endothel channel automatic background subtraction was performed using the lowest value within a one-pixel radius, the signal to noise ratio was determined to 10 and a maximum of 40 iterations were performed. For the platelet channel, automatic background subtraction was done using the “in/near object” option with a radius of 2 µm (2 pixel). The signal to noise ratio was set to 40 and a maximum of 60 iterations were performed. The PSF of our home-build LSFM setup was characterized as follows for the deconvolution: detection

NA = 0.15, refractive index = 1.554, NA of the illumination lens = 0.03, fill factor for the illumination lens = 0.5, illumination from left and a Gaussian beam profile with a width of 18 µm.

The deconvolved data was converted into the Imaris file format and binned 2x in xy-direction to achieve 1024x1024 pixel per slice.

Recognizing autofluorescence by machine learning. The data from the autofluorescence channel collected after 488 nm excitation was binned 2x in xy-direction to end up with 1024x1024 pixel per slice and imported into Ilastik. Ilastik was trained to recognize two classes "background" and "autofluorescence". The respective probabilities for both classes were rescaled from 0 – 1 to 0 – 10'000 and exported as 16-bit unit tiff images. These images were then converted into the Imaris file format.

Segmentation. The preprocessed files from the three fluorescence channels were combined into a single Imaris 9.6 file (Bitplane, Oxford Instruments, UK) and further analyzed using its surface segmentation tool. The autofluorescence was segmented using the "autofluorescence" probabilities with an intensity threshold of 5'000 (thus reflecting 50% probability). Smaller, unconnected areas were removed manually. Next, the endothelium channel was segmented using a sample-dependent intensity threshold between 200-400 and a size filter of 1'000 voxel. For both channel segmentations, the surface grain size was left at 5.2 µm. The total volume from the autofluorescence reflecting the imaged brain volume and the total volume of the endothel system were exported. Finally, the thrombi were segmented using a surface grain size of 10 µm, a sample-dependent intensity threshold between 100-350 and a volume size filter of 1'000 µm^3. Thrombi that were not in contact with the segmented vasculature were excluded from analysis. For each of the remaining and detected thrombi its volume was exported, and a size distribution, mean and standard deviation calculated.

2.2.8.11 Positron-electron tomography (PET) imaging

Experiments were performed by Barbara Schörg and colleagues, Werner Siemens Imaging Center, Department of Preclinical Imaging and Radiopharmacy, University of Tübingen, Tübingen, Germany.

Preparation of radiolabeled anti-GPIX: Anti-GPIX mAb derivative (anti-GPIX) was conjugated with the metal chelator 2,2′-(7-(1-carboxy-4-((4-isothiocyanatobenzyl)amino)-4-oxobutyl)-1,4,7-triazonane-1,4-diyl)diacetic acid (p-NCS-benzyl-NODAGA) and radiolabeled with in-house produced radioactive ^{64}Cu (Department of Preclinical Imaging and Radiopharmacy, University of Tuebingen, Tuebingen, Germany) using a labeling ratio of 2:1

(2 MBq [^{64}Cu]CuCl2 per µg of NODAGA-anti-GPIX). The labeling efficacy of the radiolabeled [^{64}Cu]Cu-NODAGA-anti-GPIX (referred to as ^{64}Cu-αGPIX) was determined by high performance liquid chromatography (HPLC) and thin layer chromatography (TLC).

In vitro cell binding assay: Washed platelets were isolated and prepared from female C57BL/6J mice. 2.5 ng of ^{64}Cu-αGPIX were added to an increasing range of cell concentrations (from 1.6×10^6 to 10×10^7 cells/vial; n = 3) and incubated for 60 min at 37 °C with continuous mixing. Cells were washed three times using PBS/1% FCS, pelleted via centrifugation (1200 rpm, 4°C, 5 min) and the activity within the pellet was measured by gamma counting (Wizard single-detector-counter, Perkin Elmer, Rotgau, Germany). Vials containing 100% of activity (equals 2.5 ng of ^{64}Cu-αGPIX, n = 3) were measured at the same time as the cell samples as reference value. Additionally. 2.5 ng of ^{64}Cu-αGPIX were added to empty vials which were washed 3 times to gain a signal for background correction (n = 3). The percentage of ^{64}Cu-αGPIX binding to the platelets was calculated and plotted as a function of cell concentration. 2.5 ng of a [^{64}Cu]Cu-NODAGA-IgG2a isotype control mAb was used to exclude non-specific background staining. An additional series of platelets was pre-incubated with 25 ng non-labeled anti-GPIX to block the specific binding sites and washed 2x before the radiotracer was added.

Serum stability: To test the stability in mouse serum over time, 22 MBq of ^{64}Cu-αGPIX were incubated for 0 h, 3 h, 5 h and 25 h in mouse serum at 37°C. Afterwards, 2 MBq were tested via TLC and injected on HPLC to determine the stability of the ^{64}Cu-αGPIX.

In vivo biodistribution of ^{64}Cu-αGPIX. *In vivo* biodistribution of ^{64}Cu-αGPIX in mice was analyzed using simultaneous PET/MRI. For this, female C57BL/6J mice were injected i.v. with 5 µg of ^{64}Cu-αGPIX and scanned after conscious radiotracer uptake periods of 3 h and 25 h. PET data was acquired for 60 min and images were reconstructed into a single static frame before fusion with the anatomical MR images. The PET reconstruction algorithms as well as the MR imaging protocols and reconstructions were the same as described below.

Simultaneous PET/MRI: Animal experiments were performed in accordance with the German federal regulations regarding the use and care of experimental animals and under approval by the local research administration. Female 9 weeks old C57BL/6J mice (Charles River, Sulzfeld, Germany) were used for simultaneous PET/MRI measurements. Mice were anesthetized using 1.5% of isoflurane (5% for induction; vaporized in 100% oxygen) followed by i.v. injection of 5 µg ^{64}Cu-αGPIX into the tail vein. Afterwards the mice were put back into their cages for conscious radiotracer uptake. 19 h after the i.v. injection of ^{64}Cu-αGPIX, the mice were anesthetized as described above. A catheter was placed into the tail vein of the mice to enable the administration of INU1-IgG/fab (or NaCl as control) during PET/MRI acquisition. Next, the animals were placed onto a warmed small-animal bed and positioned into the center field of view (FoV) of the MRI scanner (7 T ClinScan, Bruker Bio Spin MRI, Ettlingen, Germany). Short localizer MR protocols were applied to adjust the position of the mice in the FoV of the scanner. To acquire ^{64}Cu-αGPIX-PET simultaneously with MRI, a small animalPET insert was installed permanently inside the MR scanner as described previously [141].

Simultaneous PET/MRI measurements were performed over the course of 60 min. The respiration rate was monitored during the whole acquisition. INU1-IgG/fab or NaCl were administered once the PET scan was started or 15 min afterwards. Standard 3D anatomical MR protocols of the brain and the body were used for anatomical references. For a precise visualization of the vessels, a non-contrast-enhanced two-dimensional time-of-flight MR angiography (2D TOF MRA) was acquired using the following image parameters: slice thickness = 0.41 mm, in-plane spatial resolution = 0.156 x 0.156 mm^2, imaging matrix = 128 x 128, field of view = 20 x 20 mm^2, flip angle = 80°, echo time (TE) 2.695 ms, repetition time (TR) sequence = 18 ms. A maximum intensity projection (MIP) was reconstructed based on the time-of-flight angiography. PET data were stored as list-mode files and reconstructed in 12 x 5-minutes frames employing an in-house written ordered-subsets expectation maximization 2 (OSEM-2D) algorithm including random, decay, time-delay corrections and normalization.

PET/MRI image analysis. Analysis of the ^{64}Cu-αGPIX signal in the brain was performed using Inveon Research Workplace software (Siemens Preclinical Solutions, Knoxville, TN, USA). Fusion of the reconstructed PET images, MR images and 2D-TOF MR angiograms was performed and volumes of interest (VOIs) of the brain were created based on the anatomical MR images. ^{64}Cu-αGPIX accumulation in the VOIs was given in Bq/ml. The reported values represent the mean activity concentration expressed as percent injected dose per ml of tissue (% ID/ml) and were decay-corrected to the imaging timepoint. For a visual comparison of the PET images, the signal intensities have been adjusted to each other based on the injected dose indicated by common color look up tables.

Ex vivo biodistribution: After PET/MR imaging, mice were euthanized, organs and blood collected, flushed and weighed, and the activity was measured by gamma counting (Wizard single-detector-counter, Perkin Elmer, Rotgau, Germany). Values were given in decay-corrected counts and expressed as percent of injected dose per gram tissue (% ID/g). A radioactivity standard was defined as a water-based solution with defined activity (100% of the injected dose).

Statistical analysis. Data are presented as mean ± SEM and box plots as median (95% confidence intervals). For statistical analysis, One-way ANOVA followed by Dunnett's test for multiple comparisons was performed using GraphPad Prism software (V9.0.2). Differences of $p < 0.05$ were considered as significant (*$p < 0.05$ **$p < 0.01$).

2.3 Statistical data analysis

If not stated otherwise, images were analyzed using Fiji, (ImageJ, open source, released under the GPL). Data is indicated as mean ± standard deviation (SD), if not indicated otherwise. For statistical analysis, the applied statistical test is indicated in the figure legend. p-values<0.05 were considered statistically significant (*), $p<0.01$ (**), and $p<0.001$ (***), $p<0.0001$ (****). Statistical tests were performed using GraphPad Prism 6.

3 Results

3.1 Investigation of cerebral thrombosis in the time course of reperfusion injury following experimental stroke

The primary goal of acute ischemic stroke therapy is the restoration of blood flow in the ischemic tissue. However, successful recanalization is not always sufficient to guarantee survival of the penumbra. In the model of intraluminal occlusion of the MCA, complete recanalization can be mimicked by the removal of the filament. Measuring cerebral perfusion of the MCA territory using laser speckle contrast analysis (LASCA) revealed that, despite complete recanalization, reperfusion is only restored to about 40% of the value of a naïve mouse (Figure 3-1). Since the degree of cerebral perfusion after recanalization has been found to correlate with infarct progression [142] increasing the degree of reperfusion would be highly beneficial in stroke therapy. Therefore, identification of the underlying mechanisms leading to decreased perfusion after restoration of blood flow is indispensable.

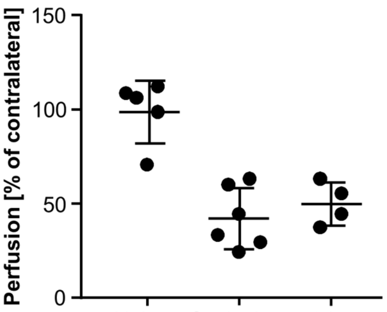

Figure 3-1: Laser speckle contrast analysis (LASCA) of cerebral perfusion after tMCAO. Cerebral perfusion was measured using the blood perfusion imager PeriCam PSI HR (Perimed) that is based on LASCA. Cerebral perfusion of naïve mice was measured as baseline value. Mice were applied to the tMCAO model and cerebral perfusion was measured while the MCA was occluded (=Occlusion) and 8 h after filament removal (=8 h) in two different sets of mice. Values are normalized to cerebral perfusion in the contralateral hemisphere. Data is indicated as mean ± SD and each dot represents one mouse.

It is well known that platelets contribute to I/R injury and thrombotic activity after recanalization is still widely seen as causative for the breakdown of the cerebral microcirculation and tissue death. To investigate the correlation of cerebral thrombosis and infarct progression, mice were subjected to the tMCAO model with a standard occlusion time of 60 min. After different reperfusion times, brains were analyzed assessing occurrence of thrombi and infarct sizes. Using TTC staining, infarcted tissue (white) can be seen after 4 h of reperfusion (Figure 3-2A). While some mice already show large infarcts, others do not, indicating high variability in infarct size at this early time point (Figure 3-2A 2^{nd} and 3^{rd} panel, Figure 3-2B). After 8 h of reperfusion, however, infarct sizes reached their maximum size (122.4 ± 29.65 mm^3) and did not further increase with longer reperfusion time (infarct size after 24 h: 124.0 ± 18.67 mm^3, Figure 3-2B).

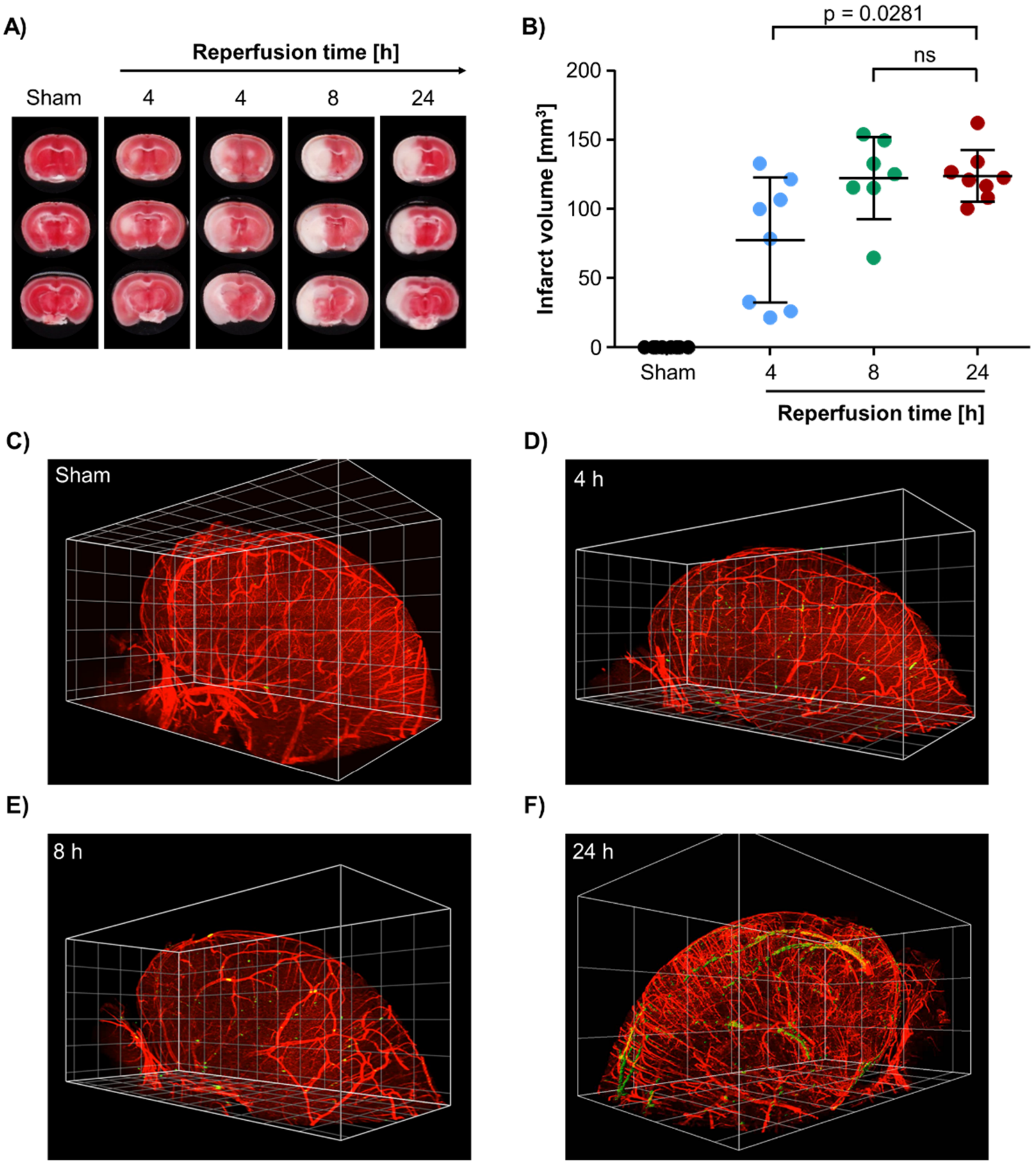

Figure 3-2: Infarct growth precedes cerebral thrombus formation following tMCAO. (A) Representative images of TTC stained brain sections to visualize infarcts. Each time point shows three consecutive brain sections from one mouse. White: Infarct, red: Viable tissue. **(B)** Edema corrected quantification of infarct volumes. Data is shown as mean ± SD and each dot represents one mouse. N=7-8 per timepoint. **(C-F)** 3D reconstruction of LSFM imaging data of the ipsilateral hemispheres of mice after **(C)** sham surgery, **(D)** 4 h of reperfusion, **(E)** 8 h of reperfusion or **(F)** 24 h of reperfusion. Red: Vessels (CD105/CD31), green: Platelets (GPIX). Grid size: 0.5 mm. Statistical differences were analyzed using two-tailed Mann-Whitney U test. P-values < 0.05 were considered statistically significant. Compared to sham, differences to all other groups are highly significant with $p < 0.001$. Light sheet microscopy data was generated by Maximilian Voll [143]. Göb *et al.,* 2021 [144].

This course of infarct progression indicates that the tissue destroying processes must occur within the first 8 h of reperfusion. To analyze the formation of thrombi within the brain vasculature in the time course of reperfusion, we imaged whole brain hemispheres using light sheet microscopy (LSFM) and visualized the appearance of thrombi in 3D reconstructions using an anti-GPIX antibody derivative [145] to label platelets (Figure 3-2C-F). Quantification of the thrombus number revealed the absence of thrombi (25 ± 18) in brains of sham operated mice (Figure 3-2C). In brains analyzed after 4 h or 8 h of reperfusion (Figure 3-2D,E), no significant increase in thrombus number could be detected (98 ± 86 and 61 ± 25, respectively). In contrast, after 24 h of reperfusion (Figure 3-2F), a significant higher number of thrombi was detected (468 ± 463).

Since the presence of residual red blood cells interferes with imaging (red blood cells absorb light and decrease penetration depth during microscopy), an indispensable step during sample preparation for LSFM is the perfusion-fixation of the brain. To exclude that absence of thrombi at early time points after recanalization is due flushing out fragile ones, cryosections of un-perfused brains were analyzed (Figure 3-3). The number of occluded and open vessels was counted in the ipsilateral hemispheres of hematoxylin and eosin stained cryosections of brains that were removed from mice after different reperfusion times following tMCAO. The percentage of occluded vessels after 4 h (21.29 ± 8.95%) or 8 h of reperfusion (24.29 ± 7.86%) was not different from that of sham operated mice (22.14 ± 8.59%). After 24 h of reperfusion, the large infarct size correlated with a significantly elevated percentage of occluded vessels in the ipsilateral hemisphere (36.83 ± 7.46%). A more specific quantification of thrombi in the brain was performed by staining of brain cryosections with a specific anti-platelet antibody (anti-GPIX) (Figure 3-3B images). In line with our previous results, thrombus number in the brain was significantly elevated (261.5 ± 115.4; Figure 3-3B) after 24 h of reperfusion compared to brains of sham operated mice (89.74 ± 84.05) or mice after 4 h or 8 h of reperfusion (30.89 ± 25.67 and 20.29 ± 19.45). This excludes potential preparation artefacts as reason for the absence of thrombi in the LSFM images at 4 h or 8 h of reperfusion.

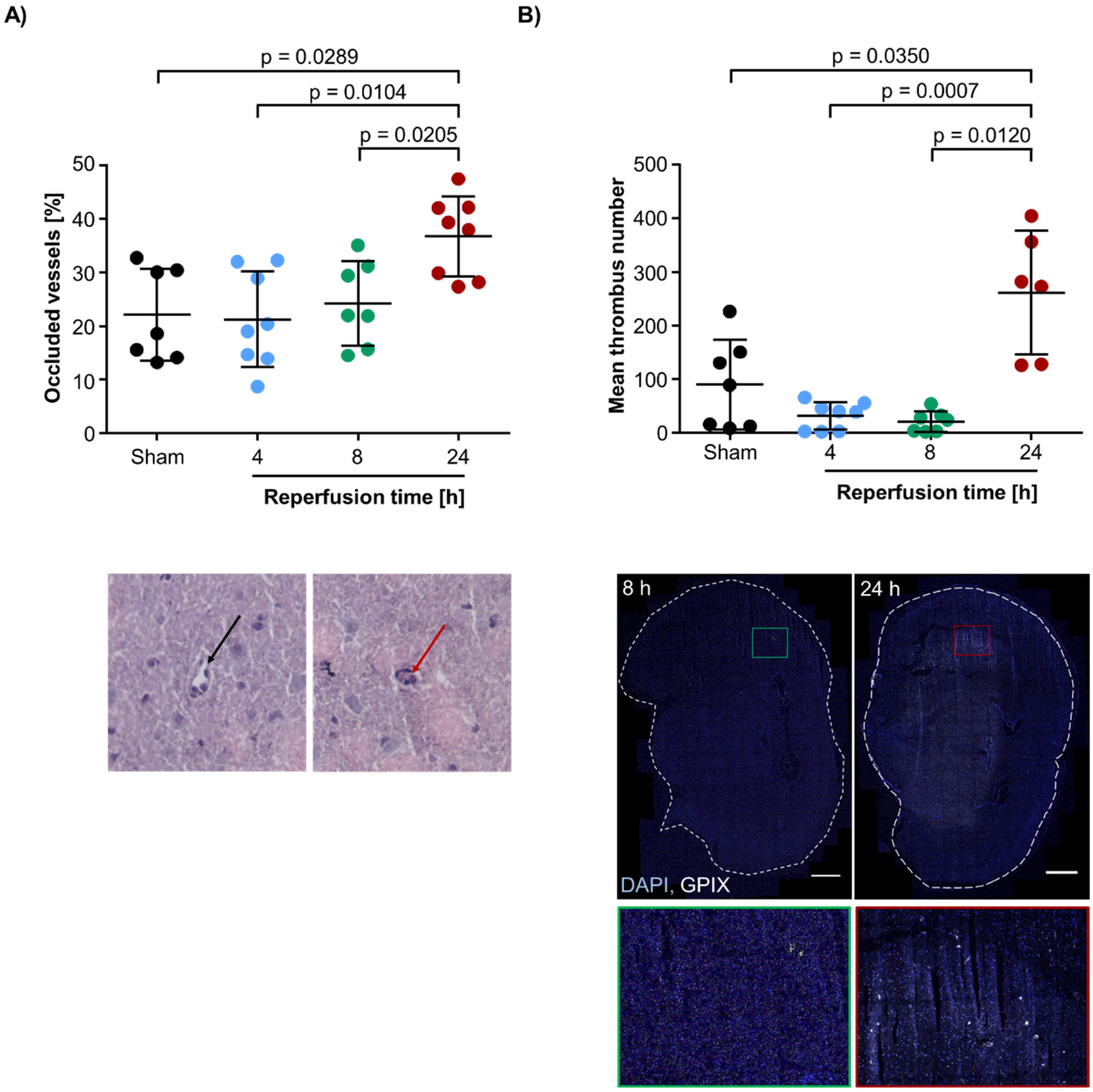

Figure 3-3: Within the first 8 h of reperfusion, no cerebral thrombi are formed. (A) Quantification of occluded vessels in hematoxylin and eosin stained cryosections. Each dot represents the mean of 3-4 sections from one mouse. N=7-8 per time point. Panel below shows exemplary images for an open vessel (black arrow) and an occluded vessel (red arrow) at 20 x magnification. For each section, the whole hemisphere was analyzed. **(B)** Quantification of the thrombus number in brain sections specifically stained for platelets. Each dot represents the mean of 3-4 sections from one mouse. N=6-8. The lower panel shows representative z-projections of brain cryosections stained for platelets (GPIX, white) and nuclei (DAPI, blue). The lower images show the magnification of the respective rectangle in the brain section. Statistical differences were analyzed using two-tailed Mann Whitney U test. P-values < 0.05 were considered statistically significant and are indicated in the figures. In all panels, data is depicted as mean ± SD and each dot represents one mouse. Göb *et al.,* 2021 [144].

For an imaging independent quantification of platelets within the ipsilateral hemisphere, Western Blot analysis of the brain tissue was performed. Quantification of GPIbβ, a platelet-specific protein (that is not released from activated platelets) in the cortical regions of the brains confirmed the results obtained with cryosections and LSFM. The relative GPIbβ content is similar in brains of sham operated mice (0.81 ± 0.11), after 4 h (1.07 ± 0.55) or 8 h (1.15 ± 0.57) of reperfusion. Again, only after 24 h of reperfusion, GPIbβ content was significantly elevated (2.39 ± 1.05; Figure 3-4), indicating an elevated number of thrombi. The contralateral hemisphere was taken as internal control and showed no increase in GPIbβ content at any time point.

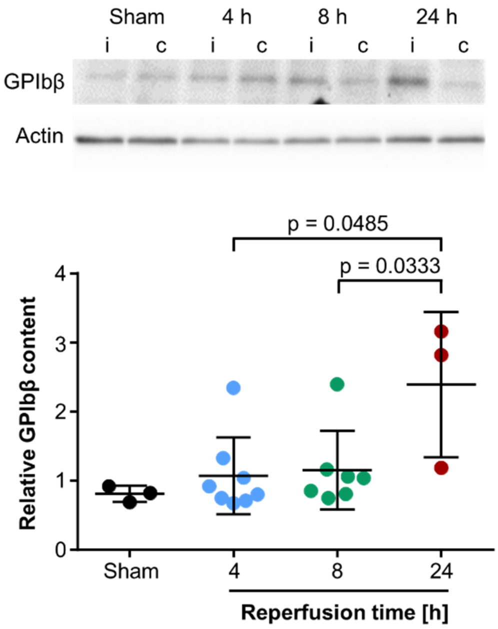

Figure 3-4: Platelet specific GPIbβ is not elevated within the first 8 h of reperfusion. Quantification of platelet GPIbβ protein (22 kDa) in brain lysates of the cortex. GPIbβ was normalized to actin (42 kDa) and is indicated as relative content. N=3-8. I: Ipsilateral; c: Contralateral. Statistical differences were analyzed using two-tailed Mann Whitney U test. P-values < 0.05 were considered statistically significant and are indicated in the figures. Data is depicted as mean ± SD and each dot represents one mouse. Göb *et al.,* 2021 [144].

Given the fact that infarct sizes have already reached their maximum after 8 h of reperfusion, the absence of occluded vessels or thrombi at this time point argues against cerebral microthrombi as reason for infarct progression during reperfusion injury.

3.2 Platelet derived PDGF induces vascular leakage upon cerebral ischemia

As shown in 3.1, platelet thrombus formation is not primarily involved in the pathogenesis of reperfusion injury. However, the contribution of platelets per se to reperfusion injury is undeniable. Besides hemostasis, another key function of platelets is the maintenance of vascular integrity. However, there are pathological states where the presence of platelets has been shown to enhance permeability, as shown in a model of rheumatic arthritis [146]. Loss of vascular integrity and breakdown of the BBB is one of the hallmarks in the pathogenesis of ischemic stroke and can be observed in stroke patients and animal models of ischemic stroke early in disease progression. Aim of this part of the thesis was to investigate a potential involvement of platelets and platelet activation in the induction of vascular leakage during reperfusion injury following ischemic stroke. The following study was conducted within the B06 (Heinze/Schuhmann/Stegner) project of the CRC/TR 240. Experiments were performed in close collaboration with Lena Zimmermann from the Department of Neurology from the University Hospital Würzburg.

First, we investigated platelets and the brain vasculature during reperfusion injury via 2-photon microscopy (2-PM). Access to the cortical brain vasculature was achieved by the application of an open cranial window that replaced a small part of the cranium (Figure 3-5A). To prevent surgery related processes from distorting the results, mice recovered for 14 days before further experiments. After recovery, mice were applied to the tMCAO model with an occlusion time of 60 min. Directly after filament removal, antibodies labeling platelets and endothelial cells as well as fluorophore coupled BSA to visualize the vessel lumen were injected. Observation of the vasculature in the ipsilateral hemisphere, revealed marked extravasation of BSA into the brain parenchyma (Figure 3-5B, upper panel) which was not observed in the vasculature of the contralateral hemisphere (Figure 3-5B, lower panel). Before leakage, repeatedly, short transient contacts of platelets with the endothelium could be observed and immediately after onset of vascular leakage, platelets were recruited to the site of injury.

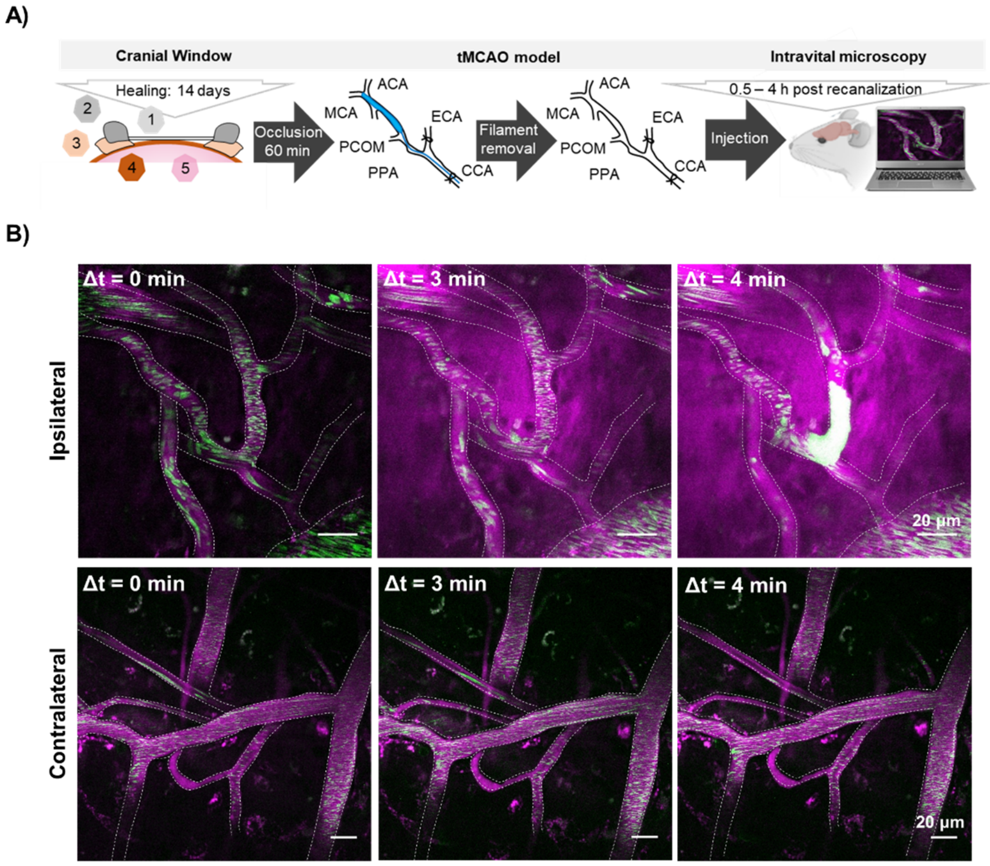

Figure 3-5: Vascular leakage could be observed in the ipsilateral hemisphere during early reperfusion phase following tMCAO. (A) Experimental design of intravital 2-photon microscopy (2-PM). An open cranial window was applied to replace a part of the cranial bone by a cover glass. 1: Cover glass; 2: Dental cement; 3: Cyanoacrylate glue; 4: Dura mater; 5: Brain parenchyma. After 14 days of recovery, mice underwent transient occlusion of the middle cerebral artery for 60 min (tMCAO). After filament removal, labeling antibodies and BSA were injected (anti-CD105-A546, magenta; anti-GPIX, green and BSA-Alexa546, magenta) and the brain vasculature was imaged for 4 h using a Leica TCS SP8 2-PM. **(B)** Representative images from timelapse recordings. Upper panel: Extravasation of BSA-Alexa546 into the brain parenchyma of the ipsilateral hemisphere and subsequent platelet recruitment to the site of injury. Lower panel: Contralateral hemisphere served as control and showed no extravasation of BSA-Alexa546. Δt indicates time between the representative images. Scale bar: 20 µm.

2-PM enables to study processes deeper within the tissue in the natural environment. However, one major drawback is the small field of view that does not allow imaging in a larger context. To visualize the extent of leakage and to overcome the small field of view, mice were subjected to tMCAO surgery and brains were removed after different time points of reperfusion. Coronal brain sections were prepared, stained to visualize endogenous albumin and the whole brain sections were imaged using a confocal microscope (Figure 3-6A). The degree of leakage was analyzed by means of the albumin signal using a five-point scoring system from 0 (no leakage) to 4 (heavy leakage) (Figure 3-6). Already after 4 h of reperfusion, first signs of leakage were observed, indicating early BBB breakdown. After 8 h of reperfusion, several albumin positive areas were visible and after 24 h of reperfusion, almost the whole ipsilateral hemisphere was stained (Figure 3-6A). Brains of sham-operated mice showed no signs of leakage, indicating an intact BBB. To quantify the albumin content in the brain tissue, total protein lysates of the cortex or basal ganglia were prepared and analyzed by Western blot. Protein lysates of corresponding regions of the contralateral hemisphere were analyzed as internal control. An increased albumin content in the ipsilateral hemisphere was noted already after 4 h of reperfusion, continued to rise and remained elevated after 8 h and 24 h of reperfusion (Figure 3-6B). As expected, protein lysates of sham operated mice showed no increased albumin content in the ipsilateral hemisphere. This was in line with the results of the immunohistochemistry and confirmed vascular leakage as an early event during reperfusion.

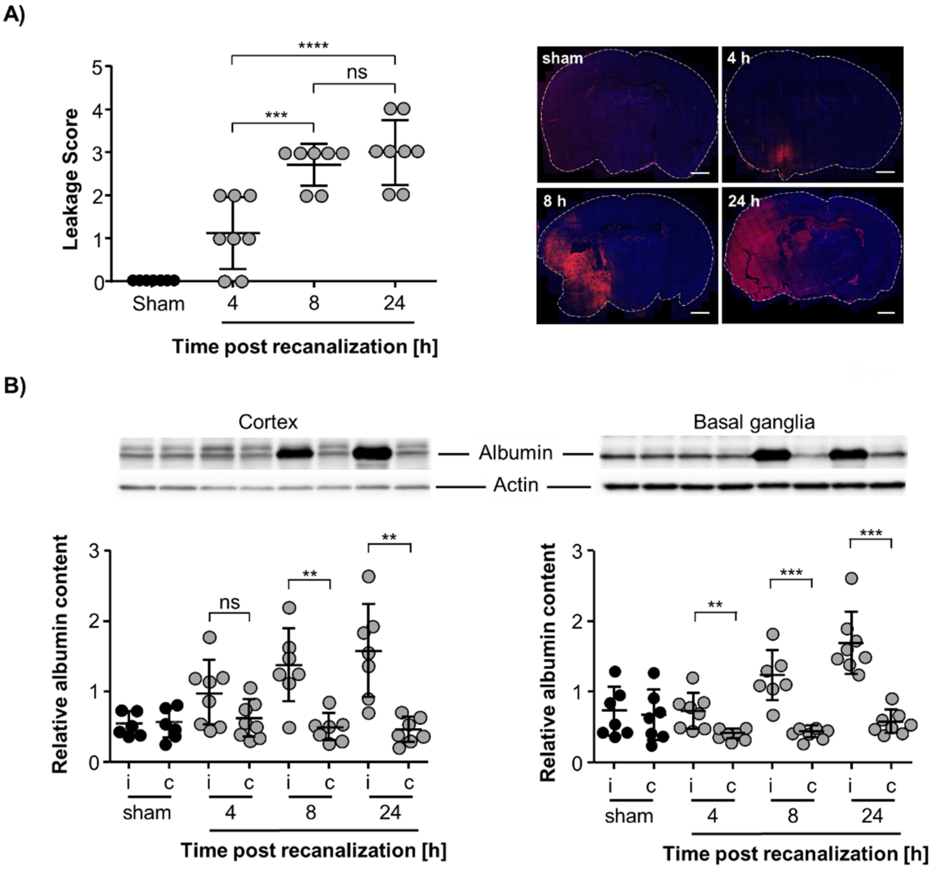

Figure 3-6: Albumin leakage in the brain tissue is an early event during reperfusion injury. Mice were subjected to the tMCAO model and brains were removed after the indicated timepoints following filament removal. **(A)** Coronal cryosections were stained for endogenous albumin (red) and cell nuclei (DAPI, blue). The degree of leakage was analyzed by means of the albumin signal according to the following score: 0: no leakage; 1: small leakage spots; 2: Minor leakages, 3: Major leakages; 4: Heavy leakage (left panel). Data is indicated as mean ± SD and each dot represents the mean for one mouse calculated from at least 3 sections. The right panel shows representative tile scans of whole brain sections for each investigated time point. Scale bar 1 mm. N=7-8. **(B)** Western Blot analysis of albumin content in total protein lysates from the cortical region (left) or the region of the basal ganglia (right). Actin content was used for normalization and results are indicated as relative albumin content. Data is indicated as mean ± SD and each dot represents one mouse. N=7-8. Statistical differences were analyzed using two-tailed Mann Whitney U test. P-values < 0.05 were considered statistically significant with: *, p<0.05; **, p<0.01; ***, p<0.001; ****, p<0.0001. Western blot analysis was performed by Lena Zimmermann.

To investigate a potential contribution of platelet activation to endothelial cell damage, an *in vitro* model of brain endothelial barrier was tested. Therefore, two brain endothelial cell lines b.END3 and b.END5 were used. Both cell lines are derived from the cerebral cortex of BALB/c mice and were immortalized by retroviral infection. Cells of both lines express the endothelial cell markers CD31 (PECAM-1) and CD105 (Endoglin) which could be detected by immunohistochemistry (Figure 3-7A) and flow cytometry (Figure 3-7B,C). Expression of CD146 (MCAM), another marker of endothelial lineage cells, was detectable in b.END3 cells but highly variable for b.END5 cells (Figure 3-7B,C). Both cell lines were positive for the characteristic intracellular markers vWF and P-Selectin (Figure 3-7B,C), confirming the endothelial nature of these cells. Next, expression and localization of tight junction proteins being important for proper formation of cell-cell contacts were investigated. Here, especially ZO-1, Claudin-5 and Occludin are essential since they are primarily present in cells with effective barrier functions [147]. Cultivated endothelial cells were stained with respective antibodies against Claudin-1, -3, and -5, Occludin and ZO-1 (Figure 3-7D). All tested tight junction proteins were expected to be localized at the cell-cell contacts; however, this was only the case for ZO-1. The other proteins were incorrectly localized in the cytoplasm (Claudin-1 and -5) or around and in the nucleus (Claudin-3 and Occludin). Since the existence of tight cell-cell contacts is an essential prerequisite for the investigation of endothelial cell monolayer integrity, b.END3 and b.END5 cell lines were declared unsuitable for the desired investigations.

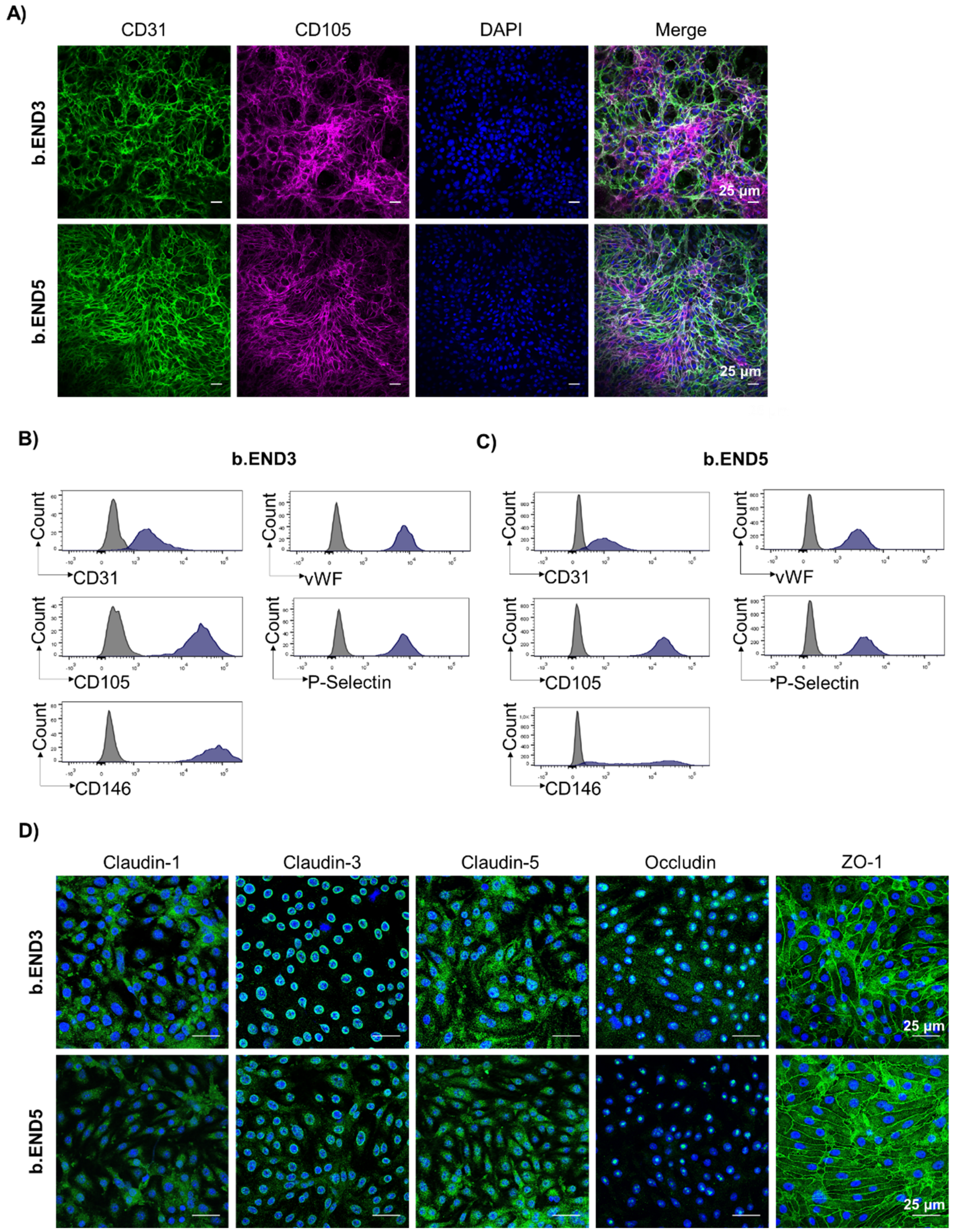

Figure 3-7: b.END3 and b.END5 cells express endothelial cell markers but show incorrect localization of essential tight junction proteins. (A) Cultivated b.END3 and b.END5 cells were fixed and stained with anti-CD31 (PECAM-1; green), anti-CD105 (Endoglin; magenta) antibodies and DAPI (cell nuclei; blue). Both cell lines were positive for the tested endothelial markers. Scale bar 25 µm. Single cell suspensions of b.END3 **(B)** and b.END5 **(C)** endothelial cells were analyzed by flow cytometry. Expression of surface markers CD31, CD105 and CD146 were measured without permeabilization, expression of intracellular markers, vWF and P-Selectin was measured after cell permeabilization on a FACS Canto. Grey histrogram is the signal of the isotype control. **(D)** Cultivated b.END3 and b.END5 cells were fixed and stained for the indicated tight junction proteins. Imaging was performed using a Leica SP8 confocal microscope. Only ZO-1 localized correctly at the cell-cell contacts. Scale Bar 25 µm.

Due to the insufficient formation of tight junctions in the brain endothelial cell lines, primary cells had to be used to establish an *in vitro* model of the endothelial barrier. Primary murine brain microvascular endothelial cells (MBMECs) were isolated from the brains of C57BL/6J mice. Isolated cells were CD31 positive and expressed essential tight junction proteins ZO-1, Occludin and Claudin-5 (Figure 3-8). The tight junction proteins were localized at the cell-cell-contacts, indicating the formation of proper tight junctions between the individual cells in the *in vitro* cell culture.

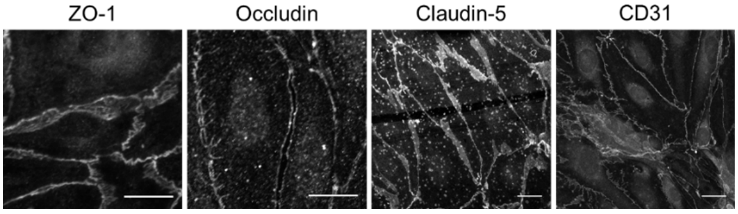

Figure 3-8: Primary murine brain microvascular endothelial cells (MBMECs) express essential tight junction proteins. MBMECs were isolated from C57BL/6J mice and cultivated on nets of cell culture inserts with a pore size of 0.4 µm. Cells were fixed with glyoxal and stained for the indicated proteins: ZO-1, Occludin, Claudin-5 and CD31. Cell preparation and staining were performed by Lena Zimmermann. Imaging was performed with a Leica SP8 confocal microscope. Scale bar 20 µm.

To determine the endothelial cell integrity of the cultured MBMEC monolayer, the trans endothelial electrical resistance (TEER) was measured. The MBMEC monolayer provides a resistance of approx. 30 $\Omega*cm^2$ (Figure 3-9B) which is in the reported range of *in vitro* cultivated murine brain endothelial cells [148, 149]. To investigate the effect of activated platelets on the endothelial cell resistance, platelet releasate was generated. For this, platelets were activated with 10 µg/ml CRP to trigger granule content release. To exclude an effect of the platelets themselves, the releasate was separated from the cell debris. For the experiment, the MBMECs were cultivated for 72 h in transwell inserts, followed by TEER monitoring for 24 h to ensure that the endothelial cells are grown to confluency. Subsequently, platelet releasate was incubated on the MBMECs for 18 h under constant surveillance of TEER values (Figure 3-9A). Strikingly, platelet releasate of WT platelets markedly decreased the endothelial resistance (Figure 3-9B), indicating disruption of the MBMEC monolayer. Platelet releasate of *Unc13d*$^{-/-}$/*Nbeal2*$^{-/-}$ mice that are deficient of α- and dense granule secretion did not affect TEER values (Figure 3-9B). This indicated that platelet granule content, released upon platelet activation, damaged brain endothelial cells *in vitro*. To investigate if α- or dense granule content was responsible for the observed effect, platelet releasate was generated from platelets of the respective single KO mice. Here, only releasate of *Unc13d*$^{-/-}$ platelets caused endothelial cell damage but not releasate of *Nbeal2*$^{-/-}$ platelets (Figure 3-9B). This indicated that α-granule, but not dense granule content harmed

MBMECs and induced loss of endothelial layer integrity. To visualize the effect of the platelet releasate on MBMEC morphology, cells were stained for CD31 and observed via confocal microscopy (Figure 3-9D). Incubation of the MBMECs with releasate of WT and *Unc13d*$^{-/-}$ platelets induced gaps in the fluorescent signal between individual cells, representing holes in the cell layer (Figure 3-9D, white arrows). In contrast, these holes were not visible upon treatment with releasate from Nbeal2-deficient or Unc13d/Nbeal2 double deficient platelets (Figure 3-9D). The surface area of holes (=absence of CD31 staining) was used for quantification. Entropy-images were calculated assessing subtle variations in the local gray level distribution. Due to the lower entropy values, holes were easier to see (Figure 3-9D, lower panel, white arrows). From the entropy image, holes were segmented using a watershed algorithm and the area covered by holes was quantified. Taken together an increased area covered by holes following treatment with releasate of WT or *Unc13d*$^{-/-}$ platelets (Figure 3-9C) correlated with a reduction in trans endothelial resistance. Treatment with releasate of Nbeal2-deficient platelets did not disrupt the cell monolayer integrity and no increase in area covered by holes was observed (Figure 3-9C). This emphasized that platelet activation and subsequent α-granule release led to endothelial layer disruption *in vitro*.

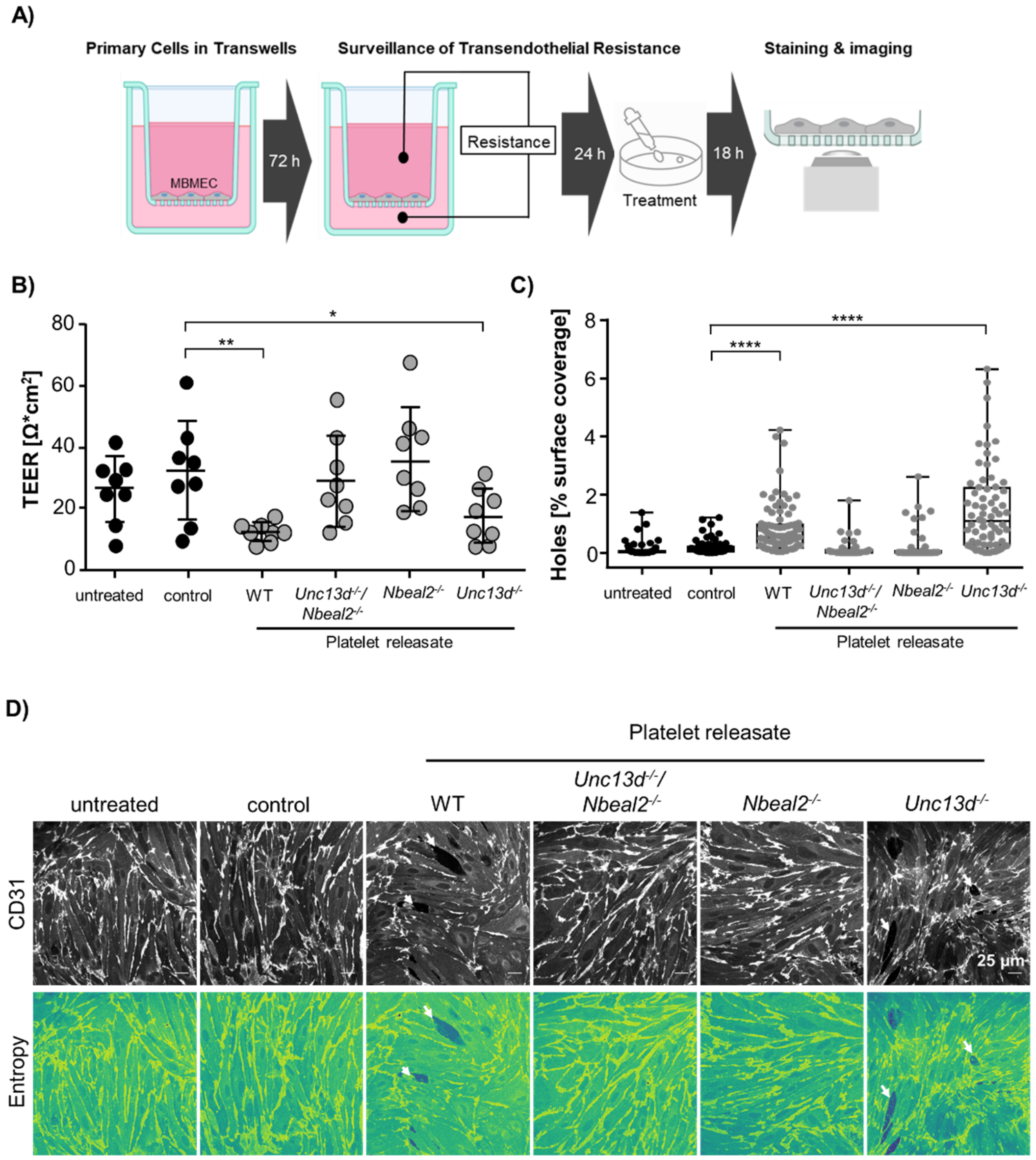

Figure 3-9: Platelet α-granule content disrupts the endothelial monolayer. (A) Experimental design of cell culture experiments. MBMECs were grown in cell culture inserts until they reached full confluency (approx. 4 days). During the last 24 h, trans endothelial resistance (TEER) was constantly monitored. When cells reached confluency, platelet releasate was applied for 18 h under constant surveillance of TEER values. Created with BioRender.com. **(B)** TEER values after 18 h of treatment with platelet releasate of mice with the indicated genotypes. Control: buffer that is used for platelet stimulation (10 µg/ml CRP in Tyrode's + Ca^{2+}). Values are indicated as mean ± SD with each point representing one measurement. Data is pooled from four experiments. **(C)** MBMECs were grown in Ibidi 18-Well chamber slides and treated with platelet releasate of the indicated mice for 18 h. Holes were segmented using scikit image for Python via watershed segmentation based on entropy images. Values are indicated as mean ± SD with each point representing one analyzed image. **(D)** Representative confocal images of **(C)** of MBMEC monolayers stained with anti-CD31 (upper panel). Lower panel shows generated entropy images. Scale bar: 25 µm. Control means treatment with Tyrode's + Ca^{2+} containing 10 µg/ml CRP as it was used for platelet stimulation to generate platelet releasate. Statistical differences were analyzed using two-tailed Mann Whitney U test. P-values < 0.05 were considered statistically significant with: *, p<0.05; **, p<0.01; ***, p<0.001; ****, p<0.0001. TEER measurements and cell culture experiments were performed by Lena Zimmermann.

To investigate whether α-granule release also influences the endothelial barrier *in vivo*, Nbeal2-deficient animals were subjected to the tMCAO model. Strikingly, the results obtained in the *in vitro* experiments could be transferred to the *in vivo* situation as no extravasation of BSA-Alexa546 could be observed from the brain vasculature in Nbeal2-deficient mice following tMCAO in the early reperfusion phase (Figure 3-10A). Furthermore, these animals display smaller infarcts than respective WT controls (Figure 3-10B and [93]). This suggests a correlation between vascular leakage mediated by platelet α-granule content and infarct development following tMCAO.

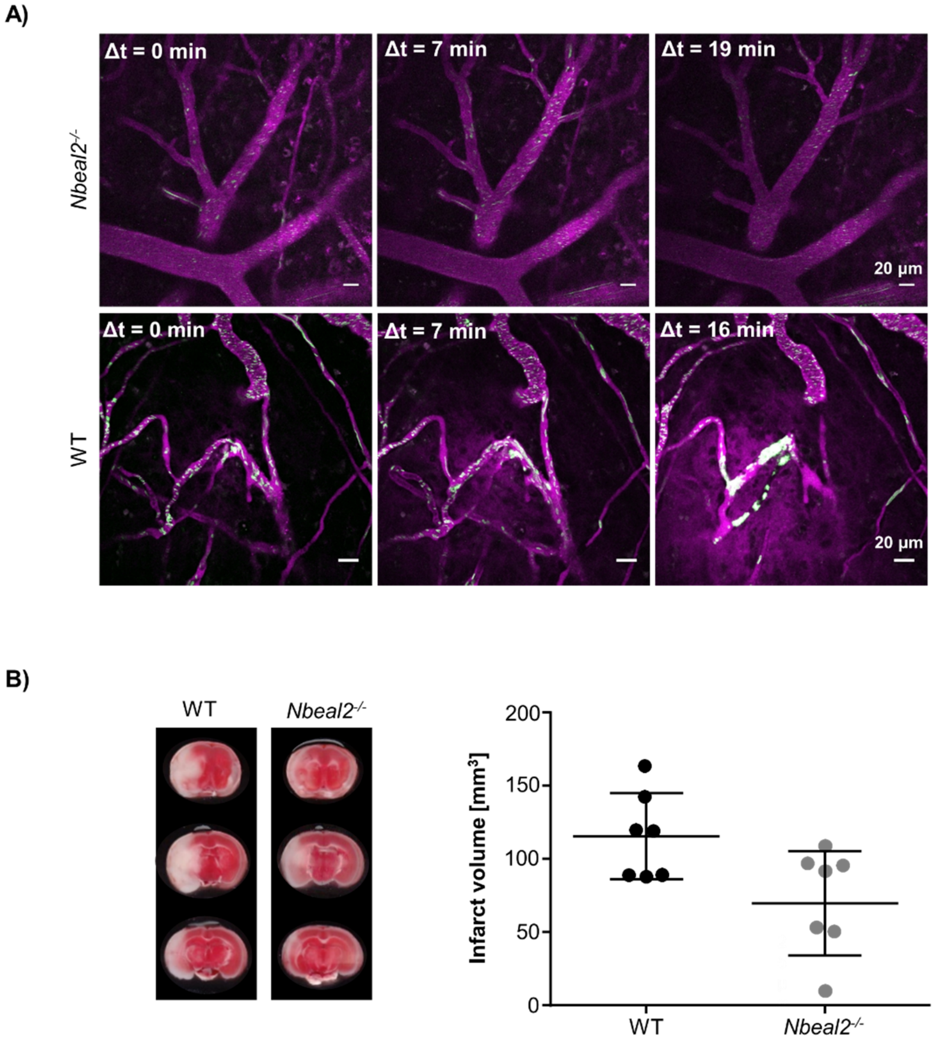

Figure 3-10: Nbeal2-deficient mice are protected from vascular leakage following tMCAO. (A) Representative snapshots from intravital imaging of the brain vasculature of *Nbeal2*$^{-/-}$ mice following tMCAO. Images were acquired using a Leica TCS SP8 2-photon microscope. Vessels and vessel lumen: Magenta (anti-CD31-Alexa546 and BSA-Alexa546); Platelets: Green (anti-GPIX). BSA-Alexa546 extravasation could be observed in WT (lower panel) but not *Nbeal2*$^{-/-}$ mice within the first 4 h of reperfusion. Time is indicated as Δt between the different images. Scale bar: 20 µm. **(B)** Representative brain sections of WT and *Nbeal2*$^{-/-}$ mice one day after tMCAO stained with TTC. White: Infarct; Red: Viable tissue. Right panel: Infarct volumes calculated from the TTC-stained brain sections. Data is indicated as mean ± SD and each dot represents one mouse.

To pinpoint the effects to a specific/distinct α-granule component causing the disruption in endothelial barrier function, further *in vitro* experiments were conducted. Denaturation of proteins in WT platelet releasate significantly reduced endothelial barrier damage (Figure 3-11B) excluding non-protein components.

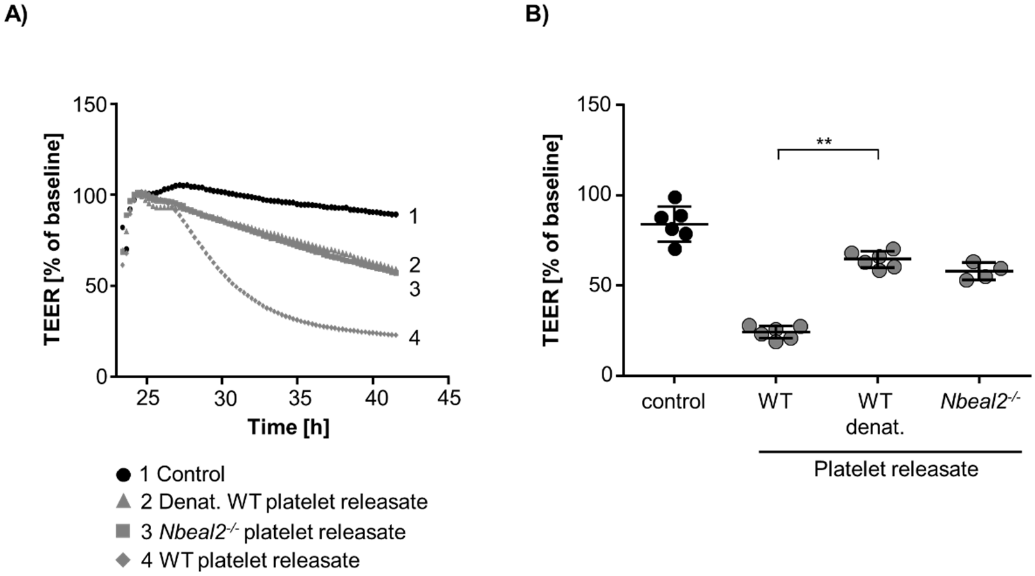

Figure 3-11: Denaturation of proteins in WT platelet releasate prevented disruption of MBMEC monolayer. (A) Representative TEER curves starting with MBMEC treatment with platelet releasates from the indicated genotypes and treatments. **(B)** TEER values after 18 h of incubation depicted as % of baseline. Protein denaturation (boiled WT platelet releasate = WT denat.) protected from the decrease in TEER to the same extent as absence of α-granules. Data is depicted as mean ± SD. Control: treated with Tyrode's + Ca^{2+} containing 10 µg/ml CRP as it was used for platelet stimulation to generate platelet releasate. Statistical differences were analyzed using two-tailed Mann Whitney U test. P-values < 0.05 were considered statistically significant with: *, $p<0.05$; **, $p<0.01$; ***, $p<0.001$; ****, $p<0.0001$. TEER measurements were performed by Lena Zimmermann.

Knowing that it is a protein, promising candidates stored in α-granules, such as the chemokines CXCL5 or PF4 and the growth factors PDGF-AB, PDGF-BB and VEGF [21] were selected based on reports in the current literature and incubated on MBMECs while recording TEER. However, none of the tested chemokines caused a decrease in TEER values (Figure 3-12A). Among the tested growth factors, a decrease in TEER was only observed after incubation of MBMECs with recombinant PDGF-AB (Figure 3-12B). This indicated that PDGF released from platelet α-granules contributed to endothelial barrier disruption. The higher amount of PDGF in WT platelet releasate compared to Nbeal2-deficent platelet releasate was confirmed by ELISA (4-fold increase compared to platelet releasate from Nbeal2-deficient platelets) (Figure 3-12C).

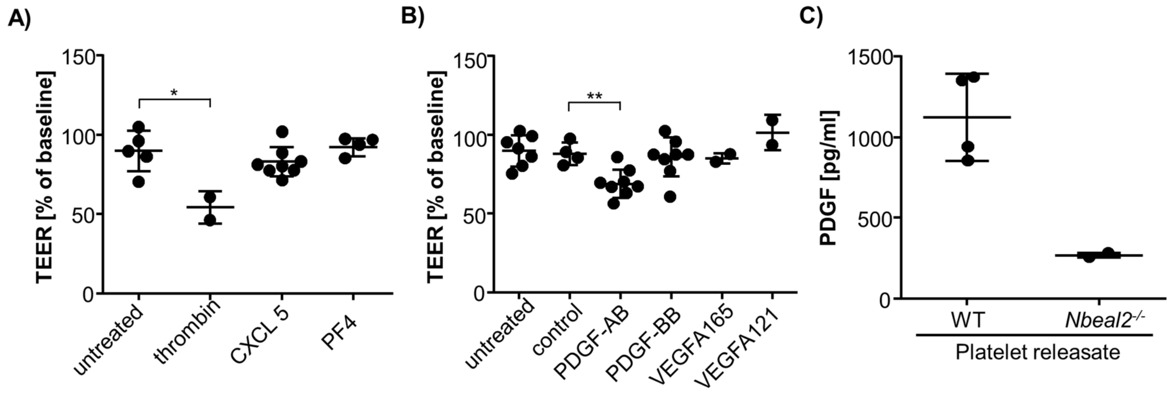

Figure 3-12: Recombinant PDGF caused disruption of the MBMEC monolayer. (A) Recombinant chemokines CXCL5 (1 µg/ml) and PF4 (40 µg/ml) were incubated on MBMECs for 18 h under constant recording of TEER. Data is indicated as mean ± SD at the 18 h timepoint. Thrombin (0.4 U/ml) was used as a positive control and led to reduced TEER values. **(B)** Recombinant growth factors PDGF-AB (10 µg/ml), PDGF-BB (10 µg/ml), $VEGFA_{165}$ (10 µg/ml) and $VEGFA_{121}$ (0.1 µg/ml) were incubated on MBMECs for 18 h under constant recording of TEER. Data is indicated as mean ± SD at the 18 h timepoint. Only PDGF-AB significantly reduced TEER. **(C)** PDGF content in platelet releasate of WT and Nbeal2-deficient mice was measured using ELISA. PDGF levels were 4-fold increased in releasates of WT platelets compared to those of Nbeal2-deficient mice. Statistical differences were analyzed using two-tailed Mann Whitney U test. P-values < 0.05 were considered statistically significant with: *, p<0.05; **, p<0.01; ***, p<0.001; ****, p<0.0001. TEER measurements and ELISA were performed by Lena Zimmermann.

These results point to a role of platelet α-degranulation in the breakdown of the BBB following ischemic stroke. Locally released platelet-derived PDGF-AB might harm endothelial cells and contribute to the early loss in endothelial barrier integrity during reperfusion.

3.3 Role of Neutrophils and NET formation in ischemic stroke

Upon brain ischemia, neutrophils are among the first hematogenous cells that are attracted to the ischemic tissue [100]. Oxygen and nutrient deprivation results in an inflammatory condition which causes neutrophils to produce ROS and NETs [100]. The role of neutrophils in ischemic stroke is discussed controversially and might be double-sided depending on the context. Therefore, the contribution of ROS production and NET formation to the pathomechanism of I/R injury of the brain was investigated using the tMCAO model. First, the effects of antibody-mediated neutrophil depletion on infarct development after tMCAO was assessed. Therefore, neutrophils were depleted in WT mice by intraperitoneal injection of anti-Ly6G antibody and mice were investigated three days after antibody injection to ensure full depletion. Absence of neutrophils from the peripheral blood at day 3 was confirmed by flow cytometry (Figure 3-13B). Furthermore, almost complete absence of neutrophils from the bone marrow was shown in cryosections of the femur (Figure 3-13C). Despite the absence of neutrophils, depleted mice showed comparable infarct sizes as control-treated mice (Figure 3-13A).

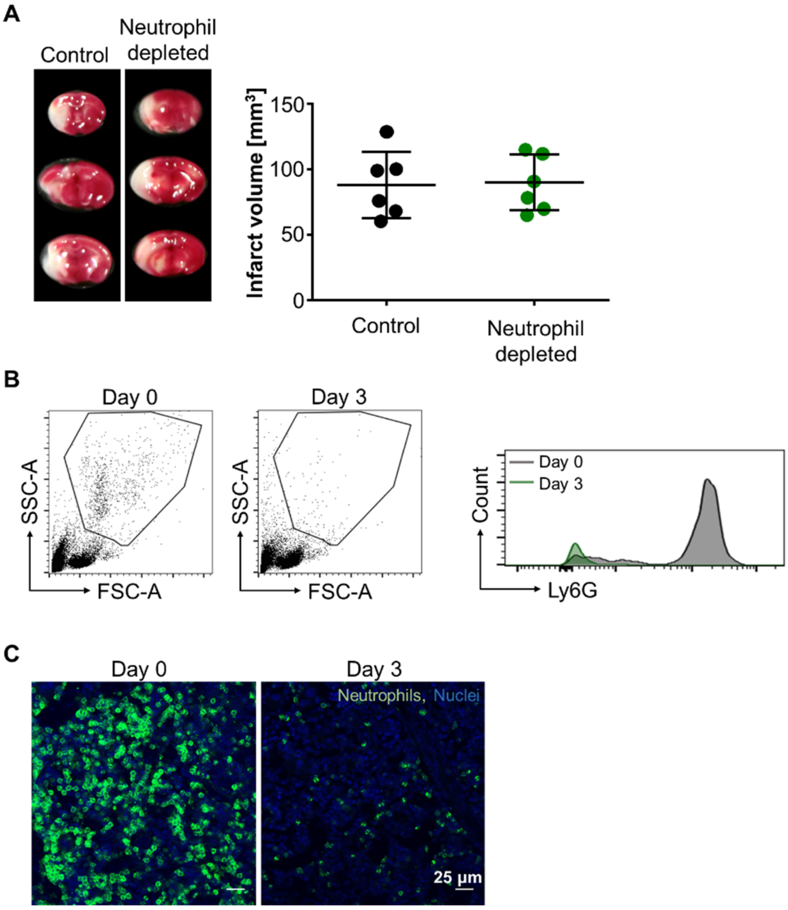

Figure 3-13: Depletion of neutrophils did not affect infarct development after tCMAO. (A) Neutrophil depletion was achieved by i.p. injection of 500 µg anti-Ly6G (RB6-8C5) 3 days prior to tMCAO. Left panel: Representative images of TTC stained brain sections of one control treated and one neutrophil-depleted mouse to visualize infarcts. Each panel shows three consecutive brain sections from one mouse. White: Infarct, red: Viable tissue. Right panel: Neutrophil-depletion did not affect infarct volume 24 h after tMCAO**.** Data is indicated as mean ± SD, each dot represents one mouse. N=6. **(B)** Flow cytometric analysis of peripheral blood before (day 0, left panel) and 3 days after neutrophil depletion (day 3, right panel). 3 days after anti-Ly6G injection, neutrophils (identified via FSC, SSC characteristics) were depleted from the peripheral blood (black gate). Right panel shows histogram of Ly6G signal at day 0 and day 3. Representative graphs of n=4. **(C)** Bone marrow sections of mice before (day 0) and 3 days after anti-Ly6G injection (day 3). Neutrophil (Ly6G, green) number was markedly reduced at day 3 after depletion. Nuclei (DAPI) are stained in blue. Scale bar 25 µm. Representative sections of n=4.

During ischemic stroke and I/R injury of the brain a variety of processes runs in a defined temporal and spatial context. Depending on the context, neutrophils might be detrimental in one phase but on the other side be beneficial in another phase. Thus, complete neutrophil depletion might cancel out potential opposing roles. Therefore, we observed single neutrophil derived processes, namely NET formation, and ROS production in more detail. To investigate the effects of NETs in the context of brain I/R injury, PAD4-deficient mice were used in the tMCAO model. In these mice, histone citrullination is not possible leading to abolished NET formation. Absence of Pad4 protein in white blood cell lysate of knockout mice was confirmed by Western Blot (Figure 3-14A). Deficiency in NET formation was confirmed in a model of lipopolysaccharide (LPS) induced lung injury. LPS inhalation induced NET formation in lungs of WT mice, as shown by staining of citrullinated histone 3 (H3Cit). In contrast, no NETs were detected in lungs of *Pad4*$^{-/-}$ mice (Figure 3-14B). In the tMCAO model, incapability of NET formation protected *Pad4*$^{-/-}$ mice since they showed reduced infarct volumes (Figure 3-14C). However, this decrease in infarct volumes did not translate in significant better neurological outcome as assessed by Grip Test and Bederson Score (Figure 3-14D). To visualize NET formation following stroke, brains were removed and cryosections were stained for H3Cit. 24 h after tMCAO, H3Cit-positive cells could be detected in the cortex (Figure 3-14E; region 1) as well as in the basal ganglia (Figure 3-14E; region 2) of the ipsilateral hemisphere of WT mice. No H3Cit staining was observed in respective regions of the contralateral hemisphere (Figure 3-14E, region 3 and 4), excluding a general unspecific neutrophil activation in the whole brain. In brain sections of *Pad4*$^{-/-}$ mice, neither in the ipsilateral nor in the contralateral hemisphere, H3Cit could be detected confirming the absence of NETs in brains of these mice (Figure 3-14E). These data indicate a contribution of NET formation to infarct progression following I/R injury of the brain.

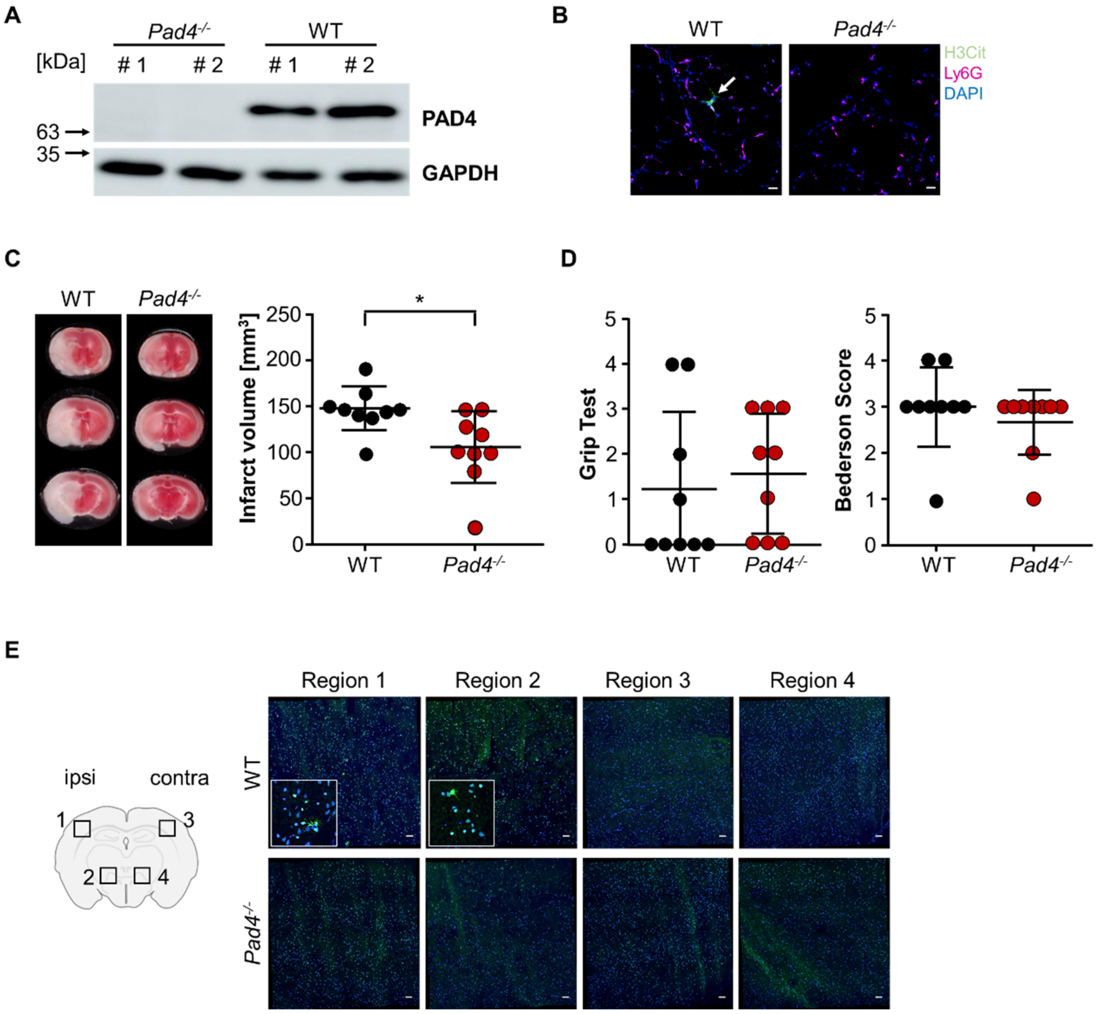

Figure 3-14: NET formation contributed to brain damage following tMCAO. (A) Western Blot of total protein lysate of peripheral white blood cells. Pad4 protein was detected in cells of WT but not *Pad4*$^{-/-}$ mice. GAPDH was used as loading control. **(B)** Lung sections of WT and *Pad4*$^{-/-}$ mice 4 h after LPS instillation. NETs (H3Cit, green) could be detected in WT but not Pad4-deficient mice. Neutrophil (Ly6G, magenta) infiltration was comparable. Nuclei were stained with DAPI (blue). Scale bar 10 µm. Experiment was performed by Philipp Burkard and Charlotte Schonhart. **(C)** Left: Representative TTC-stained consecutive brain sections of one WT and *Pad4*$^{-/-}$ mouse after tMCAO. White: infarct; Red: viable tissue. Right: Quantification of the infarct volume revealed reduction of infarct volumes for *Pad4*$^{-/-}$ compared to WT mice, n=9. Statistical differences were analyzed using two-tailed Mann Whitney U test. **(D)** Motoneuronal deficits were measured using Grip Test (left) and Bederson Score (right). No differences were observed between WT and *Pad4*$^{-/-}$ mice. Data is indicated as mean ± SD, each dot represents one mouse, n=9. **(E)** Brains were removed 24 h after tMCAO and stained for NETs (H3Cit, green) and nuclei (DAPI, blue). Cartoon shows investigated regions. 1: region in the ipsilateral cortex; 2: region of the ipsilateral basal ganglia; 3: region in the contralateral cortex; 4: region of the contralateral basal ganglia. In the ipsilateral hemisphere, H3Cit positive cells were detected in the cortex as well as in the basal ganglia (small inlets). No H3Cit positive cells were detected in the contralateral hemisphere or in any of the regions in *Pad4*$^{-/-}$ mice. Data is indicated as mean ± SD, each dot represents one mouse. Scale bar 50 µm.

Since the brain is highly vulnerable to reactive oxygen species, we investigated whether neutrophil derived ROS contribute to tissue damage following tMCAO. Therefore, *Ncf1*$^{-/-}$ mice, which are devoid of NADPH oxidase dependent ROS production, were investigated in the tMCAO model. Surprisingly, no reduction in infarct volumes or improved neurological outcome were observed in *Ncf1*$^{-/-}$ mice (Figure 3-15). This suggests that NADPH oxidase dependent ROS production is of minor importance for infarct development following tMCAO.

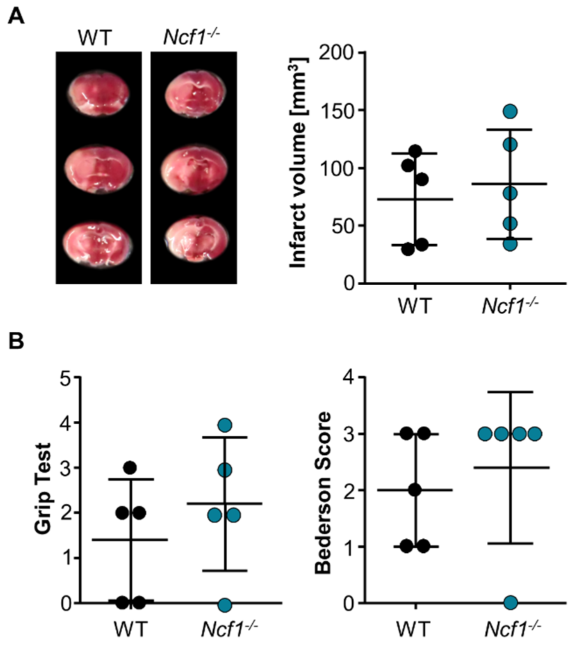

Figure 3-15: NADPH oxidase dependent ROS production did not contribute to infarct growth following tMCAO. (A) Left: Three consecutive TTC-stained brain sections of one representative WT and *Ncf1*$^{-/-}$ mouse. White: infarct; Red: Viable tissue. Right: Quantification of the infarct volume revealed no difference between WT and *Ncf1*$^{-/-}$ mice, n=5. **(B)** Ncf1-deficiency did not improve motoneuronal behavior after tMCAO as assessed with Bederson Score and Grip test. Data is indicated as mean ± SD, each dot represents one mouse, n=5.

3.4 Establishment of a genetic mouse model to visualize platelet calcium signaling *in vivo*

Platelets are activated via various receptors triggering different signaling pathways which finally all lead to an increase in the intracellular Ca^{2+} concentration [24]. In platelets, elevated levels of intracellular Ca^{2+} are essential for various steps of activation and aggregation, such as cytoskeleton rearrangement, shape change, degranulation or integrin αIIbβ3 activation [24]. This makes intracellular Ca^{2+} measurements a perfect indicator of platelet activation in different experimental settings. So far, measuring Ca^{2+} levels in cells is mainly performed using fluorescent Ca^{2+} indicators like Fura-2. However, this approach is limited to *in vitro* studies. Visualization and investigation of platelet responses under (patho-)physiological conditions in the respective cellular and molecular environment required the development of other techniques. So far the greatest advancement in performing calcium recording in living mammalian tissue came from the development of genetically encoded calcium indicators (GECIs) [150]. To study Ca^{2+} responses in platelets *in vivo*, a mouse line with an endogenous calcium sensor in platelets was generated. Mice that express the fluorescent calcium indicator protein GCaMP5G variant in a Cre recombinase inducible system

(Polr2a$^{\text{Tn(pb-CAG-GCaMP5g,-tdTomato)Tvrd}}$, JAX Stock No. 024477) were crossed with mice expressing the Cre recombinase under the control of the megakaryocyte- and platelet-specific platelet factor (PF) 4 promoter. The genetic construct is designed in a way that the red fluorescent protein tdTomato is expressed along with the GCaMP5G sensor. The tdTomato serves as control for successful recombination and the identification of the targeted cells within the tissue since basal fluorescence of the GCaMP5G sensor is low and not visible in its off-state [151]. In the resulting PF4-Cre positive mice (*PC-G5-tdT.PF4Cre*$^{+/-}$), hereinafter referred to as Kin, presence of the Cre recombinase led to the excision of the STOP cassette in the genetic construct (Figure 3-16A) and therefore to the expression of the calcium indicator GCaMP5G and tdTomato in platelets and megakaryocytes. GCaMP consists of green fluorescent protein (GFP), calmodulin (CaM) and a peptide sequence from the myosin light-chain kinase. Calcium binding induces conformational changes and leads to emission of GFP fluorescence [152]. Cryosections of femurs removed from Kin and the respective PF4 Cre recombinase negative littermates (*PC-G5-tdT.PF4Cre*$^{-/-}$ =WT) confirmed the presence of tdTomato in megakaryocytes of Kin mice (Figure 3-16B), indirectly showing the presence of the GCaMP5G sensor.

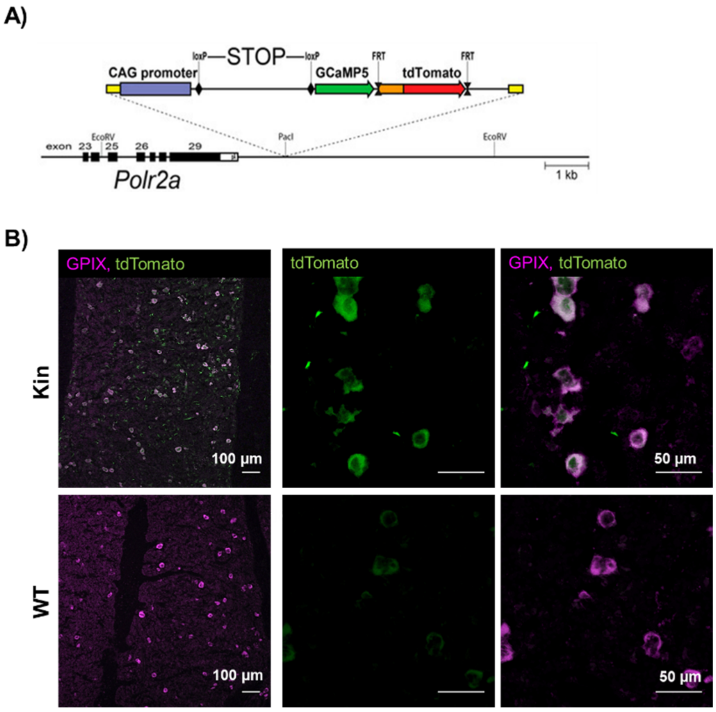

Figure 3-16: Generation of a new genetic mouse line expressing the calcium indicator GCaMP5G in platelets and megakaryocytes. (A) Schematic diagram of the *PC::G5-tdT* reporter allele in the *Polr2a* locus. The reporter cassette was inserted 3' of the last exon, without disturbing gene function. Following Cre/loxP-mediated excision of the transcriptional STOP sequence, the CAG promotor drives *GCaMP5G* and *IRES-tdTomato* expression in the Cre-expressing cells. Taken from Tvrdik and Kalani, 2017 [151]. **(B)** Crossing the reporter mice with mice expressing Cre recombinase under the platelet and megakaryocyte specific platelet factor (PF) 4 promoter led to expression of *tdTomato* (green) in megakaryocytes in the bone marrow. Z-projections of femur sections from Kin and WT mice stained with anti-GPXI (magenta).

Before using the generated mouse line for *in vivo* experiments, an impact of the present calcium sensor on platelet function and activation had to be excluded. Therefore, basic platelet parameters and platelet function were investigated. Platelet number, size and the expression of major glycoproteins on the platelet surface were comparable between WT and Kin platelets (Table 3-1).

Table 3-1: Unaltered expression of major receptors on the platelet surface of Kin platelets. Expression of platelet surface receptors was assessed by flow cytometry using a BD FACSCelesta with specific FITC-coupled antibodies. Values are indicated as mean MFI ± SD. Statistical differences were analyzed using two-tailed Mann Whitney U test. MFI: Mean fluorescent intensity. N=5, representative data from 3 independent experiments.

	WT [MFI]	**Kin [MFI]**	**p-value**
GPV	5469 ± 142	5490 ± 237	0.8668
GPVI	1172 ± 186	1495 ± 390	0.1480
α2	1105 ± 65	1083 ± 27	0.5104
CD9	23690 ± 2579	24734 ± 546	0.4223
GPIb	7610 ± 374	7504 ± 145	0.5781
GPIX	9882 ± 122	10015 ± 274	0.3623
CLEC-2	3570 ± 190	3748 ± 274	0.2706
CD84	739 ± 247	1014 ± 255	0.1210
αIIbβ3	12369 ± 638	11561 ± 277	0.0446
α5	936 ± 112	1012 ± 16	0.2027
β3	4891 ± 295	4842 ± 203	0.7707

Platelet αIIbβ3 integrin activation and degranulation-dependent P-Selectin surface exposure in response to different agonists were tested using flow cytometry. Platelets with the calcium sensor responded to all tested agonists in the same way as respective WT controls (Figure 3-17A). In line with this, platelet aggregation in response to different agonists was comparable for Kin and WT platelets (Figure 3-17B). Of note, for all experiments, both, GPCR (thrombin, U46619, ADP)- or ITAM (collagen, CRP)-dependent agonists were investigated. These data indicated that the presence of the GCaMP5G calcium sensor has no influence on platelet inside-out signaling. Importantly, Ca^{2+} binding of the sensor did not interfere with Ca^{2+} mobilization in platelets. Kin platelets showed the same time course of Ca^{2+} mobilization in response to thrombin (Figure 3-17C, left panel) and ADP (no representative curve shown). Likewise, maximal increase in intracellular Ca^{2+} in response to thrombin and ADP in Kin platelets was comparable to that of WT platelets (Figure 3-17C, right panels).

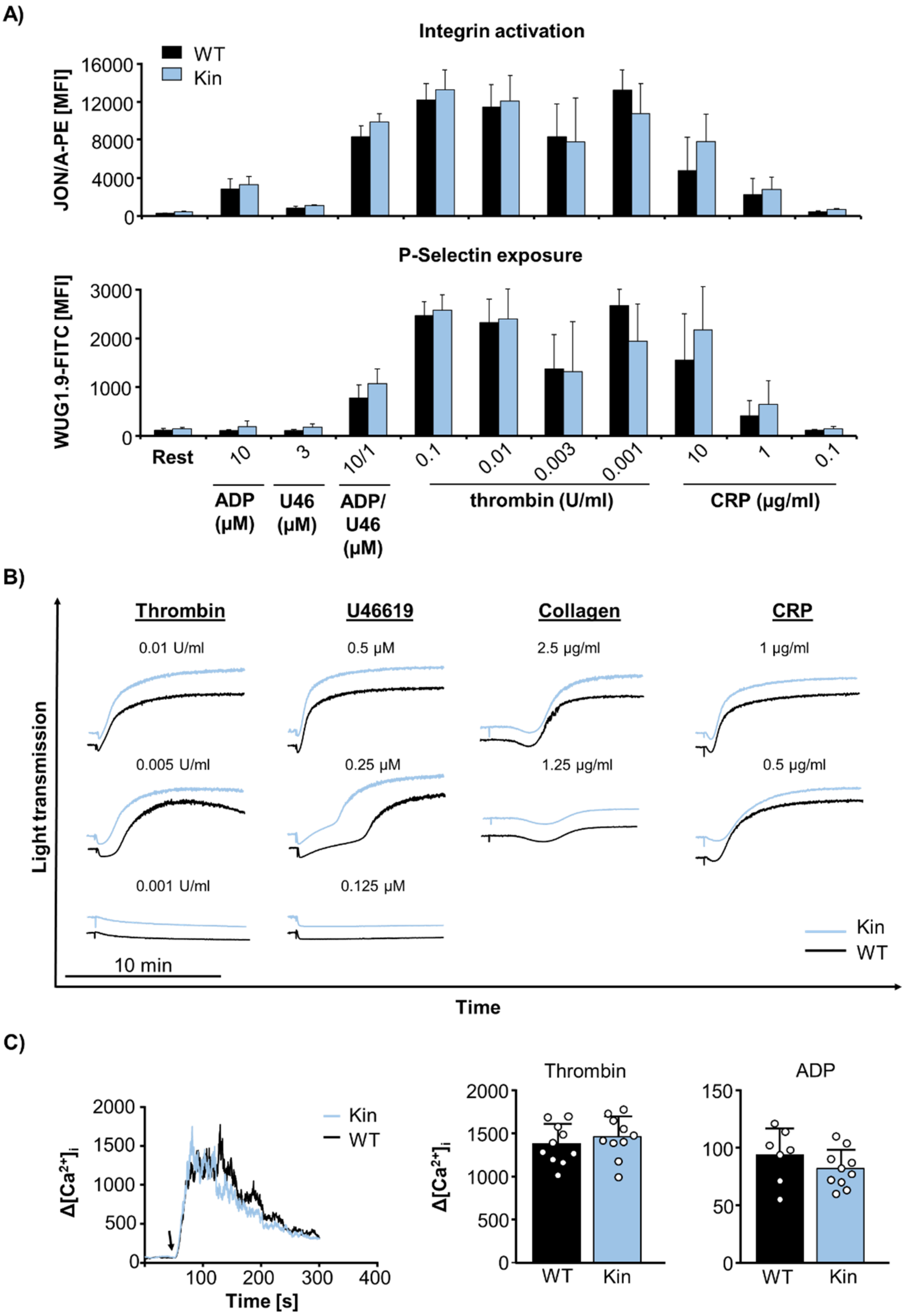

Figure 3-17: Presence of the GCaMPG5 calcium sensor did not affect platelet activation, aggregation, and calcium flux. (A) Flow cytometric analysis of integrin αIIbβ3 integrin activation (upper panel) and α-degranulation dependent P-Selectin exposure (lower panel). **(B)** Washed platelets were activated with different concentrations of the indicated agonists and light transmission was measured on a 4-channel aggregometer. U46, U46619, stable thromboxane A_2 analogue; CRP, Collagen-related peptide. Representative results of 3 independent experiments with n=5. **(C)** Left panel: Time course of intracellular Ca^{2+} mobilization in response to thrombin (addition marked by black arrow). Right panel: Maximal increase in intracellular Ca^{2+} concentration in response to the indicated agonists (thrombin 0.01 U/ml; ADP 5 µM). Each dot represents one measurement. Calcium measurements were performed by Dr. Timo Vögtle in 4 independent experiments and n=4.

To test whether the presence of the calcium sensor affects integrin outside-in signaling, Kin and WT platelets were allowed to spread on a fibrinogen-coated surface and the degree and kinetics of platelet spreading were analyzed at different time points. Platelets from Kin mice were able to form filo-and lamellipodia to the same extent and with the same kinetics as WT platelets and were able to reach a fully spread state after 30 min (Figure 3-18).

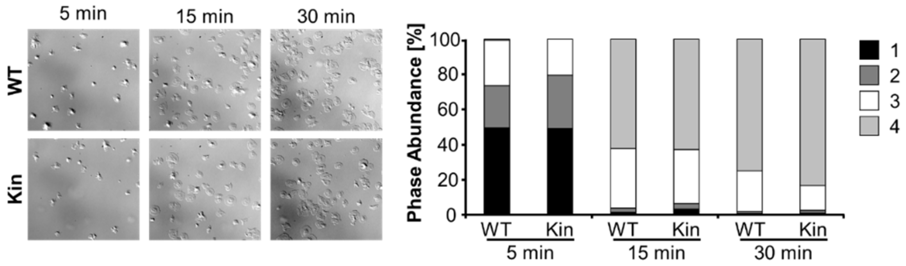

Figure 3-18: GCaMPG5 does not affect platelet spreading on fibrinogen. Washed platelets were stimulated with 0.01 U/ml thrombin and allowed to spread on fibrinogen (100 µg/ml). Different stages of platelet spreading were quantified at the indicated timepoints (right panel) and showed no alterations for Kin platelets. 1: resting; 2: formation of filopodia; 3: formation of filopodia and lamellipodia; 4: fully spread. Left panel shows representative images at the different time points analyzed. N=6.

To test platelet function in a more physiological setting, the ability of Kin platelets to form aggregates under flow conditions was tested using an *ex vivo* flow adhesion assay. Therefore, whole blood of Kin and WT mice was perfused over a collagen coated surface at a shear rate of 1000 s^{-1}, reflecting the condition in small arteries and arterioles. Platelets of both genotypes rapidly adhered and were able to form aggregates and three-dimensional thrombi within 4 min. Quantification of the surface covered by thrombi and the thrombus volume revealed no differences between WT and Kin (Figure 3-19). As the platelet function of Kin mice was not affected by the presence of the calcium sensor, this mouse line might indeed be a suitable tool for visualization of calcium responses in a variety of different *in vitro, ex vivo* and *in vivo* assays.

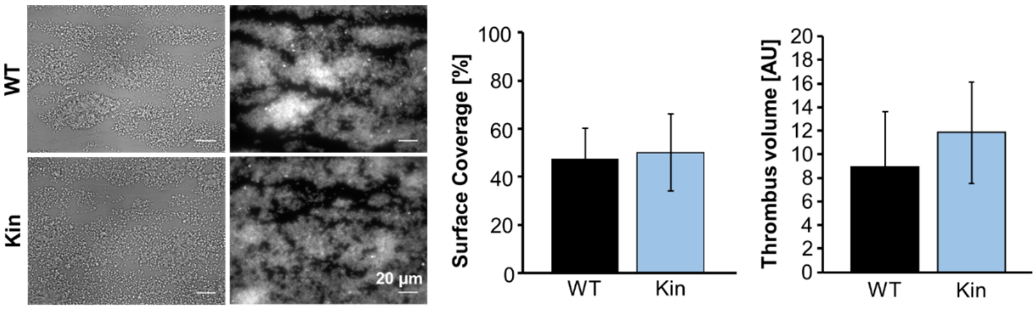

Figure 3-19: Unaltered platelet adhesion and aggregate formation of Kin platelets under flow. Platelets were stained with anti-GPIX-Alexa 647 (0.3 µg/ml) and whole blood of WT and Kin mice was perfused over collagen-coated glass cover slides at a shear rate of 1000 s^{-1}. Left panel shows representative brightfield (left) and fluorescent (right) images. Quantification of surface coverage and thrombus volume (right panel) shows no differences between WT and Kin mice. 2 experiments, n=5.

To test the suitability of the Kin mouse line to visualize calcium flux in platelets, further experiments were conducted. As already shown in Figure 3-19, perfusion of whole blood from Kin mice over a collagen coated surface led to thrombus formation, which could, in Kin mice, be seen in brightfield images and with the help of the endogenous tdTomato reporter (Figure 3-20A). Upon thrombus formation on collagen, platelets get highly activated which led to Ca^{2+} mobilization and binding to the GCaMPG5 sensor resulting in the emission of a bright GFP signal (Figure 3-20A). This confirmed the presence and functionality of the calcium sensor in the Kin mice. To see whether this genetic system also allows the visualization of Ca^{2+} flux in single platelets, blood was perfused over a vWF coated surface at high shear (1700 s^{-1}). This led to immobilization of a monolayer of platelets. These platelets were clearly not fully activated, as could be seen by their roundish, spherical morphology in the brightfield images (Figure 3-20B, upper row) and the very faint GFP signal (Figure 3-20B, lower row). Activation of the platelets by perfusion of 0.1 U/ml thrombin led to a shape change and the formation of filopodia as well as emission of a bright GFP signal (Figure 3-20B, white arrows). Altogether, these results established the newly generated Kin mouse as promising tool to visualize Ca^{2+} mobilization also in single platelets.

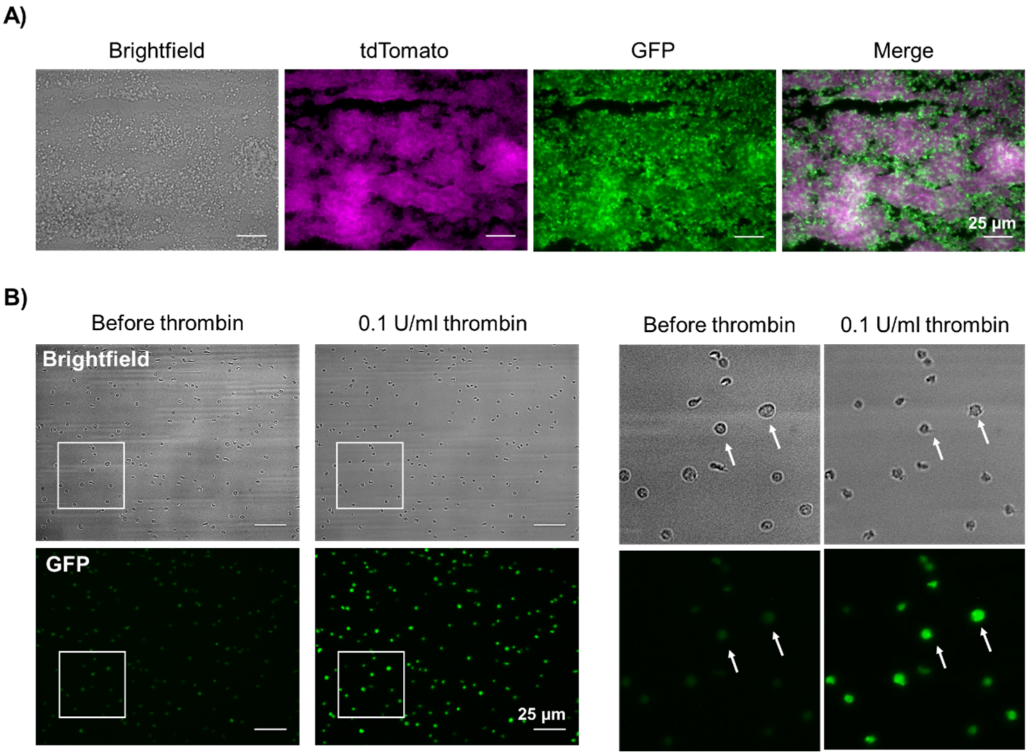

Figure 3-20: Platelet activation led to bright GFP fluorescence in platelets of Kin mice in *ex vivo* flow adhesion experiments. (A) Whole blood of Kin mice was perfused over collagen-coated glass cover slides at a shear rate of 1000 s^{-1}. Activated platelets in the formed thrombi are GFP positive indicating Ca^{2+} mobilization and binding of Ca^{2+} to the GCaMP5G sensor. **(B)** Single platelets were immobilized on vWF and afterwards activated by perfusion of 0.1 U/ml thrombin. Activated platelets emitted GFP fluorescence. Right panel shows magnification of the white squares in the overview images of the left panel. Arrows mark two individual platelets to follow platelet activation after addition of thrombin.

To follow platelet calcium signaling in more detail, platelets were allowed to spread on fibrinogen and the spreading process was constantly monitored by confocal microscopy (Figure 3-21). During spreading, GFP signals of individual platelets were changing (Figure 3-21 upper panel, blue and white arrow). When following the spreading process in detail, it could be seen that when platelets reached the focal plane of the fibrinogen, they were GFP positive indicating Ca^{2+} flux and activation (Figure 3-21 lower panel, left). Following the same platelet for a longer time, it changed from a small, roundish shape to a spread, larger appearance. In between the morphological changes, GFP fluorescence changes indicating several waves of Ca^{2+} mobilization that orchestrate the different processes necessary to achieve a fully spread state in the end (Figure 3-21 lower panel, left to right). After platelets reached a fully spread state, the GFP signal vanished.

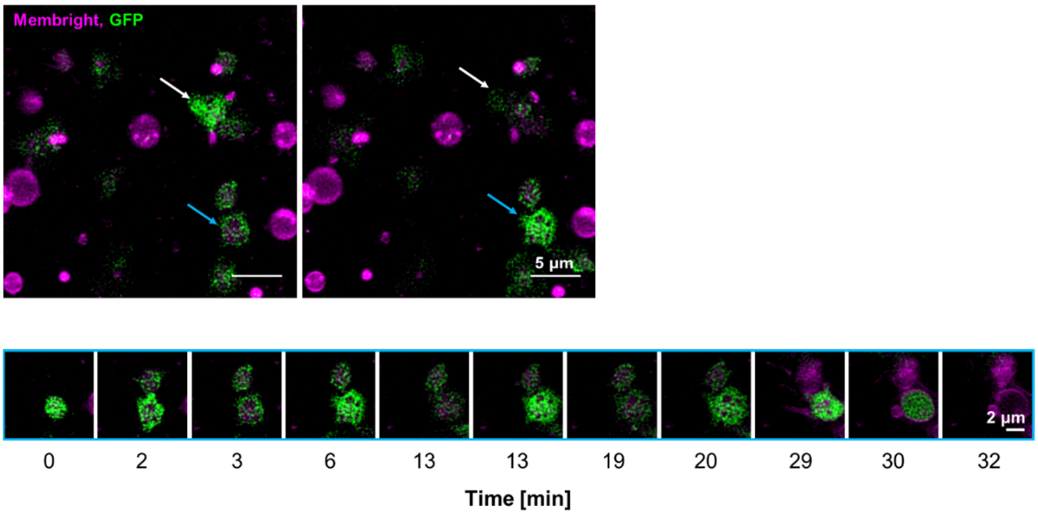

Figure 3-21: GCaMP5G allowed visualization of Ca^{2+} mobilization during platelet spreading on fibrinogen. Washed platelets of Kin mice were stained with Membright 640, activated with 0.1 U/ml thrombin and allowed to spread in fibrinogen coated Ibidi 8-Well Chamber slides. Images were taken every 8 sec. Upper panel: Overview, white and blue arrow mark one platelet at different time points showing on and off states of the GCaMP5G sensor. Lower panel: A single platelet (marked with the blue arrow in the upper panel) followed over the whole spreading process showing different waves of Ca^{2+} mobilization until the platelet reached the fully spread state.

The major advantage of genetically introduced calcium sensors is the potential use of the transgenic animals in *in vivo* models. The platelet specific calcium sensor mouse was generated with the purpose to investigate Ca^{2+} mobilization during *in vivo* platelet activation. To test whether the Kin mouse line represents a suitable model, it was tested in an arterial thrombus formation model. Here, topical application of $FeCl_3$ on the mesenteric arterioles was used to induce formation of occlusive thrombi. Thrombus formation and Ca^{2+} mobilization was followed by *in vivo* confocal microscopy. Endothelial wall injury by $FeCl_3$ induced the formation of first platelet aggregates after approx. 1 min (Figure 3-22, upper panel). Platelets in the core region of the thrombi emitted GFP fluorescence, indicating activation and Ca^{2+} mobilization. After 7 min (Figure 3-22, lower panel), an occlusive thrombus was formed. GFP signal throughout the whole thrombus indicated strong platelet activation. Comparing the site of initial thrombus formation after 1 and 7 min (Figure 3-22, white arrow) showed that during thrombus formation GFP signals change. The platelets that are located at the top where the thrombus grew were GFP positive and “older” parts of the thrombus were getting GFP negative over time. This demonstrated that the newly generated calcium reporter mouse line enables the visualization of differentiated calcium mobilization within a growing thrombus *in vivo*.

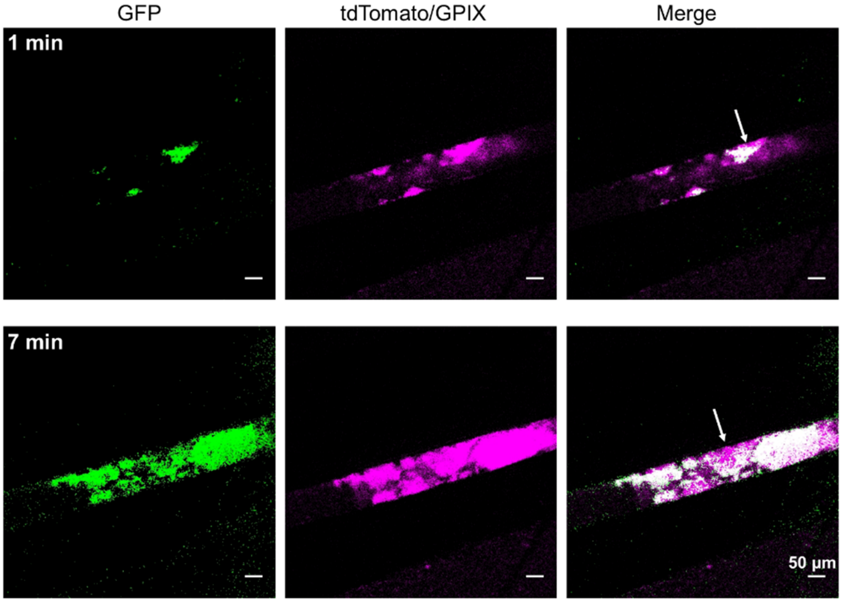

Figure 3-22: $FeCl_3$ induced thrombus formation in the mesenteric arterioles induced Ca^{2+} mobilization in platelets. Endothelial wall injury by topical application of $FeCl_3$ induces platelet activation and occlusive thrombus formation in mesenteric arterioles. 1 min (upper panel) after $FeCl_3$ application, first platelet aggregates were visible. After 7 min (lower panel) an occlusive thrombus was formed. Magenta: Platelets (anti-GPIX-A546 and tdTomato), Green: Calcium-bound GCaMP5G (GFP). Experiment was performed by Dr. Sarah Beck.

Using the newly generated Kin mouse line, Ca^{2+} mobilization in platelets could be visualized in *in vitro, ex vivo* and *in vivo* models of platelet function. Thus, this mouse line was successfully established as suitable and powerful tool for platelet research.

3.5 A novel mechanism eliciting foudroyant venous (sinus) thrombosis via CLEC-2 and GPIIb/IIIa dependent platelet activation

Thrombosis of the cerebral veins and/or the dural sinus (CV(S)T) is a rare type of stroke usually occurring in young and middle-aged adults [10, 153]. The most common symptom of CVT is severe headache (60-90%) but often patients suffer from seizures (30-40%) and present focal neurologic deficits [10]. The role of platelets in arterial thrombosis is intensively studied, for venous thrombosis however, the contribution of platelets is less investigated. CLEC-2 is an ITAM-bearing receptor that is expressed as a dimer in the platelet membrane and is already known to be involved in injury-related thrombus formation and thrombo-inflammatory diseases [154]. Several years ago, the anti-CLEC-2 antibody INU1 was generated and initially characterized by our department [128]. Surprisingly, injecting fab fragments of the INU1 antibody into mice resulted in heavy symptoms characterized by tonic/myoclonic seizures, platelet consumption and death. These observations have been already made in previous studies but the cause of the induced symptoms has not yet been clearly identified [155, 156]. However, the observed symptoms in INU1-fab injected mice resembled those seen in CVT patients. This is why in the following part of the thesis, INU1 mediated effects were investigated in detail, especially in regard to potential thrombus formation in the cerebral veins.

Incubation of mouse platelets with divalent anti-CLEC-2 antibody derivatives INU1-IgG and INU1-F(ab)$_2$ induced platelet aggregation (Figure 3-23A), downstream tyrosine phosphorylation (Figure 3-23B) and αIIbβ3 integrin activation and degranulation of α-granules (assessed by P-Selectin exposure on the platelet surface) (Figure 3-23D). Interestingly this was not the case when the monovalent INU1-fab was used. The resting state of INU1-fab treated platelets was also confirmed by scanning electron microscopy (Figure 3-23C). Although INU1-fab did not trigger platelet activation and aggregation *in vitro*, it efficiently blocked the rhodocytin and podoplanin binding site and prevented rhodocytin or podoplanin induced platelet aggregation (Figure 3-23E). This confirmed binding of the INU1-fab to platelets and excluded that insufficient binding of INU1-fab is responsible for the absent platelet activation.

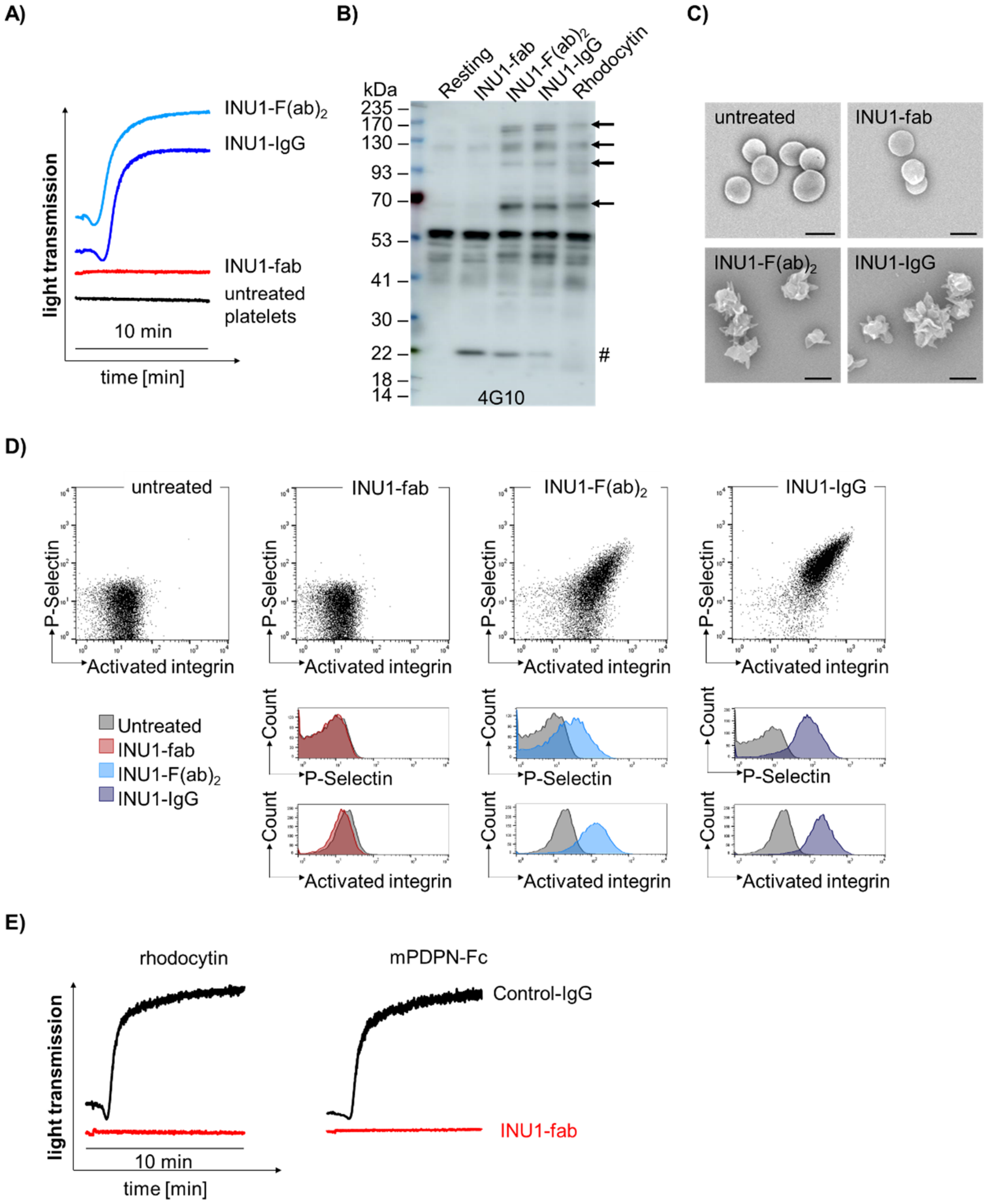

Figure 3-23: INU1-IgG and -F(ab)$_2$ but not INU1-fab induces platelet activation and aggregation *in vitro*. All antibody derivatives were added at 10 µg/ml f.c.. **(A)** Addition of INU1-IgG and INU1-F(ab)$_2$ but not INU1-fab trigger platelet aggregation *in vitro*. Light transmission was measured on a Fibrintimer 4-channel aggregometer. Representative curves of n=10. **(B)** Tyrosine phosphorylation was assessed by Western Blot (4G10) of platelet lysates after stimulation with the indicated antibody derivatives or rhodocytin. Newly phosphorylated proteins are indicated by arrows, the # indicates the band originating from the detection of the INU1-fab by the secondary antibody. Addition of the monovalent INU1-fab does not induce phosphorylation of the tested tyrosine residues. **(C)** Scanning electron microscopy pictures of *in vitro* stimulated washed platelets. Only INU1-IgG or INU1-F(ab)$_2$ but not INU1-fab induce platelet activation, which could be seen by profound morphological changes. Representative images of n=4. Scale bar 2 µm. **(D)** Flow cytometric analysis of αIIbβ3 activation and P-Selectin exposure in response to INU1 antibody derivatives. Only the divalent INU1-IgG and INU1-F(ab)$_2$ but not the monovalent INU1-fab induce integrin activation and P-Selectin exposure. Representative images of n=4. **(E)** Addition of INU1-fab (10 µg/ml, 5 min, 37°C) inhibits rhodocytin (2.4 µg/ml f.c.) or podoplanin (10 µg/ml of murine podoplanin-Fc, mPDPN-Fc) mediated platelet aggregation. Light transmission of washed platelets was measured on a Fibrintimer 4-channel aggregometer. Stegner, Göb *et al.,* in press (*Nat Cardiovasc Res*).

The results from the *in vitro* experiments do not explain the heavy symptoms of INU-fab injection. To characterize the effects of CLEC-2 targeting by INU1 *in vivo*, mice were intravenously (i.v.) injected with either INU1-IgG, INU1-F(ab)$_2$ or INU1-fab and monitored. In the first minutes after administration of INU1-IgG or INU1-F(ab)$_2$, animals were less active and showed signs of heavy breathing. However, they rapidly recovered and showed no further impairments during the remaining observation time (up to 10 days). Peripheral platelet counts (pPC) in these mice decreased within 5 min after injection to < 5% and remained below 30% for the following 24 h (Figure 3-24C) indicating immediate platelet activation and consumption. Surprisingly, INU1-fab treated mice showed no symptoms directly after injection but developed heavy neurological symptoms starting approximately 10 min after injection. INU1-fab treated mice developed an unstable gait with impaired motor control of the hind limbs and bending of the head and backside. This proceeded in focal and generalized tonic-clonic jerks often throwing the mice to one side indicating generalized seizure activity. This happened in all INU1-fab treated mice but in none of the other groups (Figure 3-24A). The initial seizures were followed by a phase in which the mice were moving around slowly or were lying exhausted and flat on the cage bottom. In this stage, mice were either unresponsive to touch or the contact induced myoclonic jerks. Often, mice underwent several rounds of seizures and exhaustion, finally resulting in death within the first 45 min in approx. 77% of the INU1-fab treated mice (Figure 3-24B). The surviving mice were in very poor conditions and had to be euthanized latest after 5 h due to animal welfare reasons. In contrast, none of the INU1-IgG or INU1-F(ab)$_2$ treated animals died (Figure 3-24B). Furthermore, a decrease in pPC was observed in the INU1-fab treated mice. At symptom onset, pPCs were reduced to 71% and further decreased to approx. 39% within 20 min. This indicates a slow, but progressive platelet consumption (Figure 3-24C).

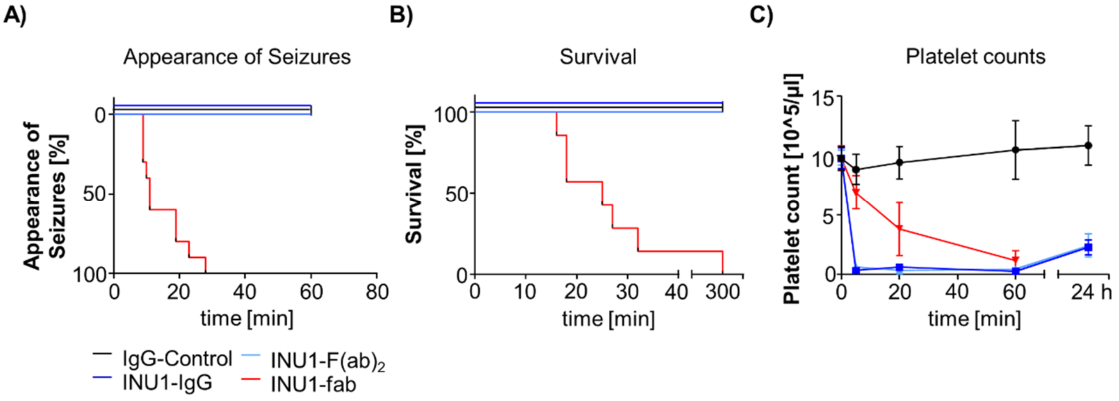

Figure 3-24: Administration of INU1-fab *in vivo* induced severe neurological symptoms and death. (A)-(C) Intravenous injection of INU1-F(ab)$_2$ (0.5 µg/g) or INU1-IgG (0.75 µg/g) led to immediate platelet consumption, whereas for INU1-fab (0.5 µg/g) platelet consumption occurred slower **(C)**. INU1-fab but not INU1-IgG or INU1-F(ab)$_2$ treatment induced neurological symptoms **(A)** and was associated with lethality **(B)**. Data is indicated as mean ± SD. N=5-10 per group. Stegner, Göb *et al.,* in press (*Nat Cardiovasc Res*).

The nature of the neurobehavioral phenotype in conjunction with the observed platelet consumption pointed towards brain thrombosis as potential mechanism of the observed symptoms. To investigate this, mice were injected i.v. with either INU1-fab, INU1-IgG or PBS (vehicle, control), the organs were removed 20 min later and prepared for histopathological analysis. In hematoxylin and eosin (H&E) stained sections of INU1-fab treated mice, numerous occluded vessels, primarily the large vessels between the two hemispheres or at the outside of the cortex, were found (Figure 3-25A). Specific fluorescence staining (anti-GPIX, platelets, green) confirmed that the vessel occluding thrombi were platelet-rich (Figure 3-25B). No obvious parenchymal damage like hemorrhages or edema formation was observed. In brains of INU-IgG or PBS treated mice no occluded vessels or thrombi were present (Figure 3-25), confirming that the observed effects were selectively driven by INU1-fab and not due to INU1-IgG induced platelet activation.

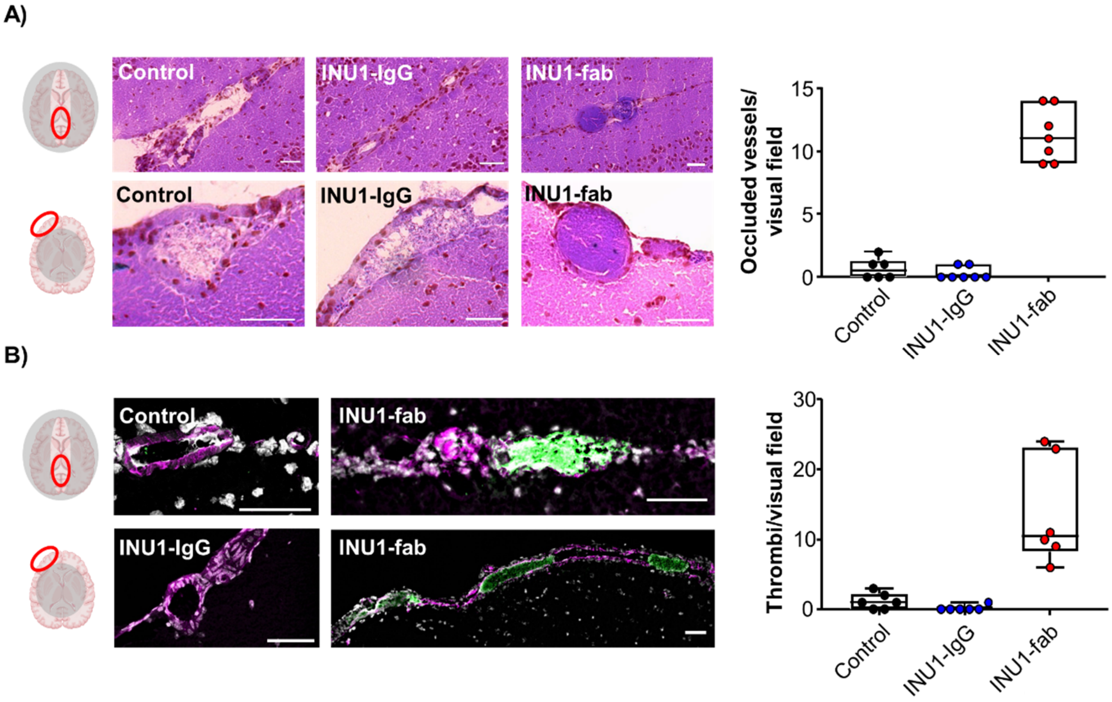

Figure 3-25: INU1-fab administration induced cerebral thrombosis. (A) and **(B)** Horizontal sections of murine brains taken 20 min after vehicle (control, n=6), INU1-IgG (0.75 µg/g; n=7) or INU1-fab (0.5 µg/g; n=6) i.v. injection revealed thrombi in the cerebral vasculature predominantly in large vessels in between the hemispheres (upper panels) or at the outside of the cortex (lower panels). Thrombi were visualized using hematoxylin and eosin **(A)** or platelet-specific anti-GPIX (green) counter-stained with anti-CD31 (vessels, magenta) and DAPI (nuclei, gray) **(B)**. Scale bar 50 µm. Right panels show quantification of thrombi per visual field, indicated as box plot from min to max with each data point representing one mouse. N=6-7. Stegner, Göb *et al.,* in press (*Nat Cardiovasc Res*).

Comparing the localization of the cerebral veins with the specific localization of the thrombi observed in cryosections of INU1-fab treated mice suggested cerebral vein thrombosis as reason for the induced symptoms. However, cryosections provide only information in 2D. To map the dynamics and localization of thrombus formation within the whole mouse body, a platelet-specific anti-GPIX mAb derivative was radiolabeled with copper-64 (^{64}Cu-αGPIX) and injected into mice (5 µg i.v.) for platelet visualization. 19 h later, mice were scanned for 60 min using simultaneous PET/MRI for obtaining baseline platelet distribution. INU1-fab or IgG was administered during acquisition via the tail vein and platelet accumulation was monitored *in vivo* for 45 min (Figure 3-26A). Over time, a gradual increase (+0.95 ± 0.50 %ID/ml) in the ^{64}Cu-αGPIX signal was detected in the brain after INU1-fab injection but not in control treated mice (+0.12 ± 0.09 %ID/ml; Figure 3-26B,D). In the brain of INU1-IgG treated mice, a marked decrease in ^{64}Cu-αGPIX signal was detected, reflecting the previously observed depletion of platelets from the circulation. Quantitative analysis of the ^{64}Cu-αGPIX signal in the last 20 min of the 45 min observation period confirmed strong accumulation of platelets in the brain of INU1-fab injected mice, but not control treated animals (Figure 3-26C). Co-localization of the platelet-specific ^{64}Cu-αGPIX signal with the simultaneously acquired 2D-TOF MRA of the cerebral vessels clearly localized the platelet signal to the cerebral (sinus) veins (Figure 3-26D).

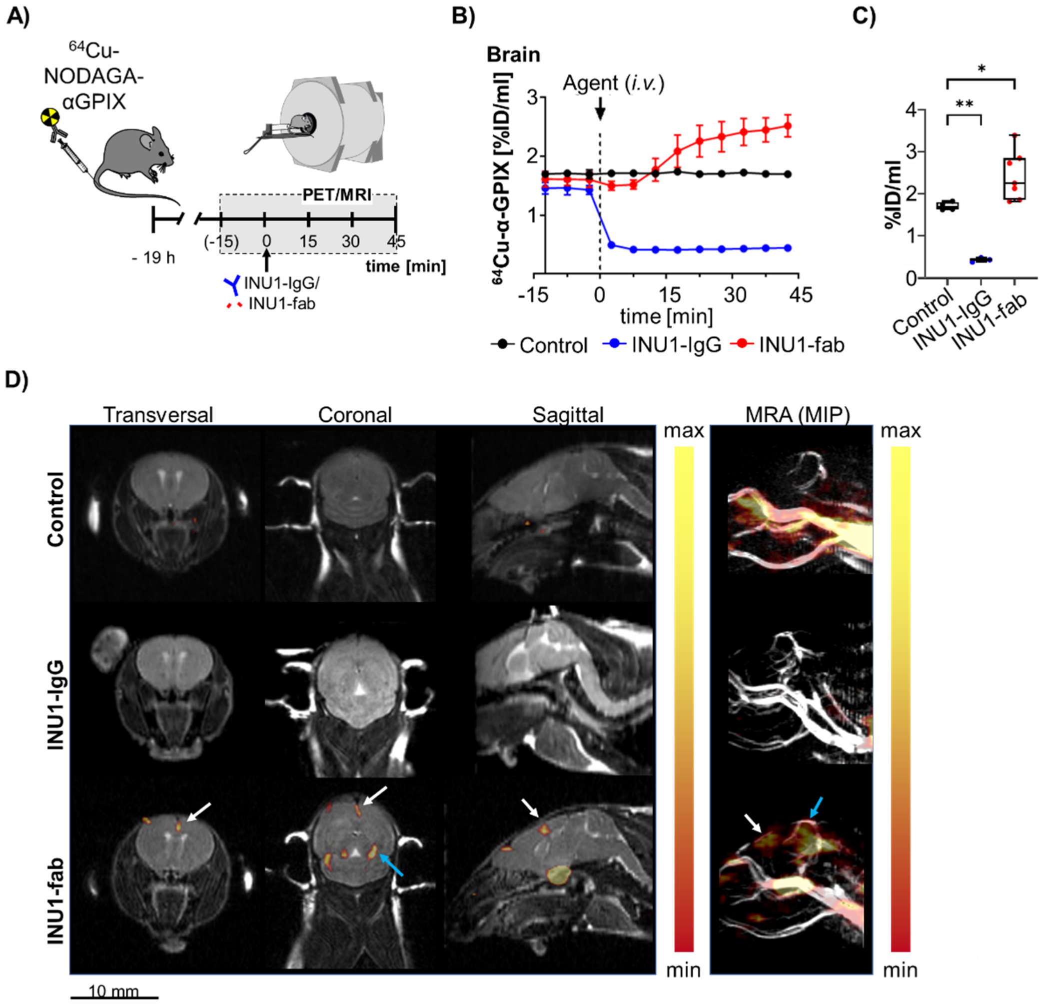

Figure 3-26: Platelets accumulate in the brain after INU1-fab administration. (A) Experimental setup and timeline of simultaneous PET/MRI measurements using [^{64}Cu]Cu-NODAGA-anti-GPIX-derivative (^{64}Cu-αGPIX) to follow platelet accumulation *in vivo*. 19 h after ^{64}Cu-αGPIX injection into naïve *WT* mice, PET/MRI measurement was started and baseline signals were acquired for 15 min. INU1-fab, INU1-IgG or vehicle were administered during acquisition and measurements continued for 45 min. **(B)** Time activity curves (TAC) of the ^{64}Cu-αGPIX signal in the brain for the indicated groups **(C)** Quantitative analysis of the ^{64}Cu-αGPIX PET signal in the brain during the last 20 min (4x5 min time frames) of image acquisition. INU1-fab induced accumulation of platelets within the brain, whereas after INU1-IgG injection, the signal was markedly decreased. **(D)** Representative PET/MRI images of the brain of control (top), INU1-IgG (middle) or INU1-fab (bottom) treated *WT* mice in the last 20 min of image acquisition (left). Corresponding maximum intensity projections (MIP) of the PET/2D-time of flight magnetic resonance angiograms (MRA) are depicted on the right, showing the vessels of the head. Data are presented as mean ± SEM percent injected dose per ml (%ID/ml). Box plots representing the median with 95% coincidence intervals, $^{*}p < 0.05$ $^{**}p < 0.01$; One-way ANOVA followed by Dunnett's test for multiple comparisons. Colored arrows are highlighting the same thrombi in different planes of the brain. These experiments were performed by Dr. Barabara Schörg at the Werner Siemens Imaging Center in Tübingen. Stegner, Göb *et al.,* in press (*Nat Cardiovasc Res*).

To specifically investigate thrombus formation in the venous vasculature, the superior sagittal sinus (SSS), a common site for CVT in humans [10, 121], was observed via intravital confocal microscopy. Access to the brain vasculature was achieved by a cranial window replacing a part of the bone with a glass cover slide (Figure 3-27A, left). Starting 7-12 min after injection of INU1-fab, rapidly evolving thrombus formation in the SSS was observed which further progressed until the death of the animal (Figure 3-27A). In contrast, no thrombotic activity was observed in vehicle or INU1-IgG injected mice. Of note, an immediate loss of circulating platelets was observed in the IgG treated mice (Figure 3-27A), which reflects the sudden drop in pPC and is in line with previous results. Neither INU1-fab nor INU1-IgG injection induced thrombus formation in the arterial vasculature of the MCA territory which was assessed by lateral placement of the cranial window and 2-PM (Figure 3-27B). This additionally points towards INU1-fab induced CVT as cause for the neurological symptoms. To overcome the limitation of the rather small fields of view in intravital microscopy, the overall extent of CVT was assessed by light sheet fluorescence microscopy (LSFM). Therefore, mice were injected with INU1-fab, INU1-IgG or PBS and after 20 min, organs were fixed by perfusion-fixation and brains were removed and prepared for microscopy. 3D reconstructions of the entire hemispheres revealed widespread appearance of INU1-fab induced thrombi in numerous, even deep large veins, but not arteries (Figure 3-27C). As expected, no thrombi were detected in the brains of INU1-IgG or PBS treated mice (Figure 3-27C). Together with the LSFM data, the results obtained in the *in vivo* experiments validate the conclusion that it is cerebral vein thrombosis causing the INU1-fab induced symptoms.

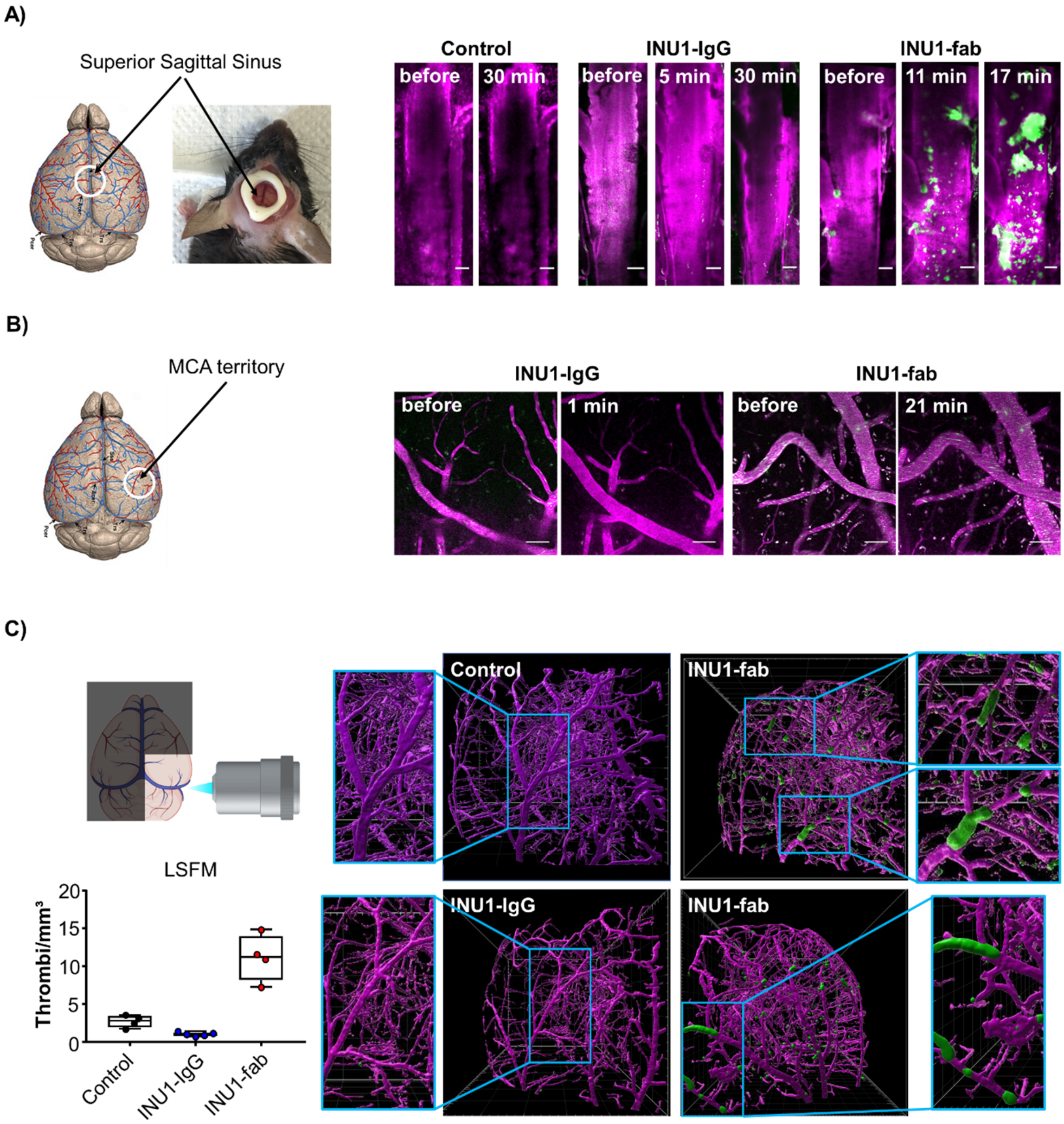

Figure 3-27: INU1-fab induced thrombi are formed within cerebral veins. A cranial window was placed above the area of the superior sagittal sinus (SSS) **(A)** or the cortical vasculature of the middle vertebral artery (MCA)-territory **(B)** allowing access to the cerebral vasculature by confocal **(A)** or 2-PM **(B)** intravital microscopy. Injection of INU1-fab (0.5 µg/g) but not INU1-IgG (0.75 µg/g) induced thrombus formation within the SSS **(A)** but not the cortical vasculature of the MCA territory **(B)**. Platelets (anti-GPIX, green), endothelial cells (anti-CD31, magenta) and vessel lumen (BSA, magenta) were labelled 15 min before imaging. **(A)** Exemplary image of the cranial window above the SSS and scheme of the superficial cerebral vasculature [157]. Snapshots of intravital confocal microscopy. Scale bar 100 µm. **(B)** Snapshots of intravital 2-PM. Scale bar 50 µm. **(C)** 3D reconstructions from light sheet fluorescence microscopy (LSFM) images of brains from mice that were fixed via perfusion 20 min after injection of INU1-fab (0.5 µg/g), INU1-IgG (0.75 µg/g) or PBS (vehicle). Platelets (anti-GPIX, green), endothelial cells (anti-CD31 and CD105, magenta) were labelled *in vivo* before perfusion-fixation. Brains were optically cleared using benzyl alcohol/benzyl benzoate (BABB) before imaging. Grid size 500 µm. INU1-fab induced thrombi were primarily localized in the larger superficial vasculature. Stegner, Göb *et al.,* in press (*Nat Cardiovasc Res*).

To further confirm the specificity of cerebral thrombus formation upon INU1-fab injection, additional organs were investigated for platelet accumulation either *in vivo* by PET/MRI (Figure 3-28A) or *ex vivo* in cryosections removed 20 min after treatment (Figure 3-28B). PET/MRI allowed the observation of platelet accumulation in response to treatment in different organs in a time-dependent manner in the living animal. Measurement of the ^{64}Cu-αGPIX signal in different organs revealed no major platelet accumulation in heart, liver and spleen nor in the jugular vein (JV) or *vena cava* (*V. cava*) in response to INU1-fab treatment (not shown). These findings were confirmed by histological analyses (data not shown). Only in the lungs an increase in ^{64}Cu-αGPIX signal was observed at later time points (Figure 3-28A). Upon INU1-IgG administration, a marked increase in ^{64}Cu-αGPIX signal was detected in the lung and a less pronounced increase in the liver. In the heart, jugular vein and *vena cava*, a decrease in signal can be noted (Figure 3-28). These observations fit to the observed breathing difficulties in INU1-IgG treated mice and the overall rapid platelet clearance from the circulation. H&E staining and platelet-specific staining of lung cryosections confirmed thrombus formation in lungs of INU1-IgG treated mice and showed that the increase in ^{64}Cu-αGPIX signal in the lungs of INU1-fab treated mice is the result of smaller platelet aggregates but not large thrombi (Figure 3-28B), explaining the absence of any signs of pulmonary problems in these mice. In cryosections of liver, kidney and spleen no major thrombus formation could be observed for the tested groups (Figure 3-28B).

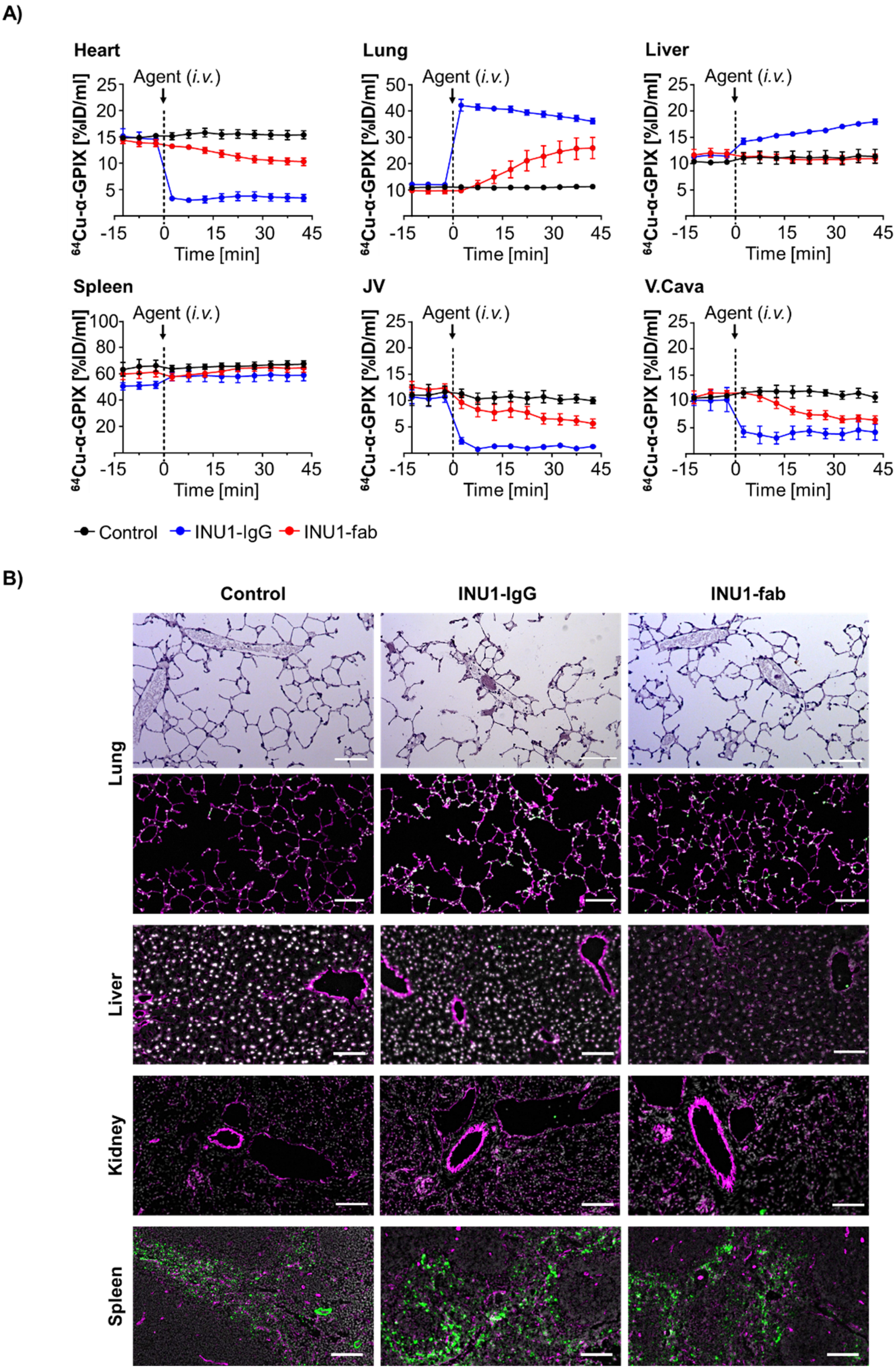

Figure 3-28: INU1-derivatives do not trigger disseminated thrombosis. (A) *In vivo* quantification of the ^{64}Cu-αGPIX PET signal represented by time activity curves (TAC) of the ^{64}Cu-αGPIX signal in the heart, lung, liver, spleen, jugular vein (JV) and *vena cava* (*V. cava*). N=4-7. Experiments were performed by Barbara Schörg in Tübingen. **(B)** Cryosections of different organs removed from *WT* mice 20 min after i.v. injection of vehicle (control), INU1-IgG (0.75 µg/g) or INU1-fab (0.5 µg/g). Thrombi/platelets were visualized using hematoxylin and eosin staining (lung, upper panel) or anti-GPIX (green) counterstained with anti-CD31 (vessels, magenta) and DAPI (cell nuclei, gray). Depicted are representative sections of, from top to bottom: lung, liver, kidney and spleen. Scale bar 100 µm, n=6. Stegner, Göb *et al.,* in press (*Nat Cardiovasc Res*).

Given the discrepancy of the rather inhibitory effect of INU1-fab on platelets *in vitro* (Figure 3-23E) and the induction of platelet aggregation *in vivo*, the mechanistic basis for the pathogenic *in vivo* effect was still unclear. Therefore, further studies were conducted to unravel the underlying mechanism. Platelet depletion before INU1-fab treatment protected mice from neurological symptoms and death. Similarly, absence of CLEC-2 (CLEC-2 depleted) or incapability of CLEC-2 signaling either by expression of a mutated, signaling dead hemITAM (*CLEC1b*$^{Y7A/Y7A}$) or by absence of the spleen tyrosine kinase (*Syk*$^{fl/fl,\ Pf4\text{-}Cre}$), an essential downstream component in the CLEC-2/ITAM signaling pathway, was protective. All mice survived and were protected from INU1-fab induced thrombocytopenia (Figure 3-29), demonstrating a critical involvement of CLEC-2 mediated ITAM signaling in the pathogenesis of INU1-fab induced CVT.

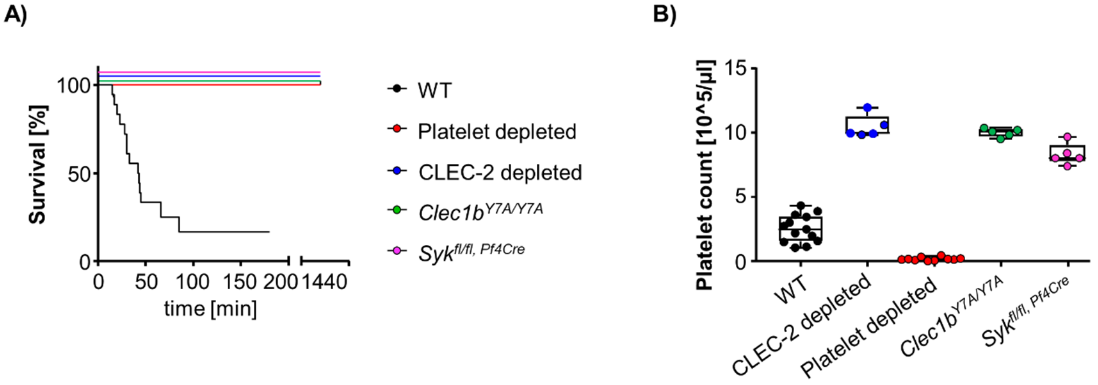

Figure 3-29: INU1-fab induced platelet consumption and mortality requires CLEC-2/ITAM signaling. (A) Platelet depletion, absence of CLEC-2 or incapability of CLEC-2 signaling protected mice from INU1-fab (0.5 µg/ml i.v.) induced mortality. **(B)** Peripheral platelet counts of the indicated groups were determined by flow cytometry 20 min after INU1-fab treatment. Stegner, Göb *et al.,* in press (*Nat Cardiovasc Res*).

Thrombus formation involves the sequential action of different adhesion receptors and autocrine/paracrine effects of released secondary mediators. To reveal potentially involved processes, certain receptors or pathways were examined for potential involvement in the INU1-fab induced pathology in the following experiments. Blockade of GPIb, which is essential for initial recruitment and adhesion of platelets to the extracellular matrix, interestingly, had no effect on INU1-fab induced platelet consumption (Figure 3-30A) but led to less severe neurological deficits (Figure 3-30B). Still 5 of 14 mice died, but the remaining mice survived and recovered from the neurological impairments within 24 h (Figure 3-30B,C). Platelet activation induces the release of α- and dense granule content, which amplifies the activation response and promotes thrombus formation. To test the involvement of granule content in the pathogenesis of INU1-fab induced CVT, *Unc13d*$^{-/-}$ mice were used. Platelets of these mice lack dense granule release and have a markedly impaired α-granule release. Upon INU1-fab injection, *Unc13d*$^{-/-}$ mice developed severe neurological symptoms and became thrombocytopenic. However, symptom onset was delayed when compared to INU1-fab treated WT mice (Figure 3-30A,B). Despite showing heavy symptoms and being in an overall bad shape in the first 4 h following INU1-fab, these mice completely recovered from the neurological symptoms within 24 h resulting in 100% survival rate (Figure 3-30B,C).

Thrombin is a powerful platelet agonist and the central protease of the coagulation cascade that finally produces fibrin. Activated platelets promote thrombin generation, further amplifying platelet activation. Thrombin is critically involved in venous thrombosis and can be targeted either directly or indirectly by different anticoagulants [158]. One widely used anti-coagulant is heparin, an indirect thrombin inhibitor that is currently used as fist-line treatment for patients with CVT [10]. Therefore, it was assessed whether heparin treatment was beneficial in the setting of INU1-fab induced CVT. Mice were pretreated with high molecular weight heparin (2 U/g) 20 min before INU1-fab injection. Heparin treatment could not prevent INU1-fab induced platelet consumption and neurological symptoms (Figure 3-30A,B). Although survival rate was higher in heparin treated mice compared to control within the first 3 h following INU1-fab injection (Figure 3-30C), after 5 h, the mice had to be euthanized due to animal welfare reasons. They were in a very bad condition characterized by severe lethargy, hypothermia, seizures and ruffled fur.

Independent of the stimulating agonist, platelet activation finally results in the shift of GPIIb/IIIa from a low to a high affinity state (inside-out signaling). High affinity GPIIb/IIIa binds to fibrinogen and other ligands crosslinking adjacent platelets to form aggregates. To investigate a potential involvement of GPIIb/IIIa in INU1-fab induced CVT, mice were treated with a GPIIb/IIIa-blocking $F(ab)_2$ (JON/A-$F(ab)_2$) 30 min before injection of INU1-fab. Strikingly, all JON/A-$F(ab)_2$ pretreated animals were fully protected from INU-fab induced neurological symptoms and mortality (Figure 3-30A,B). In addition, peripheral platelet counts remained unaltered, and SEM and flow cytometry confirmed that circulating platelets were in a resting state (Figure 3-30D). This suggests that functional GPIIb/IIIa mediates INU1-fab induced aggregate formation *in vivo* and is essentially required for platelet activation in INU1-fab induced CVT. Within one week following INU1-fab injection, JON/A-$F(ab)_2$ pretreated mice showed no signs of delayed CVT or bleeding. Of note, flow cytometric analysis confirmed the presence of JON/A-$F(ab)_2$ on the platelet surface as determined by reduced binding of JON/A-IgG^{FITC} (Figure 3-30E). Likewise, the presence of INU1-fab on the platelet surface in the presence of JON/A-$F(ab)_2$ was confirmed by reduced binding of INU1-IgG^{FITC}. JON/A-$F(ab)_2$ pretreatment did not prevent the immediate decrease in peripheral platelets upon INU1-IgG treatment (Figure 3-30G) indicating that in this case, platelet clearing was GPIIb/IIIa independent, probably by cells of the reticuloendothelial system in the spleen.

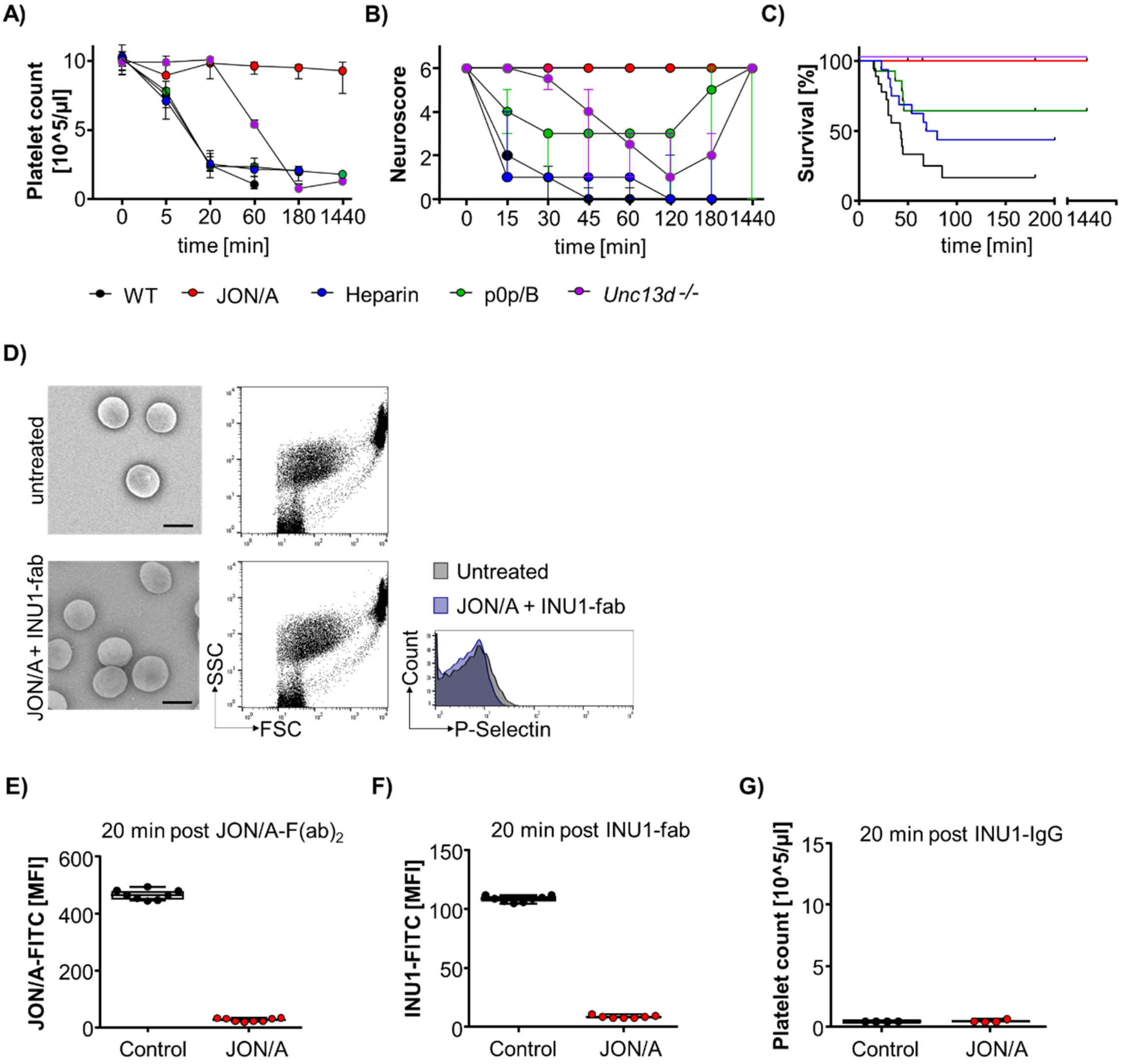

Figure 3-30: INU1-fab induced platelet consumption and CVT require functional GPIIb/IIIa. (A) Mutant or pre-treated WT mice were injected with INU1-fab (0.5 µg/g i.v.) and peripheral platelet counts (indicated as median and IQR) were monitored at the indicated timepoints over a period of 24 h. Heparin (2 U/g, Ratiopharm, Heparin-Natrium-5000 i.p.), JON/A-F(ab')$_2$ (2 µg/g, i.v.) or p0p/B-fab (2 µg/g, i.v.) were administered 30 min before INU1-fab. **(B)** Neurological symptoms following INU1-fab injection in the indicated groups were assessed using a six-point scoring system and are depicted as median and IQR: 0 = death, 1 = severe seizures or circling behavior, 2 = post-seizure lethargy, 3 = mouse lying 'exhausted' on the belly, 4 = backward bending of the head and backside, 5 = reduced motor control of the hind limbs, 6 = seemingly unaffected behavior. **(C)** Mortality of the indicated groups following INU1-fab injection. Only GPIIb/IIIa blockade fully protected the mice. **(D)** Scanning electron micrographs and flow cytometry of peripheral platelets from untreated (upper panel) or JON/A-F(ab)$_2$ pretreated mice (lower panel) 20 min after INU1-fab injection. Platelets of both groups were in a resting state. Scale bar: 2 µm. **(E)** Presence of JON/A-F(ab)$_2$ on the platelet surface was confirmed by reduced binding of JON/A-IgG^{FITC} 20 min after treatment using flow cytometry. **(F)** Presence of INU1-fab on platelets pre-treated with JON/A-F(ab)$_2$ was confirmed by the absence of INU1-IgG^{FITC} binding despite unaltered platelet counts. **(G)** Blockade of GPIIb/IIIa by JON/A-F(ab)$_2$ did not prevent INU1-IgG induced platelet consumption. Platelets were cleared from the circulation 20 min after INU1-IgG injection (0.75 µg/g i.v.; n=4) independent of GPIIb/IIIa blockade. Stegner, Göb *et al.,* in press (*Nat Cardiovasc Res*).

To investigate the effect of GPIIb/IIIa blockade in a clinically more relevant therapeutic setting, *WT* mice were injected with INU1-fab (0.5 µg/g i.v.) and 2 min after symptom onset (reduced motor control and tonic deflection of head and backside), mice received 2 µg/g JON/A-F(ab)$_2$ (i.v.). As comparison, a second set of mice was treated with 2 U/g heparin, since this is the first line treatment in humans, and both groups were compared to vehicle injected controls. In all mice, symptom onset was after 8 ± 2 min and in case of vehicle treatment, symptoms aggravated and led to death within 70 min in 11 of 12 mice (Figure 3-31). After heparin treatment, symptoms severely aggravated along with a constant decrease in peripheral platelet count (Figure 3-31A,B), finally resulting in death of 5 out of 5 mice within 38 min (Figure 3-31C). In sharp contrast, JON/A-F(ab)$_2$ treated mice showed reduced mobility and were mostly immobile during the first 45 min but developed no other types of neurological impairments or seizures. These mice fully recovered within 2-3 h (Figure 3-31A) and had a markedly higher survival rate (Figure 3-31C). Despite a slight decrease after symptom onset, peripheral platelet counts remained stable and no further decrease was noted (Figure 3-31B), suggesting that GPIIb/IIIa blockade immediately interrupted platelet activation and consumption. *In vivo* confocal microscopy of the superior sagittal sinus (SSS) revealed that injection of JON/A-f(ab)$_2$ 2 min after the onset of INU1-fab induced thrombus formation in the SSS prevented further progression of thrombus formation (Figure 3-31D). Without GPIIb/IIIa blockade, thrombus formation continued as already shown earlier (Figure 3-31D and Figure 3-27A). This is in line with the observation that the decrease in pPC is prevented by treatment with JON/A-F(ab)$_2$.

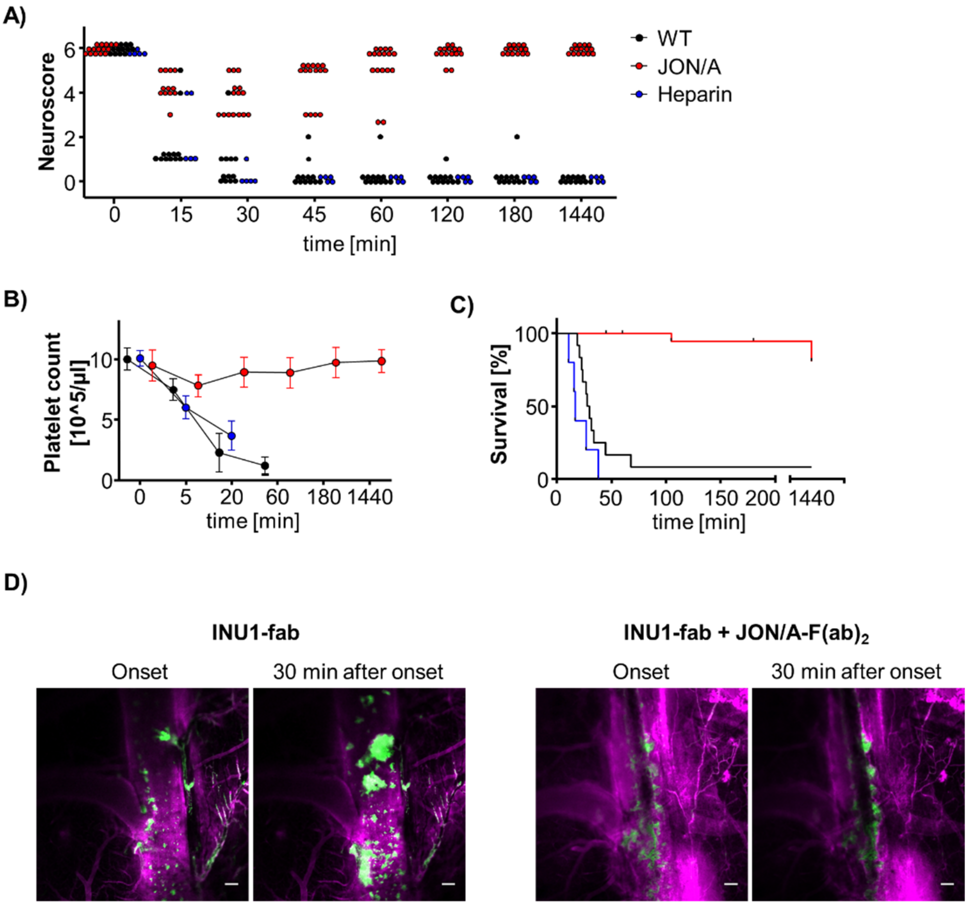

Figure 3-31: Therapeutic blockade of GPIIb/IIIa after symptom onset but not heparin prevents mice from INU1-fab induced CVT and death. *WT* mice were injected with 0.5 µg/g INU1-fab i.v. and 2 min after symptom onset received either JON/a-F(ab)$_2$ (2 µg/g) or heparin (2U/g) i.v. **(A)** Neurological symptoms were monitored from the time of INU1-fab injection and scored according to a six-point scoring system: 0 = death, 1 = severe seizures or circling behavior, 2 = post-seizure lethargy, 3 = mouse lying 'exhausted' on the belly, 4 = backward bending of the head and backside, 5 = reduced muscle control of the hind limbs, 6 = seemingly unaffected behavior. **(B)** Platelet counts (indicated as mean ± SD) were measured at different time points using flow cytometry. JON/A-F(ab)$_2$ but not heparin-treatment prevented the INU1-fab induced decrease in peripheral platelet counts. **(C)** JON/A-F(ab)$_2$ treatment markedly increased survival following INU1-fab injection. Heparin treatment was not beneficial. **(D)** *In vivo* confocal microscopy of the superior sagittal sinus. INU1-fab was injected via a jugular vein catheter and 2 min after onset of thrombus formation, JON/A-F(ab)$_2$ (3 µg/g) was injected. No progression of thrombus formation was observed in JON/A-F(ab)$_2$ treated mice. Representative images at the onset (=time of treatment) of thrombus formation and 30 min after treatment. Platelets (anti-GPIX, green), endothelial cells (anti-CD31, magenta) and vessel lumen (BSA, magenta) were labelled 15 min before imaging. Scale bar 100 µm. Stegner, Göb *et al.,* in press (*Nat Cardiovasc Res*).

Due to the promising results obtained with the *Unc13d*$^{-/-}$ mice and the success of antibody-mediated blockade of GPIIb/IIIa in improving symptoms and outcome after INU1-fab injection, platelet inhibiting drugs were tested regarding their potential in preventing INU1-fab induced CVT. Classical platelet inhibitors Clopidogrel and acetyl salicylic acid (ASA) were compared to the GPIIb/IIIa inhibitor Eptifibatide. Pre-treatment of *WT* mice with Clopidogrel and ASA delayed symptom onset, similar to what was observed in *Unc13d*$^{-/-}$ mice, but could not reduce lethality (Figure 3-32B,C). Only Clopidogrel but not ASA was beneficial in maintaining platelet counts (Figure 3-32D). Due to moderate solubility of Eptifibatide and limitations in injection volume, the highest dose that could be administered to mice was 20 µg/g (i.p.). At this concentration, Eptifibatide could only partially inhibit platelet aggregation (Figure 3-32A). Despite incomplete platelet inhibition, mice pre-treated with Eptifibatide were protected from INU1-fab induced lethality and thrombocytopenia and recovered from the initial neurological symptoms within 24 h (Figure 3-32B).

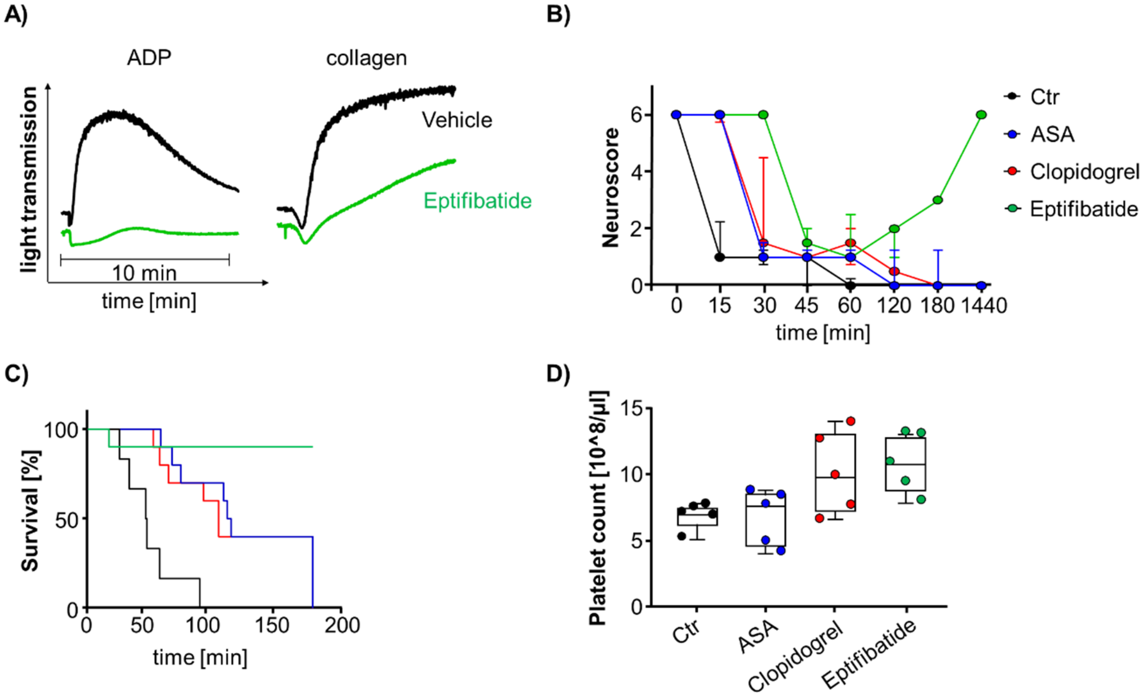

Figure 3-32: Partial blockade of GPIIb/IIIa with eptifibatide prevents INU1-fab induced lethality whereas platelet inhibition with acetyl salicylic acid (ASA) or Clopidogrel does not. (A) The maximum dose of Eptifibatide that could be administered (20 µg/g i.p.) was only partially inhibiting platelet aggregation. Platelets in platelet rich plasma were stimulated with the ADP (10 µM) or collagen (10 µg/ml) and platelet aggregation was measured on a Fibrintimer 4-channel aggregometer. Shown are representative curves of n=4. **(B)** Mice were pretreated with the indicated drugs and subsequently injected with INU1-fab (0.5 µg/g) and neurological symptoms were scored using a six-point scoring system 0 = death, 1 = severe seizures or circling behavior, 2 = post-seizure lethargy, 3 = mouse lying 'exhausted' on the belly, 4 = backward bending of the head and backside, 5 = reduced motor control of the hind limbs, 6 = seemingly unaffected behavior. Only among Eptifibatide treatment, mice recovered. **(C)** Survival rates of the indicated groups following INU1-fab induced CVT. **(D)** Platelet count was determined 20 min after INU1-fab treatment using flow cytometry. Eptifibatide and Clopidogrel but not ASA prevented INU-fab induced platelet consumption. Stegner, Göb *et al.,* in press (*Nat Cardiovasc Res*).

Combining 2D histological analysis with advanced imaging techniques such as LSFM, PET/MRI and *in vivo* confocal microscopy, we could unravel foudroyant cerebral venous thrombus formation as reason for the heavy neurological symptoms induced by the anti-CLEC-2 INU1-fab-fragment. Using respective genetically modified mice and treatments, it was shown that the observed effects are CLEC-2 and CLEC-2 signaling dependent but that only cooperative CLEC-2 and GPIIb/IIIa signaling drives CVT and platelet consumption *in vivo*. The results presented here indicate that targeting GPIIb/IIIa or CLEC-2/CLEC-2 signaling provide new targets for the treatment of CVT that might be superior to the current first line treatment with heparin.

4 Discussion

4.1 Infarct growth precedes cerebral thrombosis following experimental stroke

The primary therapeutic goal for acute ischemic stroke patients is the recanalization of the occluded vessel and restoration of cerebral blood flow. However, even if recanalization is successful, not all patients benefit and further infarct growth can be observed [45]. The degree of cerebral perfusion after recanalization correlates with infarct progression [142] which underscores the importance of uncovering the underlying mechanisms of reperfusion injury and failure. Reasons for absent/incomplete reperfusion or collapse of the microcirculation are discussed in many ways [5]. Several experimental mouse studies showed a positive correlation of the occurrence of occluded vessels/thrombi with infarct sizes one day after tMCAO [159-161]. This led to the assumption that formation of thrombi in the cerebral microvasculature is responsible for further vascular occlusion and thus infarct growth. Indeed, thrombi in the cerebral microcirculation that are either re-formed at the site of the initial occlusion, embolize from the initial thrombus or are newly formed during reperfusion would be a plausible explanation for insufficient reperfusion. However, just the presence of thrombi within the infarcted brain area is no proof for them to be the reason for tissue death. Here the temporal context is of utmost importance. Are thrombi present before or after tissue death? The kinetics of infract progression presented in this thesis suggest that processes leading to tissue death must occur within the first 8 h of reperfusion. Using different complementary approaches, we revealed that thrombi could only be detected at significantly elevated levels in the cerebral vasculature after full infarct development (Figure 3-2 and Figure 3-3). In the performed experiments, the percentage of occluded vessels in hematoxylin and eosin-stained sections served as indicator for the thrombotic activity and specific platelet staining to determine cerebral thrombi. Both methods show the limitation, that also in the sham group some occluded vessels/thrombi could be detected, indicating that the death of mice triggers some thrombotic activity. The occurrence of thrombotic "background" in the sham group could be reduced by using Western Blot analysis of the platelet specific protein GPIbβ or using LSFM. Regardless of the method used, infarct growth always preceded thrombus formation. This leads to the conclusion that the occurrence of thrombi in the infarcted brains is the consequence and not the cause of ongoing tissue death following tMCAO. These findings are in line with the observation that blockade of platelet aggregation by targeting GPIIb/IIIa was not beneficial in stroke therapy [50, 51]. The presence of thrombi in the infarcted brain areas at later stages of stroke pathology is most likely part of tissue regeneration processes. An essential step during ischemic tissue regeneration is the regrowth of new blood vessels (angiogenesis). Increased vascularization in areas surrounding the infarcted tissue is associated with improved functionality [162].

Platelets contain a variety of factors that orchestrate angiogenesis in different stages such as vascular-endothelial growth factor (VEGF), fibroblast growth factor (FGF), epidermal growth factor (EGF), angiopoetin-1 (Ang1) and platelet-derived endothelial growth factor (PDGF) that are released upon activation [163]. Furthermore, platelets were shown to be involved in the recruitment of and interaction with progenitor cells, by SDF-1 secretion or the P-Selectin/PSGL-axis [164], thereby contributing to tissue remodeling. Thus, platelets might be actively recruited to sites of tissue injury as part of tissue healing processes promoting the role of platelets in response to tissue injury [163]. However, there is a second side to the coin when it comes to the role of platelets in stroke. Although it is not platelet aggregation and thrombus formation, evidence is given that platelets do contribute to reperfusion injury. The absence or blockade of platelet receptors other than GPIIb/IIIa or platelet components has been shown to be beneficial in experimental stroke [54]. Blocking initial platelet adhesion by fab fragments against the platelet adhesion receptor GPIbα improves cerebral perfusion and leads to reduced infarct sizes following tMCAO [82]. Upon GPIbα blockade, reduced tissue damage is also observed in the occlusion phase in conditions of permanent ischemia [165]. This promotes the concept that the platelets' role in infarct progression is different from 'just' thrombosis and evidence is given that it might be rather of immune-modulating nature. Recently, we could identify the CD84 receptor as link between platelets and T-cells, playing essential roles in infarct development after tMCAO [166]. Other studies have shown that platelets and neutrophils contribute to the obstruction of the cerebral microcirculation in the course of the no-reflow phenomenon [104]. Clearly, future studies are needed to elucidate how platelets exactly contribute to the ongoing tissue damage following ischemic stroke.

4.2 Platelet derived PDGF induces vascular leakage upon cerebral ischemia

Breakdown of the BBB is one of the hallmarks of the pathology of ischemic stroke. Loss of barrier integrity leads to increased paracellular permeability. Consequently, plasma and plasma components extravasate into the brain parenchyma. BBB disruption can be observed in mice and men in the early phase of ischemic stroke progression [71-76]. Breakdown of the BBB in the early phase after ischemic stroke is associated with a higher risk of life-threatening complications such as edema and hemorrhagic transformation and is associated with poor clinical prognosis [167]. Elucidating underlying processes is essential for a better understanding of the disease and the development of new therapeutic strategies. The important aspect is the timing, since in the post-acute phase (72 h to 6 weeks) of ischemic stroke, angiogenesis is associated with an increased BBB permeability, however, in this setting, this is highly beneficial [167, 168]. Although, BBB breakdown is intensively studied, and various reasons and contributors are discussed, the exact pathomechanisms still remain largely elusive. In stroke therapy, recanalization of the occluded vessel and restoring reperfusion in the ischemic tissue is so far the only option but a double-edged sword. It is essential for the survival of the penumbral tissue but at the same time, it might promote the flow of water and osmotic solutes through the damaged BBB in the brain parenchyma and thereby contribute to reperfusion injury and promote tissue damage [167]. Platelets are known to be critically involved in the pathogenesis of reperfusion injury following ischemic stroke [54] and tissue ischemia promotes a platelet activating environment [163]. Since platelets are highly abundant in the blood, they are already present in the affected areas during occlusion and immediately after recanalization. Recent studies show that blockade of platelet GPIbα during vessel occlusion delays cerebral infarct progression already during occlusion and thus before reperfusion [165]. This indicates that there are platelet-dependent detrimental processes that begin during MCA occlusion and continue during the reperfusion phase. Platelet activation leads to release of platelet granule content, which consists of a variety of chemokines, small molecules, and growth factors. Since platelet aggregation and thrombus formation could be excluded as cause for infarct growth despite recanalization (see section 3.1), the impact of platelet granule content on the brain endothelial cells was investigated in this part of the thesis. First, leakage of the cerebral vasculature was systematically monitored during the 24-hour reperfusion phase following tMCAO. Thereby vascular leakage was confirmed as early event in disease progression, already detectable within the first 4 hours of reperfusion, confirming the tMCAO model as appropriate tool to study BBB disruption and vascular permeability. Next, an *in vitro* system of the endothelial barrier was established. Immortalized cell lines represent an important tool in *in vitro* research since they provide the possibility to reduce the number of laboratory animals needed. For being suited as good replacement, the used cells must have the appropriate properties to answer the question under investigation. Two established murine brain endothelial cell lines, b.END3 and b.END5, were tested on their suitability as model of endothelial barrier properties. Since both cell lines fail to form proper cell-cell contacts in culture and can therefore not be used for further studies investigating barrier properties. This observation is in line with the literature, where immortalized cell lines are described to be not suitable to mimic the complexity of the BBB [169]. Since for primary endothelial cells better preservation of *in vivo* characteristics is described [169], we continued our studies with primary brain microvascular endothelial cells (MBMECs). MBMECs express the essential barrier forming tight junction proteins, ZO-1, Occludin and Claudin-5 (Figure 3-8) and trans endothelial resistance measurements confirmed a tight MBMEC monolayer. Within the inflammatory environment of the ischemic brain, multiple platelet-activating agonists are present [170]. Platelet activation leads to secretion of platelet granule content that potentially influence the surrounding cells and the BBB. Using the established *in vitro* model, platelet α-granule content was shown to directly act on the MBMECs and to disrupt the integrity of the endothelial cell layer. In line with the *in vitro* experiments, mice that lack α-granules (*Nbeal2*$^{-/-}$) are protected from vascular leakage in the early reperfusion phase. The fact that these mice show reduced infarct sizes following tMCAO strengthens a correlation between vascular leakage and infarct progression during reperfusion injury. This is in line with the fact that BBB breakdown in stroke patients correlates with outcome [71, 72]. The selective effect of α-granule content observed here, contrasts with the observation that also *Unc13d*$^{-/-}$ mice, lacking dense granule secretion, are protected in experimental stroke [91] despite absent effects of dense granule content on MBMEC integrity. This suggests that the protection of *Unc13d*$^{-/-}$ mice in experimental stroke might be due to different reasons. Instead of directly affecting vascular integrity, the abolished dense granule secretion reduces the amplification of platelet activation and might thereby lead to reduced tissue damage. Furthermore, the used *Unc13d*$^{-/-}$ mice are no platelet-specific knockouts and Munc13-4 is also expressed by other cells, as it is detected in lung and spleen tissue [171]. Especially T cells are essential contributors to reperfusion injury [172, 173], so that possible defects in T cell function in Munc13-4-deficient mice might contribute to the observed effects *in vivo*. Along with the abolished dense granule secretion, Munc13-4-deficient platelets also have a reduced α-granule secretion [91], which might contribute to the observed *in vivo* effects. *In vitro*, the residual α-granule secretion is probably sufficient to damage the endothelial cells. Denaturation of platelet releasate failed to disrupt the MBMEC monolayer, indicating that the responsible factor was a protein. Platelet α-granules contain a plethora of molecules of which many might interfere with vascular integrity. They contain chemokines including CXCL1, 4, 5, 7, 8, 12 and CCL2, 3 and 5. Their release contributes to the recruitment, activation, chemokine secretion and differentiation of other vascular and hematologic cells [21, 174]. Besides chemokines, platelet α-granules contain several pro- and anti-angiogenic proteins. Angiogenic factors like vascular endothelium growth factor (VEGF), platelet-derived growth factor (PDGF), fibroblast growth factor (FGF), and insulin-like growth factor (IGF) [23] induce growth and proliferation of endothelial cells and fibroblasts and promote vessel wall permeability [21]. To identify the responsible α-granule component, we tested different potential chemokines and growth factors. CXCL 5 and PF4 were selected because stroke patients show markedly elevated levels in the CSF and plasma, respectively [175, 176]. However, neither recombinant CXCL 5 nor PF4 incubation of the MBMECs decreased endothelial resistance excluding these two factors as platelet derived mediators of endothelial disruption. Elevated PF4 levels might be a general marker of platelet activation present in stroke patients. CXCL 5 is an important neutrophil chemoattractant, so its role is potentially the recruitment of immune cells to the sites of inflammation and the contribution to general neutrophil homeostasis [177]. A direct effect on the endothelial cells seems to be absent.

VEGF-A was originally identified in two biological effects, vascular permeability and angiogenesis [178]. It was selected as promising candidate since it is known to disrupt endothelial cell-cell junctions *in vitro* [179]. Furthermore, VEGF-A administration to rats 1 h after MCA occlusion leads to increased extravasation of intravenously administered contrast agent. This increase in vascular leakage correlates with increased infarct sizes [180]. Surprisingly, in our setting, both tested VEGF-A isoforms had no influence on endothelial cell layer integrity (Figure 3-12). However, the role of VEGF-A on vascular permeability is complex and highly dependent on the timely context. It leads to vascular leakage, increased infarct sizes and hemorrhagic transformation, when administered early after MCA occlusion (1 h). In contrast, late administration (48 hours post MCA occlusion) is beneficial and promotes angiogenesis and improves neurological recovery in rats [180]. Following ischemic stroke in rats, VEGF-A expression is increased in the ischemic penumbra in neurons, astrocytes, macrophages and endothelial cells [178]. This suggests that platelet-derived VEGF-A might not play a predominant role, at least not in our model of direct interaction on endothelial cells under normoxic conditions.

Like VEGF, PDGF is stored in platelet α-granules and promotes vessel wall permeability and angiogenesis [21, 181]. The PDGF family consists of five biologically active PDGF proteins, the homodimers PDGF-AA, -BB, -CC and -DD and the heterodimer PDGF-AB [182]. There are two PDGF receptors, PDGFR-α and -β, each responding to more than one PDGF isoform [182]. The PDGF-α receptor binds to the A-, B- and C-chains of PDGF, whereas PDGFR-β only binds to the PDGF-BB and DD-chains [181].

We confirmed the presence of PDGF in platelet α-granule releasate and tested two specific isoforms, PDGF-AB and -BB in the model of trans-endothelial electrical resistance. Interestingly, only incubation of recombinant PDGF-AB but not PDGF-BB induced endothelial damage. Like VEGF, PDGF probably has a dual role in stroke progression. Studies in human patients show on the one hand, that lower plasma levels of PDGF-AB/BB 5 days after stroke are associated with a higher degree of dependency in daily life activities [183]. On the other hand, higher PDGF-AB/BB plasma levels are correlating with insufficient reperfusion after mechanical thrombectomy worsening outcome [184]. Often, studies or test systems do not discriminate between the PDGF isoforms so that the exact contribution of single isoforms to the various processes remains unclear. In a model of permanent MCAO in mice, absence of PDGFR-β aggravated edema formation, increased transcellular permeability and impaired functional recovery following cerebral ischemia [185]. This indicates that the PDGF-BB/PDGFR-β axis rather promotes BBB integrity, which fits to the observation that recombinant PDGF-BB does not affect MBMEC monolayer integrity. This is further supported by other studies showing beneficial effects of PDGF-BB in conditions of brain ischemia (summarized in [186]). In contrast, in a model of intracerebral hemorrhage, suppression of PDGFR-α prevented neurological deficits, brain edema and preserved BBB integrity indicating that PDGFR-α signaling contributes to BBB impairment [187]. Given the different consequences of PDGF binding to different receptor isoforms, it must be assessed in further experiments which receptor isoforms are expressed on the MBMECs used in the model of trans endothelial resistance. So far, the *in vitro* model involves only endothelial cells, however for future studies, co-culture of the MBMECs with astrocytes and/or pericytes might increase basal TEER and better reflect the *in vivo* situation since it is closer to the situation within the NVU [169, 188]. Meanwhile, also *in vitro* models of the human BBB are successfully established [189]. Testing platelet releasate and recombinant human PDGF in these models might help to translate the findings to the human system. Furthermore, PDGF and PDGFR are expressed by various cells of the neurovascular unit [181] and in the neuronal system, platelets are not the only source of PDGF. It is also expressed by several cell types, such as neurons, astrocytes and oligodendrocytes [181]. To specifically address the role of platelet-derived PDGF not only on endothelial cells but also in the pathogenesis of I/R injury and BBB integrity in the overall context, platelet-specific PDGF-deficient mice are planned to be generated and analyzed in the tMCAO model.

4.3 NET-formation but not neutrophil-derived ROS production contributes to reperfusion injury following ischemic stroke

Neutrophils are primarily known for their essential role in eliminating invading pathogens. Therefore, they possess various defense mechanisms like an efficient ROS production machinery and the capability to release chromatin as neutrophil extracellular traps (NETs). These tools are crucial for immune defense but can also harm the host’s structures. To avoid the undue harm to the host, neutrophil action needs to be outbalanced and finely orchestrated. Meanwhile neutrophils are known to play essential roles not only upon infection but also in the context of other pathological states such as ischemic stroke. However, not only detrimental effects of neutrophils have been described. Upon cerebral ischemia, neutrophil granulocytes are the first hematogenous cells that are recruited to the brain. Recent research points to differentiated functions and important contributions to the post ischemic response and resolution of inflammation and tissue repair [100, 190]. This potential dual role of neutrophil function is in line with the observation that complete neutrophil depletion before tMCAO is not beneficial for the outcome (Figure 3-13). Depletion of neutrophils might lead to absence of potential detrimental but also possible beneficial effects, which might balance each other out. This finding is contradictory to some reports in the literature, where absence of neutrophils led to reduced infarct volume and neurological damage [191, 192]. However, studies of neutrophil depletion have not consistently demonstrated improved outcomes [105]. When the number of neutrophils is increased with G-CSF treatment, ischemic stroke is not worsened in patients and results from animal studies with increased neutrophil numbers even show beneficial effects [105]. This supports the hypothesis that under certain conditions, neutrophils might be not only be harmful but even beneficial. When comparing different studies, it is important to note that the timing of the analysis may be critical for the observed results since neutrophils are recruited to the brain in a specific time-window and have a short lifetime in tissues [102]. Also, the use of different experimental stroke models might affect the observed roles of neutrophils. Another fact that needs to be considered, not only for this study, is, that neutrophil depletion might be incomplete. Despite the complete absence of neutrophils in the peripheral blood, neutrophils might not be completely depleted from the bone marrow. In the study presented here, the same antibody was used for depletion and 3 days later for staining of the bone marrow sections. It cannot be excluded that there is still antibody bound to the neutrophils in the bone marrow that prevented binding of the newly applied staining antibody. This phenomenon is meanwhile known as antigen masking and might have led already in previous studies to overestimation of depletion efficacy [193]. For further experiments, depletion efficacy in bone marrow and tissues should be controlled and quantified with the help of reporter mice that allow antibody-independent visualization of neutrophils.

Novel therapeutic strategies should consider local and selective targeting of neutrophils rather than nonselective overall inhibition or depletion. A possible selective approach could be inhibition of ROS production. Upon inflammatory conditions, neutrophils produce high levels of ROS which induce endothelial damage, capillary leakage and enhance inflammation [190]. One central mechanism of ROS production in neutrophils is via the activation of the NADPH oxidase. For the NADPH oxidase 7 isoforms are reported: NOX1, 2, 3, 4, 5 and DUOX1 and 2. In this study *Ncf1*$^{-/-}$ mice that lack the NADPH subunit Ncf1 (p47^{phox}) were used. Deficiency of the NADPH isoform NOX2 protects mice in ischemic stroke models [111, 194, 195]. Since p47^{phox} is essential for NOX2 activation [195], we investigated whether absence of p47^{phox} is sufficient to protect mice from ischemic stroke. Surprisingly, the *Ncf1*$^{-/-}$ mice are not protected in the tMCAO model as they had comparable infarct volumes as the respective WT controls (Figure 3-15). But the result presented here, is in line with a study of Kleinschnitz and colleagues who used *NOX2*$^{-/-}$ mice in the tMCAO model with an occlusion time of 60 min followed by a 23-hour reperfusion phase (the same conditions that were used in the study presented here). Under these conditions, they could not show any beneficial effect of NOX2-deficiency on stroke outcome [196]. Other studies showing protective effects of NOX2-deficiency were conducted with shorter or longer occlusion times or under conditions of permanent ischemia [195]. This indicates a differentiated role of ROS production that might be dependent on the timely context and sensitive to the time of ischemia and reperfusion. Further studies are needed to elucidate this into more detail.

Another promising target for specific anti-neutrophil therapy in ischemic stroke is the inhibition of NET formation. Initially known for their role in trapping and killing pathogens preventing systemic distribution [112], NETs have been shown to contribute to the pathogenesis of certain immune-related diseases [197]. In the ischemic brain tissue, NET formation is induced by various stimuli, among these also ROS production and release of DAMP molecules [190]. Following experimental stroke in mice, increased levels of extracellular chromatin can be measured. In conditions of sterile neutrophilia and septicemia, two DNA degrading enzymes, DNAse I and DNAse1-like 3 degraded NETs in the circulation and prevented intravascular NETs formed clots from obstructing blood vessels [198]. In the setting of ischemic stroke, treatment with recombinant DNAse I reduced infarct volumes and improved neurological symptoms [120]. In line with this observation, *Pad4*$^{-/-}$ mice, who are unable to release NETs, had smaller infarcts after tMCAO than the respective WT controls (Figure 3-14). To facilitate NETosis, citrullination of histones is essential to enable unwrapping of the DNA. Therefore, staining citrullinated histone 3 is a well-established marker for NETs. H3Cit positive cells could only be found in the ipsilateral hemisphere after tMCAO in WT mice, but not in the contralateral hemisphere or in the brain of *Pad4*$^{-/-}$ mice (Figure 3-14). These results indicate that NET formation is involved in the pathogenesis of I/R injury of the brain and might represent a selective new therapeutic target.

4.4 Establishment of a genetic mouse model to visualize platelet calcium signaling *in vivo*

Calcium is a ubiquitous second messenger that plays essential roles in excitable cells and signal transduction. In platelets, agonist-induced increase in cytosolic Ca^{2+} concentration is a common endpoint downstream of all receptor types and essential for platelet activation [24]. This renders the measurement of intracellular Ca^{2+} increase an ideal surrogate for platelet activation. First experiments to visualize changes in intracellular Ca^{2+} were performed using the Ca^{2+} sensitive bioluminescent protein aequorin that had to be directly injected into cells [199]. To allow non-invasive cell loading, Ca^{2+} sensitive dyes such as fura-2 and its modifications were developed [199]. The next big step in Ca^{2+} imaging was the introduction of genetically introduced Ca^{2+} indicators (GECIs). Nowadays, both, small-molecule calcium-sensitive dyes and GECIs are used to measure Ca^{2+} changes, but GECIs have the advantage of allowing chronic, noninvasive imaging of defined cells and compartments [200].

The single-fluorescent protein Ca^{2+} sensor GCaMP5G used in this study was developed from the predecessor GCaMP3 which enhanced sensitivity, Ca^{2+}-saturated brightness and Ca^{2+} affinity [200]. Here, mice expressing the GCaMP5G sensor specifically in platelets and megakaryocytes were generated by intercrossing the respective reporter mice (Polr2a$^{Tn(pb\text{-}CAG\text{-}GCaMP5g,\text{-}tdTomato)Tvrd}$, JAX Stock No. 024477) with mice expressing the Cre recombinase under the PF4 promotor. For simplicity, the resulting reporter mice were referred to as Kin mice. The genetic design of the generated mouse line allowed the visualization of sensor-bearing cells via the tdTomato signal also when calcium levels are low. This allowed the identification of activated and not activated platelets in situ, which is particularly important in the *in vivo* situation where numerous other cell types are present. Since calcium sequestration and buffering in platelets expressing the sensor might affect their function, this had to be excluded before using the Kin mice for further experiments. The presence of the sensor did not affect the expression of major glycoproteins on the platelet surface and platelet functionality was not impaired regarding platelet activation, aggregation and spreading (Figure 3-17 and Figure 3-18). Importantly, the sensor had no effect on the kinetics of intracellular Ca^{2+} flux, indicating that the sensor is not buffering Ca^{2+} levels in platelets. This is in line with previous studies using this reporter mouse with other Cre-systems and describing no influence of the sensor on the respective cellular function for example in neuronal cells [201]. Having confirmed an unaltered platelet function under static conditions, the response of the GCaMP5G sensor to platelet activation was tested under flow conditions. Collagen-induced platelet activation under intermediate shear resulted in Ca^{2+} mobilization which translated into bright GFP fluorescence of the reporter. Under conditions of high shear, platelet adhesion to the ECM is mediated by interactions of platelet GPIbα with vWF, however this interaction is not strong enough to induce platelet activation. Indeed, platelets that adhere to a vWF coated surface under high shear are not fully activated, which is reflected by their resting morphology and the very faint GFP signal from the sensor. When thrombin was perfused over these platelets after adhesion, emission of GFP signal indicated platelet activation. This underscores the power of the Kin mouse in enabling the visualization of Ca^{2+} flux in single platelets without any external manipulation of the cells. Since Ca^{2+} binding to the GCaMP sensors is rapid and reversible [202] also transient signals can potentially be visualized. Oscillating calcium signals have been reported to be important for stable platelet adhesion and thrombus growth [203]. Performing long-term imaging of Kin platelets during spreading on fibrinogen showed that, platelets exhibit several waves of intracellular Ca^{2+} increase and decrease throughout the spreading process until the final fully spread state is achieved (Figure 3-21). Being able to visualize this oscillation and repetitive Ca^{2+} waves affirm the newly generated reporter mouse line as valuable tool for the investigation of platelet calcium responses. Having proven the suitability of the reporter mouse for *in vitro* studies, we aimed to extent the use to the *in vivo* situation. Here, GECIs are highly beneficial. One of the major advantages of the endogenously expressed calcium indicator is the possibility to perform *in vivo* imaging without platelet transfusion of dye-loaded platelets or similar manipulations. Prior to platelet transfusion, multiple steps of platelet processing are needed. Here, each step bears the risk of platelet pre-activation and induction of alterations in platelet function. Transfused, exogenous platelets might behave differently within the recipient organism and are cleared faster from the circulation than endogenous platelets. The newly generated Kin mouse line overcomes all these limitations since no platelet transfusion is necessary to investigate Ca^{2+} signaling *in vivo*. In a model of arterial thrombosis, the Kin mouse proved to be a powerful tool to visualize Ca^{2+} mobilization in platelets during thrombus formation *in vivo* in the living animal (Figure 3-22). This ultimately confirmed the suitability of the Kin mice to study of Ca^{2+} signaling in platelets. Taken together the obtained results show that the newly generated platelet calcium reporter mouse line is a promising tool to image and record calcium responses in different stages of platelet activation either *in vitro, ex vivo* or *in vivo* without interfering with physiological platelet function. This mouse line will help to elucidate and characterize MK signaling and platelet responses in various pathological conditions.

4.5 A novel mechanism eliciting foudroyant venous (sinus) thrombosis via CLEC-2 and GPIIb/IIIa dependent platelet activation

Cerebral venous sinus thrombosis (CV(S)T) is a cause of stroke in young and middle-aged adults, with a sex-ratio towards women, which is primarily due to sex-specific risk factors of oral contraception, pregnancy and puerperium [10]. Recently, CVT came into public focus since cases of CVT were reported after SARS-CoV-2 virus infection or vaccination with the ChAdOx1 nCov-19 vaccine [126]. In this part of the thesis, it was discovered that the anti-CLEC-2 fab fragment, INU1-fab, induces a thrombotic syndrome in mice that mainly affects the brain vasculature, thus mimicking human CV(S)T. The *in vivo* effects are in stark contrast to the observation, that INU1-fab does not activate platelets *in vitro*. *In vivo* administration of INU1-fab induces heavy neurological symptoms characterized by a series of tonic-myoclonic seizures followed by exhaustion and lethargy ultimately leading to death (Figure 3-24). *In vivo*, all INU1 antibody derivatives induce a thrombocytopenia, however, upon INU1-fab injection the kinetics are slower, pointing to a different mechanism. The neurobehavioral symptoms together with the observed platelet consumption in INU1-fab treated mice suggest the brain as main injury site and point to thrombosis as potential mechanism. Cerebral thrombus formation upon INU1-fab injection could be confirmed in histological sections and in whole brain hemispheres using LSFM (Figure 3-25 and Figure 3-27). Using cryosections and intravital confocal microscopy revealed selective thrombus formation in the cerebral veins which correlates with the neurological symptoms. Injection of INU1-IgG leads to formation of small thrombi in the lung and platelet accumulation in the liver (Figure 3-28) but without inducing severe neurological symptoms or long-term impairments of the mice. This is in line with the rapid platelet clearance and the observed pulmonary problems of these mice directly after treatment. Using mice lacking CLEC-2 or CLEC-2 signaling in platelets it could be shown that CLEC-2 induced hemITAM signaling is an essential process in INU1-fab induced CVT. 'Classical' platelet-dependent thrombus formation involves a finely tuned sequence of different adhesion and activation receptors and release of secondary mediators. The GPIb-IX-V complex mediates platelet recruitment and is involved in arterial and venous thrombosis [15, 88, 204, 205]. For INU1-fab induced CVT however, GPIb seems to be of minor importance since blockade of GPIbα was only partially beneficial (Figure 3-30). Release of secondary mediators from platelet α- and dense granules upon platelet activation is an important amplifier of the activation response and promotes thrombus formation. *Unc13d*$^{-/-}$ mice lacking dense granule release and showing markedly decreased α-granule release [91] are protected from INU1-fab induced death but not from platelet consumption or neurological symptoms (Figure 3-30). This indicates that platelet activation and its amplification partly contribute to the pathology of INU1-fab induced CVT. In line with the partial protection using the blocking anti-GPIbα fab fragment or *Unc13d*$^{-/-}$ mice, classical platelet inhibitors, such as Clopidogrel or ASA, are also only partially protective and could not prevent INU1-fab induced lethality (Figure 3-32). Thrombin, the central protease of the coagulation system, is a powerful platelet activator and a key factor in the pathogenesis of thrombosis [158]. Heparin, a widely used indirect thrombin inhibitor, is currently the recommended first-line treatment for CVT [10, 205, 206]. However, neither prophylactic (pre-treatment of mice before INU1-fab) nor therapeutic (after symptom onset) heparin administration could protect mice from INU1-fab induced platelet consumption, neurological symptoms, and death (Figure 3-30 and Figure 3-31). This indicates that in the setting of CLEC-2 mediated CVT, thrombin is not directly involved in the central pathomechanism. Platelet activation, irrespective of the agonist, finally results in the shift of GPIIb/IIIa from a low affinity to a high affinity state (inside-out signaling) which enables efficient ligand binding and crosslinking of platelets to form aggregates. Ligand binding to GPIIb/IIIa induces signal transduction in the platelet (outside-in signaling) further contributing to platelet activation processes [207, 208]. Inhibition of GPIIb/IIIa is a very powerful strategy to inhibit platelet function and is routinely used in the setting of thrombotic complications in ischemic heart disease [209, 210]. Pretreatment of mice with the anti-GPIIb/IIIa JON/A-F(ab)$_2$ completely protects mice from any INU1-fab induced symptoms, platelet consumption and death. Impressively, GPIIb/IIIa blockade shortly after disease onset stopped disease progression, platelet consumption, thrombus formation and markedly increased survival of the treated animals. The fact that JON/A-F(ab)$_2$ treatment does not preventing INU1-IgG induced platelet clearance (Figure 3-30) indicates that fully (CLEC-2/ITAM)-activated platelets are cleared GPIIb/IIIa-independently. Together with the results obtained upon blockade of platelet activation (GPIbα-blockade, Clopidogrel, ASA) this suggests that the protection of GPIIb/IIIa blockade from INU1-fab induced CVT results from a different mechanism than solely inhibition of platelet activation. Hypothetically, INU1-fab could alter CLEC-2 confirmation and thereby facilitate the interaction with a so far unknown ligand being present predominantly in the cerebral veins with GPIIb/IIIa being required to mediate or stabilize this interaction. Although the selectivity for the cerebral venous system still needs to be determined, a systemic agonist triggering direct ITAM receptor clustering is unlikely to drive CVT since in the brains of INU1-IgG treated mice no signs of thrombosis could be detected. Likewise, anti-GPVI antibodies trigger ITAM-dependent platelet activation but do not induce cerebral thrombosis in mice [133, 211, 212]. The clinical picture induced by INU1-fab injection resembles the description of rapidly progressive CVT in young COVID patients [213, 214]. For arterial thrombosis, the critical contribution of platelets is known and widely accepted. For venous thrombosis, so far, coagulation was more in focus and anticoagulation the main therapeutic strategy. But there is increasing evidence that platelets also contribute to the formation of venous thrombi [205, 215, 216]. Recently, in patients who developed thrombotic thrombocytopenia and CV(S)T following COVID vaccination, activating antibodies against platelet factor 4 (PF4) have been detected [217-219]. These antibodies induce clustering of the ITAM-coupled Fc gamma receptor IIa (FcγR)IIa thereby triggering downstream signaling similar to that of CLEC-2 [28, 220]. FcγRIIa is not expressed in murine platelets [220], making it difficult to investigate a possible link to CVT in mouse models *in vivo*. To investigate the role of FcγR in human CVT humanized mouse models might be a valuable tool. Smith and colleagues developed a humanized mouse model where all murine FcγRs have been deleted and human FcγRs have been inserted into the mouse genome which leads to the full expression pattern of human FcγRs [221]. The results presented here, clearly show a contribution of CLEC-2 dependent (hem)ITAM signaling and pathological platelet activation as a possible trigger of CVT. Thus, CLEC-2 might be a so far overseen receptor contributing to pathological platelet activation leading to CVT, which should be further investigated and might be a new idea for selective targeting of thrombotic inflammatory diseases. The fact that only GPIIb/IIIa blockade but not classical platelet inhibition fully prevented the disease led to the conclusion that only the cooperative signaling of INU1-fab bound CLEC-2 and GPIIb/IIIa receptors triggered platelet activation in a way that resulted in foudroyant CVT. These results suggest, that Clopidogrel and ASA might be not as protective in acute CVT as GPIIb/IIIa blockers or inhibitors of CLEC-2/ITAM signaling.

However, targeting GPIIb/IIIa must be considered with care. Being beneficial in ischemic heart disease [209, 210] on the one hand, on the other hand detrimental side effects with severe bleeding complications are observed in the context of GPIIb/IIIa blockade in ischemic stroke [49, 50]. Further unraveling the exact mechanism and involved molecules would provide more specific therapeutic targets, decreasing the risk of side effects.

4.6 Concluding remarks and future perspectives

The findings presented in this thesis provide new insights in the role of platelets in the pathomechanism of ischemic stroke. It was shown that platelet aggregation and thrombus formation in the cerebral vasculature is not the reason for secondary infarct growth after recanalization. However, at later stages, thrombi can be detected within the infarcted territories of the brain. The reason and consequences of this late thrombus formation remains to be investigated. Here, long-term experiments observing mice for more than 24 h after tMCAO might help to elucidate if thrombi are maybe contributing to tissue remodeling and resolution of the inflammation. Although it is not thrombus formation that causes infarct growth during the reperfusion phase, it could be single platelets interacting for example with immune cells that obstruct the microcirculation. To elucidate the contribution of other platelet receptors or the interaction with immune cells, further *in vivo* and *ex vivo* experiments are needed. To this end, the newly established calcium reporter mouse line is beneficial and can be used to observe platelet activation within the brain vasculature following tMCAO. As shown in the second part of this thesis, platelet activation, especially α-dense granule secretion is an essential contributor to BBB breakdown in the early reperfusion phase. The discovery of platelet derived PDGF being harmful to brain endothelial cells links platelet activation to stroke progression and offers room for numerous further investigations. Analysis of the respective platelet specific PDGF knockout mouse in experimental stroke models will help to transfer and expand the observed effects to the *in vivo* situation. Improving the *in vitro* model of the BBB by co-culturing endothelial cells with other cells of the neurovascular unit, such as pericytes or astrocytes is needed for a better reconstruction of the *in vivo* situation and being able to consider more contributing factors. To test whether the effect of PDGF on murine endothelial cells is also true for the human situation, *in vitro* models of the human BBB are a good tool for further experiments. Knowing that platelet activation and granule release is contributing to endothelial damage, the platelet activating stimulus at sites of BBB breakdown still remains elusive and needs to be identified. Again, the use of the newly established calcium reporter mouse in appropriate *in vivo* experiments offers the possibility to identify time point and site of platelet activation during disease progression.

The role of neutrophils in ischemic stroke is still not understood and controversially discussed. Depletion of peripheral neutrophils had no effect on neurological outcome following experimental stroke. However, abolishing NET formation was beneficial, whereas defective NADPH-dependent ROS production was not. This confirmed the assumption of a double-sided effect of potentially beneficial and detrimental roles of neutrophils that are balanced out by complete depletion and therefore need more specific investigation. In this study it was shown that NET-formation worsens stroke outcome, but the underlying mechanisms are elusive. Studies investigating the trigger of NET-formation might help to reveal the spatio-temporal sequence of neutrophil activation. Regarding ROS production, a potential compensation of NADPH-deficiency with NADPH-independent ROS production might restore brain damage in the Ncf1 knockout mice. This needs to be investigated in additional experiments. An impact of platelets on neutrophil function by forming platelet-neutrophil complexes can be investigated in *in vitro* experiments. Using platelets of the established calcium reporter mice in this setting, allows the visualization of platelet activation in the presence of neutrophils.

This thesis establishes cerebral venous thrombus formation as cause for the severe neurological symptoms upon injection of fab fragments of the anti-CLEC2 antibody INU1. Despite showing an essential contribution of GPIIb/IIIa, this study could not provide detailed mechanistic insights regarding the nature of the contribution. Here further studies are needed and establishing an appropriate *in vitro* system would be highly beneficial. However, this is also very challenging, since so far in none of the tested *in vitro* assays, effects of INU1-fab were detectable. Moreover, the reason for specificity of thrombus formation in the venous system is not clear yet and requires additional investigations.

5 References

1. Virani, S.S., et al., Heart Disease and Stroke Statistics-2020 Update: A Report From the American Heart Association. *Circulation*, 2020. **141**(9): p. e139-e596 doi: 10.1161/CIR.0000000000000757.
2. Wafa, H.A., et al., Burden of Stroke in Europe: Thirty-Year Projections of Incidence, Prevalence, Deaths, and Disability-Adjusted Life Years. *Stroke*, 2020. **51**(8): p. 2418-2427 doi: 10.1161/STROKEAHA.120.029606.
3. Conn, P., *Neuroscience in Medicine*. 2003.
4. Purves D, A.G., Fitzpatrick D, et al., editors, *The Blood Supply of the Brain and Spinal Cord. Available from: https://www.ncbi.nlm.nih.gov/books/NBK11042/*. 2001: Sunderland (MA): Sinauer Associates.
5. El Amki, M. and S. Wegener, Improving Cerebral Blood Flow after Arterial Recanalization: A Novel Therapeutic Strategy in Stroke. *Int J Mol Sci*, 2017. **18**(12)doi: 10.3390/ijms18122669.
6. Shuaib, A., et al., Collateral blood vessels in acute ischaemic stroke: a potential therapeutic target. *Lancet Neurol*, 2011. **10**(10): p. 909-921 doi: 10.1016/S1474-4422(11)70195-8.
7. Kawano, H., et al., Relationship Between Collateral Status, Contrast Transit, and Contrast Density in Acute Ischemic Stroke. *Stroke*, 2016. **47**(3): p. 742-749 doi: 10.1161/STROKEAHA.115.011320.
8. Kilic, T. and A. Akakin, Anatomy of cerebral veins and sinuses. *Front Neurol Neurosci*, 2008. **23**: p. 4-15 doi: 10.1159/000111256.
9. Uddin, M.A., T.U. Haq, and M.Z. Rafique, Cerebral venous system anatomy. *J Pak Med Assoc*, 2006. **56**(11): p. 516-519 doi.
10. Silvis, S.M., et al., Cerebral venous thrombosis. *Nat Rev Neurol*, 2017. **13**(9): p. 555-565 doi: 10.1038/nrneurol.2017.104.
11. Herculano-Houzel, S., et al., Mammalian Brains Are Made of These: A Dataset of the Numbers and Densities of Neuronal and Nonneuronal Cells in the Brain of Glires, Primates, Scandentia, Eulipotyphlans, Afrotherians and Artiodactyls, and Their Relationship with Body Mass. *Brain Behav Evol*, 2015. **86**(3-4): p. 145-163 doi: 10.1159/000437413.
12. Todorov, M.I., et al., Machine learning analysis of whole mouse brain vasculature. *Nat Methods*, 2020. **17**(4): p. 442-449 doi: 10.1038/s41592-020-0792-1.
13. Shih, A.Y., et al., The smallest stroke: occlusion of one penetrating vessel leads to infarction and a cognitive deficit. *Nat Neurosci*, 2013. **16**(1): p. 55-63 doi: 10.1038/nn.3278.
14. Italiano, J.E., Jr., S. Patel-Hett, and J.H. Hartwig, Mechanics of proplatelet elaboration. *Journal of thrombosis and haemostasis : JTH*, 2007. **5 Suppl 1**: p. 18-23 doi: 10.1111/j.1538-7836.2007.02487.x.
15. Stegner, D. and B. Nieswandt, Platelet receptor signaling in thrombus formation. *J Mol Med (Berl)*, 2011. **89**(2): p. 109-121 doi: 10.1007/s00109-010-0691-5.
16. Savage, B., F. Almus-Jacobs, and Z.M. Ruggeri, Specific synergy of multiple substrate-receptor interactions in platelet thrombus formation under flow. *Cell*, 1998. **94**(5): p. 657-666 doi.
17. Canobbio, I., C. Balduini, and M. Torti, Signalling through the platelet glycoprotein Ib-V-IX complex. *Cellular signalling*, 2004. **16**(12): p. 1329-1344 doi: 10.1016/j.cellsig.2004.05.008.

18. Offermanns, S., Activation of platelet function through G protein-coupled receptors. *Circulation research*, 2006. **99**(12): p. 1293-1304 doi: 10.1161/01.RES.0000251742.71301.16.

19. Varga-Szabo, D., I. Pleines, and B. Nieswandt, Cell adhesion mechanisms in platelets. *Arterioscler Thromb Vasc Biol*, 2008. **28**(3): p. 403-412 doi: 10.1161/ATVBAHA.107.150474.

20. Ruggeri, Z.M., J.A. Dent, and E. Saldivar, Contribution of distinct adhesive interactions to platelet aggregation in flowing blood. *Blood*, 1999. **94**(1): p. 172-178 doi.

21. Blair, P. and R. Flaumenhaft, Platelet alpha-granules: basic biology and clinical correlates. *Blood Rev*, 2009. **23**(4): p. 177-189 doi: 10.1016/j.blre.2009.04.001.

22. King, S.M. and G.L. Reed, Development of platelet secretory granules. *Semin Cell Dev Biol*, 2002. **13**(4): p. 293-302 doi: 10.1016/s1084952102000599.

23. Rendu, F. and B. Brohard-Bohn, The platelet release reaction: granules' constituents, secretion and functions. *Platelets*, 2001. **12**(5): p. 261-273 doi: 10.1080/09537100120068170.

24. Varga-Szabo, D., A. Braun, and B. Nieswandt, Calcium signaling in platelets. *J Thromb Haemost*, 2009. **7**(7): p. 1057-1066 doi: 10.1111/j.1538-7836.2009.03455.x.

25. Love, P.E. and S.M. Hayes, ITAM-mediated signaling by the T-cell antigen receptor. *Cold Spring Harb Perspect Biol*, 2010. **2**(6): p. a002485 doi: 10.1101/cshperspect.a002485.

26. Bergmeier, W. and L. Stefanini, Platelet ITAM signaling. *Curr Opin Hematol*, 2013. **20**(5): p. 445-450 doi: 10.1097/MOH.0b013e3283642267.

27. Suzuki-Inoue, K., M. Osada, and Y. Ozaki, Physiologic and pathophysiologic roles of interaction between C-type lectin-like receptor 2 and podoplanin: partners from in utero to adulthood. *J Thromb Haemost*, 2017. **15**(2): p. 219-229 doi: 10.1111/jth.13590.

28. Stegner, D., E.J. Haining, and B. Nieswandt, Targeting glycoprotein VI and the immunoreceptor tyrosine-based activation motif signaling pathway. *Arterioscler Thromb Vasc Biol*, 2014. **34**(8): p. 1615-1620 doi: 10.1161/ATVBAHA.114.303408.

29. Severin, S., et al., Syk-dependent phosphorylation of CLEC-2: a novel mechanism of hem-immunoreceptor tyrosine-based activation motif signaling. *The Journal of biological chemistry*, 2011. **286**(6): p. 4107-4116 doi: 10.1074/jbc.M110.167502.

30. Nieswandt, B. and S.P. Watson, Platelet-collagen interaction: is GPVI the central receptor? *Blood*, 2003. **102**(2): p. 449-461 doi: 10.1182/blood-2002-12-3882.

31. Watson, S.P., J.M. Herbert, and A.Y. Pollitt, GPVI and CLEC-2 in hemostasis and vascular integrity. *J Thromb Haemost*, 2010. **8**(7): p. 1456-1467 doi: 10.1111/j.1538-7836.2010.03875.x.

32. Lorenz, V., et al., Targeted downregulation of platelet CLEC-2 occurs through Syk-independent internalization. *Blood*, 2015. **125**(26): p. 4069-4077 doi: 10.1182/blood-2014-11-611905.

33. Hughes, C.E., et al., CLEC-2 activates Syk through dimerization. *Blood*, 2010. **115**(14): p. 2947-2955 doi: 10.1182/blood-2009-08-237834.

34. Allen, C.L. and U. Bayraktutan, Risk factors for ischaemic stroke. *Int J Stroke*, 2008. **3**(2): p. 105-116 doi: 10.1111/j.1747-4949.2008.00187.x.

35. Bogousslavsky, J., G. Van Melle, and F. Regli, The Lausanne Stroke Registry: analysis of 1,000 consecutive patients with first stroke. *Stroke*, 1988. **19**(9): p. 1083-1092 doi: 10.1161/01.str.19.9.1083.

36. Puyal, J., V. Ginet, and P.G. Clarke, Multiple interacting cell death mechanisms in the mediation of excitotoxicity and ischemic brain damage: a challenge for neuroprotection. *Prog Neurobiol*, 2013. **105**: p. 24-48 doi: 10.1016/j.pneurobio.2013.03.002.

37. Manning, N.W., et al., Acute ischemic stroke: time, penumbra, and reperfusion. *Stroke*, 2014. **45**(2): p. 640-644 doi: 10.1161/STROKEAHA.113.003798.

38. Saver, J.L., Time is brain--quantified. *Stroke*, 2006. **37**(1): p. 263-266 doi: 10.1161/01.STR.0000196957.55928.ab.

39. National Institute of Neurological, D. and P.A.S.S.G. Stroke rt, Tissue plasminogen activator for acute ischemic stroke. *N Engl J Med*, 1995. **333**(24): p. 1581-1587 doi: 10.1056/NEJM199512143332401.

40. Gravanis, I. and S.E. Tsirka, Tissue-type plasminogen activator as a therapeutic target in stroke. *Expert Opin Ther Targets*, 2008. **12**(2): p. 159-170 doi: 10.1517/14728222.12.2.159.

41. Campbell, B.C.V., et al., Ischaemic stroke. *Nat Rev Dis Primers*, 2019. **5**(1): p. 70 doi: 10.1038/s41572-019-0118-8.

42. Catanese, L., J. Tarsia, and M. Fisher, Acute Ischemic Stroke Therapy Overview. *Circ Res*, 2017. **120**(3): p. 541-558 doi: 10.1161/CIRCRESAHA.116.309278.

43. Liaw, N. and D. Liebeskind, Emerging therapies in acute ischemic stroke. *F1000Res*, 2020. **9**doi: 10.12688/f1000research.21100.1.

44. Espinosa de Rueda, M., et al., Combined Multimodal Computed Tomography Score Correlates With Futile Recanalization After Thrombectomy in Patients With Acute Stroke. *Stroke*, 2015. **46**(9): p. 2517-2522 doi: 10.1161/STROKEAHA.114.008598.

45. Zhu, Z., et al., Combination of the Immune Modulator Fingolimod With Alteplase in Acute Ischemic Stroke: A Pilot Trial. *Circulation*, 2015. **132**(12): p. 1104-1112 doi: 10.1161/CIRCULATIONAHA.115.016371.

46. Stoll, G. and B. Nieswandt, Thrombo-inflammation in acute ischaemic stroke - implications for treatment. *Nat Rev Neurol*, 2019. **15**(8): p. 473-481 doi: 10.1038/s41582-019-0221-1.

47. Nour, M., F. Scalzo, and D.S. Liebeskind, Ischemia-reperfusion injury in stroke. *Interv Neurol*, 2013. **1**(3-4): p. 185-199 doi: 10.1159/000353125.

48. Qureshi, A.I., et al., Reocclusion of recanalized arteries during intra-arterial thrombolysis for acute ischemic stroke. *AJNR Am J Neuroradiol*, 2004. **25**(2): p. 322-328 doi.

49. Kleinschnitz, C., et al., Targeting platelets in acute experimental stroke: impact of glycoprotein Ib, VI, and IIb/IIIa blockade on infarct size, functional outcome, and intracranial bleeding. *Circulation*, 2007. **115**(17): p. 2323-2330 doi: 10.1161/CIRCULATIONAHA.107.691279.

50. Adams, H.P., Jr., et al., Emergency administration of abciximab for treatment of patients with acute ischemic stroke: results of an international phase III trial: Abciximab in Emergency Treatment of Stroke Trial (AbESTT-II). *Stroke*, 2008. **39**(1): p. 87-99 doi: 10.1161/STROKEAHA.106.476648.

51. Kellert, L., et al., Endovascular stroke therapy: tirofiban is associated with risk of fatal intracerebral hemorrhage and poor outcome. *Stroke*, 2013. **44**(5): p. 1453-1455 doi: 10.1161/STROKEAHA.111.000502.

52. Fluri, F., M.K. Schuhmann, and C. Kleinschnitz, Animal models of ischemic stroke and their application in clinical research. *Drug Des Devel Ther*, 2015. **9**: p. 3445-3454 doi: 10.2147/DDDT.S56071.

53. Braeuninger, S., et al., Focal cerebral ischemia. *Methods Mol Biol*, 2012. **788**: p. 29-42 doi: 10.1007/978-1-61779-307-3_3.

54. Stegner, D., V. Klaus, and B. Nieswandt, Platelets as Modulators of Cerebral Ischemia/Reperfusion Injury. *Front Immunol*, 2019. **10**: p. 2505 doi: 10.3389/fimmu.2019.02505.

55. Nieswandt, B., C. Kleinschnitz, and G. Stoll, Ischaemic stroke: a thrombo-inflammatory disease? *J Physiol*, 2011. **589**(17): p. 4115-4123 doi: 10.1113/jphysiol.2011.212886.

56. Stamatovic, S.M., R.F. Keep, and A.V. Andjelkovic, Brain endothelial cell-cell junctions: how to "open" the blood brain barrier. *Curr Neuropharmacol*, 2008. **6**(3): p. 179-192 doi: 10.2174/157015908785777210.

57. Butt, A.M., H.C. Jones, and N.J. Abbott, Electrical resistance across the blood-brain barrier in anaesthetized rats: a developmental study. *J Physiol*, 1990. **429**: p. 47-62 doi: 10.1113/jphysiol.1990.sp018243.

58. McConnell, H.L., et al., The Translational Significance of the Neurovascular Unit. *J Biol Chem*, 2017. **292**(3): p. 762-770 doi: 10.1074/jbc.R116.760215.

59. Daneman, R. and A. Prat, The blood-brain barrier. *Cold Spring Harb Perspect Biol*, 2015. **7**(1): p. a020412 doi: 10.1101/cshperspect.a020412.

60. Abbott, N.J., Blood-brain barrier structure and function and the challenges for CNS drug delivery. *J Inherit Metab Dis*, 2013. **36**(3): p. 437-449 doi: 10.1007/s10545-013-9608-0.

61. Abdullahi, W., D. Tripathi, and P.T. Ronaldson, Blood-brain barrier dysfunction in ischemic stroke: targeting tight junctions and transporters for vascular protection. *Am J Physiol Cell Physiol*, 2018. **315**(3): p. C343-C356 doi: 10.1152/ajpcell.00095.2018.

62. Ronaldson, P.T. and T.P. Davis, Blood-brain barrier integrity and glial support: mechanisms that can be targeted for novel therapeutic approaches in stroke. *Curr Pharm Des*, 2012. **18**(25): p. 3624-3644 doi: 10.2174/138161212802002625.

63. Haseloff, R.F., et al., Transmembrane proteins of the tight junctions at the blood-brain barrier: structural and functional aspects. *Semin Cell Dev Biol*, 2015. **38**: p. 16-25 doi: 10.1016/j.semcdb.2014.11.004.

64. Fanning, A.S., et al., The tight junction protein ZO-1 establishes a link between the transmembrane protein occludin and the actin cytoskeleton. *J Biol Chem*, 1998. **273**(45): p. 29745-29753 doi: 10.1074/jbc.273.45.29745.

65. Lampugnani, M.G. and E. Dejana, Adherens junctions in endothelial cells regulate vessel maintenance and angiogenesis. *Thromb Res*, 2007. **120 Suppl 2**: p. S1-6 doi: 10.1016/S0049-3848(07)70124-X.

66. Williams, M.J., et al., Cadherin-10 is a novel blood-brain barrier adhesion molecule in human and mouse. *Brain Res*, 2005. **1058**(1-2): p. 62-72 doi: 10.1016/j.brainres.2005.07.078.

67. Meng, W. and M. Takeichi, Adherens junction: molecular architecture and regulation. *Cold Spring Harb Perspect Biol*, 2009. **1**(6): p. a002899 doi: 10.1101/cshperspect.a002899.

68. Bell, A.H., et al., The Neurovascular Unit: Effects of Brain Insults During the Perinatal Period. *Front Neurosci*, 2019. **13**: p. 1452 doi: 10.3389/fnins.2019.01452.

69. Muoio, V., P.B. Persson, and M.M. Sendeski, The neurovascular unit - concept review. *Acta Physiol (Oxf)*, 2014. **210**(4): p. 790-798 doi: 10.1111/apha.12250.

70. Sweeney, M.D., A.P. Sagare, and B.V. Zlokovic, Cerebrospinal fluid biomarkers of neurovascular dysfunction in mild dementia and Alzheimer's disease. *J Cereb Blood Flow Metab*, 2015. **35**(7): p. 1055-1068 doi: 10.1038/jcbfm.2015.76.

71. Brouns, R., et al., Biochemical markers for blood-brain barrier dysfunction in acute ischemic stroke correlate with evolution and outcome. *Eur Neurol*, 2011. **65**(1): p. 23-31 doi: 10.1159/000321965.

72. Zhang, W., et al., The blood brain barrier in cerebral ischemic injury – Disruption and repair. *Brain Hemorrhages*, 2020. **1**(1): p. 34-53 doi: https://doi.org/10.1016/j.hest.2019.12.004.

73. Nadareishvili, Z., et al., Post-Stroke Blood-Brain Barrier Disruption and Poor Functional Outcome in Patients Receiving Thrombolytic Therapy. *Cerebrovasc Dis*, 2019. **47**(3-4): p. 135-142 doi: 10.1159/000499666.

74. Nagaraja, T.N., et al., Acute leakage patterns of fluorescent plasma flow markers after transient focal cerebral ischemia suggest large openings in blood-brain barrier. *Microcirculation*, 2008. **15**(1): p. 1-14 doi: 10.1080/10739680701409811.

75. Hoffmann, A., et al., Early Blood-Brain Barrier Disruption in Ischemic Stroke Initiates Multifocally Around Capillaries/Venules. *Stroke*, 2018. **49**(6): p. 1479-1487 doi: 10.1161/STROKEAHA.118.020927.

76. Shi, Y., et al., Rapid endothelial cytoskeletal reorganization enables early blood-brain barrier disruption and long-term ischaemic reperfusion brain injury. *Nat Commun*, 2016. **7**: p. 10523 doi: 10.1038/ncomms10523.

77. Jiao, H., et al., Specific role of tight junction proteins claudin-5, occludin, and ZO-1 of the blood-brain barrier in a focal cerebral ischemic insult. *J Mol Neurosci*, 2011. **44**(2): p. 130-139 doi: 10.1007/s12031-011-9496-4.

78. Radak, D., I. Resanovic, and E.R. Isenovic, Link between oxidative stress and acute brain ischemia. *Angiology*, 2014. **65**(8): p. 667-676 doi: 10.1177/0003319713506516.

79. Gelderblom, M., et al., Temporal and spatial dynamics of cerebral immune cell accumulation in stroke. *Stroke*, 2009. **40**(5): p. 1849-1857 doi: 10.1161/STROKEAHA.108.534503.

80. Xiang, J., et al., Mechanisms Underlying Astrocyte Endfeet Swelling in Stroke. *Acta Neurochir Suppl*, 2016. **121**: p. 19-22 doi: 10.1007/978-3-319-18497-5_4.

81. Fernandez-Klett, F., et al., Early loss of pericytes and perivascular stromal cell-induced scar formation after stroke. *J Cereb Blood Flow Metab*, 2013. **33**(3): p. 428-439 doi: 10.1038/jcbfm.2012.187.

82. Pham, M., et al., Sustained reperfusion after blockade of glycoprotein-receptor-Ib in focal cerebral ischemia: an MRI study at 17.6 Tesla. *PLoS One*, 2011. **6**(4): p. e18386 doi: 10.1371/journal.pone.0018386.

83. De Meyer, S.F., et al., Platelet glycoprotein Ibalpha is an important mediator of ischemic stroke in mice. *Exp Transl Stroke Med*, 2011. **3**: p. 9 doi: 10.1186/2040-7378-3-9.

84. Kleinschnitz, C., et al., Deficiency of von Willebrand factor protects mice from ischemic stroke. *Blood*, 2009. **113**(15): p. 3600-3603 doi: 10.1182/blood-2008-09-180695.

85. Stegner, D., et al., Pharmacological inhibition of phospholipase D protects mice from occlusive thrombus formation and ischemic stroke--brief report. *Arterioscler Thromb Vasc Biol*, 2013. **33**(9): p. 2212-2217 doi: 10.1161/ATVBAHA.113.302030.

86. Thielmann, I., et al., Redundant functions of phospholipases D1 and D2 in platelet alpha-granule release. *J Thromb Haemost*, 2012. **10**(11): p. 2361-2372 doi: 10.1111/j.1538-7836.2012.04924.x.

87. van Eeuwijk, J.M., et al., The Novel Oral Syk Inhibitor, Bl1002494, Protects Mice From Arterial Thrombosis and Thromboinflammatory Brain Infarction. *Arterioscler Thromb Vasc Biol*, 2016. **36**(6): p. 1247-1253 doi: 10.1161/ATVBAHA.115.306883.

88. Massberg, S., et al., A crucial role of glycoprotein VI for platelet recruitment to the injured arterial wall in vivo. *J Exp Med*, 2003. **197**(1): p. 41-49 doi: 10.1084/jem.20020945.

89. Goebel, S., et al., The GPVI-Fc fusion protein Revacept improves cerebral infarct volume and functional outcome in stroke. *PLoS One*, 2013. **8**(7): p. e66960 doi: 10.1371/journal.pone.0066960.

90. Coller, B.S., Anti-GPIIb/IIIa drugs: current strategies and future directions. *Thromb Haemost*, 2001. **86**(1): p. 427-443 doi.

91. Stegner, D., et al., Munc13-4-mediated secretion is essential for infarct progression but not intracranial hemostasis in acute stroke. *J Thromb Haemost*, 2013. **11**(7): p. 1430-1433 doi: 10.1111/jth.12293.

92. Yamauchi, K., et al., Effects of ticagrelor in a mouse model of ischemic stroke. *Sci Rep*, 2017. **7**(1): p. 12088 doi: 10.1038/s41598-017-12205-w.

93. Deppermann, C., et al., Gray platelet syndrome and defective thrombo-inflammation in Nbeal2-deficient mice. *J Clin Invest*, 2013doi: 10.1172/JCI69210.

94. Sowerby, J.M., et al., NBEAL2 is required for neutrophil and NK cell function and pathogen defense. *J Clin Invest*, 2017. **127**(9): p. 3521-3526 doi: 10.1172/JCI91684.

95. Deppermann, C., et al., Platelet secretion is crucial to prevent bleeding in the ischemic brain but not in the inflamed skin or lung in mice. *Blood*, 2017. **129**(12): p. 1702-1706 doi: 10.1182/blood-2016-12-750711.

96. Morowski, M., et al., Only severe thrombocytopenia results in bleeding and defective thrombus formation in mice. *Blood*, 2013. **121**(24): p. 4938-4947 doi: 10.1182/blood-2012-10-461459.

97. Yilmaz, G. and D.N. Granger, Leukocyte recruitment and ischemic brain injury. *Neuromolecular Med*, 2010. **12**(2): p. 193-204 doi: 10.1007/s12017-009-8074-1.

98. Iadecola, C., M.S. Buckwalter, and J. Anrather, Immune responses to stroke: mechanisms, modulation, and therapeutic potential. *J Clin Invest*, 2020. **130**(6): p. 2777-2788 doi: 10.1172/JCI135530.

99. Garcia, J.H., et al., Influx of leukocytes and platelets in an evolving brain infarct (Wistar rat). *Am J Pathol*, 1994. **144**(1): p. 188-199 doi.

100. Strecker, J.K., et al., Neutrophil granulocytes in cerebral ischemia - Evolution from killers to key players. *Neurochem Int*, 2017. **107**: p. 117-126 doi: 10.1016/j.neuint.2016.11.006.

101. Buck, B.H., et al., Early neutrophilia is associated with volume of ischemic tissue in acute stroke. *Stroke*, 2008. **39**(2): p. 355-360 doi: 10.1161/STROKEAHA.107.490128.

102. Planas, A.M., Role of Immune Cells Migrating to the Ischemic Brain. *Stroke*, 2018. **49**(9): p. 2261-2267 doi: 10.1161/STROKEAHA.118.021474.

103. del Zoppo, G.J., et al., Polymorphonuclear leukocytes occlude capillaries following middle cerebral artery occlusion and reperfusion in baboons. *Stroke*, 1991. **22**(10): p. 1276-1283 doi: 10.1161/01.str.22.10.1276.

104. El Amki, M., et al., Neutrophils Obstructing Brain Capillaries Are a Major Cause of No-Reflow in Ischemic Stroke. *Cell Rep*, 2020. **33**(2): p. 108260 doi: 10.1016/j.celrep.2020.108260.

105. Jickling, G.C., et al., Targeting neutrophils in ischemic stroke: translational insights from experimental studies. *J Cereb Blood Flow Metab*, 2015. **35**(6): p. 888-901 doi: 10.1038/jcbfm.2015.45.

106. Enzmann, G., et al., The neurovascular unit as a selective barrier to polymorphonuclear granulocyte (PMN) infiltration into the brain after ischemic injury. *Acta Neuropathol*, 2013. **125**(3): p. 395-412 doi: 10.1007/s00401-012-1076-3.

107. Zrzavy, T., et al., Dominant role of microglial and macrophage innate immune responses in human ischemic infarcts. *Brain Pathol*, 2018. **28**(6): p. 791-805 doi: 10.1111/bpa.12583.

108. Perez-de-Puig, I., et al., Neutrophil recruitment to the brain in mouse and human ischemic stroke. *Acta Neuropathol*, 2015. **129**(2): p. 239-257 doi: 10.1007/s00401-014-1381-0.

109. Rodrigo, R., et al., Oxidative stress and pathophysiology of ischemic stroke: novel therapeutic opportunities. *CNS Neurol Disord Drug Targets*, 2013. **12**(5): p. 698-714 doi: 10.2174/1871527311312050015.

110. El-Benna, J., et al., p47phox, the phagocyte NADPH oxidase/NOX2 organizer: structure, phosphorylation and implication in diseases. *Exp Mol Med*, 2009. **41**(4): p. 217-225 doi: 10.3858/emm.2009.41.4.058.

111. Kahles, T., et al., NADPH oxidase plays a central role in blood-brain barrier damage in experimental stroke. *Stroke*, 2007. **38**(11): p. 3000-3006 doi: 10.1161/STROKEAHA.107.489765.

112. Brinkmann, V., et al., Neutrophil extracellular traps kill bacteria. *Science*, 2004. **303**(5663): p. 1532-1535 doi: 10.1126/science.1092385.

113. Bonaventura, A., et al., The Pathophysiological Role of Neutrophil Extracellular Traps in Inflammatory Diseases. *Thromb Haemost*, 2018. **118**(1): p. 6-27 doi: 10.1160/TH17-09-0630.

114. Lewis, H.D., et al., Inhibition of PAD4 activity is sufficient to disrupt mouse and human NET formation. *Nat Chem Biol*, 2015. **11**(3): p. 189-191 doi: 10.1038/nchembio.1735.

115. Li, P., et al., PAD4 is essential for antibacterial innate immunity mediated by neutrophil extracellular traps. *J Exp Med*, 2010. **207**(9): p. 1853-1862 doi: 10.1084/jem.20100239.

116. Rohrbach, A.S., et al., Activation of PAD4 in NET formation. *Front Immunol*, 2012. **3**: p. 360 doi: 10.3389/fimmu.2012.00360.

117. Yang, M.L., et al., Citrullination and PAD Enzyme Biology in Type 1 Diabetes - Regulators of Inflammation, Autoimmunity, and Pathology. *Front Immunol*, 2021. **12**: p. 678953 doi: 10.3389/fimmu.2021.678953.

118. Laridan, E., et al., Neutrophil extracellular traps in ischemic stroke thrombi. *Ann Neurol*, 2017. **82**(2): p. 223-232 doi: 10.1002/ana.24993.

119. Geiger, S., et al., Nucleosomes in serum of patients with early cerebral stroke. *Cerebrovasc Dis*, 2006. **21**(1-2): p. 32-37 doi: 10.1159/000089591.

120. De Meyer, S.F., et al., Extracellular chromatin is an important mediator of ischemic stroke in mice. *Arterioscler Thromb Vasc Biol*, 2012. **32**(8): p. 1884-1891 doi: 10.1161/ATVBAHA.112.250993.

121. Stam, J., Thrombosis of the cerebral veins and sinuses. *N Engl J Med*, 2005. **352**(17): p. 1791-1798 doi: 10.1056/NEJMra042354.

122. Coutinho, J.M., et al., The incidence of cerebral venous thrombosis: a cross-sectional study. *Stroke*, 2012. **43**(12): p. 3375-3377 doi: 10.1161/STROKEAHA.112.671453.

123. Devasagayam, S., et al., Cerebral Venous Sinus Thrombosis Incidence Is Higher Than Previously Thought: A Retrospective Population-Based Study. *Stroke*, 2016. **47**(9): p. 2180-2182 doi: 10.1161/STROKEAHA.116.013617.

124. Bousser, M.G. and J.M. Ferro, Cerebral venous thrombosis: an update. *Lancet Neurol*, 2007. **6**(2): p. 162-170 doi: 10.1016/S1474-4422(07)70029-7.

125. Ferro, J.M. and D. Aguiar de Sousa, Cerebral Venous Thrombosis: an Update. *Curr Neurol Neurosci Rep*, 2019. **19**(10): p. 74 doi: 10.1007/s11910-019-0988-x.

126. Taquet, M., et al., Cerebral venous thrombosis and portal vein thrombosis: A retrospective cohort study of 537,913 COVID-19 cases. *EClinicalMedicine*, 2021. **39**: p. 101061 doi: 10.1016/j.eclinm.2021.101061.

127. Yenigun, M., et al., Sinus thrombosis-do animal models really cover the clinical syndrome? *Ann Transl Med*, 2015. **3**(10): p. 138 doi: 10.3978/j.issn.2305-5839.2015.05.14.

128. May, F., et al., CLEC-2 is an essential platelet-activating receptor in hemostasis and thrombosis. *Blood*, 2009. **114**(16): p. 3464-3472 doi: 10.1182/blood-2009-05-222273.

129. Gruner, S., et al., Multiple integrin-ligand interactions synergize in shear-resistant platelet adhesion at sites of arterial injury in vivo. *Blood*, 2003. **102**(12): p. 4021-4027 doi: 10.1182/blood-2003-05-1391.

130. Zehentmeier, S., et al., Static and dynamic components synergize to form a stable survival niche for bone marrow plasma cells. *Eur J Immunol*, 2014. **44**(8): p. 2306-2317 doi: 10.1002/eji.201344313.

131. Nieswandt, B., et al., Identification of critical antigen-specific mechanisms in the development of immune thrombocytopenic purpura in mice. *Blood*, 2000. **96**(7): p. 2520-2527 doi.

132. Unkeless, J.C., Characterization of a monoclonal antibody directed against mouse macrophage and lymphocyte Fc receptors. *J Exp Med*, 1979. **150**(3): p. 580-596 doi: 10.1084/jem.150.3.580.

133. Nieswandt, B., et al., Long-term antithrombotic protection by in vivo depletion of platelet glycoprotein VI in mice. *J Exp Med*, 2001. **193**(4): p. 459-469 doi: 10.1084/jem.193.4.459.

134. Bergmeier, W., et al., Flow cytometric detection of activated mouse integrin alphaIIbbeta3 with a novel monoclonal antibody. *Cytometry*, 2002. **48**(2): p. 80-86 doi: 10.1002/cyto.10114.

135. Hofmann, S., et al., The SLAM family member CD84 is regulated by ADAM10 and calpain in platelets. *J Thromb Haemost*, 2012. **10**(12): p. 2581-2592 doi: 10.1111/jth.12013.

136. Nieswandt, B., et al., Expression and function of the mouse collagen receptor glycoprotein VI is strictly dependent on its association with the FcRgamma chain. *J Biol Chem*, 2000. **275**(31): p. 23998-24002 doi: 10.1074/jbc.M003803200.

137. Slaba, I., et al., Imaging the dynamic platelet-neutrophil response in sterile liver injury and repair in mice. *Hepatology*, 2015. **62**(5): p. 1593-1605 doi: 10.1002/hep.28003.

138. Haining, E.J., et al., CLEC-2 contributes to hemostasis independently of classical hemITAM signaling in mice. *Blood*, 2017. **130**(20): p. 2224-2228 doi: 10.1182/blood-2017-03-771907.

139. Ruck, T., et al., Isolation of primary murine brain microvascular endothelial cells. *J Vis Exp*, 2014(93): p. e52204 doi: 10.3791/52204.

140. Amich, J., et al., Three-Dimensional Light Sheet Fluorescence Microscopy of Lungs To Dissect Local Host Immune-Aspergillus fumigatus Interactions. *mBio*, 2020. **11**(1)doi: 10.1128/mBio.02752-19.

141. Wehrl, H.F., et al., Simultaneous PET-MRI reveals brain function in activated and resting state on metabolic, hemodynamic and multiple temporal scales. *Nat Med*, 2013. **19**(9): p. 1184-1189 doi: 10.1038/nm.3290.

142. Demeestere, J., et al., Review of Perfusion Imaging in Acute Ischemic Stroke: From Time to Tissue. *Stroke*, 2020. **51**(3): p. 1017-1024 doi: 10.1161/STROKEAHA.119.028337.

143. Gorelashvili, M.G. *Investigation of megakaryopoiesis and the acute phase of ischemic stroke by advanced fluorescence microscopy.* Doctoral thesis, 2018

144. Gob, V., et al., Infarct growth precedes cerebral thrombosis following experimental stroke in mice. *Sci Rep*, 2021. **11**(1): p. 22887 doi: 10.1038/s41598-021-02360-6.

145. Stegner, D., et al., Thrombopoiesis is spatially regulated by the bone marrow vasculature. *Nat Commun*, 2017. **8**(1): p. 127 doi: 10.1038/s41467-017-00201-7.

146. Cloutier, N., et al., Platelets can enhance vascular permeability. *Blood*, 2012. **120**(6): p. 1334-1343 doi: 10.1182/blood-2012-02-413047.

147. Wolff, A., et al., In Vitro Blood-Brain Barrier Models-An Overview of Established Models and New Microfluidic Approaches. *J Pharm Sci*, 2015. **104**(9): p. 2727-2746 doi: 10.1002/jps.24329.

148. Kuzmanov, I., et al., An In Vitro Model of the Blood-brain Barrier Using Impedance Spectroscopy: A Focus on T Cell-endothelial Cell Interaction. *J Vis Exp*, 2016(118)doi: 10.3791/54592.

149. Schuhmann, M.K. and F. Fluri, Effects of Fullerenols on Mouse Brain Microvascular Endothelial Cells. *Int J Mol Sci*, 2017. **18**(8)doi: 10.3390/ijms18081783.

150. Girven, K.S. and D.R. Sparta, Probing Deep Brain Circuitry: New Advances in in Vivo Calcium Measurement Strategies. *ACS Chem Neurosci*, 2017. **8**(2): p. 243-251 doi: 10.1021/acschemneuro.6b00307.

151. Tvrdik, P. and M.Y.S. Kalani, In Vivo Imaging of Microglial Calcium Signaling in Brain Inflammation and Injury. *Int J Mol Sci*, 2017. **18**(11)doi: 10.3390/ijms18112366.

152. Chen, T.W., et al., Ultrasensitive fluorescent proteins for imaging neuronal activity. *Nature*, 2013. **499**(7458): p. 295-300 doi: 10.1038/nature12354.

153. Bushnell, C. and G. Saposnik, Evaluation and management of cerebral venous thrombosis. *Continuum (Minneap Minn)*, 2014. **20**(2 Cerebrovascular Disease): p. 335-351 doi: 10.1212/01.CON.0000446105.67173.a8.

154. Rayes, J., S.P. Watson, and B. Nieswandt, Functional significance of the platelet immune receptors GPVI and CLEC-2. *J Clin Invest*, 2019. **129**(1): p. 12-23 doi: 10.1172/JCI122955.

155. May, F. *The role of the (hem)ITAM-coupled receptors C-type lectin-like receptor 2 (CLEC-2) and Glycoprotein (GP) VI for platelet function: in vitro and in vivo studies in mice.* Doctoral thesis, 2011

156. Lorenz, V. *Cellular regulation of the hemITAM-coupled receptor C-type lectin-like receptor 2 (CLEC-2): In vitro and in vivo studies in mice.* Doctoral thesis, 2015

157. Xiong, B., et al., Precise Cerebral Vascular Atlas in Stereotaxic Coordinates of Whole Mouse Brain. *Front Neuroanat*, 2017. **11**: p. 128 doi: 10.3389/fnana.2017.00128.

158. Mackman, N., et al., Therapeutic strategies for thrombosis: new targets and approaches. *Nat Rev Drug Discov*, 2020. **19**(5): p. 333-352 doi: 10.1038/s41573-020-0061-0.

159. Cherpokova, D., et al., SLAP/SLAP2 prevent excessive platelet (hem)ITAM signaling in thrombosis and ischemic stroke in mice. *Blood*, 2015. **125**(1): p. 185-194 doi: 10.1182/blood-2014-06-580597.

160. Langhauser, F., et al., Kininogen deficiency protects from ischemic neurodegeneration in mice by reducing thrombosis, blood-brain barrier damage, and inflammation. *Blood*, 2012. **120**(19): p. 4082-4092 doi: 10.1182/blood-2012-06-440057.

161. Dittmeier, M., et al., Pretreatment with rivaroxaban attenuates stroke severity in rats by a dual antithrombotic and anti-inflammatory mechanism. *Thromb Haemost*, 2016. **115**(4): p. 835-843 doi: 10.1160/TH15-08-0631.

162. Adamczak, J.M., et al., In vivo bioluminescence imaging of vascular remodeling after stroke. *Front Cell Neurosci*, 2014. **8**: p. 274 doi: 10.3389/fncel.2014.00274.

163. Eisinger, F., J. Patzelt, and H.F. Langer, The Platelet Response to Tissue Injury. *Front Med (Lausanne)*, 2018. **5**: p. 317 doi: 10.3389/fmed.2018.00317.

164. Massberg, S., et al., Platelets secrete stromal cell-derived factor 1alpha and recruit bone marrow-derived progenitor cells to arterial thrombi in vivo. *J Exp Med*, 2006. **203**(5): p. 1221-1233 doi: 10.1084/jem.20051772.

165. Schuhmann, M.K., et al., Platelets and lymphocytes drive progressive penumbral tissue loss during middle cerebral artery occlusion in mice. *J Neuroinflammation*, 2021. **18**(1): p. 46 doi: 10.1186/s12974-021-02095-1.

166. Schuhmann, M.K., et al., CD84 Links T Cell and Platelet Activity in Cerebral Thrombo-Inflammation in Acute Stroke. *Circ Res*, 2020. **127**(8): p. 1023-1035 doi: 10.1161/CIRCRESAHA.120.316655.

167. Bernardo-Castro, S., et al., Pathophysiology of Blood-Brain Barrier Permeability Throughout the Different Stages of Ischemic Stroke and Its Implication on Hemorrhagic Transformation and Recovery. *Front Neurol*, 2020. **11**: p. 594672 doi: 10.3389/fneur.2020.594672.

168. Navarro-Sobrino, M., et al., A large screening of angiogenesis biomarkers and their association with neurological outcome after ischemic stroke. *Atherosclerosis*, 2011. **216**(1): p. 205-211 doi: 10.1016/j.atherosclerosis.2011.01.030.

169. Thomsen, M.S., et al., The blood-brain barrier studied in vitro across species. *PLoS One*, 2021. **16**(3): p. e0236770 doi: 10.1371/journal.pone.0236770.

170. Shaik, N.F., R.F. Regan, and U.P. Naik, Platelets as drivers of ischemia/reperfusion injury after stroke. *Blood Adv*, 2021. **5**(5): p. 1576-1584 doi: 10.1182/bloodadvances.2020002888.

171. Koch, H., K. Hofmann, and N. Brose, Definition of Munc13-homology-domains and characterization of a novel ubiquitously expressed Munc13 isoform. *Biochem J*, 2000. **349**(Pt 1): p. 247-253 doi: 10.1042/0264-6021:3490247.

172. Yilmaz, G., et al., Role of T lymphocytes and interferon-gamma in ischemic stroke. *Circulation*, 2006. **113**(17): p. 2105-2112 doi: 10.1161/CIRCULATIONAHA.105.593046.

173. Kleinschnitz, C., et al., Early detrimental T-cell effects in experimental cerebral ischemia are neither related to adaptive immunity nor thrombus formation. *Blood*, 2010. **115**(18): p. 3835-3842 doi: 10.1182/blood-2009-10-249078.

174. Gleissner, C.A., P. von Hundelshausen, and K. Ley, Platelet chemokines in vascular disease. *Arterioscler Thromb Vasc Biol*, 2008. **28**(11): p. 1920-1927 doi: 10.1161/ATVBAHA.108.169417.

175. Zaremba, J., P. Skrobanski, and J. Losy, The level of chemokine CXCL5 in the cerebrospinal fluid is increased during the first 24 hours of ischaemic stroke and correlates with the size of early brain damage. *Folia Morphol (Warsz)*, 2006. **65**(1): p. 1-5 doi.

176. Levine, P.H., et al., Human platelet factor 4: preparation from outdated platelet concentrates and application in cerebral vascular disease. *Am J Hematol*, 1981. **10**(4): p. 375-385 doi: 10.1002/ajh.2830100407.

177. Mei, J., et al., Cxcr2 and Cxcl5 regulate the IL-17/G-CSF axis and neutrophil homeostasis in mice. *J Clin Invest*, 2012. **122**(3): p. 974-986 doi: 10.1172/JCI60588.

178. Greenberg, D.A. and K. Jin, Vascular endothelial growth factors (VEGFs) and stroke. *Cell Mol Life Sci*, 2013. **70**(10): p. 1753-1761 doi: 10.1007/s00018-013-1282-8.

179. Weis, S.M. and D.A. Cheresh, Pathophysiological consequences of VEGF-induced vascular permeability. *Nature*, 2005. **437**(7058): p. 497-504 doi: 10.1038/nature03987.

180. Zhang, Z.G., et al., VEGF enhances angiogenesis and promotes blood-brain barrier leakage in the ischemic brain. *J Clin Invest*, 2000. **106**(7): p. 829-838 doi: 10.1172/JCI9369.

181. Sil, S., et al., PDGF/PDGFR axis in the neural systems. *Mol Aspects Med*, 2018. **62**: p. 63-74 doi: 10.1016/j.mam.2018.01.006.

182. Kazlauskas, A., PDGFs and their receptors. *Gene*, 2017. **614**: p. 1-7 doi: 10.1016/j.gene.2017.03.003.

183. Hutanu, A., et al., Plasma Biomarkers as Potential Predictors of Functional Dependence in Daily Life Activities after Ischemic Stroke: A Single Center Study. *Ann Indian Acad Neurol*, 2020. **23**(4): p. 496-503 doi: 10.4103/aian.AIAN_74_19.

184. Grosse, G.M., et al., Circulating Cytokines and Growth Factors in Acute Cerebral Large Vessel Occlusion-Association with Success of Endovascular Treatment. *Thromb Haemost*, 2021doi: 10.1055/a-1544-5431.

185. Shen, J., et al., PDGFR-beta restores blood-brain barrier functions in a mouse model of focal cerebral ischemia. *J Cereb Blood Flow Metab*, 2019. **39**(8): p. 1501-1515 doi: 10.1177/0271678X18769515.

186. Vasefi, M. and M.A. Beazely, Neuroprotective effects of direct activation and transactivation of PDGFβ receptors. *Vessel Plus*, 2020. **4**: p. 24 doi: 10.20517/2574-1209.2020.16.

187. Ma, Q., et al., PDGFR-alpha inhibition preserves blood-brain barrier after intracerebral hemorrhage. *Ann Neurol*, 2011. **70**(6): p. 920-931 doi: 10.1002/ana.22549.

188. Shayan, G., et al., Murine in vitro model of the blood-brain barrier for evaluating drug transport. *Eur J Pharm Sci*, 2011. **42**(1-2): p. 148-155 doi: 10.1016/j.ejps.2010.11.005.

189. Appelt-Menzel, A., et al., Establishment of a Human Blood-Brain Barrier Co-culture Model Mimicking the Neurovascular Unit Using Induced Pluri- and Multipotent Stem Cells. *Stem Cell Reports*, 2017. **8**(4): p. 894-906 doi: 10.1016/j.stemcr.2017.02.021.

190. Chen, R., et al., New Insight Into Neutrophils: A Potential Therapeutic Target for Cerebral Ischemia. *Front Immunol*, 2021. **12**: p. 692061 doi: 10.3389/fimmu.2021.692061.

191. Neumann, J., et al., Very-late-antigen-4 (VLA-4)-mediated brain invasion by neutrophils leads to interactions with microglia, increased ischemic injury and impaired behavior in experimental stroke. *Acta Neuropathol*, 2015. **129**(2): p. 259-277 doi: 10.1007/s00401-014-1355-2.

192. Herz, J., et al., Role of Neutrophils in Exacerbation of Brain Injury After Focal Cerebral Ischemia in Hyperlipidemic Mice. *Stroke*, 2015. **46**(10): p. 2916-2925 doi: 10.1161/STROKEAHA.115.010620.

193. Boivin, G., et al., Durable and controlled depletion of neutrophils in mice. *Nat Commun*, 2020. **11**(1): p. 2762 doi: 10.1038/s41467-020-16596-9.

194. Jackman, K.A., et al., Reduction of cerebral infarct volume by apocynin requires pretreatment and is absent in Nox2-deficient mice. *Br J Pharmacol*, 2009. **156**(4): p. 680-688 doi: 10.1111/j.1476-5381.2008.00073.x.

195. Zhang, L., et al., NADPH Oxidase: A Potential Target for Treatment of Stroke. *Oxid Med Cell Longev*, 2016. **2016**: p. 5026984 doi: 10.1155/2016/5026984.

196. Kleinschnitz, C., et al., Post-stroke inhibition of induced NADPH oxidase type 4 prevents oxidative stress and neurodegeneration. *PLoS Biol*, 2010. **8**(9)doi: 10.1371/journal.pbio.1000479.

197. Papayannopoulos, V., Neutrophil extracellular traps in immunity and disease. *Nat Rev Immunol*, 2018. **18**(2): p. 134-147 doi: 10.1038/nri.2017.105.

198. Jimenez-Alcazar, M., et al., Host DNases prevent vascular occlusion by neutrophil extracellular traps. *Science*, 2017. **358**(6367): p. 1202-1206 doi: 10.1126/science.aam8897.

199. Perez Koldenkova, V. and T. Nagai, Genetically encoded Ca(2+) indicators: properties and evaluation. *Biochim Biophys Acta*, 2013. **1833**(7): p. 1787-1797 doi: 10.1016/j.bbamcr.2013.01.011.

200. Akerboom, J., et al., Optimization of a GCaMP calcium indicator for neural activity imaging. *J Neurosci*, 2012. **32**(40): p. 13819-13840 doi: 10.1523/JNEUROSCI.2601-12.2012.

201. Gee, J.M., et al., Imaging activity in neurons and glia with a Polr2a-based and cre-dependent GCaMP5G-IRES-tdTomato reporter mouse. *Neuron*, 2014. **83**(5): p. 1058-1072 doi: 10.1016/j.neuron.2014.07.024.

202. Cai, B., et al., A cell-based functional assay using a green fluorescent protein-based calcium indicator dCys-GCaMP. *Assay Drug Dev Technol*, 2014. **12**(6): p. 342-351 doi: 10.1089/adt.2014.584.

203. Nesbitt, W.S., et al., Intercellular calcium communication regulates platelet aggregation and thrombus growth. *J Cell Biol*, 2003. **160**(7): p. 1151-1161 doi: 10.1083/jcb.200207119.

204. Brill, A., et al., von Willebrand factor-mediated platelet adhesion is critical for deep vein thrombosis in mouse models. *Blood*, 2011. **117**(4): p. 1400-1407 doi: 10.1182/blood-2010-05-287623.

205. Sang, Y., et al., Interplay between platelets and coagulation. *Blood Rev*, 2021. **46**: p. 100733 doi: 10.1016/j.blre.2020.100733.

206. Ferro, J.M., et al., European Stroke Organization guideline for the diagnosis and treatment of cerebral venous thrombosis - endorsed by the European Academy of Neurology. *Eur J Neurol*, 2017. **24**(10): p. 1203-1213 doi: 10.1111/ene.13381.

207. Ley, K., et al., Integrin-based therapeutics: biological basis, clinical use and new drugs. *Nat Rev Drug Discov*, 2016. **15**(3): p. 173-183 doi: 10.1038/nrd.2015.10.

208. Durrant, T.N., M.T. van den Bosch, and I. Hers, Integrin alphaIIbbeta3 outside-in signaling. *Blood*, 2017. **130**(14): p. 1607-1619 doi: 10.1182/blood-2017-03-773614.

209. Yang, M., et al., Platelet Glycoprotein IIb/IIIa Receptor Inhibitor Tirofiban in Acute Ischemic Stroke. *Drugs*, 2019. **79**(5): p. 515-529 doi: 10.1007/s40265-019-01078-0.

210. Authors/Task Force, m., et al., 2014 ESC/EACTS Guidelines on myocardial revascularization: The Task Force on Myocardial Revascularization of the European Society of Cardiology (ESC) and the European Association for Cardio-Thoracic Surgery (EACTS)Developed with the special contribution of the European Association of Percutaneous Cardiovascular Interventions (EAPCI). *Eur Heart J*, 2014. **35**(37): p. 2541-2619 doi: 10.1093/eurheartj/ehu278.

211. Boylan, B., et al., Anti-GPVI-associated ITP: an acquired platelet disorder caused by autoantibody-mediated clearance of the GPVI/FcRgamma-chain complex from the human platelet surface. *Blood*, 2004. **104**(5): p. 1350-1355 doi: 10.1182/blood-2004-03-0896.

212. Dutting, S., M. Bender, and B. Nieswandt, Platelet GPVI: a target for antithrombotic therapy?! *Trends Pharmacol Sci*, 2012. **33**(11): p. 583-590 doi: 10.1016/j.tips.2012.07.004.

213. Baldini, T., et al., Cerebral venous thrombosis and severe acute respiratory syndrome coronavirus-2 infection: A systematic review and meta-analysis. *Eur J Neurol*, 2021. **28**(10): p. 3478-3490 doi: 10.1111/ene.14727.

214. Cavalcanti, D.D., et al., Cerebral Venous Thrombosis Associated with COVID-19. *AJNR Am J Neuroradiol*, 2020. **41**(8): p. 1370-1376 doi: 10.3174/ajnr.A6644.

215. von Bruhl, M.L., et al., Monocytes, neutrophils, and platelets cooperate to initiate and propagate venous thrombosis in mice in vivo. *J Exp Med*, 2012. **209**(4): p. 819-835 doi: 10.1084/jem.20112322.

216. Montoro-Garcia, S., et al., The Role of Platelets in Venous Thromboembolism. *Semin Thromb Hemost*, 2016. **42**(3): p. 242-251 doi: 10.1055/s-0035-1570079.

217. Greinacher, A., et al., Thrombotic Thrombocytopenia after ChAdOx1 nCov-19 Vaccination. *N Engl J Med*, 2021. **384**(22): p. 2092-2101 doi: 10.1056/NEJMoa2104840.

218. Schultz, N.H., et al., Thrombosis and Thrombocytopenia after ChAdOx1 nCoV-19 Vaccination. *N Engl J Med*, 2021. **384**(22): p. 2124-2130 doi: 10.1056/NEJMoa2104882.

219. Scully, M., et al., Pathologic Antibodies to Platelet Factor 4 after ChAdOx1 nCoV-19 Vaccination. *N Engl J Med*, 2021. **384**(23): p. 2202-2211 doi: 10.1056/NEJMoa2105385.

220. Qiao, J., et al., The platelet Fc receptor, FcgammaRIIa. *Immunol Rev*, 2015. **268**(1): p. 241-252 doi: 10.1111/imr.12370.

221. Smith, P., et al., Mouse model recapitulating human Fcgamma receptor structural and functional diversity. *Proc Natl Acad Sci U S A*, 2012. **109**(16): p. 6181-6186 doi: 10.1073/pnas.1203954109.

6 Appendix

6.1 Abbreviations

2-PM	2-photon microscopy
A	Ampere
aa	Amino acid
AC	Adenylcylclase
ADP	Adenosine diphosphate
AJ	Adherens junction
Ang1	Angiopioetin-1
approx.	Approximately
°C	Degree celsius
ASA	Acetyl salicylic acid
ATP	Adenosine triphosphate
BBB	Blood brain barrier
bFGF	Basic fibroblast growth factor
Bq	Becquerel
BSA	Bovine serum albumin
c	Contralateral
CCL-2	CC-chemokine ligand 2
CD	Cluster of differentiation
CLEC-2	C-type lectin receptor 2
CNS	Central nervous system
COVID	Coronavirus disease
CRP	Collagen related peptide
CSF	Cerebrospinal fluid
CVT	Cerebral vein thrombosis
CXCL	Chemokine (C-X-C motif) ligand
DAG	Diacylglycerol
DAMP	Damage-associated molecular pattern
DAPI	4'-6-Diamino-2-phenylindole
DIC	Differential interference contrast
DMEM	Dulbecco's modified eagle medium
DNA	Deoxyribonucleic acid
EC	Endothelial cell
ECL	Enhanced chemiluminescence
ECM	Extracellular matrix

EGF	Epidermal growth factor
ESL-1	E-selectin-ligand-1
EU	European Union
f.c.	Final concentration
FACS	Fluorescence-activated cell sorting
$FcR\gamma$	Fc receptor γ chain
FCS	Fetal calf serum
FGF	Fibroblast growth factor
FITC	Fluorescein 5-isothiocyanate
FSC	Forward scatter
g	Gram
g	Gravitation force
GAPDH	Glyceraldehyde 3-phosphate dehydrogenase
GECI	Genetically introduced Ca^{2+} indicators
GFP	Green fluorescent protein
GP	Glycoprotein
GPCR	G protein coupled receptor
h	Hours
H&E	Hematoxylin and eosin
HMGB-1	High-Mobility-Group-Protein B1
HRP	Horseradish peroxidase
HT	Hemorrhagic transformation
i	Ipsilateral
Ig	Immunoglobulin
i.p.	Intraperitoneal
i.v.	Intravenous
I/R	Ischemia/Reperfusion
ICH	Intracerebral hemorrhage
IGF	Insulin-like growth factor
IP_3	Inositol-1,4,5-triphosphate
ITAM	Immunoreceptor tyrosine-based activation motif
JAM	Junctional adhesion molecule
kDa	Kilodalton
Kin	Knockin
KO	Knockout
l	Liter
LASCA	Laser Speckle Contrast Imaging

LAT	Linker for activation of T cells
LFA-1	Lymphocyte function-associated antigen-1
LMWH	Low molecular weight heparin
LPS	Lipopolysaccharide
LSFM	Light sheet fluorescence microscopy
m	Meter
M	Molar
MBMEC	Murine brain microvascular endothelial cells
MCA	Middle cerebral artery
MFI	Mean fluorescence intensity
min	Minute
MK	Megakaryocyte
MMP	Metalloproteinase
mPDPN	Murine Podoplanin
MPO	Myeloperoxidase
MRI	Magnetic resonance imaging
MT	Mechanical thrombectomy
NADPH	Nicotinamide adenine dinucleotide phosphate
Nbeal2	Neurobeachin-like protein 2
Ncf1	Neutrophil cytosolic factor 1
NET	Neutrophil extracellular trap
NOX2	NADPH oxidase 2
NVU	Neurovascular unit
o/n	Over night
OCW	Open Cranial Window
PAD4	Peptidyl arginase deaminase 4
PAGE	Polyacrylamide gel electrophoresis
PAR	Protease-activated receptor
PBS	Phosphate buffered saline
PCR	Polymerase chain reaction
PDGF	Platelet derived growth factor
PE	Phycoerythrin
PET	Positron-electron tomography
PF4	Platelet factor 4
PFA	Paraformaldehyde
PGI_2	Prostacyclin 2
PI3K	Phosphoinositide-3-kinase

PIP_2	Phosphatidylinositol-4,5-phosphate
PIP_3	Phosphatidylinositol-3,4,5-phosphate
PL	Phospholipase
PMA	Phorbol 12-myristate 13-acetate
PMCA	Plasma membrane Ca^{2+} ATPase
PMN	Polymorphonucelar leukocyte
pPC	Peripheral platelet counts
PRP	Platelet rich plasma
PSGL-1	P-Selectin glycoprotein ligand-1
RNS	Reactive nitrogen species
ROCE	Receptor-operated calcium entry
ROS	Reactive oxygen species
(r)tPA	(Recombinant) tissue Plasminogen Activator
rpm	Revolutions per minute
RPMI	Roswell Park Memorial Institute
RT	Room temperature
s	Second
SAH	Subarachnoidal hemorrhage
SD	Standard deviation
SDF-1	Stromal cell-derived factor 1
SDS	Sodium dodecyl sulphate
SEM	Scanning electron microscopy
SEM	Standard error of the mean
SERCA	Sarcoplasmic/endoplasmic Ca^{2+} ATPase
SFK	Src family kinase
SLP-76	SH2 domain-containing leukocyte protein of 76 kDa
SOCE	Store-operated calcium entry
SSC	Side scatter
SSS	Superior sagittal sinus
Syk	Spleen tyrosine kinase
TBS	Tris buffered saline
TEER	Transendothelial electrical resistance
TF	Tissue factor
TJ	Tight junction
tMCAO	Transient middle cerebral artery occlusion
TNFα	Tumor necrosis factor α
TTC	2,3,5-triphenyltetrazolium chloride

TXA_2	Thromboxane A_2
U	Unit
UV	Ultraviolet
V	Volt
VCAM-1	Vascular cell adhesion protein-1
VEGF	Vascular endothelial growth factor
VLA-4	Very late antigen-4
vWF	von Willebrand factor
W	Watt
WT	Wildtype
ZO-1	Zonula occludens 1
Ω	Ohm

6.2 Script for image processing

Script used for the quantification of holes between MBMECs (2.2.7.2)

```
# Segmentation of channel 2: CD31 staining

# 1. Importing of all required function from scikit-image
from skimage.filters.rank import entropy
from skimage.morphology import disk, label
from skimage import io
from skimage.segmentation import watershed
from skimage.measure import label, regionprops
from skimage.color import label2rgb

# ...from matplotlib and numpy
import matplotlib.pyplot as plt
import matplotlib.patches as mpatches
from matplotlib import interactive
import numpy as np
# ...glob: the glob module is used to retrieve files/pathnames matching a
specified pattern
import glob

# 2. set the parameter
interactive(True)  # the image will be shown
dpi = 100 # Arbitrary. The number of pixels in the image will always be
identical
list_labels = []
list_areas = []

# Define thresholds: need to be set according to entropy in holes
threshold_background = 1.5 #  all pixel with entropy lower will be assigned
to background
threshold_cell = 3.0 # all pixel with entropy higher will be assigned to
filaments

# 3. Select the input data
# paste the complete path to your data here in " "
# do not delete the "r"
img = io.imread(r"…")
total_nr_of_pixel = img.size  # get number of pixel per image

# 4. Generate the entropy image based on the original image
entropy_img = entropy(img, disk(5)) # disk size in pixel gives search area

histogram = plt.hist(entropy_img.flat, bins=100)
plt.savefig('histogram_entropy_whole.png')

height1, width1 = np.array(entropy_img.shape, dtype=float) / dpi
fig1 = plt.figure(figsize=(width1, height1), dpi=dpi)
ax1 = fig1.add_axes([0, 0, 1, 1])
ax1.axis('off')
ax1.imshow(entropy_img, interpolation='none') # obtained is the entropy
image!
fig1.savefig('Entropy_whole' + ".tif",
bbox_inches='tight',transparent=True, pad_inches=0, format="tif")

# 5. Watershed segmentation
# A: generate empty array with zeros
markers = np.zeros(entropy_img.shape, dtype=np.uint)

# B: Place markers in regions selected regions
# non-indexed regions are 0!
markers[(entropy_img < threshold_background)] = 2 # nearly absent
flourescence of holes in the cell layer
```

```
markers[(entropy_img > threshold_cell)] = 1 # highly flourescent cell
boundaries

# C: watershed segmentation
segmentation = watershed(entropy_img, markers) # returns binary image

# 6. closing holes
from scipy.ndimage.morphology import binary_closing, binary_fill_holes
image_closed = binary_closing(segmentation - 1, structure=np.ones((5,5)))
bool_img = binary_fill_holes(image_closed)
segmentation_filled = np.copy(bool_img.astype(np.uint8) * 255)
#plt.imshow(segmentation_filled)

height2, width2 = np.array(segmentation_filled.shape, dtype=float) / dpi
fig2 = plt.figure(figsize=(width2, height2), dpi=dpi)
ax2 = fig2.add_axes([0, 0, 1, 1])
ax2.axis('off')
ax2.imshow(segmentation_filled, interpolation='none') # obtained is the
segmented image!
fig2.savefig('Segmentation_whole' + ".tif",
bbox_inches='tight',transparent=True, pad_inches=0, format="tif")

# 7. getting statistics
binary_image = segmentation_filled == 0
covered_area = np.sum(binary_image == False)  # calculate the covered area
in pixel
covered_area_in_perc = covered_area/ total_nr_of_pixel * 100  # convert
calculated are to percent
print("Covered area [px]:", covered_area)
print("Covered area [%]:", covered_area_in_perc)

# label image regions
label_image = label(segmentation_filled)
# to make the background transparent, pass the value of `bg_label`,
# and leave `bg_color` as `None` and `kind` as `overlay`
image_label_overlay = label2rgb(label_image, image=img, bg_label=0)

height3, width3, nr_of_channel = np.array(image_label_overlay.shape,
dtype=float) / dpi
fig3 = plt.figure(figsize=(width3, height3), dpi=dpi)
ax3 = fig3.add_axes([0, 0, 1, 1])
ax3.axis('off')
ax3.imshow(image_label_overlay, interpolation='none')
fig3.savefig('Overlay_whole' + ".tif",
bbox_inches='tight',transparent=True, pad_inches=0, format="tif")
plt.show()

region = regionprops(label_image)

for region in regionprops(label_image):
    if region.area >= 100:
        list_labels.append(region.label)
        list_areas.append(region.area)
        filename = 'Regions_whole.txt'
        np.savetxt(
            filename,
            np.vstack(
                [
                    list_labels,
                    list_areas
                ]
            ).T,
            delimiter='\t'
        )
```

6.3 Acknowledgements

The work presented in this thesis was accomplished in the group of Prof. Dr. David Stegner at the Institute of Experimental Biomedicine I, University Hospital and Rudolf Virchow Center for Translational Bioimaging, University of Würzburg. During my time as a PhD student from April 2017 to January 2022 many people supported and accompanied me, whom I would like to express my gratitude.

First and foremost, I would like to thank my supervisor Prof. Dr. David Stegner for his constant support and confidence in my abilities. For his mentorship, scientific input and for introducing me to the scientific community by giving me the possibility to present my work at international conferences and symposia. Thank you for helping me develop and grow scientifically and personally throughout the time of my PhD thesis.

I thank the members of my thesis committee, Prof. Dr. Katrin Heinze and Prof. Dr. Guido Stoll for their support, fruitful discussions and for reviewing my thesis.

Many thanks to the TR240-B06-Team for their constant support, valuable discussions, and the nice and inspiring working atmosphere.

I thank the AG Schuhmann from the Department of Neurology for their help and support. Especially Lena for all the performed experiments, her effort and for being so much fun to work with. Thank you for the great teamwork.

I would like to thank the AG Heinze and the team of the core unit fluorescence imaging for access to their microscopes and for their help and support. Especially Jürgen Pinnecker for technical assistance and Dr. Katherina Hemmen for image analysis.

I thank Prof. Dr. Alma Zernecke-Madsen for providing access to the SP8 2-photon microscope.

I would like to thank the Graduate School of Life Sciences and the German Excellence Initiative for the financial support and the team of the GSLS for organizing the study program, the transferable skill courses and their help.

The herein presented work would not have been possible without all the people in the back. Thanks to Dr. Dr. Katharina Remer and the team of the animal facility in the RVZ and ZEMM for their help with the mouse business. Thanks to all technicians and secretaries for supporting me and for their excellent work keeping the institute running.

I thank all current and former members of the AG Stegner for their help and great working atmosphere. Especially Max for introducing me to intravital microscopy and Ewa for her help with genotyping, organ sectioning and immunofluorescence stainings.

I would like to thank the current and former members of the Institute for being a great team and sharing their knowledge with me. Thanks to ‘Office 1’ and ‘Office 2’ for scientific input, support and the nice and cheering working atmosphere. Especially to Julia, Inga, Philipp, Patricia and Yvonne for always having an open ear, the scientific and non-scientific coffee and lunch breaks, their encouragement and many great memories. Special thanks to Sarah who was introducing me to scientific research during my bachelor’s thesis and who was an important factor for me choosing this institute for my doctoral thesis. Thank you for always taking care of me, your constant encouragement, scientific discussions, and your support and help in any situation. Thanks for all the fun moments and great memories in and outside the lab.

Thanks to Julia, Sarah, and Lena for carefully proof-reading this thesis.

I am very grateful for having a loving family and great friends. Without their support I would not be where I am now. Therefore, I would like to thank all of you for your everlasting support and constant encouragement.

Lastly, I would like to thank Thomas for his patience and always believing in me.

6.4 Curriculum vitae

6.5 Publications

6.5.1 Articles

Göb V, Voll MG, Zimmermann L, Hemmen K. Stoll G, Nieswandt B, Schuhmann MK, Heinze KG, Stegner D. Infarct growth precedes cerebral thrombosis following experimental stroke in mice. *Sci Rep* 11(1):22887, doi: 10.1038/s41598-021-02360-6, 2021.

Stegner D*, **Göb V***, Krenzlin V, Beck S, Hemmen K, Schuhmann MK, Schörg BF, Hackenbroch C, May F, Burkard P, Pinnecker J, Zernecke A, Rosenberger P, Greinacher A, Pichler BJ, Heinze KG, Stoll G, Nieswandt B. Foudroyant cerebral venous (sinus) thrombosis triggered through CLEC-2 and GPIIb/IIIa dependent platelet activation. Accepted in *Nat Cardiovasc Res*, 2021.

Heil HS, Aigner M, Maier S, Gupta P, Evers LMC, **Göb V**, Kusch C, Meub M, Nieswandt B, Stegner D, Heinze KG. Mapping densely packed αIIbβ3 receptors in murine blood platelets with expansion microscopy. Accepted in *Platelets*, 2021.

Beck S, Stegner D, Loroch S, Baig AA, **Göb V**, Schumbrutzki C, Eilers E, Sickmann A, May F, Nolte MW, Panousis C, Nieswandt B. Generation of a humanized FXII knock-in mouse – A powerful model system to test novel anti-thrombotic agents. *J Thromb Haemost* 19(11): 2835-40, doi: 10.1111/jth.15488, 2021.

Scheller I*, Beck S*, **Göb V**, Gross C, Neagoe RAI, Aurbach K, Bender M, Stegner D, Nagy Z, Nieswandt B. Thymosin β4 is essential for thrombus formation by controlling the G-actin/F-actin equilibrium in platelets. *Haematologica*, doi: 10.3324/haematol.2021.278537, 2021.

Schuhmann MK, Stoll G, Bieber M, Vögtle T, Hofmann S, **Klaus V**, Kraft P, Seyhan M, Kollikowski AM, Papp L, Heuschmann PU, Pham M, Nieswandt B, Stegner D. CD84 links T cell and platelet activity in cerebral thrombo-inflammation in acute stroke. *Circ Res* 127(8): 1023-35, doi: 10.1161/CIRCRESAHA.120.316655, 2020.

Gorelashvili MG, Angay O, Hemmen K, **Klaus V**, Stegner D, Heinze KG. Megakaryocyte volume modulates bone marrow niche properties and cell migration dynamics. *Haematologica* 105(4):894-904, doi: 10.3324/haematol.2018.202010, 2020.

Stegner D, Hofmann S, Schuhmann MK, Kraft P, Herrmann AM, Popp S, Höhn M, Popp M, **Klaus V**, Post A, Kleinschnitz C, Braun A, Meuth SG, Lesch KP, Stoll G, Kraft R, Nieswandt B. Loss of Orai2-Mediated Capacitative Ca(2+) entry is neuroprotective in acute ischemic stroke. *Stroke* 50(11):3238-45, doi: 10.1161/STROKEAHA.119.025357, 2019.

*Both authors contributed equally

6.5.2 Review

Stegner D*, **Klaus V***, Nieswandt B. Platelets as modulators of cerebral ischemia/reperfusion injury. Front Immunol 10: 2505 (2019) doi: 10.3389/fimmu.2019.02505.

*Both authors contributed equally

6.5.3 Poster presentations

XXVIIInd Congress of the International Society on Thrombosis and Haemostasis, July 2020, Milan (Online):
“A novel reporter mouse line enables *in vivo* imaging of intracellular calcium fluxes in platelets”

International Symposium of the Graduate School of Life Science: EUREKA!, Würzburg, Germany, October 2019:
“Establishment of a genetic mouse model to visualize platelet calcium signaling in vivo”

Symposium of the Collaborative Research Center CRC/TR240, Neckarsulm, Germany, May 2019:
“Modulators of neuro inflammation in the ischemic brain”

International Symposium of the Graduate School of Life Science: EUREKA!, Würzburg, Germany, October 2018:
“Studying ischemia reperfusion injury in the brain using different imaging techniques”

6.6 Affidavit

I hereby confirm that my thesis entitled "Pathomechanisms underlying ischemic stroke" is the result of my own work. I did not receive any help or support from commercial consultants. All sources and/or materials applied are listed and specified in the thesis.

Furthermore, I confirm that this thesis has not yet been submitted as part of another examination process neither in identical nor in similar form.

Würzburg, January 2022

Göb, Vanessa Aline Domenica

6.7 Eidesstattliche Erklärung

Hiermit erkläre ich an Eides statt, die Dissertation „Pathomechanismen des ischämischen Schlaganfalls" eigenständig, d.h. insbesondere selbständig und ohne Hilfe eines kommerziellen Promotionsberaters, angefertigt und keine anderen als die von mir angegebenen Quellen und Hilfsmittel verwendet zu haben.

Ich erkläre außerdem, dass die Dissertation weder in gleicher noch in ähnlicher Form bereits in einem anderen Prüfungsverfahren vorgelegen hat.

Würzburg, Januar 2022

Göb, Vanessa Aline Domenica